Plasma loop and strapping field dynamics: reproducing solar eruptions in the laboratory.

Thesis by

Quoc Bao N. Ha

In Partial Fulfillment of the Requirements

for the Degree of

Doctor of Philosophy

California Institute of Technology

Pasadena, California

2016

(Defended June 16, 2015)

© 2016
Quoc Bao N. Ha
All Rights Reserved

To my parents for their continual support.

Acknowledgments

I want to start by recognizing Paul Bellan, my adviser. My first interaction with Paul was at a plasma physics conference in 2006. I was anxious about presenting my research at such a big conference. Paul was the first person to stop at my poster. He immediately put me at ease with a joke, and we clicked on a scientific, and on a personal level. I knew then that I wanted to go to Caltech to do research with him. The journey since that moment has been thoroughly enjoyable. I am amazed by how Paul sustains a high level of research output, while always making time for his students. He seems to have an endless capability to nurture the growth of his students. He is a great scientist, writer, and mentor. Above all, he is a generous human being, and I am truly blessed to have had the opportunity to grow under his guidance.

Thank you to my thesis committee members: Brent Fultz, Gregg Hallinan, and Jay Polk.

Brent Fultz chaired my candidacy committee. My interactions with Brent have been limited, but pleasant. I never felt rushed when meeting with him, and left those meetings relaxed and confident. Brent makes an effort to share the tasty snacks around his office, and has a natural ability to connect with students. Thank you for guiding me from candidacy to defense.

It is difficult for students in the plasma group, to find faculty members who can relate to our research. It was to my great surprise to learn that Gregg Hallinan researches coronal mass ejections on other stars. Gregg, I am very happy that you are on my committee.

My own interactions with Jay Polk have been pleasant, but I have also learned

a lot about Jay from others. While we were working on plasma physics problem sets, Angie Capece would occasionally mention how grateful she is to have Jay as an adviser. Rory Perkins mentioned that Jay asked some of the most insightful questions during Rory's defense. Jay, I look forward to sharing the bits that I have learned about space and plasma physics with you.

Thank you to the entire plasma group. Eve Stenson, Auna Moser, Deepak Kumar, and Rory Perkins are my senior. Of the four, Deepak is the most senior. Deepak's sense of humor, and his willingness to help the younger students stuck me. Auna and Rory stepped up after Deepak graduated. Both did admirable jobs of leading the way, and knowing what was going on. Rory is a close friend and mentor. I'm grateful for the time that he takes from his busy schedule to call me, and make sure that I'm doing OK. Thanks, man.

The most influential senior grad student to my Caltech experience is Eve Stenson. She shared an office with me and was my mentor while she was here at Caltech. Eve is an excellent writer and thorough scientist. She is an excellent source of laboratory knowledge. I swiveled my chair around countless times to ask her questions, but she never seems to get sick of me. Thank you Eve!

Mark Kendall and I started graduate school together. We fed off each others jokes and I loved hearing the Mark's ridiculous stories. He is an excellent scientist and hilarious friend. Mark, I wish you all the best.

Xiang Zhai and Vernon Chaplin joined the group a little after I did, though we three are finishing at the same. Vernon is funny, disciplined, and an excellent scientist. I'm grateful to both Vernon and his wife, Cathy Chaplin, for their friendship, and their tasty food. Vernon is instrumental in my post-graduation employment. Xiang is my scientist role model. He is funny, productive, and does not hesitate to help others with their work. His extraordinary accomplishments are matched by his authentic sense of modesty, making him a pleasure to work with.

Zachary Tobin joined the group a few years after I did. In research and outside of research, Zach is the guy who does what needs to get done. I'm grateful to Zach for wrestling with the IDL code to get the data acquisition system online.

Magnus Haw is an exceptional dancer, activist, and scientist. As his senior, I'm supposed to mentor him, to temper his expectations about experimental research, and to encourage his personal growth. Instead, I become a better scientist just by interacting with him. His programming skills, his work ethic, and his scientific intuition are top notch. Most importantly, he reminds me to take the time to ask to better questions instead of blindly solving poorly-posed questions. I have a little voice in my head that reminds me: what would Magnus do?

Thank you KB Chai for showing me how to be a productive scientist. The acknowledgments of previous graduate students gush about the benefit of having a post-doc present to model the habits of a successful young scientist. It has been instructive to learn how you approach a challenging experimental task, and how you systematically derive its solution.

To the new grad students, Pakorn Wonwaitayakornkul, Ryan Marshall, and Young Dae Yoon: you guys have to take classes and soak up as much knowledge as possible before the seniors in the group graduate. It is quite a tall order but it is clear to me that all three of you are motivated learners. Keep up the good work.

I want to thank the SURF students Federico Presutti and Patricio Arrangoiz. You guys made my work with Hall sensors a whole lot easier.

Thank you Connie Rodriguez. Eleonora Vorobieff, and Christy Jenstad for your administrative support. I hear horror stories from group alumni about how much worse it can get. You three make the paperwork, and other organizational tasks so easy to complete.

Thank you Dave Felt for help with the electronics. You and Paul provide continuity across different generations of graduate students. Your design tips have saved me hours of troubleshooting.

A great big thank you to machinist Mike Gerfen. You are an excellent machinist and a cool person. May your future be filled with many remote control car races, and many snowboarding extravaganzas. Thank you to Joe Haggerty, Ali Kiani, and Brad over at GALCIT. You guys took care of the precise machining, so that I could focus on drawing pretty shapes on a computer screen.

I am grateful to the support staff (Regina, Jose, and others) who keep Watson immaculate. I have seen Watson restrooms devolve into a terrible mess, and shudder to think of what would happen without the staff's diligence.

Keeping in touch with old friends is incredibly difficult, but Igor Konfisakhar is the exception. This tenacious guy refuses to be forgotten, and is my link to my teenage years. Thanks man.

I've had great new friendships with Tulasi Parashar, Henry Kozachkov, Max Cubillos, Brian Standley, Himanshu Mishra, Angie Capece, Devvrath Khatri, Sidd Bikkannavar, Tommy Nguyen, Matthew Kelly, Andy Lampersky, Scott Geraedts, David Brown, and so many others.

In particular, Henry and Andy were excellent roommates and added flair to my life. Henry's command of the English language is so powerful that I would pay money to listen to his tirades. I'm also harnessing his editing skills for good, which is a euphemism for asking him to read this entire thesis! He is loyal to his friends and family, and is the first person that I would call if I run out of gas while riding a motorcycle on the freeway. Thanks for bailing me out man! As for Andy, I will only say that he is Andy-guy, and that it has been fun.

There are certain people around whom friendships at Caltech are linked. One such person is Paula Popescu, who is a tireless and caring friend. She organizes themed parties and fun outings, and is a binding force for many physics and applied physics friends, including Itamar Yaakov, Brian Willett, Kevin Engel, Evan O'Connor, Dan Betea, Laura Book, Essie, Milevoje Lukic, and Kari Hodge.

The Caltech Ballroom Dance Club has been an essential part of my experience here at Caltech. I want to acknowledge the many friendships, including Neil Halelamien, Catherine Beni, Raj Kulkarni, Artemis Ailianou, Vivian Zhang, Connie Wang, Jennifer Walker, Sophianna Banholzer, Caitlin Scott, Jay Daigle, Tom Tyranowski, Eduardo Garcia, Raina Storer, Lydia Dennis, Jessie Rosenberg, Victoria Chernow, Megan and Robert Nix, and Wendy Li. In particular, I want to thank Neil Halelamien for being a trusted confidant, and a dear friend. I also want to acknowledge Catherine Beni for being an exceptional individual in so many ways. Caltech is a

nexus for talented people, and Catherine is a model for the excellence that comes from hard work and incredible intellect. She also plays a mean game of Super Smash Brothers, and is a wonderful friend. To her, I say: "MUD!"

One of the many treasures at Caltech are the folks at the Caltech Y. I've had the pleasure of working with Alycen Chan, Liz Jackman, Athena Castro, Greg Fletcher, and Christopher Kealy. The Caltech Y keeps Caltech students sane by organizing volunteering opportunities, hiking expeditions, movie outings, final exam decompression, and so much more. They have made my time at Caltech enjoyable, and I see them doing the same for many other students.

I want to thank Tom Mannion for his role in my development as a leader and a chef. Tom, Denise Okamoto, and Lorrie Yamakazi ensure that students have a blast at Caltech.

I would like to acknowledge Susan Hackwood and everyone at the California Council of Science and Technology for their role in my growth as a leader. Susan invited me to join her for CCST meetings and introduced me to many established scientists and policy makers. A tremendous portion of my growth can be attributed to Susan's time and attention. She is my role model, and I hope to make the same impact on those that I meet, as Susan has done for me.

Another part of my growth came from pursuit of Aikido. I owe a deep gratitude to Tim Sullivan and Erik Henriksen for introducing me to this fine art. They have both poured countless hours into my practice. In particular, I wanted to thank Tim for his mentoring and his friendship. One of my darkest times in graduate school came after realizing that I had wasted two years due to a miscalculation. Tim helped me recover physical and mentally from despair. The quirky British humor is a tremendous plus!

To all my friends at Daiwa: Hideki and Tomoko Okuda, Michael Head, Tom Atherton, Crystal Siri, Birte Feld, Evon and Jane Hochstein, Rick, Florian Morino, Eric, and so many others. Your endless friendships and open arms were welcome sights whenever I trained at the dojo. I want to particularly thank the late Jack Arnold Sensei and the late Toma Rosenzweig. They are both great martial artists with gentle souls and warm hearts.

If I were to claim that I have a second family, it would be the Hurt family. I thank Nicole Bouley-Ford and Will Ford for introducing me to the Hurts. I cherish the discussions about leadership and management with Bill Hurt. Sally Hurt is kind, intelligent, and full of bright smiles. Bill and Sally embody many of the traits that I hold in high regard: modesty, generosity, kindness, and a deep love for the people around them. These traits extend to the rest of the Hurt family and I want to thank Bernadette Glenn, Douglas Murray, Mark Purnell, Kelly Purnell, and their many children, including Alex, Lydia, Kate, Kristen, Stephanie, Molly, Emmy. It has been wonderful to spend time with you all. I want to thank Bernadette for being an advocate and mentor. It is my great pleasure to connect Bassam Helou with the Hurt family. Bassam has done a wonderful job of integrating with the Hurt family, and I am confident that he will do well. Finally, I want to thank Vivian for her friendship and support. She has my back when I needed help and is a model nurse.

I've had the pleasure of being close to Jamie Garman for many years. We connected on a deep level, and a large part of my personal growth can be attributed to this intelligent, beautiful, and driven woman; she brings out my silliness and knows how to make me laugh, even under the most distressing of times. Perhaps her greatest contribution to my growth is that she taught me how to recognize my own needs, and to speak up for what I want. For that and so much more, she has my deepest gratitude.

Last but certainly not least, I would like to thank my family. Those in my family do not express our love verbally. Instead, my parents work tirelessly to support us; I can not believe that they raised a family on a graduate student salary! My parents demonstrate their love through their unwavering devotion and support, as well as a plethora of "loving" insults. Being called a "monkey" in my childhood was annoying, but I cherish such playful insults in adulthood. To my sister, for putting up with with me as an older brother, and for dealing with having similar names while growing up: that was really confusing! You have grown so much, and are making a difference in the world while I'm still chugging away as a student. I can always count on you to fiercely defend your brothers and to tell hilarious stories. To my little brother, for

growing up to be a cool guy: the eleven years between us did not stop us from having close bond. I'm very glad that you are around to take care of our parents while I am in grad school. You are a reliable guy, and I know that I can count on you.

Abstract

Coronal mass ejections (CMEs) are dramatic eruptions of large, plasma structures from the Sun. These eruptions are important because they can harm astronauts, damage electrical infrastructure, and cause auroras. A mysterious feature of these eruptions is that plasma-filled solar flux tubes first evolve slowly, but then suddenly erupt. One model, torus instability, predicts an explosive-like transition from slow expansion to fast acceleration, if the spatial decay of the ambient magnetic field exceeds a threshold.

We create arched, plasma filled, magnetic flux ropes similar to CMEs. Small, independently-powered auxiliary coils placed inside the vacuum chamber produce magnetic fields above the decay threshold that are strong enough to act on the plasma. When the strapping field is not too strong and not too weak, expansion force build up while the flux rope is in the strapping field region. When the flux rope moves to a critical height, the plasma accelerates quickly, corresponding to the observed slow-rise to fast-acceleration of most solar eruptions. This behavior is in agreement with the predictions of torus instability.

Historically, eruptions have been separated into gradual CMEs and impulsive CMEs, depending on the acceleration profile. Recent numerical studies question this separation. One study varies the strapping field profile to produce gradual eruptions and impulsive eruptions, while another study varies the temporal profile of the voltage applied to the flux tube footpoints to produce the two eruption types. Our experiment reproduced these different eruptions by changing the strapping field magnitude, and the temporal profile of the current trace. This suggests that the same physics underlies both types of CME and that the separation between impulsive and gradual

classes of eruption is artificial.

Contents

List of Figures

List of Tables

Chapter 1

Introduction

1.1 Thesis outline

This thesis is written for two separate audiences: (i) thesis committee members who are presumed to be interested in the results and (ii) future graduate students, who are presumed to be interested in the details. As such, the thesis main body attempts to be succinct with only the relevant details, whereas the appendix is lengthy. The reader is encouraged to peruse the appendix to view useful definitions, mathematical relationships, nuts and bolts, and an in-depth look at some of the solar models. Due to the organization of this thesis, there will be some repetition between the main body and the appendix.

The basic structure of the thesis is as follows. The introduction motivates the study of the sun, presents a brief introduction to plasma, describes the experimental setup, and defines important solar terminology. Chapter 2 is dedicated to the reproduction of the slow rise to fast acceleration of a solar eruption. This chapter contains an overview of the debate, the set-up, a generalized implementation of torus instability, results, and discussions addressing important questions in solar physics. Chapter 3 gives the conclusion. The conscious decision to have a single main chapter is due to the time restrictions for thesis writing.

1.2 The sun

It is difficult to exaggerate the importance of the Sun to life on Earth. Evidence of the prime role of the Sun is evident in its status as a deity among human civilizations and cultures[1]. With the power to sustain life comes the power to harm, and the sun is certainly capable of violence. Large solar eruptions release energetic particles and magnetic energy into the solar system. If these eruptions hit the Earth, the solar magnetic field can cancel out part of the Earth's magnetosphere, effectively lowering the Earth's protective shields and resulting in powerful geomagnetic storms.

Countless solar eruptions have impacted the earth since the beginnings of civilization, but societies are increasingly susceptible to geomagnetic storms, since modern humans depend on an always-functioning electrical infrastructure. In 1989, a solar eruption caused a geomagnetic storm which induced large electric currents in the long-distance electrical power transmission lines in Quebec, Canada. These currents interacted with and overwhelmed transformers, causing catastrophic failures, and the entire province was left without electricity for over nine hours! Another example is the outage of two Canadian telecommunications satellites in January 1994 due to enhanced energetic electron fluxes. Even though the first satellite recovered after a few hours, the repair of the second satellite took 6 months and costs over 50 million dollars [19].

A recent "near miss" event occurred in July 2012 when a coronal mass ejection (CME) hit NASA's Solar Terrestrial Relations Observatory (STEREO [20])-A, a satellite on the same solar orbit as the Earth but during the eruption was located ahead of the earth by about a week [21]. Scientists used STEREO-A's magnetic measurement to model the theoretical impact of this CME had it struck the Earth. Their models predicted a larger storm than the 1989 Quebec storm in the best case scenario and a storm surpassing the largest solar storm on written record in the worst case scenario. This "largest solar storm" is known as the Carrington event of 1859 and was reported to have caused auroras as far south as Hawaii, and to have knocked out the global

[1]Solar gods include the Aztec Huitzlopochtli, the Mayan Kinich Ahau, the Egyptions Ra, the Greek Helios, the Roman Sol, the Arabian Malakbel, etc.

telegraph network.

The close-call of July 2012 motivated question about the frequency of extreme solar storms and the likelihood of Earth impact. Riley [22] assumed that the frequency of occurrence scales as an inverse power of the severity[2] and estimated the probability that another Carrington-like storm would occur in the next decade to be 12%. This is comparable to the likelihood of a serious earthquake in California over the same time interval. A 2008 National Academy report [19] estimates the cost of a "severe geomagnetic storm scenario" to be 1-2 trillion dollars, with a recovery time of 4-10 years.

One major difference between solar storms and earthquakes is that scientists can obtain early warning from satellites observing the sun and potentially predict oncoming solar storms. Unfortunately, predictions of solar eruptions are exceedingly difficult and the arrival times of significant space weather events have only been accurate to ± 12 hours [20]. Much of the uncertainty is due to the complicated nature of eruptions. After leaving the solar atmosphere, erupted structures can confound simple estimates by speeding up, slowing down, or rotating. The ambient solar field may deflect the eruption, resulting in non-radial propagation [23]. Many models do not consider these nuances and instead rely on nominal values to make their predictions. The community has not agreed on the geometry of the eruptive structure, resulting in a healthy debate between 2-D loops, spherical shells, cylindrical shells, ice-cream cones, and graduated cylindrical shells (side view of arched structure) [4, 24].

The magnetic field orientation also plays a central role in how solar eruptions interact with the earth. CMEs with a southward magnetic field can cancel the Earth's northward magnetic field, thereby enhancing the injection of magnetic energy into the Earth's magnetosphere. In contrast, northward-directed solar magnetic fields have minimal interactions with the Earth [25]. Even though the magnetic orientation of the eruption determines whether a storm will have a catastrophic impact, most existing space weather models do not include information about the underlying magnetic structure [26, 27]. These models rely on measurements from spacecraft at the

[2]This is similar to the scaling of earthquake frequency and their severity.

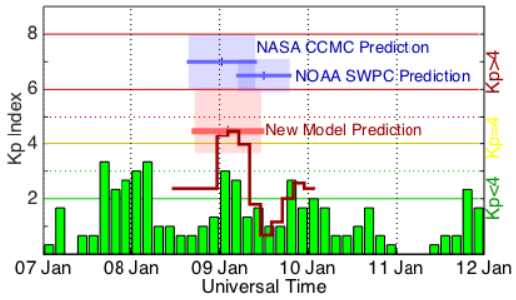

Figure 1.1: (From Fig. 6 of Ref. [1]) False alarm due to failed prediction about geo-effetiveness of Jan 10 event by current NASA & NOAA models. The NASA and NOAA predictions are of a serious solar storm whereas measurements (in green) show little geo-consequence.

first Lagrangian position to determine the magnetic orientation. This means that information about the magnetic field orientation is not available until approximately 1 hour before Earth impact. Unfortunately, this may not be enough time to arrive at the correct prediction.

There are societal consequences for accurately predicting low-probability high-damage events, as demonstrated by the L'Aquila, Italy earthquake and corresponding debate [28]. The trials of the Italian scientists who failed to predict this earthquake highlight the challenges of communicating probabilistic events to the general community. Scientist must balance a 98 percent probability of a false alarm against a 2 percent chance of failing to issue a warning for a catastrophe. While the L'Aquila event focused on the latter, there are tangible consequences associated with false alarms. One example of a solar eruption false alarm is from Ref. [1] and shown in Fig. 1.1. Scientists use a logarithmic Kp index to predict the severity of a solar event where $Kp \geq 5$ is considered a solar storm and $Kp = 8$ represents a severe solar storm. The latest NASA and NOAA models predicted a powerful storm but actual Kp measurements shown in green reveal negligible consequences due to the eruption.

There is much to be done in order to improve our space weather predictive capabilities. In theory, we should be able to predict an upcoming solar storm through accurate modeling of the underlying physics. Unfortunately, there is no standard

model for CMEs and much of our understanding is still empirical and based on qualitative arguments about magnetic field lines.

1.3 Motivating questions

There are many hotly debated solar physics questions as of the writing of this thesis [29] and two of these will be addressed herein. The first question is most fundamental: what causes the slow-rise to fast eruption of CMEs? The next question is 'Should fast and slow CMEs be attributed to different models?' In the process of addressing these questions, we create a framework that unifies two different models of solar eruption.

1.3.1 Demonstration of slow-rise to fast eruption.

Measurements of CMEs near the earth are consistent with coherent magnetic, twist-carrying coronal structures (i.e., flux ropes) [4, 30], but there is debate on whether the flux rope structure existed prior to the eruption or if it was formed during the eruption by magnetic reconnection. Recent observations [31] and simulations [32] suggest that the magnetic flux rope structure exists before the eruption and triggers the eruption through a "loss of equilibrium" mechanism. One such mechanism, the torus instability [33], occurs when a strapping field in the corona decays sharply as a function of height, allowing a rapid acceleration of the flux rope when it rises above a critical height.

We reproduce the slow rise to fast acceleration of laboratory flux ropes in the lab, and our results are in agreement with the torus instability.

1.3.2 Impulsive vs Gradual CMEs.

Historically, CMEs are divided into two categories: impulsive (fast) and gradual (slow) [29, 34]. Impulsive eruptions occur at very high speeds and decelerate while gradual CMEs exhibit a slow acceleration[3]. It is thought that impulsive CMEs are tied to

[3]Impulsive CMEs velocities are over 750 km/s whereas gradual CMEs velocities are around 400 km/s.

flare-associated events while gradual CMEs are associated with filament eruptions. There is recent evidence, however, that such a distinction may be artificial. Feynman and Ruzmaikin [35] present observations of a fast, flare-associated CME with corresponding erupting filament. Statistical studies by Vrsnak et al. [36] and Yurchyshen et al. [37] found no reason to separate the two types of CMEs. Chen & Krall [38] and Torok & Kliem [39] numerically reproduce impulse and gradual CMEs by "flux injection" and by "torus instability," respectively.

We are able to produce impulsive and gradual CMEs in the laboratory by changing the profile of the current trace (flux injection), and by changing the strapping field (torus instability). We expect the sun to use both approaches to produce fast and slow CMEs, so the distinction between impulsive and gradual CMEs is likely artificial.

1.3.3 Unifying flux injection and torus instability

The Kliem & Torok implementation of torus instability [33] focuses on the profile of the strapping field interacting with a current loop. The flux injection model [40] focuses on the applied voltage across the footpoints of a plasma arch. Chen [41] argues that the Kliem & Torok implementation does not have footpoints, and is therefore inconsistent with the boundary conditions. Our experiment has footpoints, adjustable strapping field profiles, and adjustable voltage profiles, so elements from both models are applicable.

We present a simple model for a nearly-circular plasma, with boundary conditions determined by an adjustable power supply. This model connects flux injection and torus instability to our experimental setup.

1.4 Introduction to plasmas

Plasmas are ionized gases and make up 99 percent of the known universe. However, the typical human environment is too dense and too cool for plasma to exist. Figure 1.2 is a log-log plot of temperature and density; solids, liquids, and gases occupy the lower right hand corner of the plot whereas plasma makes up the rest of the figure.

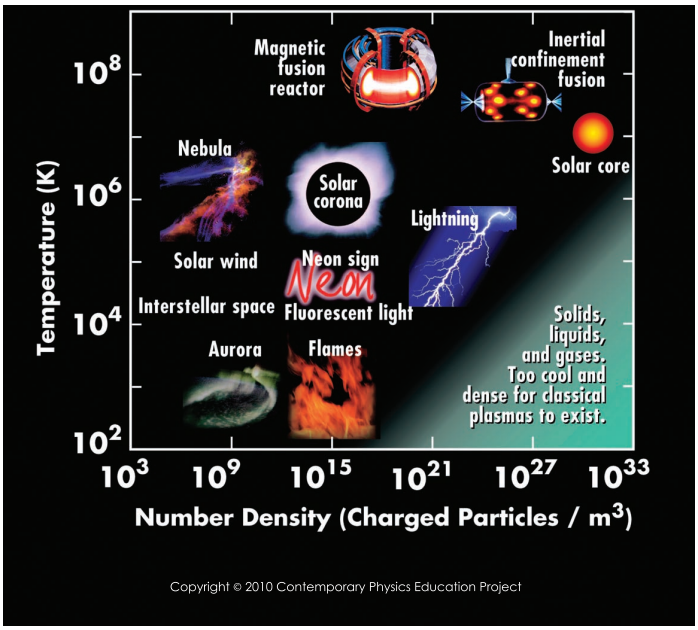

Figure 1.2: Temperature vs density chart for plasmas. (From: Contemporary Physics Education Project).

Plasmas can be cool and diffuse like the beautiful auroras of the polar skies or dense and extremely hot like the center of the sun. Their ionized nature means that their behavior is influenced by magnetic fields. The three fundamental parameters that characterize a plasma are: temperature, number density, and magnetic field [42].

Consider plasmas with equal numbers of positive and negative charges[4]. Even though the plasma is considered "neutral" as a whole, there are localized regions of strong electric field. Within these regions, the forces due to an isothermal pressure gradient must balance the electrostatic electric field to determine the localized density distribution. Assuming that thermally induced perturbations are sufficient slow, the density distribution of the electrons and ions are given by the Boltzmann relation

$$n_\sigma = n_{\sigma,0} \exp(-q_\sigma \phi / \kappa T_\sigma)$$

where $\sigma \in \{e, i\}$ is the particle species, T_σ is the temperature, q_σ is the charge, ϕ is the electrical potential, κ is Boltzmann's constant, and $n_{\sigma,0}$ represents a constant

[4]Non-neutral plasmas contain only a single charge and dusty plasmas also include charged "dust" as a third type of particle.

density.

The charges self-organize because same-polarity charges repel and opposite-polarity charges attract; this self-organization creates an effective screening effect. For example, an ion will attract electrons around it while repelling nearby ions. The charge of the surrounding electrons screen the charge of the ion so that an observer sufficiently far away will not see the electric potential associated with the ion. The length scale of this screening effect plays a fundamental role in plasma physics and is known as the Debye length:

$$\lambda_D \approx \lambda_{D,e} = \left(\frac{\epsilon_0 \kappa T_e}{n e^2} \right)^{1/2}$$

where $n \approx n_i$ is the system density and the system Debye length (λ_D) is approximately the Debye length of the electrons ($\lambda_{D,e}$). This self-organization occurs for all particles in the plasma and only makes sense if enough particles exist within a volume (λ_D^3) to provide screening. Thus, a criterion for an ionized gas to be considered a plasma is $n\lambda_D^3 \gg 1$, where n is the number density of the ionized gas [42]. In order for the shielding to be relevant, the plasma characteristic length must be much greater than the Debye length so that the plasma can be considered quasi-neutral. Thus, the two defining features of a plasma are:

1. $n\lambda_D^3 \gg 1$
2. $L \gg \lambda_D$

The inclusion of a steady state magnetic field introduces interesting behavior to individual particles and to the collective plasma. A charged particle in a magnetic field exhibits cyclotron motion by making circular or helical orbits along a guiding center as shown in Fig. 1.3 (a). If both electric and magnetic fields are present, the particle undergoes an $\mathbf{E} \times \mathbf{B}$ drift as shown in 1.3 (b). This drift is independent of the charge of the particle, so both positive and negative charges move in the same direction. Things get even more interesting when the particles follow curved magnetic field lines or enter a non-uniform and/or time dependent magnetic region. Needless to say, plasmas exhibit many complicated but interesting behaviors; the field of plasma

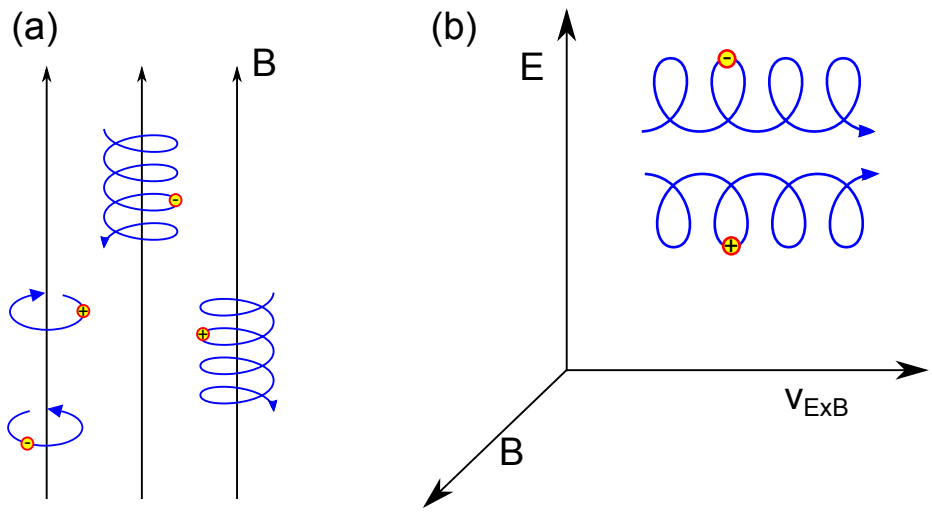

Figure 1.3: (a) Particles make circular cyclotron orbits about magnetic field lines or helical orbits along the magnetic field lines. (b) A particle experiencing both a magnetic and electric field will tend to drift in the direction of $\hat{\mathbf{E}} \times \hat{\mathbf{B}}$. This movement is independent of the particle charge.

physics attempts to describe the essential concepts behind these behavior.

1.5 Magnetohydrodynamics

There are many levels of plasma description from tracking individual particles to magnetohydrodynamics (MHD); additional information about the different description of the plasma can be found in Sec. B.1. MHD approximates the plasma as a single conductive fluid and is the least accurate of all the descriptions. Nevertheless, it is still tremendously useful because many systems do not require the additional precision of the other descriptions and MHD provides the most efficient and intuitive method for assessing the plasma. Complicated geometries are also difficult to model and are often only analytically feasible in the context of MHD.

The MHD equations relevant to solar phenomena are:

- The continuity equation:

$$\frac{\partial \rho_m}{\partial t} + \nabla \cdot (\rho_m \mathbf{U}) = 0 \tag{1.1}$$

where ρ_m is the mass density and $\mathbf{U}$ is the center of mass velocity.

- The equation of motion:

$$\rho_m \frac{D\mathbf{U}}{Dt} = \mathbf{J} \times \mathbf{B} - \nabla P - \rho_m \mathbf{g} \tag{1.2}$$

where $\mathbf{J}$ is the current density, $\mathbf{B}$ is the magnetic field, P is the thermal pressure, and $\rho_m \mathbf{g}$ is the force of gravity, which is typically important on the Sun but is not found in standard MHD derivations.

- Ohm's law for resistive MHD:

$$\mathbf{E} + \mathbf{U} \times \mathbf{B} = \eta \mathbf{J} \tag{1.3}$$

where $\mathbf{E}$ is the electric field and η is the plasma resistivity.

- Faraday's law:

$$\nabla \times \mathbf{E} = -\frac{\partial \mathbf{B}}{\partial t}$$

- Ampere's law in the limit of velocities much less than the speed of light:

$$\nabla \times \mathbf{B} = \mu_0 \mathbf{J}$$

- Divergence free condition:

$$\nabla \cdot \mathbf{B} = 0$$

- Energy equation of state:

$$\frac{P}{\rho_m^{5/3}} = const \tag{1.4}$$

where $\gamma = 5/3$ for an adiabatic equation of state.

MHD focuses on low-frequency, long-wavelength, and magnetic behavior of the plasma. The following conditions are required for MHD to be valid:

- Quasi-neutrality, meaning that the characteristic length scale must be much larger than the Debye length (λ_D).
- The plasma must be collisional. This means that collision time is much less than the time scales of interest so that the pressure can be approximated as isotropic and the system is at a near Maxwellian.
- Characteristic velocity is much slower than the speed of light, meaning that the displacement term is dropped from Ampere's law.
- Characteristic time scale of phenomena is long compared to electron cyclotron motion qB/m so that the electron inertia term can be dropped.

In the limit when resistance is negligible ($\eta \to 0$), the system is known as Ideal MHD.

The concept of frozen-in flux (Sec. B.2) is important in ideal MHD. It is intuitive to think of frozen-in flux as plasma and magnetic field lines moving as an ensemble in order to preserve the field-line topology [42]. This is a strong topological constraint which prevents the magnetic field lines from "tearing" and "reconnecting" even if doing so would result in an energetically favorable configuration. Thus, even a small amount of resistivity can have large impacts on plasma stability since it allows the plasma field line topology to change within localized regions.

1.6 Magnetic Reconnection

Magnetic reconnection describes the topological change of a magnetic configuration due to a "tearing" and "reconnecting" of magnetic field lines at a magnetic null point (Fig. 1.4 (a)). The resulting change in the topology allows the system to relax to lower energy configurations, thereby releasing free energy (Fig. 1.4 (b)). This free energy has been attributed to many space processes, including the Earth's magnetosphere, solar flares, and star formation [29, 43, 44]. Reconnection has also been observed in laboratory experiments [45–47].

The simplest reconnection model is the Sweet-Parker reconnection [48, 49]. Flows of plasma bring magnetic field lines together so that field gradients become strong at

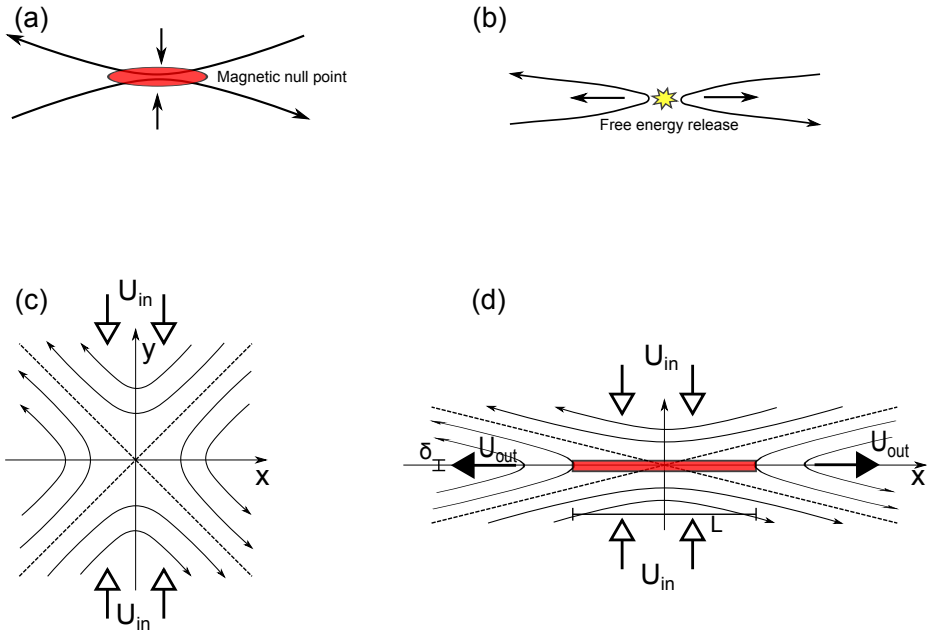

Figure 1.4: Cartoons depicting reconnection. (a) Two field lines come together and interact a magnetic null point. (b) The corresponding change in field topology is associated with a release of energy. (c) Bulk plasma flows U_{in} carry magnetic field lines flows towards a magnetic null. (d) The compression of field lines creates a thin current sheet (red) where reconnection occurs. Outward plasma flow U_{out} carries newly reconnected flux away from the reconnection site.

a localized region (Fig. 1.4 (c)). The interaction of field lines forms a thin current sheet (Fig. 1.4 (d)) where non-ideal MHD reconnection behavior occurs. The rate of reconnection is determined by the dimensions of the current sheet (δ, L), which scale as:

$$\frac{\delta}{L} = \frac{1}{\sqrt{S_{in}}} \tag{1.5}$$

where S_{in} is the inflow region's Lundquist number. The Lundquist number, a measure of how well the magnetic field is frozen into the plasma, is

$$S_{in} = \frac{\mu_0 v_{a,in} L}{\eta}$$

where $v_{a,in} = B_{in}/\sqrt{\mu_0 \rho_m}$ is the Alfven velocity of the inflow, and η is the resistivity of the system.

While a general Sweet-Parker reconnection model has been demonstrated in the laboratory [50], the reconnection rate predicted by Eq. 1.5 is many orders of magnitude too slow to describe solar flares [51], which have $S_{in} \sim 10^{11}$. This slowness in Sweet-Parker is attributed to the pile-up of the large amount of mass that must flow through the very narrow ($\sim \delta$) current channel. Petschek [52] proposed that, outside the immediate reconnection region, standing waves could drive outflows, dramatically increasing the reconnection rate. The Petschek model predicts reconnections rates that scale as

$$\frac{v_{out}}{v_a} \sim \frac{1}{\ln(S_{in})}$$

which is insensitive to S_{in}. Nevertheless, the Petschek model has been criticized as not being self-consistent [53] and modern researchers are looking beyond Resistive MHD towards the smaller length scales when ions are no longer considered magnetized [54–56]. This regime – Hall MHD reconnection – is a current topic of research and the details can be found in Ref. [43].

1.7 Dimensionless form

A remarkable feature of plasmas is that the same qualitative phenomena occur in plasmas with temperatures, densities, and magnetic fields that differ by many orders of magnitude. This scalability permits predictions about novel behavior using intuition about known plasma behavior. One way to take advantage of the scalability of plasmas is by rewriting the MHD equations in dimensionless form to extract dimensionless constants. In particular, the continuity equation (Eq. 1.1) and the equation of motion (Eq. 1.2) become

$$\frac{\partial \bar{\rho}_m}{\partial \bar{\tau}} = -\bar{\nabla} \cdot (\bar{\rho}_m \bar{\mathbf{U}})$$

$$\bar{\rho}_m \left(\frac{\partial}{\partial \bar{\tau}} + \bar{\mathbf{U}} \cdot \bar{\nabla} \right) \bar{\mathbf{U}} = \left(\bar{\nabla} \times \bar{\mathbf{B}} \right) \times \bar{\mathbf{B}} - \beta \bar{\nabla} \bar{P} + \gamma \bar{\rho}_m \bar{\mathbf{g}} \tag{1.6}$$

and the induction equation is obtained by taking the curl of resistive Ohm's law (Eq. 1.3), yielding

$$\frac{\partial \bar{\mathbf{B}}}{\partial \bar{\tau}} = \nabla \times (\bar{\mathbf{U}} \times \bar{\mathbf{B}}) + \frac{1}{S} \bar{\nabla}^2 \bar{\mathbf{B}} \tag{1.7}$$

Three dimensionless constants capture the essential physics of the system:

$$\beta = \frac{2\mu_0 P}{B^2} \tag{1.8}$$

$$S = \frac{\mu_0 L v_A}{\eta} \tag{1.9}$$

$$\gamma = \frac{gL}{v_A} \tag{1.10}$$

where L is a typical length scale and $v_A = B/\sqrt{\mu_0 \rho_m}$ is the characteristic Alfven velocity. The plasma β is a ratio of thermal pressure to magnetic pressure. The Lundquist number S is a ratio of Alfven time scale to the resistive time scale. There is no standard name for γ which compares the gravity to magnetic forces.

In the solar corona, and $\beta \ll 1$ so magnetic forces dominate thermal forces. $S \gg 1$, which means that the plasmas are highly conducting and Ideal MHD is applicable. The magnetic energy density is 800 times more powerful than the gravitational energy density in the solar corona [57] so γ is negligible.

1.8 Limits of observation and numerical studies

Observation of solar filaments, arched plasma structures associated with eruptions, have various limitations. Solar observations are unable to measure the magnetic field in the corona precisely and so solar models extrapolate the coronal magnetic field from photospheric magnetic measurements [32, 58]. The best photospheric magnetic measurements are obtained from filaments positioned on the face of the sun, but observers lack the ability to determine the geometry and configuration of those filaments directly; the converse is true for filaments close to the limb of the sun [59]. As a result, eruptions with excellent imaging diagnostics are severely lacking in magnetic information. Even when quality photospheric magnetic measurements are available, the process of extrapolating the magnetic field into the corona has its limitations. Extrapolation results differ depending on the underlying assumptions [30] and even the best non-linear force-free algorithms struggle to extrapolate the force-free corona magnetic field from the boundary measurements obtained from a "forced" photosphere [60].

The methods of modeling the magnetic field listed in increasing levels of sophistication are potential field source surface, force-free field, non-linear force-free field (NLFFF) employing line-of-sight magnetograms, NLFFF employ complete vector magnetograms, and MHD models. The advantage of the field models is that they are data-driven and constrained by observations. Unfortunately they are static, so independent field models must be generated for each time step to evolve the system. In contrast, MHD models are intrinsically dynamic but they are initialized by idealized magnetic fields and are not constrained by observations. Almost all solar eruptions models suffer from poor knowledge about the initial conditions of the magnetic field and this problem is unlikely to be addressed until satellites are sent to directly probe the sun[5].

Although we have more satellites in the sky than ever before, there are limitations to what can be done observationally. Scientists do not have control over the behavior

[5]See: Solar Probe Plus mission set for 2018 launch.

of the Sun and must wait for it to do something interesting. The sun is happy to oblige with powerful eruptions during solar maximum but can also stubbornly refuse to display interesting eruptions during periods of solar minimum. When an eruption occurs, scientists hope that satellites are properly positioned to image the event. Most satellites are along the Sun-earth axis and thus provide a single view of eruptions. A pair of satellites (STEREO-A and STEREO-B [20]) fly ahead and behind the earth and the additional perspective of an eruption can be used to extract 3D information [61]. Unfortunately, STEREO satellites may not be in the best position to capture eruption images and the satellites have "black-out" periods of several months corresponding to when both spacecrafts are on the far side of the sun. One such black-out period (March 2015 to July 2015) is in effect as of the writing of this thesis. Furthermore, the STEREO mission has a finite lifetime [4], which means that future observers may be restricted to a single viewpoint.

Much of what we know about the sun is from empirical statistical studies based on observations and numerical models which depend heavily on information about the magnetic field, the quality of which is lacking. This has made it difficult to effectively predict solar weather from observations and numerical modeling alone.

1.9 Contribution of laboratory experiments

Many of the shortcomings of numerical and observational studies can be addressed by laboratory experiments. Unlike observations, experiments provide repeatability, permitting the use of statistics to investigate specific phenomena. Laboratory diagnostics can directly measure solar-relevant laboratory plasmas and can be set up to extract the desired spatial and temporal information about specific plasma processes. Desirable plasma parameters can be varied independently to extract the essential physics. Unlike numerical studies and theoretical analysis, no "potentially unphysical" simplifying assumptions are made; laboratory plasmas obey all the laws of physics.

Laboratory experiments (see Fig. 1.5) can provide some insight into the behavior of solar-relevant plasma loops in an ambient magnetic field [2, 3]. The dimensionless

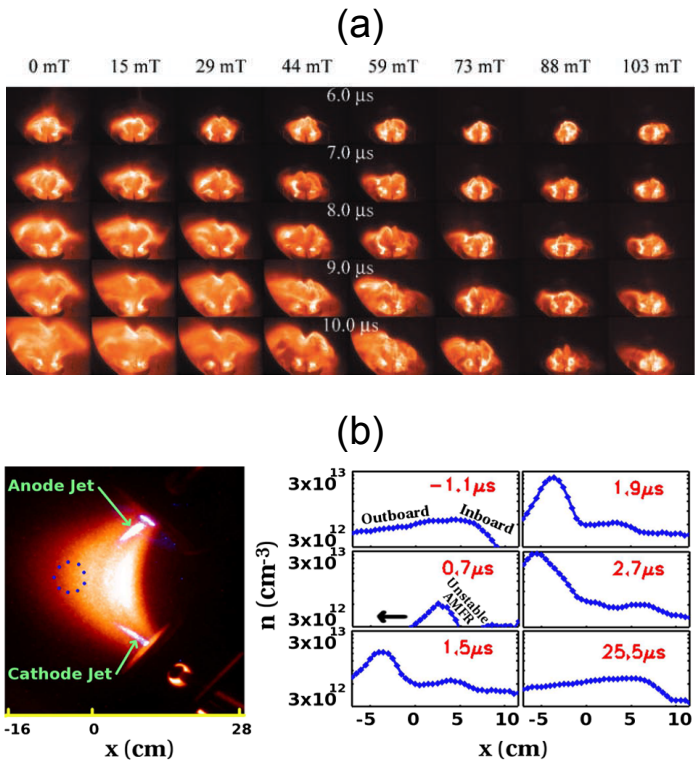

Figure 1.5: (a) Ref. [2] showed that a strong strapping field can inhibit plasma expansion. (b) Ref. [3] demonstrated the eruption of a solar-relevant plasma structure by injecting hot plasma into the footpoints.

numbers for laboratory plasmas must match the numbers for solar plasmas to take advantage of plasma scalability (Sec. 1.7), so solar experiments have been designed so that $\beta \ll 1$ and $S \gg 1$. Hansen and Bellan [2] designed such an experiment and demonstrated that a sufficiently strong strapping field can completely inhibit plasma loop expansion in the lab. This result is expected to scale to confined solar eruptions — an eruption that rises rapidly from the solar surface but does not escape the solar atmosphere.

The smaller scale separation is the main limitation of laboratory experiments. The Lundquist number is $S \sim 10^8 - 10^{11}$ for solar plasmas due to the immense length scale of plasma. In contrast, laboratory plasmas are more likely to have to $S \sim 10 - 10^3$ since there is a restriction on the length scale of laboratory experiments[6]. This inability to match the immense Lundquist numbers of astrophysical phenomena means that not all of the relevant solar physics is captured by laboratory experiments. Since S is found in the denominator in Eq. 1.7, however, laboratory experiments with $S = 100$ capture 99% of the essential physics (instead of 99.999999999% of the physics for $S \sim 10^{11}$). Such experiments can produce powerful insights into solar eruptions, provided that the boundary conditions and dimensionless numbers requirements are satisfied.

1.10 Experimental set-up and useful concepts

This section outlines the most common set-up for the majority (but not all) of the work presented in this thesis; a more in-depth discussion can be found in the Appendix (Sec. D). This section also contains useful concepts and terminologies that are used throughout this thesis.

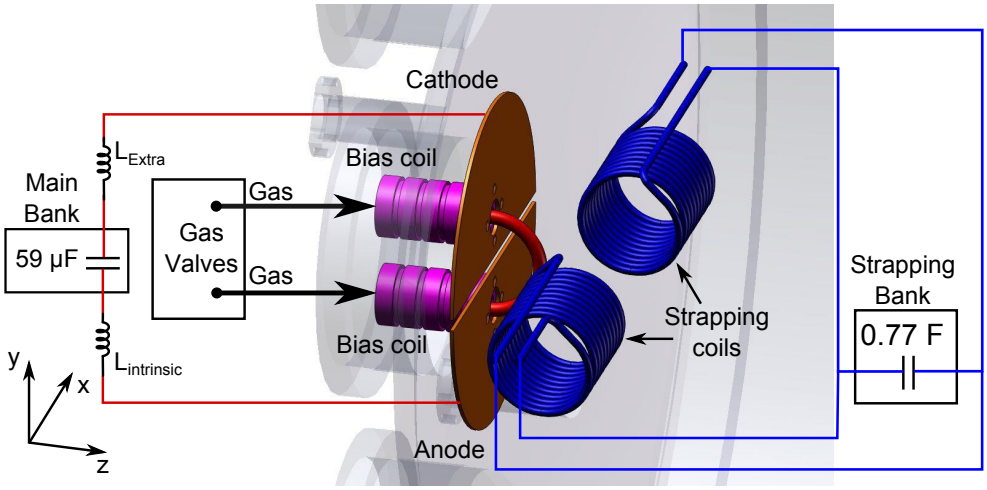

Figure 1.6: The cathode and anode define the $x-y$ plane of the coordinate system, with the gap separating cathode from anode defining the origin. The bias coils (purple) generate arched magnetic fields similar to a horseshoe magnet. Strapping coils (blue) are inside the vacuum chamber for the majority of the work in this thesis.

1.10.1 Laboratory set-up

The experimental setup is shown in Fig. 1.6. A pulsed, magnetic plasma gun consisting of anode, cathode, and bias coils is mounted at the end of a 1.5 m long, 0.92 m diameter vacuum chamber with 10^{-7} torr base pressure. The chamber is much larger than the plasma, thus simulating a half-infinite space, and the chamber axis defines the z direction (height). The bias coils located behind the electrodes generate arched magnetic fields in the $y-z$ plane. The magnetic field is nominally 1.5 kG at the foot points and 250 G at the apex. Fast valves puff gas through the center of the bias coils into the vacuum chamber. High voltage applied to the electrodes by a 59 μF capacitor ionizes hydrogen gas to form an arched plasma of density $n \sim 10^{21}$ m^{-3}. The capacitor is typically charged to 2.5-5 kV driving 30-70 kA of current which flow in the y direction at the plasma loop apex. Additional inductance (L_{extra}) can be added to the intrinsic inductance of the system ($L_{intrinsic}$) to slow down the current pulse. The plasma temperature T is estimated to be 2-4 eV, corresponding to $\beta = 2\mu_0 n k_B T/B^2 \sim 0.2$, so magnetic forces are expected to dominate.

[6]Surprisingly, this restriction is often the size of the laboratory chamber door. What is the largest vacuum chamber that can be brought into the laboratory?

A 0.77 F capacitor bank powers two 7.6 cm diameter strapping field coils mounted 9.5 cm in front of the electrode. The strapping coils each have 11 turns and are placed in a coaxial configuration inside the chamber to produce a maximum 875 G strapping field in the x direction so that the $J_y \times B_x^{strap}$ force inhibits plasma loop expansion, where J_y is the electric current density in the plasma loop.

1.10.2 Diagnostics

The work in this thesis relies on three diagnostics techniques: imaging diagnostics, magnetic diagnostics, and circuit analysis. Each technique has its own strengths and weaknesses, but together they construct a robust picture of the plasma dynamics.

Imaging provides *location-dependent scalar* measure of the plasma emission intensity. Imaging diagnostics are intuitive and visual information is compelling and easy to understand. However, cameras compress 3-D information into 2-D images resulting in ambiguities. Two cameras can resolve basic projection effects, but three-dimensional structures are difficult to reconstruct without additional viewpoints. The plasma is also difficult to image because it is amorphous and somewhat transparent. Thus, imaging diagnostics normally gives qualitative information unless carefully calibrated (Sec. G.1).

While imaging provides clues about the underlying magnetic structure, it does not capture the magnetic information that is important in a $\beta \ll 1$ configuration. Magnetic probes permit direct measurement of the magnetic field. The probe cluster inside the chamber measures the magnetic field associated with the plasma while magnetic Hall sensors (Chapter E) measure the slower magnetic field associated with the bias coils and the strapping field. Magnetic measurements provide direct quantitative insight into the dynamics of the plasma but the measurements are difficult to analyze and are unintuitive. Magnetic information is often compared to an idealized model in order to gain insight into the behavior of the plasma. Magnetic fields are also a *location-dependent vector* quantity, meaning that magnetic probes only provide a local description of the plasma.

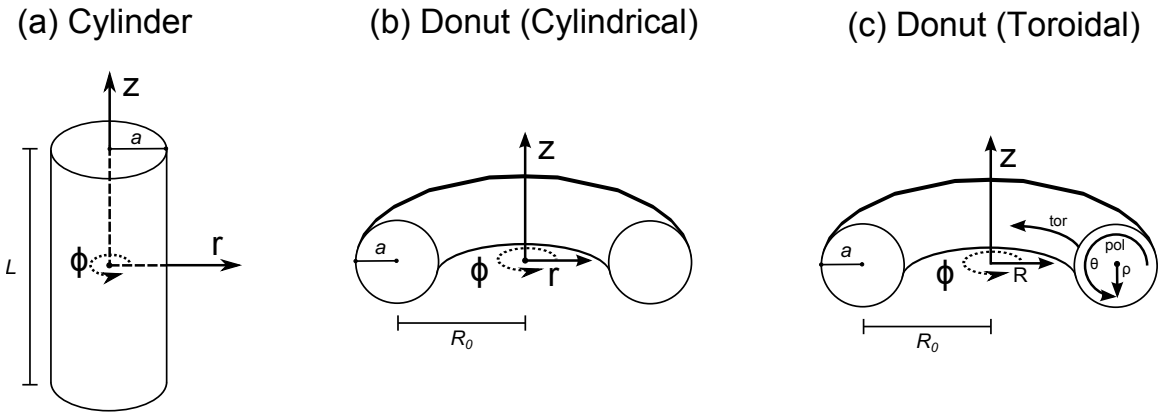

Figure 1.7: Application of *cylindrical* coordinate system to (a) a cylinder of radius a and length L and (b) a hoop of aspect ratio R_0/a. (c) A donut expressed in *toroidal* coordinates.

Circuit analysis complements imaging and magnetic diagnostics by providing a *scalar* quantitative description of the system. The voltage measured across the plasma footpoints measures the magnetic flux injected into system. The plasma current is a fundamental MHD parameter and drives loop expansion. The plasma can be modeled as a variable inductor and its inductance is a global measure of the plasma structure: greater plasma expansion means increased plasma inductance. Thus, inductance calculations can quantify whether a plasma is expanding and also the rate of that expansion.

A more in-depth look at imaging (Secs. D.6.1 and G.1), magnetic (Secs. D.6.2 and G.2), and circuit analysis (Sec. G.3) can be found in the Appendix.

1.10.3 Axial, Poloidal, and Toroidal

Cylindrical coordinates are the natural choice for axisymmetric systems. In the case of a cylinder of radius a and length L, the $\hat{r}$, $\hat{\phi}$, and $\hat{z}$ direction are typically aligned, as shown in Fig. 1.7 (a). It is common to align the length of the cylinder with the $\hat{z}$ axis, which is then called the *axial* direction. A donut-shaped configuration, aka torus, is defined by its major radius R and minor radius a, and the conventional way of applying cylindrical coordinates is shown in Fig. 1.7 (b). The z axis is aligned with the symmetric axis of a torus.

A useful concept in axisymmetric configuration (spheres, cylinders, and donuts) is the concept of toroidal and poloidal. The *toroidal* direction refers to the $\hat{\phi}$ direction whereas the *poloidal* direction refers to the remaining two directions[7]. For describing particles within the donut, a length ρ along the minor radial direction with rotation θ is introduced and the overall geometry is called *toroidal* coordinates. The left-handed[8] toroidal coordinate for a hoop is shown in 1.7 (c).

One useful feature of separating vectors into poloidal and toroidal components is to simplify the mathematics into intuitive components. For example, suppose we separated the current $\mathbf{J} = \mathbf{J}_{tor} + \mathbf{J}_{pol}$ and the magnetic field $\mathbf{B} = \mathbf{B}_{tor} + \mathbf{B}_{pol}$, then

$$\mathbf{J} \times \mathbf{B} = \mathbf{J}_{tor} \times \mathbf{B}_{pol} + \mathbf{B}_{pol} \times \mathbf{J}_{tor} + \mathbf{J}_{pol} \times \mathbf{B}_{pol}$$

where we note that $\mathbf{J}_{tor} \times \mathbf{B}_{tor} = 0$, since it is the cross-product of parallel vectors. It is also easy to see that $\mathbf{J}_{pol} \times \mathbf{B}_{pol} = (\mathbf{J} \times \mathbf{B})_{tor}$[9] and similarly that $\mathbf{J}_{tor} \times \mathbf{B}_{pol} + \mathbf{B}_{pol} \times \mathbf{J}_{tor} = (\mathbf{J} \times \mathbf{B})_{pol}$. For axisymmetric systems, $(\mathbf{J} \times \mathbf{B})_{tor} = 0$, so the force

$$\mathbf{J} \times \mathbf{B} = \mathbf{J}_{tor} \times \mathbf{B}_{pol} + \mathbf{B}_{pol} \times \mathbf{J}_{tor} \tag{1.11}$$

is purely in the $\hat{\mathbf{r}}$ and $\hat{\mathbf{z}}$ or poloidal direction.

Another useful intuitive concept comes from Ampere's law $\nabla \times \mathbf{B} = \mu_0 \mathbf{J}$ which basically states that a toroidal current produces a poloidal magnetic field and vice-versa.

1.10.4 Solar Terminology

The following section defines common solar concepts which will be used in this thesis.

Coronal mass ejection (CMEs) are transient large-scale ejection of mass from the sun due to magnetic eruptions. While CMEs and flares are both magnetic disruptions, CMEs are observed by white-light emissions of erupting mass in

[7] This is $\hat{r}$ and $\hat{z}$ in cylindrical coordinates but could be $\hat{\rho}$ and $\hat{\theta}$ in spherical coordinates.
[8] The poloidal rotation is left-handed with respect to the corresponding cylindrical coordinates.
[9] For example, $\mathbf{J}_{pol} \times \mathbf{B}_{pol} = (J_r \hat{\mathbf{r}} + J_z \hat{\mathbf{z}}) \times (B_r \hat{\mathbf{r}} \times B_z \hat{\mathbf{z}}) = (J_r \times B_z + J_z \times B_r) \hat{\boldsymbol{\phi}}$.

(a) Three-part coronal mass ejection

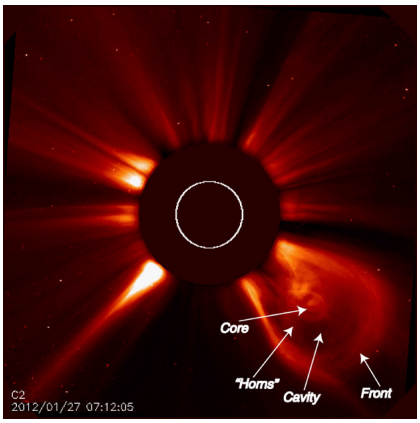

(b) X3.1 flare from AR 12192 captured by SDO

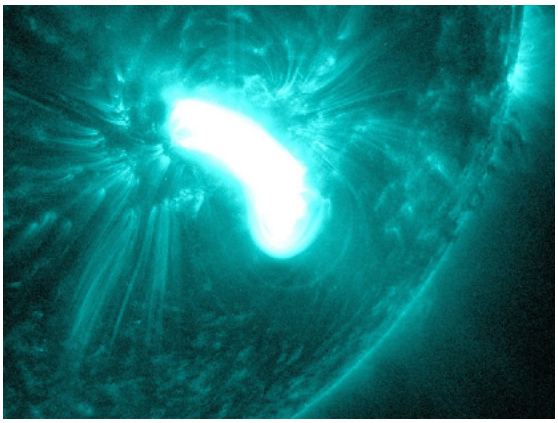

Figure 1.8: (a) CME with three part structure (from Ref. [4]) The front represents density build-up in front of the CME, the so-called "flux rope" is the CME cavity, and the prominence is the core located at the bottom of the flux rope. (b) X-class flare as viewed in 131 angtrom light.

the outer corona and heliosphere whereas flares are often observed in X-rays. The arch-typical morphology of a CME has "three-part" (Fig. 1.8 (a)) structure even though not all CMEs show this structure [4, 62]; there is typically a bright leading edge followed by a darker cavity containing a bright core. About 70% of CMEs are associated with an erupting filament[10] [62] though fast CMEs tend to be associated with flares. CMEs occur about 1-3 times a day and release approximately $10^{12} - 10^{13}$ kg of mass per ejection, resulting in 10% of the mass loss rate of the steady solar wind [63]. The interaction between the Earth's magnetosphere and the ionized particles and magnetic flux associated with CMEs causes geomagnetic storms which can disrupt satellites and electrical infrastructure back on Earth.

Prominences and filaments both refer to the cool dense plasma feature above a magnetic neutral line in current systems that builds up over several days. Historically, the term prominences referred to bright loops appearing on the limb of the sun whereas filaments referred to darker loops on the face of the sun. They are now accepted as the same structure. The existence of dense cool

[10] CMEs associated with a filament often display a three part structure: a bright, high density front moving ahead of a dark, low-density cavity, within which rests a filament.

plasma in the corona over several days indicates that filaments are surrounded by magnetic field. The magnetic field supports the dense plasma against the pull of gravity and is also the only means of preventing the matter from heating via thermal conduction [64]. The filament is the core in the three-part CME structure of Fig. 1.8 (a).

Flux ropes are force-free 3-D magnetic structures with helical magnetic field lines fields wrapped around a center axial field. This structure is able to store a large amount of free magnetic energy and support filaments against the gravity of the sun. Kuperus & Raadu [65] provided one of the first formal definitions of a flux rope in cylindrical geometry. They permit a surface return current in order to match the magnetic field at the boundary of the flux rope but made no claim about whether the flux rope contains a net current. As summarized by Bellan [66], later models diverged on the topic of net current with some authors arguing that the current must vanish outside the flux tube (like a coaxial cable) while others argue that net current may be finite. Regardless of the details about the current, all parties agree on the helical nature of flux ropes and many models now extend flux ropes to arch-shaped configurations [33, 40]. The flux rope is the cavity in the three-part CME structure of Fig. 1.8 (a).

Flares are rapid magnetic energy releases in the corona. The energy accelerates non-thermal particles, resulting in heating of the coronal and chromospheric plasmas. The acceleration of these particles result in a broad-spectrum emission in X-ray, EUV, white light, and radio. Historically, they were identified mainly by transient spikes of emissions in hard X-ray, soft X-ray, and radio. They exist across many different energy scales and microflares and nanoflares have approximately 10^{-6} and 10^{-9} the energy of the largest flares, respectively. They may or may not be associated with a CME and are observed as intense brightenings, as shown in Fig. 1.8 (b).

Open vs closed field lines: The divergence-free condition of Maxwell's equation states that all magnetic field lines must close upon themselves so any field line

radiating from the sun must eventually make its way back to the solar surface. In the solar context, open-field regions are where the plasma leaves the sun as solar wind and closed-field regions are regions which trap pockets of plasma in quasi-static equilibrium.

Sunspots are regions of intense magnetic field on the sun. When looking at the sun in the visible spectrum, they are observed as dark blemishes on the solar surface. They are often represented by a dark central umbrae feature and a gray penumbrae feature.

Dipole, Bipole, Quadrupole are terms best understood as idealized magnetic configurations, representing configurations of sunspot groups classified by the Mount Wilson Magnetic Classification. While the original paper by [Hale and Nicholson, 1938] is not readily accessible, a summary of this classification can be found in solar textbooks [67] or at solar weather websites. Classification α applies to a sunspots group with unipolar sunspots (dipoles). Classification β applies to sunspot groups with both positive and negative polarities, with clear division between opposing polarities (bipoles). Classification δ refers to a single sunspot with two opposite polarity umbrae within the same penumbra (i.e. two opposite polarity dark spots within the gray sunspot region) and is often associated with quadrupolar field configurations. If a specific region has irregularly spaced positive and negatively spaced polarities which are not amenable to obvious classification, they are called γ regions. The γ can also be used as a qualifier for α, β, and γ sunspots. For example, a $\beta - \gamma$ sunspot region is characterized by bipolar behavior, but without a continuous division between the polarities. Similarly, a $\beta - \gamma - \delta$ region is a $\beta - \gamma$ region with additional delta spots.

Chapter 2

Experimental reproduction of slow rise to fast acceleration

2.1 Introduction to solar eruptions

One of the great advances in solar physics is the Carmichael-Sturrock-Hirayama-Kopp-Pneuman (CSHKP) model, the "standard" model for flares [68–71]. The CSHKP model (Sec. C.1) describes most flare observations, including the power source of the flares, the coronal streamer structure, the often-observed rising prominence, the brightening of chromospheric footpoints, flare signatures in X-ray, EUV, and Hα, and the increased height and footpoints separation of the magnetic structure. The model presents the physical mechanisms behind these observations but does not specify what causes the initial magnetic arcade configuration to go unstable. Regardless, the strength of the model drove the paradigm that reconnection rapidly evolves the solar magnetic field, resulting in large solar flares which are the fundamental cause of thermally driven material ejection, geomagnetic storms, auroras, interplanetary shock disturbances in the solar wind, solar proton events, and polar cap absorption events[1] (summarized in Fig 2.1).

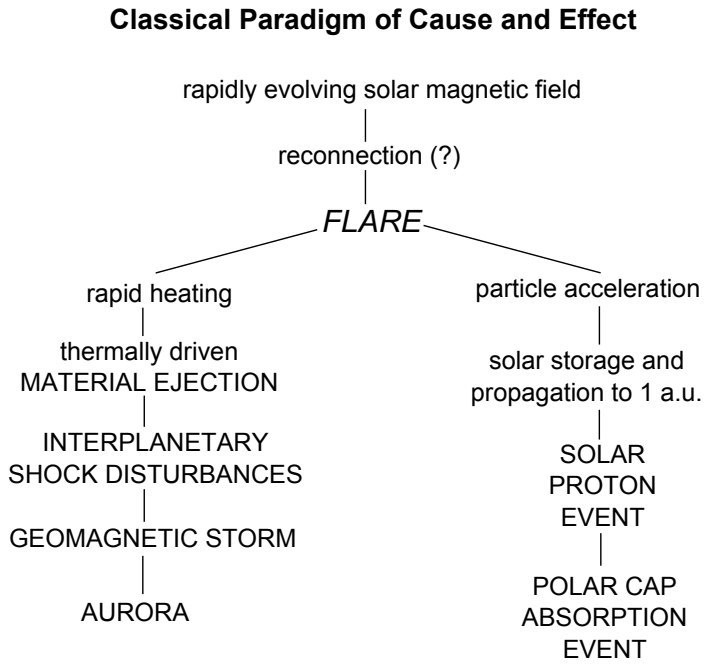

Figure 2.1: Adapted from Ref. [5]. Paradigm with flares playing a central role. Capital letters indicate observational phenomena and lowercase letters indicate physical processes or descriptive processes.

2.1.1 Coronal mass ejections

Gosling et al. [72] are among the first to report observation of sporadic ejections of large quantities of mass (10^{15}-10^{16} g) from the Sun at velocities ranging from 200 km/s to 1100 km/s. These so-called coronal mass ejections (CMEs), often have material concentrated into clearly distinguishable loops and are believed to remain connected to the sun at their footpoints. CMEs are about 40% associated with flares and 70% associated with eruptive prominences [62]. Even when a CME has a corresponding filament eruption, most of the material within the CME originates from the corona [73], suggesting that CMEs are related to but distinct from prominence eruptions. Gosling [5] summarizes evidence against the classical flare paradigm and place CMEs as the main driver of many geo-effective events (Fig. 2.2). He argues that flares occur in smaller, magnetically-complex regions, and are perhaps the result of reconnection. CMEs are associated with larger magnetic regions than flares, though the processes

[1]Fading of cosmic ray signature at the poles due to enhanced ionization in the D region of the ionosphere and associated with > 20 MeV protons.

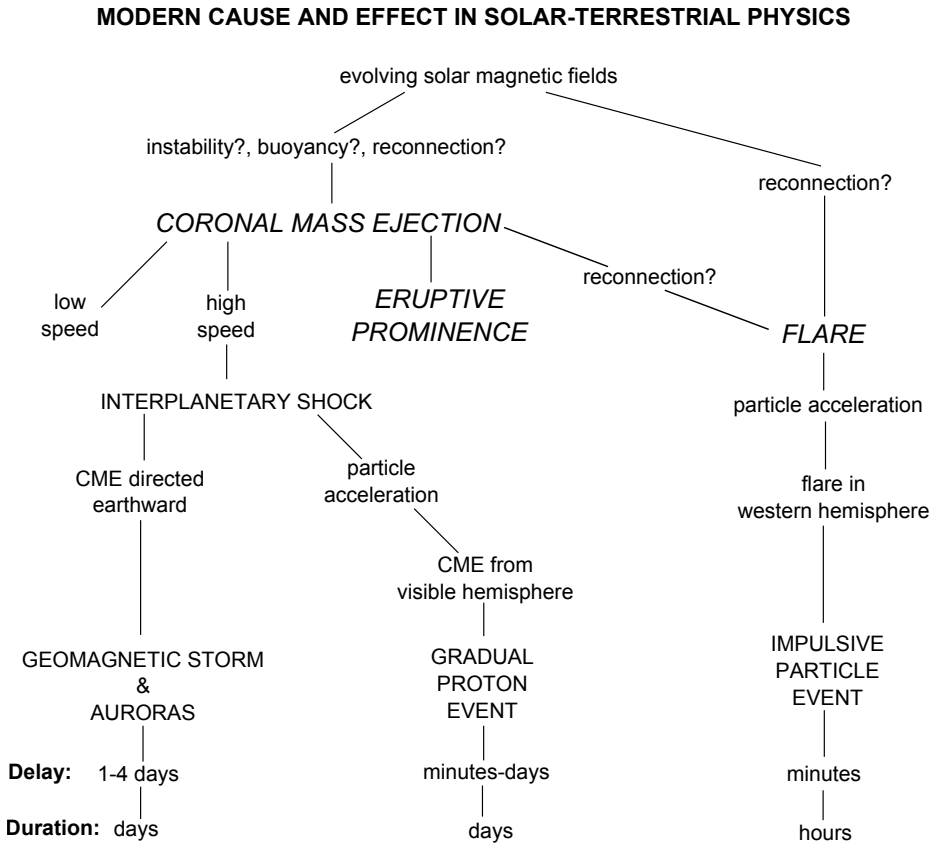

Figure 2.2: Adapted from Ref. [5]. Paradigm with CMEs playing a central role. Capital letters indicate observational phenomena and lowercase letters indicate physical processes or descriptive processes.

Parameter	Value
Kinetic energy (CME, prominence, shock)	10^{26} J
Heating and radiation	10^{26} J
Work done against gravity	10^{25} J
Volume involved	10^{25} m^3
Energy density	10 J/m^3

Table 2.1: (Reproduction) Energy requirements for a moderately large CME

Forms of Energy	Observed Avg Values	Energy Density (J/m^3)
Kinetic ($(m_p n V^2)/2$)	$n = 10^{15}$m^{-3}, $V = 10^3$ m/s	10^{-6}
Thermal (nkT)	$T = 10^6$ K	0.01
Gravitational ($m_p ngh$)	$h = 10^8$ m, $g = 274$ m/s^2	0.05
Magnetic ($B^2/2\mu_0$)	$B = 10^{-2}$ T	40

Table 2.2: (Reproduction) Estimate of Coronal Energy Sources

that trigger the release of CMEs are not well understood.

2.1.2 Observed characteristics: nature of CMEs

Early CME models suggest that thermal pressure powers the eruption and invoke images of bomb blasts. These "thermal blast" model are likely motivated by the flare-centric paradigm which claims that reconnection in flares heats up nearby plasma, producing rapid expansion of the chromosphere and the corona around the flare site [5]. Today, better satellite evidence and energy composition studies of CMEs have rendered thermal blast models obsolete. The basic energies for a CME have been calculated by Forbes [57] and are reproduced in Table 2.1. The photospheric magnetic field is unperturbed by eruptions, suggesting that the energy for eruptions originates in the corona [29]. Estimates of coronal energy sources are shown in Table 2.2, and only the magnetic energy in the corona has sufficient energy density to drive a moderately large CME eruption [57]. This has lead to a consensus that eruptions are magnetically driven, though the details are still under debate.

2.2 Debate

A mysterious feature of many CMEs is that they remain stable in the solar atmosphere for days/weeks, before rapidly erupting in the matter of minutes/hours. It is helpful to organize the debate regarding CMEs into two stages: before eruption and during eruption. The CME is stable for days before an eruption, and many scientists believe that energy slowly builds up during this stage. Those arguing against energy build-up argue that sufficient injected energy is injected during the eruption to drive the eruption, so a separate build-up stage is not necessary. At the beginning of the eruption phase, CMEs leave quasi-equilibrium and slowly rises to some critical threshold after which they experience rapid acceleration. Once the eruptive process is over, most CMEs propagate with nearly constant speed into the solar system system.

2.2.1 Before eruption: store and release vs dynamo

Before the eruption, most models have a slow build-up "storage" phase when free energy is added to the system. Popular build-up methods include the slow twisting of field lines to add free energy, the loading of mass to compress some sort of magnetic spring, or the flow of photospheric plasma to cancel magnetic flux [74]. In contrast, dynamo theories argue that rapid generation of magnetic flux is introduced by real-time stressing of the magnetic field during an eruption [74]. Chen [40] introduces a flux injection dynamo model where "flux injection" corresponds to a specified increase in the poloidal flux $\Phi_p(t)$. He argues that the dynamics of the erupting structures can be fit to a $d\Phi_p(t)/dt$ profile. In essence, the difference between these two classes of models is their assumption about the energy conservation during the eruption. Storage models assume that energy is held constant during the eruption, whereas dynamo models add energy into the CMEs during the eruption.

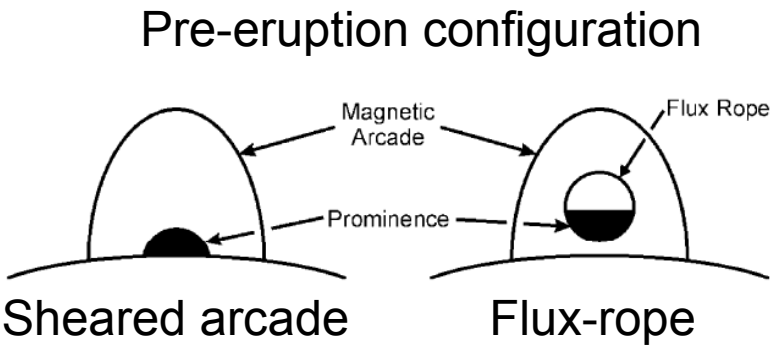

Figure 2.3: Adapted from Ref. [6]. Over-simplified representation of pre-eruptive configuration for sheared arcade models compared to flux-rope models. The dark region represents the so called "core field" where energy is built up.

2.2.2 Eruption

There is a general consensus that solar eruptions expel magnetic flux ropes into the solar system [4, 75]. The debate is whether the flux-rope exists before the eruption [40, 76, 77], or whether it is formed during the eruption as a result of magnetic reconnection (Fig. 2.3). For the former, magnetic reconnection is a secondary effect resulting from the interactions between a rising flux rope and the background ambient field. For the latter, the initial field configuration is a magnetic arcade [78] and magnetic reconnection creates the flux rope as part of the eruption process [8, 9, 79]. Models supporting each side have been sorted into "sheared arcade" models and "flux rope" models in Secs. C.3 and C.4, respectively.

Much debate during the eruption phase is about the trigger. The trigger is a mechanism that dynamically perturbs the pre-eruptive configuration and causes the core field to erupt. This trigger can be attributed to a large injection of poloidal flux for flux injection models [40, 80], or attributed to the passing of some critical threshold for storage and release models. For those in the "flux rope" camp, this critical threshold marks of loss of equilibrium due to MHD instability [33, 65] or MHD catastrophe [11]. The physical onset-criterion corresponds to an assumption about the "decay index" of the overlying field [33] or changes in the strength of the main polarities in the active region [11]. For those in the "sheared arcade" camp, the critical threshold is the onset of "fast" arcade shearing [8] or the onset of fast(er)

reconnection [7, 9]. There is no quantitative onset-criterion for sheared arcade models, except arguments that the rate of magnetic reconnection must be sufficiently fast enough to produce the observed kinetic energy of the eruption.

Once the eruption has been triggered, there are two suggested driver mechanisms: (i) the Lorentz force or (ii) increasingly fast magnetic reconnection. Models which permit net current cite the Lorentz force for driving plasma loop expansion. Models without net current cite the formation of a large current sheet where magnetic reconnection can drive the eruption. Lynch at al, [81] presents simulations demonstrating eruptive flare reconnection driving the eruption, though the authors note that their magnetic structures are artificial and their numerical simulations do not have sufficient spatial resolution.

2.2.3 Caltech experiment overview

The Caltech experiment features an arched plasma loop connected to a current source power supply as described in Sec. 1.10.1 and in Fig 2.4. A current source powers the setup by injecting poloidal flux into the system. By modifying the profile of the current, the rate of poloidal flux injection can be adjusted to reproduce a strongly driven (dynamo) configuration or a slow build-up configuration.

A capacitor bank powers two strapping field coils mounted in front of the electrode. The strapping coils produce magnetic field oriented so the $\mathbf{J} \times \mathbf{B}_{strap}$ force inhibits plasma loop expansion, where $\mathbf{J}$ is the electric current density in the plasma loop. The plasma represents a pre-existing flux-rope structure that expands due to the presence of arched currents. The plasma apex expands into a region of strong strapping field and is slowed down. In the limit of No Strapping field (NS), the hoop force dominates expansion dynamics [82] and the apex accelerates and erupts. In the limit of Large Strapping (LS) field, the plasma apex is completely inhibited from expanding. A customized Intermediate Strapping (IS) field has been found which captures the essential physics of the torus instability and reproduces the slow rise to fast acceleration associated with the majority of coronal mass ejections [83]. The

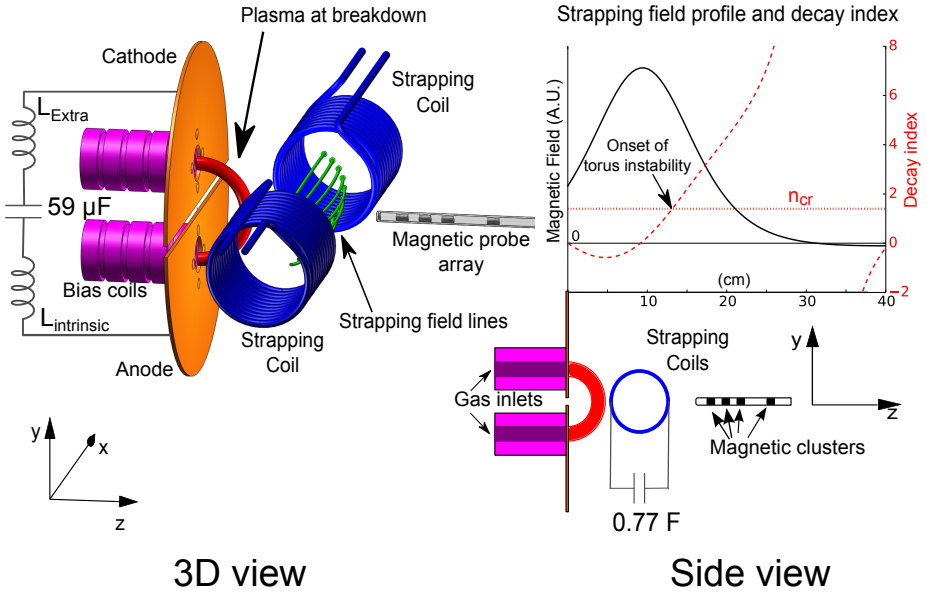

Figure 2.4: Schematic representation of experiment. The cathode and anode define the $x-y$ plane of the coordinate system, with the gap separating cathode from anode defining the origin. The bias coils (purple) generate arched magnetic fields similar to a horseshoe magnet. Independently powered coils (blue) produce strapping field (green arrows) and the plot in the upper part of the side view shows how the strapping field magnitude varies along the z axis. In the plot, the up-sloping dashed line (red) shows the calculated decay index of the strapping field and the horizontal dotted line (red) shows the calculated instability threshold. Additional inductance (L_{extra}) can be added to the intrinsic inductance of the system ($L_{intrinsic}$) to slow down the current pulse. The plasma (red) starts small but grows to many times its original size as it expands into the vacuum chamber.

IS configuration slows plasma expansion at early times, allowing expansion forces to build up and contribute to the rapid acceleration of the plasma when it moves past the strapping field peak. The sudden rapid acceleration also comes from the steep spatial decay of the strapping field, a feature that is not present in Ref. [2] which employs a uniform strapping field.

Plasma dynamics are captured by two fast cameras and by magnetic probe clusters placed at 17.5 cm, 19.5 cm, 21.5 cm, and 25.5 cm in front of the electrode along the chamber axis. One camera is a movie camera with line of sight perpendicular to the side view and provides the primary means of measuring plasma dynamics. The other camera faces the electrode from the opposite end of the vacuum chamber and provides disambiguation of projection effects. The strapping coils block viewing of the early plasma evolution so imaging-based analysis is restricted to $z \geq 11$ cm. The magnetic probes provide localized, *in situ* measurements and can precisely time the plasma motion. Information about the overall plasma structure is obtained by measuring the voltage and current across the electrodes and calculating the inductance of the plasma. The experiment is reproducible and shots can be repeated every two minutes. High resolution data are obtained by averaging repeated shots with the same parameters.

2.3 Theory

We now discuss the relevant MHD theory describing the plasma. In Ideal MHD, the equation of motion is given by Eq. 1.2:

$$\rho_m \frac{D\mathbf{U}}{Dt} = \mathbf{J} \times \mathbf{B} - \nabla P$$

where for a plasma with $\beta \ll 1$, the force corresponding to the pressure term ∇P — the so-called "tire tube force," — can be neglected, so we consider only the $\mathbf{J} \times \mathbf{B}$ forces. These forces are normally separated into *toroidal* and *poloidal* components

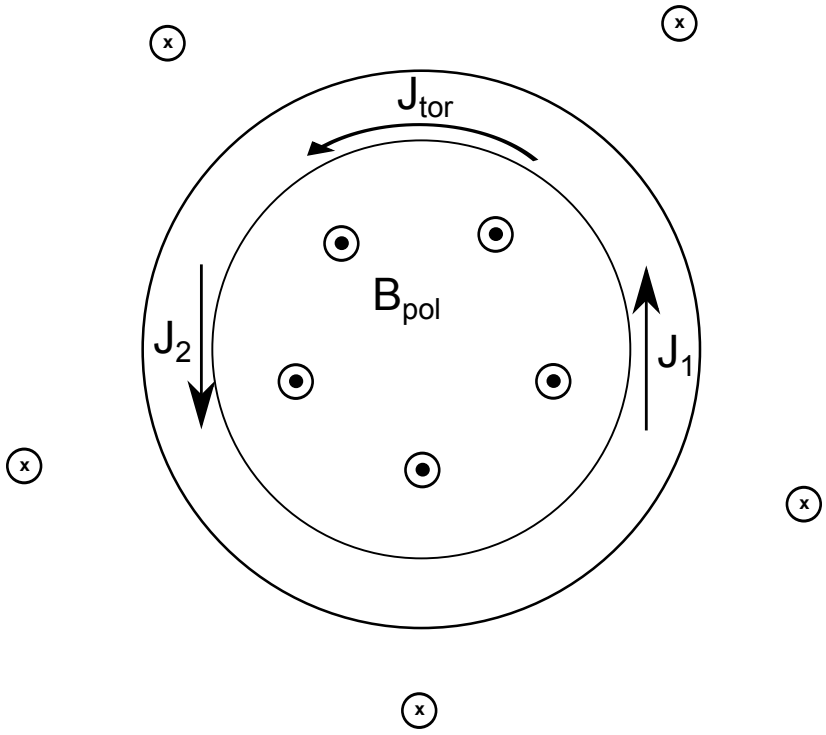

Figure 2.5: Depiction of the hoop force.

(Sec. 1.10.3) and the relevant forces in the major radial direction are

$$\rho_m \frac{D\mathbf{U}}{Dt} = \mathbf{J}_{tor} \times \mathbf{B}_{pol} + \mathbf{J}_{pol} \times \mathbf{B}_{tor} + \mathbf{J}_{tor} \times \mathbf{B}_{strap}$$

which are the hoop force, tension force, and strapping force, respectively. Each force will be discussed separately.

2.3.1 Hoop Force

The hoop force is a manifestation of the idea that anti-parallel currents repel, so that a ring of current will tend to get larger. There are three intuitive ways to see this (Fig. 2.5): (i) repulsion of anti-parallel currents $\mathbf{J}_1$ and $\mathbf{J}_2$, (ii) greater density of B_{pol} inside the ring results in a magnetic pressure that pushes the loop outwards, and (iii) the toroidal current $\mathbf{J}_{tor}$ produces a poloidal magnetic field $\mathbf{B}_{pol}$, which in turn results in a net outward $\mathbf{J} \times \mathbf{B}$ force.

Instead of directly evaluating $\mathbf{J}_{tor} \times \mathbf{B}_{pol}$ over the entire volume, the standard

approach is an energy argument using a virtual displacement. This was first demonstrated by Shafranov [84] and reproduced by many others [33, 85, 86]. The energy associated with a loop of current-carrying plasma is:

$$U = \frac{1}{2} L I^2$$

where L is the loop inductance and I is the current. The hoop force is obtained by making a virtual radial displacement to the loop and looking at how the energy of the loop changes:

$$F_{hoop} = -\frac{\partial U}{\partial R}$$

The poloidal flux through the loop is given by $\Phi = LI$ so $U = \Phi^2/(2L)$. The loop is modeled as a perfect conductor, so the poloidal flux through the loop is constant. The hoop force can be rewritten as:

$$F_{hoop} = -\frac{\partial}{\partial R}\frac{\Phi^2}{2L} = -\frac{\Phi^2}{2}\frac{\partial}{\partial R}\frac{1}{L} = -\frac{I^2 L^2}{2}\frac{\partial}{\partial L}\left(\frac{1}{L}\right) \times \frac{\partial}{\partial R} L(R) = \frac{1}{2} I^2 \frac{\partial L}{\partial R}. \qquad (2.1)$$

The inductance of a loop of major radius R, and minor radius a, is a standard calculation which can be found in Jackson [87]. The solution in the limit of large aspect ratio ($R/a \gg 1$) is

$$L = \mu_0 R \left[\ln\left(\frac{8R}{a}\right) - 2 + \frac{l_i}{2}\right] \qquad (2.2)$$

where l_i is a term of order unity which captures the internal current distribution. For example, $l_i = 0$ if the current is strictly on the skin of the loop whereas $l_i = 1/2$ if the current is uniformly distributed through the loop. Assuming a uniform current distribution, the hoop force is obtained by plugging Eq. 2.2 into Eq. 2.1, yielding:

$$F_{hoop} = \frac{\mu_0 I^2}{2}\left(1 + \ln\left(\frac{8R}{a}\right) - \frac{7}{4}\right) \qquad (2.3)$$

so the force per unit length is given by

$$f_{hoop} = \frac{\mu_0 I^2}{4\pi R}\left(\ln\left(\frac{8R}{a}\right) - \frac{3}{4}\right) \tag{2.4}$$

which depends quadratically on the current.

While this derivation of the hoop force relies on the inductance of a perfectly circular loop, the hoop force for a non-circular object is quite similar. For example, the inductance of a square with wire radius ρ and length L can be found in [88]. In the limit where $l \gg \rho$, the solution is

$$L = \frac{\mu_0 4L}{2\pi}\left[\ln\left(\frac{4L}{\rho}\right) - 1.910\right].$$

If we approximate the perimeter of the square ($4L$) as the circumference of a circle with radius $R = L/2$, then the expression simplifies to:

$$L \approx \mu_0 R\left[\ln\left(\frac{8R}{\rho}\right) - 1.910\right]$$

which is very similar to Eq. 2.2. A similar study by Cooke [89] for elliptical loops finds that the Eq. 2.2 is 90% accurate even when the ratio of the major radius to the minor radius is greater than a factor of 2. Ref. [89] finds that inductance is about 5/6 that of the circular loop, even for highly eccentric ellipse. Thus, the inductance of large aspect ratio ("skinny") circular loop is robust and can be applied to non-idealized situations.

Another potential issue is the assumption that the loop is "skinny" and how much error is introduced when working with "fat" loops. Zic et al. [90] study the inductance in the low aspect ratio limit by introducing the terminology $\eta = a/R$, which is the inverse of the aspect ratio. They find that Eq. 2.2 is accurate to within 1% for $\eta < 0.02$, but overestimate by 10% for $n \approx 0.1$, and by 100% for $n \approx 0.55$. They note that the internal current distribution can play large role in the internal inductance l_i which becomes an important term in the fat loops approximation. For example, the $l_i/2$ term is approximately the same size as the other terms in the square bracket of

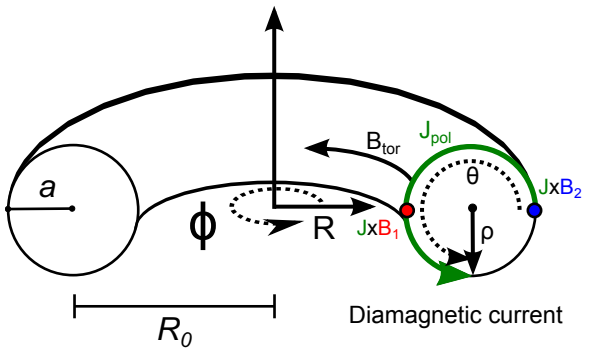

Figure 2.6: Tension force comes from $\mathbf{J}_{pol} \times \mathbf{B}_{tor}$ and is a consequence of the $1/R$ dependence of $\mathbf{B}_{tor}$ so that $\mathbf{J} \times \mathbf{B}_1 \neq \mathbf{J} \times \mathbf{B}_2$. The direction of the force is determined by J_{pol}, i.e., by whether the plasma is paramagnetic or diamagnetic.

Eq. 2.2 when $\eta = 0.5$. Ref. [90] proposes the use of:

$$\frac{L(\eta)}{R_0} = A\left(\log(\frac{8}{\eta}) - B + \frac{l_i}{2}\right)$$

and provides numerically determined values for constants A and B for different density distributions. In the large aspect ratio limit, $A = \mu_0$ and $B = 2$, thus matching Eq. 2.2.

After taking into account the non-circular shape and the aspect-ratio of Caltech plasma loops, Eq. 2.2 is expected to approximate the plasma inductance to within 30%, resulting in a negligible correction to the hoop force. The hoop force depends quadratically on the current, so errors in current measurements play a much larger role. Stenson [82] reports as little as 10 % of the current may flow through the cross-section of the visible plasma loop, suggesting that not all the current measured by the Rogowski coil contributes to the hoop force[2]. A factor of 10 decrease in current results in a factor of 100 decrease in the hoop force calculations, which can significantly change the behavior of the plasma. For a thoughtful discussion about the hoop force, see Ref. [17].

2.3.2 Tension force

The tension force can be conceptualized by thinking of magnetic field lines as rubber bands. If these field lines are pulled at a given point, the corresponding "tension force" will "resist." This behavior can be evaluated directly by considering the relevant $\mathbf{J}\times\mathbf{B}$ forces. When studying forces along the R direction on a toroidal plasma, the tension force is given by $\mathbf{J}_{pol}\times\mathbf{B}_{tor}$. In toroidal coordinates, $R = R_0+\rho\cos\theta$, $Z = \rho\sin\theta$, and the poloidal current is determined by Ampere's law applied to $B_{tor} = B_\phi$, yielding

$$J_{pol} = \frac{R_0}{\mu_0 R}\frac{\partial B_\phi}{\partial \rho}$$

where the toroidal radius ρ is as shown in Fig. 2.6. The tension force can be calculated by integrating over the volume of interest:

$$\mathbf{J}_{pol}\times\mathbf{B}_{tor} = -\frac{\pi R_0^2}{\mu_0}\int\left(\frac{\partial B_\phi^2}{\partial r}\right)\frac{\cos\theta}{R}\rho d\rho d\theta$$

To simplify the analysis, we assume a large aspect ratio so that

$$\frac{1}{R}\sim\frac{1}{R_0}\left(1-\frac{\rho}{R_0}\cos\theta\right)$$

where a Taylor expansion is applied to the "small" element ρ/R_0. Recalling that $\int_0^{2\pi}\cos\theta d\theta = 0$ and $B_\phi = 0$ for $\rho > a$, we are left with

$$F_{tension} = \frac{\pi}{\mu_0}\int_0^{2\pi}\cos^2\theta d\theta\int_0^a\frac{\partial B_\phi^2}{\partial\rho}\rho^2 d\rho = 2\pi^2 a^2\left(\frac{B_{\phi,vac}^2}{2\mu_0}-\frac{\langle B_\phi^2\rangle}{2\mu_0}\right) \tag{2.5}$$

where $B_{\phi,vac}^2$ is the vacuum toroidal magnetic field at $R = R_0$ when no plasma is present and

$$\langle B_\phi^2\rangle = \frac{2}{a^2}\int_0^a B_\phi^2\rho d\rho$$

represents the average value of B_ϕ^2.

[2]Some of the missing current may be arcing from anode to cathode instead of flowing through the plasma.

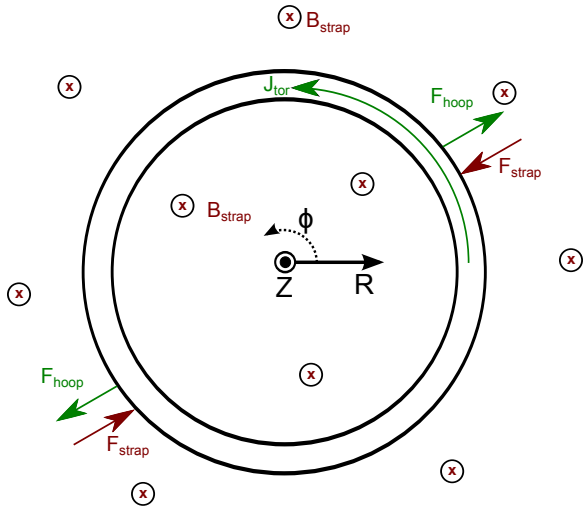

Figure 2.7: Depiction of strapping force and hoop force. The strapping field is oriented into the page and interacts with $\mathbf{J}_{tor}$.

Equation 2.5 shows that the tension force may be described in terms of magnetic energy: the tension force on the plasma is due to the difference between the plasma toroidal field and the vacuum toroidal field [85]. If the plasma is diamagnetic, then $\left\langle B_\phi^2 \right\rangle < B_{\phi,vac}^2$ so the tension force is oriented outwards. If the plasma is paramagnetic, then $\left\langle B_\phi^2 \right\rangle > B_{\phi,vac}^2$ so the tension force is oriented inwards.

The concept of a diamagnetic tension force encouraging plasma expansion seems counter-intuitive, but can be understood by comparing the $\mathbf{J}_{tor} \times \mathbf{B}_{pol}$ force at $R = R_0 - a$ to at $R = R_0 + a$. For example, assume diamagnetic plasma current (green in Fig. 2.6) flows strictly on the skin of the plasma. The skin currents produce a toroidal magnetic field with scaling $B_{tor} \sim 1/R$ [91], so that the field is stronger at $R = R_0 - a$ than at $R + a$. Thus, $\mathbf{J} \times \mathbf{B}_1 > \mathbf{J} \times \mathbf{B}_2$, resulting in a net outwards force. A similar argument can be used to show that paramagnetic tension force results in a net inwards force. The plasmas in the lab are paramagnetic, so the tension force is expected to resist the hoop force expansion.

2.3.3 Strapping force

A current carrying loop of plasma will tend to expand in vacuum unless additional forces are introduced to "strap" it down. This external force comes in the form of a

$\mathbf{J}_{tor} \times \mathbf{B}_{strap}$ force where the strapping field $\mathbf{B}_{strap}$ is created by external coils and the orientation of the field is chosen so that $\mathbf{J}_{tor} \times \mathbf{B}_{strap}$ points in the $-\hat{\mathbf{R}}$ direction as shown in Fig. 2.7. For example, if the toroidal current is in the $\hat{\boldsymbol{\phi}}$ direction, then the strapping field must be oriented in the $-\hat{\mathbf{z}}$ direction. This field is known as a vertical field in the tokamak literature [84–86, 92] and strapping field in the solar literature [33, 40]. It is also possible to think of the strapping field from the perspective of magnetic pressure. Recall that $\mathbf{J}_{tor}$ produces denser regions of poloidal field inside the loop than outside of the loop, resulting in greater magnetic pressure inside the loop (Fig. 2.5). The strapping field lines can be thought as decreasing pressure inside the loop and increasing magnetic pressure outside of the loop.

The strapping force can be calculated by integrating the $\mathbf{J} \times \mathbf{B}$ of force over the plasma volume:

$$\mathbf{F}_{strap} = \int \mathbf{J}_{tor} \times \mathbf{B}_{strap} 2\pi R dS \tag{2.6}$$

If we assume that $\mathbf{B}_{strap}$ is essentially constant over the cross section of the plasma and that $\mathbf{J}_{tor}$ is uniformly distributed within the loop, then

$$F_{strap} = -2\pi R I B_{strap} \tag{2.7}$$

where $I = \pi a^2 J_{tor}$ is the current flowing through the loop. Eq. 2.7 has the same form as a wire of length $2\pi R_0$, carrying a current I, in a uniform field $\mathbf{B}_{strap}$.

2.3.4 Equilibrium

Combining the hoop force (Eq. 2.3), tension force (Eq. 2.5), and strapping force (Eq. 2.7) yields the following equation of motion:

$$m\frac{d^2R}{dt^2} = \frac{\mu_0 I^2}{2}\left(\ln\left(\frac{8R}{a}\right) - \frac{3}{4}\right) - 2\pi^2 a^2 \left(\frac{B^2_{\phi,vac}}{2\mu_0} - \frac{\left\langle B^2_\phi \right\rangle}{2\mu_0}\right) - 2\pi R I B_{strap} \tag{2.8}$$

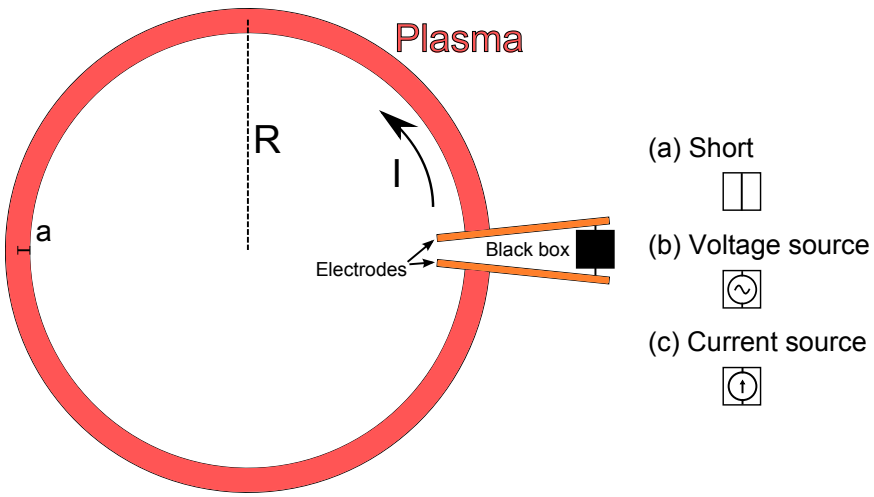

Figure 2.8: Nearly-circular plasma connected to a black-box power supply. The power supply can be (a) a short, (b) a voltage source, or (c) a current source.

where m is the mass of the plasma ring. Thus, the strapping field required for equilibrium is

$$B_{strap} = \frac{1}{2\pi RI}\left(\frac{\mu_0 I^2}{2}\left(\ln\left(\frac{8R}{a}\right) - \frac{3}{4}\right) - 2\pi^2 a^2\left(\frac{B_{\phi,vac}^2}{2\mu_0} - \frac{\langle B_\phi^2\rangle}{2\mu_0}\right)\right)$$

2.4 Torus instability

Suppose the tension force were negligible, so that only the hoop force and strapping force are considered. The simplified equation of motion can be expressed in terms of force per unit volume as

$$\rho_m \frac{d^2R}{dt^2} = \frac{I^2}{4\pi^2 a^2 R^2}\left(L + \mu_0 R/2\right) - \frac{IB_{strap}}{\pi a^2} \tag{2.9}$$

where $L + \mu_0 R/2 = \mu_0 \ln(8R/a) - 3/4)$ and L is the loop inductance given by Eq. 2.2. Equilibrium is determined by the balance between the hoop force and the strapping field. The torus instability considers the stability of this equilibrium configuration.

The approach here is a generalization of the approach outlined by Kliem and Torok [33]. Instead of a circular plasma loop, we consider a nearly-circular loop with electrodes connected to a black box, as shown in Fig 2.8. The near-circular nature

of the plasma means that the simplified equation of motion (Eq. 2.9) remains a good approximation. The presence of the electrodes and power supply permit the application of different boundary conditions.

2.4.1 General algorithm

We adapt the algorithm developed in Ref. [33], making an ansatz about the magnetic field and assuming self-similar expansion to make the problem analytically tractable, while retaining the essential physics.

The general algorithm is as follows:

1. Consider the system in equilibrium at some $R = R_0$ and use subscripts to denote values determined at equilibrium.

2. Make ansatz that $\mathbf{B}_{strap}(R) = \hat{\mathbf{B}} R^{-n}$ for $R \geq R_0$. Assume that $\mathbf{B}_{strap}(R < R_0)$ is finite and has been tailored to achieve equilibrium at $R = R_0$.

3. Use boundary conditions at electrodes to express current as a function of R, i.e., $I = I(R)$. Substitute $I(R)$ into the equation of motion.

4. Simplify mathematics by:

   (a) Normalizing distance (ρ) to R_0 so that $\rho = 1$ at equilibrium. Normalize time τ to a "hybrid" Alfven time.

   (b) Assuming self-similar expansion so that $R/a(R) \sim const$ and the logarithmic term $\ln(8R/a) \sim const$.

5. Use $d(d^2\rho/d\tau^2)/d\rho|_{\rho=1} > 0$ to determine the condition for instability.

The derivation in Ref. [33] looks at a closed conducting loop and is limited to the short-circuit boundary condition [41]. Our set-up does not have this restriction so we consider the following boundary conditions: (i) short circuit, (ii) voltage source, and (iii) constant current source.

2.4.2 Short circuit

Consider the situation in Fig. 2.8 (a) where the black box contains a short. The flux within the loop

$$\Phi_{loop} = \Phi_{plasma} = LI \tag{2.10}$$

is conserved and strapping field does not penetrate inside the loop due to perfect loop conductivity[3]. In this limit, the loop current is given by

$$I(R) = \frac{L_0 I_0}{L} = \frac{c_0 R_0 I_0}{cR} \tag{2.11}$$

where $c = L/(\mu_0 R)$. R_0 and I_0 represent the major radius and current at equilibrium, so $c_0 = L_0/\mu_0 R_0$. Plug Eq. 2.11 into the equation of motion (Eq. 2.9) and normalize according to $\rho = R/R_0$ and $\tau = t/T$, where

$$T = \frac{(2c_0+1)^{1/2}}{2\sqrt{2}} \frac{a}{V_{Ai}} \tag{2.12}$$

where $V_{Ai} = \sqrt{B^2_{strap,0}/(\mu_0 \rho_{m,0})}$ is the Alfven velocity determined by equilibrium values of strapping field and mass density. T is then a "hybrid" Alfven time of the minor radius. Simplifying the math yields the following equation of motion:

$$\frac{d^2\rho}{d\tau^2} = \left(\frac{c_0}{c}\right) \frac{(2c+1)}{2c_0+1} \rho^{-2} \left[1 - \rho^{2-n} \frac{c}{c_0} \frac{(2c+1)}{(2c_0+1)}\right] \tag{2.13}$$

After assuming a self-similar expansion so that $c(R) = c_0$, we apply the instability criterion

$$\frac{d}{d\rho}\left(\frac{d^2\rho}{d\tau^2}\right)\bigg|_{\rho=1} > 0$$

to obtain

$$n_{cr} = 2 \tag{2.14}$$

[3]There are nuances to this argument, depending on whether the strapping field is present when current is introduced to the loop.

as the critical decay index. This means that the system is unstable if the strapping field falls off more sharply than R^{-2}.

2.4.3 Voltage source

In contrast to the short-circuit situation, a voltage source boundary condition can model the effect of strapping field penetrating into the plasma loop. In this case, the flux within the loop is now

$$\Phi_{loop} = \Phi_{plasma} + \Phi_{strap} = LI - 2\pi \int_0^R B_{strap} r dr \tag{2.15}$$

where the strapping flux diffuses into the center of the loop. This flux criterion is assumed by both Bateman [85] and KT [33] for tokamak stability and solar eruptions, respectively. Equation 2.15 holds if the loop evolves slowly over the diffusion time scale. While tokamak plasmas are highly conductive, their conductivity is finite and a strapping field applied over a long period can penetrate into the plasma. Similarly, solar loops are stable for days so ambient flux can penetrate the loop. When tokamaks become unstable or solar loops erupts, Eq. 2.15 may not hold since the instability time scale may be shorter than the magnetic diffusion time scale. If the instability time scale is too short, no new strapping flux may diffuse into the plasma and the conserved flux is

$$\Phi_{loop,R_0} = \Phi_{plasma} + \Phi_{strap,R_0} = LI - 2\pi \int_0^{R_0} B_{strap} r dr = L_0 I_0 \tag{2.16}$$

where the subscript denote the value at equilibrium. The problem described by Eq. 2.16 reduces to a modified version of the short-circuit problem. These nuances about boundary conditions are glossed over by KT. Chen [41] points out that the lack of footpoints in the KT derivation requires imposing the short-circuit boundary conditions (Eq. 2.10).

The presence of electrodes permits more flexible boundary conditions. For exam-

ple, during eruption, Eq. 2.15 can be rewritten as

$$V_{electrode} = \frac{d\Phi_{loop}}{dt} = \frac{d}{dt}(\Phi_{loop,R_0}) + \frac{d}{dt}(\Phi_{strap,R>R_0}) = \frac{\partial}{\partial R}\left(\int_{R_0}^{R} B_{strap} r dr\right)\frac{dR}{dt}$$

where we assume a perfectly conducting plasma ($d\Phi_{loop,R_0}/dt = 0$) and a strapping field with no time dependence ($\partial\Phi_{strap}/\partial t = 0$). Thus, the voltage across the footpoints represents the strapping field diffusing into the plasma loop. Equation 2.15 can be expressed as a voltage source condition on the electrodes (Fig. 2.8 (b)).

Assuming that Eq. 2.15 holds, the current is given by

$$I = \frac{L_0 I_0 - 2\pi \int_{R_0}^{R} B_{strap} r dr}{L} \tag{2.17}$$

where we note that $LI - \int_0^R B_{strap} r dr = L_0 I_0 - 2\pi \int_{R_0}^{R} B_{strap} r dr$. The ansatz that $B_{strap}(R) = \hat{B} R^{-n}$ for $R > R_0$ and is at equilibrium at $R = R_0$ means that

$$B_{strap}(R) = \frac{I_0}{4\pi R_0^2}\left(L_0 + \frac{\mu_0 R_0}{2}\right) R_0^n R^{-n}, \quad R \geq R_0 \tag{2.18}$$

Substituting Eq. 2.18 into Eq. 2.17 yields an expression for current which can then be plugged into the equation of motion, normalized, and solved (see Ref. [33] for complete details). The resulting critical decay index is

$$n_{cr} = \frac{3}{2} - 4c_0 \tag{2.19}$$

where $c_0 = L_0/(\mu_0 R_0)$. For laboratory plasmas, a typical value of c_0 is 2.5 to 10 so

$$n_{cr} \approx 1.5$$

2.4.4 Constant current source

Instead of passively responding to the plasma, the power supply could inject energy into the system, as in a constant current configuration (Fig. 2.8 (c)). The current is

given by

$$I = I_0 \tag{2.20}$$

and the force balance equation takes the form

$$\rho_m \frac{d^2R}{dt^2} = \frac{I_0^2}{4\pi^2 b^2 R^2}\left(L + \frac{\mu_0 R}{2}\right) - \frac{I_0 B_{strap}(R)}{\pi b^2}$$

In the large aspect ratio limit, $L \sim \mu_0 R \ln(8R/a) \gg \mu_0 R/2$, so the equation becomes

$$\rho_m \frac{d^2R}{dt^2} = \frac{I_0^2 L}{4\pi^2 b^2 R^2} - \frac{I_0 B_{strap}(R)}{\pi b^2}$$

Once again, we assume a self-similar expansion so $c(R) = L/\mu_0 R$ is constant. Specifically, $c = c_0 = L_0/(\mu_0 R_0)$. We make a similar ansatz about the strapping field so $B_{strap}(R) = \hat{B}R^{-n}$ for $R > R_0$, and set $B(R_0) = (I_0 L_0/(4\pi R_0^2))(R_0^n R^{-n})$.

At equilibrium, the equation of motion becomes

$$0 = \frac{I_0^2 \mu_0 R c_0}{4\pi^2 b^2 R^2} - \frac{I_0^2 \mu_0 R_0 c_0}{R_0^2} R_0^n R^{-n} \rightarrow 0 = \frac{1}{R} - \frac{1}{R_0} R_0^n R^{-n}$$

and can be normalized to $\rho = R/R_0$ to obtain

$$0 = \frac{1}{\rho} - \frac{1}{\rho^n}.$$

Thus, the instability criterion for constant current boundary conditions is

$$n > 1 \tag{2.21}$$

2.4.5 Physical systems and interpretation

A system described by the constant flux assumption (Eq. 2.10) is the most stable of the cases considered. When the plasma loop expands, the field lines just outside the loop are unable to diffuse into it, resulting in a pile-up. This pile-up resists plasma expansion, and the system is stable unless the magnetic field falls off more sharply

than $\sim R^{-2}$. If the strapping field is allowed to diffuse into the loop (Eq. 2.15), then there is no stabilizing pile-up effect and the system is unstable if the magnetic field decreases more sharply than $\sim R^{-1.5}$. Or else, if the system is driven by an external power supply, as to maintain constant current (Eq. 2.20), then the plasma is unstable if the field decrease more sharply than $\sim R^{-1}$[4].

Unfortunately, physical systems may not conform to the simplified description of Eqs. 2.14, 2.19, and 2.21. All three theoretical descriptions assume self-similarity, but the minor radius of a solar loop often varies along the loop, resulting in non-MHD effects like flows [66]. Solar "loops" also have footpoints and are arched-shaped instead of fully circular. Simulations by Olmedo and Zhang [93] suggest that n_{cr} is smaller for partial loop than for complete loops. These details make it impractical to prescribe a single critical threshold.

Nevertheless, the essence of the torus instability is that a system can go unstable if the magnetic field decreases sufficiently sharply. Though the torus instability is often cited as a driver of solar eruptions [13, 32, 33, 94, 95], no experimental verification has been performed. In the Caltech solar experiment, we study hoop-force dominated plasma loops expanding in a sharply decaying strapping field, demonstrating that a plasma loop can go from slow rise to fast eruption due to torus instability.

2.5 Results

A key assumption in our implementation of the torus instability is that two forces dominate plasma dynamics: the hoop force and the strapping force. In this section, we provide experimental verification that the hoop force dominates plasma dynamics when no strapping field is applied. We study plasma dynamics for strapping fields of different amplitudes, and highlight results from three configurations: No Strapping field (NS), Intermediate Strapping field (IS), and Large Strapping field (LS). These three configurations corresponds to a peak B_x of 0 G, 250 G, and 500 G, respectively

[4] A useful analogy is the snow height required to stop a runaway snowplow. Lower snow height will stop a snowplow, if the snow can pile up. In contrast, if the snowplow engine is engaged, then higher snow height would be required to stop the snowplow.

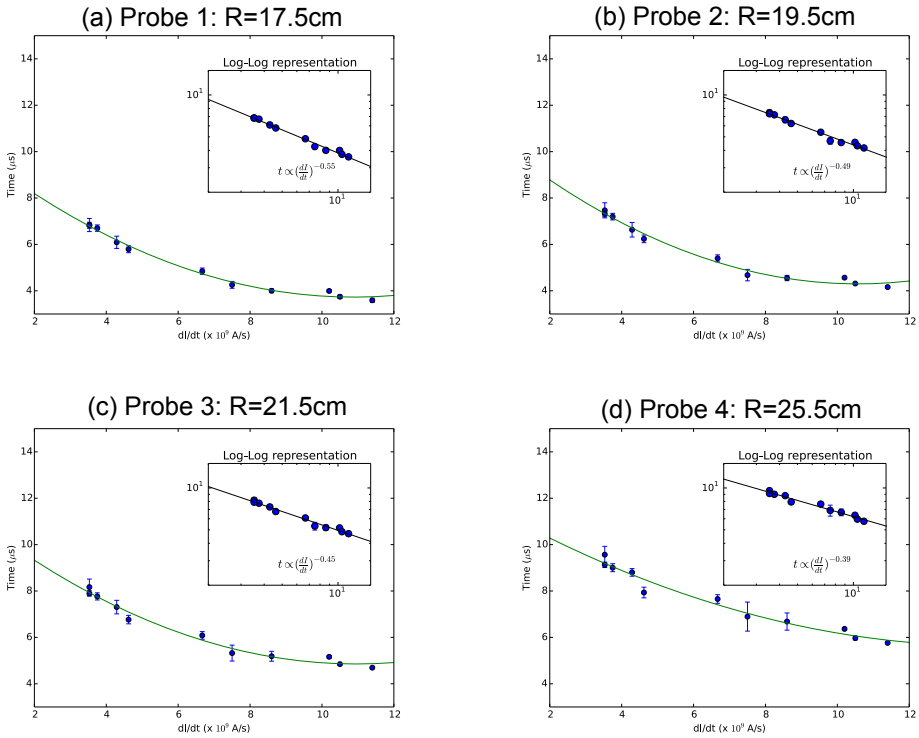

Figure 2.9: Time for the plasma to travel to the magnetic probe clusters. dI/dt is varied by changing the peak current I_0 and the rise time of the current pulse τ independently. The inset is a log-log representation of the data and shows the relation $t_{probe} \propto (I_0/\tau)^{-\gamma}$ where $\gamma = 0.55, 0.49, 0.45$, and -0.39 for probes 1-4, respectively.

(See plot in Fig. 2.4 side view).

2.5.1 Hoop force dominates

Stenson and Bellan [82] use camera images to study the acceleration of plasma loops. They conclude that expansion is dominated by the hoop force (Eq. 2.4):

$$f_{hoop} = \frac{\mu_0 I^2}{4\pi R}\left[\ln\left(\frac{R}{a}\right) + 1.08 + \frac{l_i}{2}\right] \tag{2.22}$$

where I is the current, R is the major radius of a loop, a is the minor radius, and l_i represents the internal inductance due to the internal current distribution of the loop. The equation of motion for an infinitesimal segment of the loop with length ds

and mass dm can be expressed as a second order differential equation for $R(t)$:

$$\ddot{R}(t) = \frac{\alpha}{4\pi^2}\frac{\mu_0}{m_i n a^2}\frac{I(t)^2}{R(t)} \tag{2.23}$$

where $\alpha = (\ln(R/a) + 1.08 + l_i/2)$, m_i is the ion mass, and n is the number density of the plasma. Stenson and Bellan assume that n and a are time-independent, consistent with laboratory observations.

By assuming a linear time dependence for the current $I(t) = I_0 t/\tau$, and approximating α as constant due to slow variation of $\ln(R/a)$, Stenson and Bellan show that for times $t < \tau$, the expansion of the plasma due to the hoop force has the form

$$R(t) = \frac{1}{2\pi}\sqrt{\frac{\mu_0\alpha}{2m_i n}}\frac{I_0}{a\tau}t^2 \tag{2.24}$$

where I_0 is the peak current, τ is the rise time of the current trace. Equation 2.24 predicts constant loop acceleration for $t \leq \tau \approx 8.5\ \mu s$ and $t \propto (I_0/\tau)^{-0.5}$ for a fixed R.

Since the strapping coils in our experiment block the plasma from the camera viewpoint at early times, we use magnetic measurements to verify that the NS plasma expansion is dominated by the hoop force. This is done by measuring the polarity reversal of the B_x component of the magnetic field. Figure 2.9 plots plasma travel time to four magnetic probe clusters as a function of I_0/τ. We vary I_0/τ by either:

1. Adding inductance into the system to increase τ while adjusting the charging voltage of the 59 μF capacitor bank to maintain I_0, or

2. Increasing the charging voltage of the capacitor bank to increase I_0.

Applying a log-log fit to the data (Fig. 2.9 insets) gives $t_{probe} \propto (I_0/\tau)^{-\gamma}$ where $\gamma = 0.55$ for the first probe cluster (Fig. 2.9 (a)) and $\gamma = 0.47 \pm 0.06$ across all four clusters. This near square root dependence indicates that the hoop force dominates plasma dynamics in the absence of a strapping field. The fit is weaker for the fourth probe cluster (Fig. 2.9 (d)) at $R = 25.5$ cm. This is attributed to the falling current trace at later times, violating the assumption of a linearly rising current.

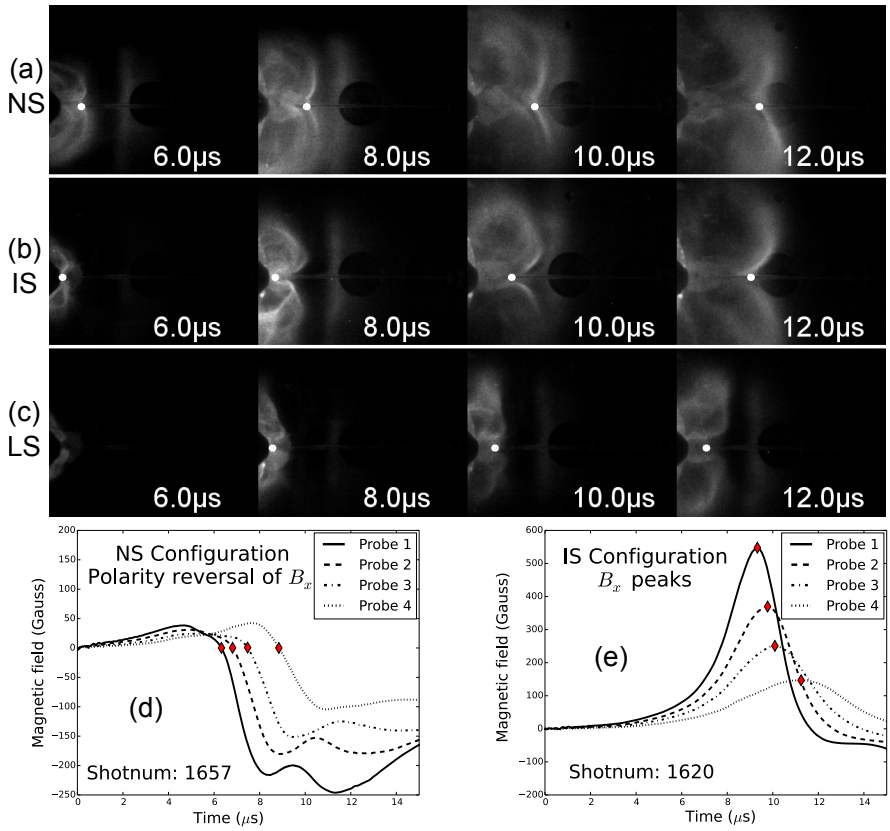

Figure 2.10: Imaging and magnetic diagnostics. The dots in (a), (b), and (c) represent the location of the plasma apex and are determined by looking at intensity slices along the z-axis and selecting the local intensity maximum. (d) and (e) show B_x component of the magnetic trace across all four magnetic probe clusters. The diamonds correspond to the bright (high density) leading edges from the camera images.

2.5.2 Imaging and Magnetic diagnostics

Imaging and magnetic diagnostics were used to determine the location of the apex of the plasma as shown in Fig. 2.10 (a-e). For complete details about the diagnostic technique, see Appendix sections G.1 and G.2.

When no strapping field is applied (NS), the acceleration occurs at low heights and images of the plasma show near-constant expansion of the plasma apex (white circle in Fig. 2.10 (a)) after 6 μs. The application of a strapping field introduces a $\mathbf{J} \times \mathbf{B}$ strapping force which opposes plasma expansion. Images of the plasma loops (Fig. 2.10 (a-c)) show more compact plasmas for the IS and LS configuration than for the NS configuration. The dots in Fig. 2.10 represent the location of the plasma

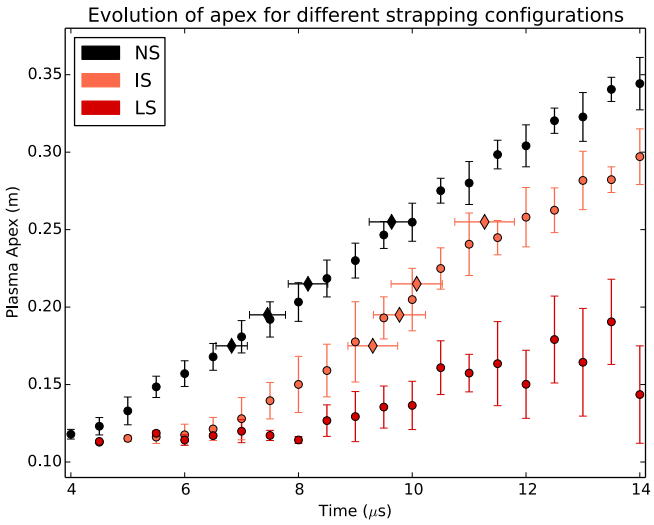

Figure 2.11: Height (z) vs time plot of different strapping configurations. The circles represent data obtained from imaging the plasma. The diamonds represent plasma position determined by the magnetic probes. In the LS configuration, the plasma does not reach the magnetic probe in the 14 μs time interval.

apex and are determined by looking at intensity slices along the z-axis and selecting the local intensity maximum. The black circle at the center of each frame is a vacuum chamber window.

Figure 2.10 (a) shows the NS configuration where most of the acceleration occurs at low apex height and the plasma expands at near constant velocity after 8 μs. Figure 2.10 (b) shows the IS configuration plasma demonstrating slow-rise to fast-acceleration. The apex of the plasma loop is slowed as it passes the region of strong strapping field between 6 μs - 8 μs while the upper and lower section continues to expand outwards. Between 8 μs - 10 μs, the apex of the plasma rapidly accelerates as it experiences a sharp decay in the strapping field. Figure 2.10 (c) shows LS configuration. The strong strapping field slows down the entire plasma structure and completely inhibits bulk plasma motion along the z-axis.

The mean distance between the apex and the electrodes at a given time is extracted from camera images and plotted as black circles in Fig. 2.11. The distance vs time measurements from Fig. 2.11 are smoothed and numerically differentiated to obtain velocity. This process is repeated on velocity vs time calculations to obtain

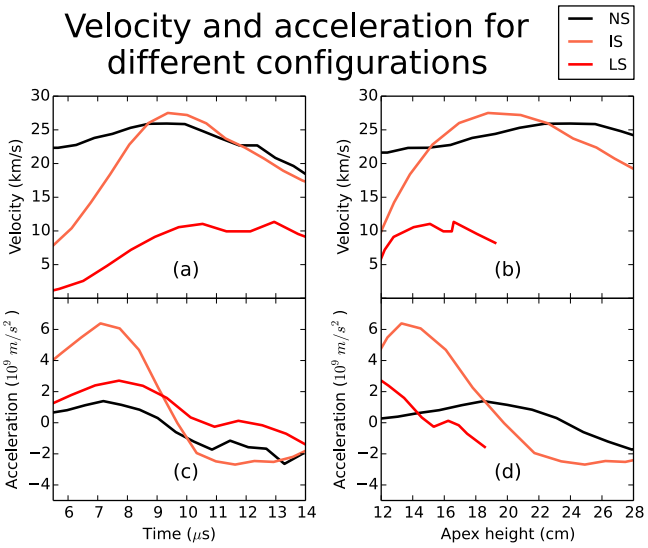

Figure 2.12: (a) Velocity obtained by smoothing the distance vs time measurements and then taking the numerical derivative for the three strapping configurations shown in Fig. 2.11. (b) Velocity as a function of apex height (z). (c) and (d) show acceleration obtained by smoothing the velocity and applying a numerical derivative.

acceleration. We apply the same apex extraction, smoothing, and numerical differentiation techniques to the NS, IS, and LS configurations and append the results to Figs. 2.11 and 2.12; the NS, IS, and LS configurations are color-coded as black, orange, and red, respectively.

The diamonds in Fig. 2.11 represent the average time for the plasma to travel to the magnetic probe clusters. We determine the plasma expansion time to a given magnetic cluster by measuring when the polarity reversal of the B_x component of the magnetic field occurs (Fig. 2.10 (d)); B_x reverses sign on the axis of the loop. In the LS configuration, the plasma is completely confined and the velocity peaks (Fig. 2.12) once the driving current begins to decay at 10 μs (Fig. 2.13(b)). The apex does not reach the magnetic probe until $t > 15$ μs and the estimated expansion velocity is essentially zero.

2.5.3 Demonstration of slow rise to fast eruption

Our main result is the IS data which demonstrate a slow initial rise of the plasma apex followed by a rapid expansion. The nominal Alfven velocity of the system $v_A = B/\sqrt{\mu_0 \rho} \approx 40$ km/s and we define "fast" to be $v > 20$ km/s and "slow" to be $v < 13$ km/s. The sudden increase in velocity (slow to fast transition at $6 - 9$ μs in Fig. 2.12 (a), $12 - 20$ cm in Fig. 2.12 (b)) corresponds to the plasma escaping the region of strong strapping field (centered at $z = 9.5$ cm in Fig. 2.4 side view). This escape coincides with a seven-fold increase in the plasma apex acceleration ($6 - 9$ μs in Fig. 2.12 (c)).

The increased acceleration is attributed to two effects: the build-up of the hoop force within the strapping region and the sharp decay of the strapping field once the plasma has left the strapping region. The build-up of the hoop force comes from the $f \sim I^2/R$ scaling of Eq. 2.22. The IS configuration slows down the expansion of the plasma apex within the strapping region, effectively holding R approximately constant. The peak amplitude I_0 and the slope I_0/τ of the driving current pulse are configured so that the current continues to increase when the plasma is slowed down (Fig. 2.13 (b)). In the IS configuration, the current pulse peaks at $8 - 9$ μs, matching the time when the plasma loop apex passes the strapping field coils. Thus, the resulting decay of the strapping force experienced by the plasma loop when it expands beyond the strapping coils is accompanied by a relative increase in the hoop force due to the peaking of the current.

The steepness of the strapping field decay is captured by the magnetic decay index $n = -(z/B_x)(dB_x/dz)$. The value of n varies with axial position z (up-sloping dashed line in Fig. 2.4 side view) and when n is greater than a critical n_{cr}, the plasma loop is predicted to undergo torus instability [33], i.e., the restoring force associated with the strapping field decays more rapidly than the hoop force. The value of n_{cr} has been predicted to range between $1-2$ [33, 58, 96, 97] depending on geometry and boundary conditions (See Sec. 2.4). As a guideline, we use $n_{cr} = 3/2 - 1/(4c_0)$ from Ref. [33] where $c_0 = L/\mu_0 R$ is the same as α in Eq. 2.24. While there are concerns [41]

about the lack of footpoints in Ref. [33], simulations including footpoints [93] suggest that the essential physics of torus instability should apply. For our experiment, we calculate $\alpha \approx 2.5$ at plasma formation resulting in $n_{cr} \approx 1.4$, which is plotted as the dotted horizontal line in Fig. 2.4 side view. The torus instability is expected approximately when the plasma loop moves to the right of the intersection of the dashed up-sloping line and this dotted horizontal line.

The height vs time plots in Fig. 2.11 were obtained using both imaging (circles) and magnetic probe data (diamonds). When no strapping field is applied (NS), the polarity reversal of B_x correlates well with the high density region of the plasma, i.e., the axis of the current flowing along the plasma loop. When a 250 G strapping field is applied (IS), the loop location is given by the peak of B_x (Fig. 2.10 (e)) rather than by the polarity reversal (Fig. 2.10 (d)). We attribute this difference to two effects: the strapping flux concentrates in regions of high plasma density (Fig. 2.10 (e)) and the strapping force rotates the flux rope, thereby converting B_y and B_z components into B_x component. These two effects make it difficult to identify plasma structure in a strapping field from magnetic probes alone.

2.5.4 Circuit diagnostics

The load inductance is a measure of the entire plasma structure and is expected to scale as $L \sim \mu_0 R\alpha$ where $\alpha \approx 2.5$. We calculate the time evolution of the inductance by neglecting resistance and using $V = L(dI/dt) + I(dL/dt)$, where V is the voltage measured across the plasma footpoints and I is the current through the plasma (Fig. 2.13 (a) and (b)). This equation can be discretized for a time step Δt:

$$L_{j+1} = L_{j-1} + \frac{2V_j \Delta t}{I_j} - \frac{L_j}{I_j}\left(I_{j+1} - I_{j-1}\right). \tag{2.25}$$

To obtain an initial condition, we assume $L_0 = V_0/(dI/dt)_0$, since I is very small at early times. Furthermore, since plasma expansion is minimal at early times, we assume $L_{-1} = L_0$. Resistance is non-negligible at breakdown and the plasma is cold slightly after breakdown, so we assume Eq. 2.25 is valid for $t > 2\mu s$. The solutions

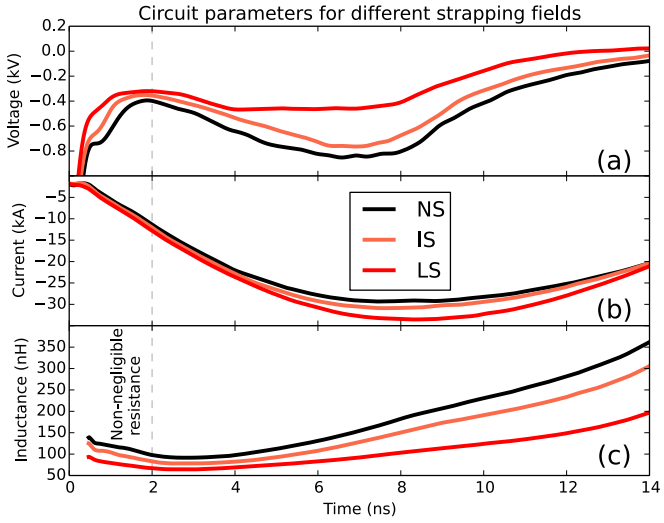

Figure 2.13: (a) Measured voltage and (b) measured current for different strapping field configurations. (c) Calculated inductance vs time from voltage and current measurements using Eq. 2.25.

are then valid for the time interval of interest $2\mu s < t < 14\mu s$; I is finite during this interval so Eq. 2.25 is well-behaved.

Figure 2.13 (c) shows the inductance calculated using Eq. 2.25 for NS, IS, LS configurations; each plot is constructed using the average of ≈ 30 measurements for current and voltage. Figure 2.13 (c) shows that a stronger strapping field leads to a smaller initial inductance and a slower inductance growth. By using $R \sim L/(\mu_0 \alpha)$ at 2 μs, the calculated major radii are 3.2 cm, 2.2 cm, and 2.0 cm for NS, IS, and LS configurations, respectively. Similar calculations at the time of peak current ($t = 8.5$ μs) yield $R \sim 6.2$ cm, 5 cm, and 3.3 cm, respectively. The calculations are within a factor of 2 of the measured apex values in Fig. 2.11.

2.5.5 Varying the driving current

A faster rise in current corresponds to a rapid build up of expansion forces and is expected to accelerate the plasma quickly. A slower rise in current corresponds to the slower build-up of expansion forces. By adjusting L_{extra} and main bank charging voltage, it is possible to modify the slope of the driving current while preserving

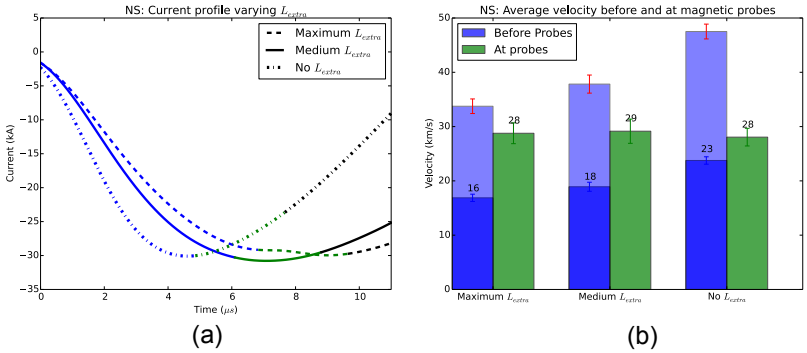

Figure 2.14: (a) Different current profiles for the NS configuration. Blue represents time before the plasma reaches the magnetic probe and green represents when the plasma is at the magnetic probes. (b) Average velocities before the magnetic probes (dark blue) and average velocities during the magnetic probe (dark green). The light green represents velocity just before the magnetic probes assuming the plasma starts in quasi-static equilibrium and experiences constant acceleration

peak current. Figure 2.14 (a) shows the NS current profile for three different L_{extra} configurations: None, Medium, Maximum[5].

Since the magnetic probe array comprises four clusters at known locations, the average velocity of the plasma can be obtained by tracking persistent probe features (Sec. G.2 and Figs. 2.10 (d) and (e)). If the initial height of the plasma apex is known, the average velocity from plasma formation to the first magnetic probe at $z = 17.5$ cm can be also calculated. Camera images show that application of strapping field results in a smaller initial plasma than if no field were applied, consistent with the estimates using inductance. We use $z = 6$ cm and $z = 4$ cm as the initial plasma apex position for NS and IS configurations, respectively. Since the plasma starts at in quasi-static equilibrium, and Eq. 2.24 predicts constant acceleration, the velocity at the first probe is approximately double the average velocity.

Figure 2.14 (b) shows the average velocities for None, Medium, and Max L_{extra} configurations when no strapping field is applied. When no extra inductance is applied, the average plasma velocity before the first magnetic probe (dark blue) is greater than the corresponding average velocities when inductance is added. Nevertheless, all three configurations exhibit the same average velocity at the probes (green). This sug-

[5]The data from the previous sections are taken with the Maximum L_{extra} configuration.

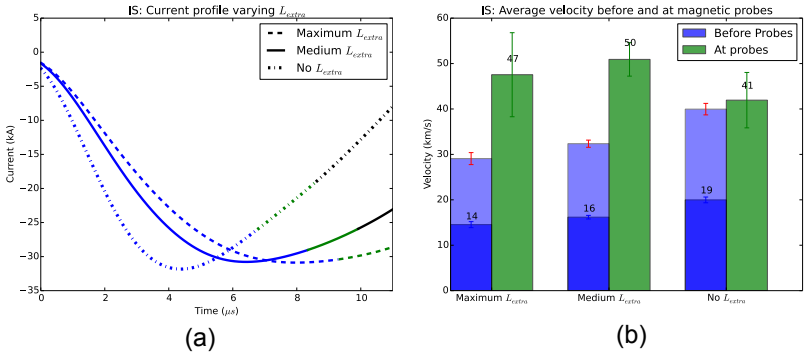

Figure 2.15: (a) Different current profiles for the IS configuration. Blue represents time before the plasma reaches the magnetic probe and green represents when the plasma is at the magnetic probes. (b) Average velocities before the magnetic probes (dark blue) and average velocities during the magnetic probe (dark green). The light green represents velocity just before the magnetic probes assuming the plasma starts in quasi-static equilibrium and experiences constant acceleration

gests that the Maximum and Medium configurations undergo weaker acceleration over longer periods of time. The estimated velocities using Eq. 2.24 (light blue) match the Maximum configuration quantitatively, but are too large for the Medium and None configuration, suggesting that the constant acceleration assumption eventually breaks down. One of the requirements for constant acceleration is linearly increasing current. The current traces in Fig. 2.14 (a) is colored blue before the plasma reaches the magnetic probe, green when the plasma is at the four magnetic probes, and black when the plasma passes the magnetic probes. The current in the None configuration is falling when the plasma reaches the probes, so Eq. 2.24 no longer applies. Similarly, the current for the Medium configuration is about to peak so Eq. 2.24 may not work as well. Equation 2.24 is expected to apply for the Maximum configuration up to 8 μs, consistent Fig. 2.12 (c), which shows decreased acceleration at 8 μs and even deceleration at later times.

Figure 2.15 shows the three L_{extra} configurations when IS strapping field is applied. The strapping field slows down the plasma so that the current traces (Fig. 2.15 (a)) are past the peak by the time the plasma reaches the magnetic probe. Figure 2.15 (b) shows the average velocities before and at the probe. Both Medium and Maximum L_{extra} configurations suggest a slow rise to fast eruption configuration. As described

earlier, the enhanced acceleration is attributed to the decay of the strapping field and the peaking of the current trace when the plasma moves past the peak strapping field region. The current rises too quickly in the None configuration, accelerating the plasma past the strapping coils. While there is an increase in velocity at the probe, this configuration does not reproduce a slow rise follow by rapid acceleration.

The plasma velocities at the probes in Fig. 2.15 (b) are also larger than the calculated velocities reported for IS configuration in Fig. 2.12. This suggests that the magnetic flux rope may be moving faster in IS configuration than the bright high density plasma. Previous works [17, 98] suggest that the magnetic flux rope (the current channel) is wider than the bright high density plasma from camera images. When no strapping field is applied, both the high density region and the flux rope are expected to move with comparable velocities. The IS configuration may accelerate the magnetic flux rope structure to higher velocities than apparent in visible images. This is compatible with CMEs where the bright prominence represents the high-density plasma (the core in Fig. 1.8) located within (but at the bottom of) a larger erupting magnetic flux rope (the cavity in Fig. 1.8).

2.6 Conclusion and Discussion

Our observations demonstrate that torus instability is a means by which magnetic flux ropes may change from slow-rise to fast-acceleration. We present measurements from three diagnostics – imaging, magnetic measurements, and circuit analysis – and show a quantitative match between all three diagnostics. The Kliem and Torok implementation of torus instability assumes a hypothetical perturbation on the flux rope, without specifying the nature of said perturbation. Our results suggest that "increasing current" is an embodiment of this perturbation and the time dependence of the current is important. We find the most dramatic acceleration for IS-like configurations occurs when we tailor the current pulse to peak as the plasma enters the region of steeply decaying strapping field.

2.6.1 Scaling to the sun

Since Lorentz forces do not have an intrinsic length scale, it is reasonable to expect that our results should scale to solar loops provided that solar stratification is taken into account. The β of the solar atmosphere varies between the photosphere and the outer corona [74]. Our results should apply in the lower corona where $\beta \ll 1$ and the magnetic energy density is 800 times the gravitational energy density [57]. The NS configuration corresponds to fast, impulsive CMEs with large accelerations at low heights and little acceleration at greater heights [99]. The LS configuration corresponds to failed eruptions [94], i.e., the solar filament erupts from the solar surface, but fails to escape the solar atmosphere. The IS configuration, our new result, provides the first experimental demonstration of the slow-rise to fast-acceleration; this configuration corresponds to the majority of CMEs [83].

2.6.2 Is reconnection necessary for CME eruptions?

The proponents of sheared arcade models believe that magnetic reconnection forms the flux rope during the eruption process (Sec. C.3). The launch of the Solar Dynamic Observatory (SDO) [100] is intended to help address the question of whether reconnection is necessary for the formation of magnetic flux ropes. The Atmospheric Imaging Assembly (AIA) [101] telescope on SDO has temporal cadence of 12 s and is equipped with multi-temperature ultraviolet passbands. These features allow it to make clear observations of eruptive structures in the lower corona [102]. By studying low corona images of an eruption, Zhang et al. [31] report unambiguous evidence of the presence of a flux rope before and during a solar eruption.

Amari et al. [32] numerically reconstruct the magnetic field in an active region and report a pre-existing magnetic flux rope prior to the eruption. They used photospheric magnetic information from the Solar Optical Telescope aboard the satellite Hinode [103] to reconstruct a fully data-driven picture spanning both pre-eruption phase and eruption phase.

These studies suggest that a magnetic flux rope exists before the eruption pro-

cess. The laboratory reproduction of a slow rise to fast acceleration of a pre-existing magnetic flux rope can be considered experimental evidence that reconnection, while important, is not necessary for slow-rise to fast-acceleration of arched flux ropes.

2.6.3 Current vs voltage sources

The idea of a current source powering solar eruptions is unpopular in the solar community and many solar models invoke flux conservation by stating that the photosphere is a conductive surface, so no voltages appear across flux rope footpoints. One measure of plasma resistivity is the Spitzer resistivity which scales as $T^{-3/2}$. The photosphere ($\sim$ 6000 K) is at a much lower temperature than the solar corona ($\sim 10^6$ K), so currents are more likely to flow through the coronal flux rope than through the photosphere. This current flow introduces a voltage across the footpoints, thus breaking the flux conservation assumption.

Of the solar models, the flux injection model [40] describes boundary conditions that are similar to the experimental set-up. In fact, "flux injection" corresponds to the application of voltage to the electrodes, thereby driving a current. The capacitor bank in the experiment acts like a current source (Sec. D.4.1 and Ref. [104]) so the current profile is insensitive to the evolving plasma. In contrast, the voltage profile can vary depending on the behavior of the plasma. The voltage measured across the plasma footpoints (6 μs - 8 μs in Fig. 2.13 (a)) can vary significantly depending on the whether the plasma is completely strapped (LS) or has erupted (NS, IS); in contrast, the current in 2.13 (b) show minor differences. The effectiveness of the Chen model in fitting the voltage to solar eruptions from the sun out to the Earth suggests that loops on the sun may also be powered by current sources.

2.6.4 Loss of equilibrium: converging models

As the scientific understanding of CMEs mature, different models converge towards a common picture. The respective authors of the catastrophe model and torus instability model have agreed that the onset of "catastrophe" occurs at the same location

as the onset of torus instability [105]. This result is intuitive, since both arguments rely on the same force balance for equilibrium, it follows that both should produce an onset of eruption at the same point. The key distinction between the two models is that stability analysis focuses on the critical point without specifying the pre-eruptive evolution, whereas catastrophe analysis includes the pre-eruptive evolution, but does not consider unstable equilibria away from the critical point. Both approaches assume that the plasma loop is completely isolated from the solar surface during an eruption, so energy is conserved.

In contrast, the flux injection model assumes a partially toroidal plasma powered by a sub-photospheric dynamo, which acts like a current source [40]. Flux injection fits eruption dynamics to a seven-parameter temporal function of the footpoint voltages. One key feature is the presence of footpoints, which play an important role in the scaling of solar eruptions [80]. The presence of footpoints also relaxes the constant flux requirement commonly invoked by other models.

The analysis of the torus instability in this thesis assumes a nearly complete circle with electrodes as footpoints (Fig. 2.8). This implementation does not require the constant flux assumption of torus instability in Ref. [33], but retains the equation of motion. The voltage appearing across the electrode represents the change in poloidal flux as the plasma expands. As the loop expands, it encloses more poloidal flux from the strapping field, which cancels the poloidal flux produced by currents flowing along the loop. New poloidal flux can also be injected by increasing currents flowing through the plasma footpoints. The presence of electrodes ties the poloidal flux of the strapping field (torus instability) with the poloidal flux from flux injection.

In practice, laboratory plasmas are influenced by both the injection of poloidal flux from the driving current, and the cancellation of poloidal flux by the strapping field. The rate of change of poloidal flux injection is represented by the voltage of the NS configuration (black line in Fig. 2.13 (a)). Application of strapping field removes this poloidal flux, and the rate of poloidal flux removal results in lower voltages for IS and LS configurations compared to the NS configuration (red and orange lines in Fig. 2.13 (a)). The implementation of the torus instability in this thesis ties together

the fundamental ideas of flux injection and torus instability, thereby tying together two major loss-of-equilibrium eruptive CME models.

2.6.5 Fast and slow CMEs

For decades, CMEs have been separated into impulsive (fast) and gradual (slow) classes but there is increasing support for a unified structure. Chen & Krall [38] reproduce both fast and slow CMEs by varying the width and amplitude of their voltage profile across their flux rope footpoints. They propose that the distinction between fast and slow CMEs is determined entirely by the absence (fast) or presence (slow) of sustained acceleration after the initial acceleration phase; a wider voltage pulse results in sustained acceleration. This is consistent with the velocity measurements for None, Medium, and Maximum L_{extra} configuration. The None configuration produces a brief but rapidly rising current pulse which drives rapid acceleration early on but little acceleration and even deceleration when the plasma loop reaches the magnetic probes. Medium and Maximum configurations have wider current profiles, resulting in acceleration when the plasma loop reaches the magnetic probes.

Torok and Kliem [39] built on their work in Ref. [33] to numerically simulate both fast and slow CMEs. They were able to produce both "fast" and "slow" CMEs by varying both the decay index and the strength of the strapping field. The NS configuration produces fast plasma loop expansion, reminiscent of impulsive CMEs. Similarly, the IS configuration starts slow but rapidly accelerates, similar to gradual CMEs. The decay index of our strapping field (red dashed line in Fig. 2.4 side view) is not fixed but varies as a function of height. Nevertheless, we were able to reproduce fast, slow, and confined eruptions by adjusting the amplitude of the strapping field.

Our results suggest that fast and slow CMEs can be described by the same underlying physics. We confirm that models from both Refs. [38] and [39] are capable of producing fast and slow eruptions and assert that both the power supply driving the footpoints and the overlying strapping index play a significant role in determining the dynamics of solar eruptions.

2.6.6 Solar statistical studies

While our experiments study the essential physics of torus instability without focusing on specific critical decay indices, solar observers have completed statistical studies on various decay indices. Xu et al. [106] look at CME velocities and found that a larger decay index corresponds to faster CMEs. Liu [107] uses the decay index to differentiate between successful eruptions and failed eruptions. The implementation of the torus instability in Sec. 2.4 presents an interesting criterion for solar statistical studies: the critical decay index is $n_{cr} = 1$ for a constant current plasmas and $n_{cr} = 2$ for a constant flux plasmas. While real solar plasmas are neither constant flux nor constant current, a statistical study may provide insight on which boundary condition provides the better approximation. Such a study would be challenging to implement precisely without magnetic field data, and must take care to only consider eruptions where the hoop and strapping forces dominate.

2.6.7 Limitations of laboratory results and future studies

While our results are compelling, there are limitations associated with our set-up. Much of the torus instability theory comes from tokamak physics and assumes an axisymmetric configuration. Our configuration is not axisymmetric so we do not expect the theory to apply perfectly. Nevertheless, arched solar flux ropes match Caltech plasmas better than the axisymmetric plasmas of tokamak theory.

We placed small strapping coils inside the vacuum chamber to create our strapping field. This allows us to make magnetic fields that were both strong enough to interact with the plasma yet decay sharply enough to study the torus instability. Unfortunately, these coils only provide the tailored magnetic field profile along the plasma apex. Due to the localized nature of the strapping field, the parts of the plasma loop would go around the region of strong strapping field, introducing unwanted physics. We also focused our imaging and camera diagnostics on the plasma apex in order to obtain robust statistics and reproducibility. Circuit analysis provides insight into the global plasma structure, and such analysis indicates that our conclusion holds for the

other parts of the plasma. Less rigorous imaging analysis along other sections of the plasma loop reveals that those sections experience the same effect as the apex, but to a smaller extent.

The strapping coils also block camera imaging at early times. While Stenson and Bellan studied plasma dynamics at early times in detail [82, 108], they did not do so in the presence of a strapping field. As our magnetic diagnostics do not extend to low heights we must rely on circuit analysis to quantify plasma behavior at these heights. Thus, circuit analysis provides information about early times and we have shown that the inferred parameters quantitatively match the other diagnostics at later times. Even so, our knowledge of plasma behavior at early times is weak compared to the regime studied in this thesis.

We also claim that the vacuum chamber is much larger than the plasma simulating a half-infinite space. This is true during the initial plasma formation but may not hold for much later times. At later times, we expect plasma-chamber interactions, but have not quantified how this affects our overall results.

2.7 Chapter Summary

- CMEs are a fundamental aspect of solar weather and are believed to drive geomagnetic storms.
- The essence of torus instability compares the relative spatial decay of hoop force and strapping force. If the strapping field decays sufficiently quickly, the plasma is expected to be unstable to perturbation. An "increasing current" is one such perturbation.
- By including footpoints in a nearly circular loop, we generalize the Kliem and Torok implementation to be consistent with different boundary conditions. This model relates flux injection to other loss-of-equilibrium models.
- Magnetic diagnostics show that the hoop force dominates Caltech plasma loops expansion.

- IS configuration reproduces the slow rise to fast eruption behavior of CME eruptions. This demonstrates that a pre-existing flux rope may go from slow-rise to fast-acceleration without the need for magnetic reconnection, in support of loss of equilibrium models.

- The high Spitzer resistivity of the photosphere compared to the coronal suggests that a voltage can develop across solar flux rope footpoints. The successful capture of solar eruption dynamics by fitting to footpoint voltages (flux injection model) suggests that a current source may act as boundary condition for solar loops.

- There is a convergence of loss-of-equilibrium solar models. At the moment, two important remaining models are flux injection and torus instability. Our theoretical generalization of torus instability to include electrodes and experimental work relates torus instability to flux injection.

- We experimentally demonstrate that both torus instability and flux injection may produce fast and slow CMEs, addressing an important debate on whether fast and slow CMEs should be considered distinct or whether they have the same underlying mechanism. Our work suggests the latter, and we present supporting evidence by adjusting the profile of the driving current pulse, and by varying the magnitude of the strapping field.

- The generalized torus instability model predicts different critical decay index depending on constant flux or constant current boundary conditions. This critical decay index is amenable to solar statistical studies.

- Our work focuses on the apex of the plasma and may miss important physics along other sections of the plasma loop. We also do not have direct imaging and magnetic diagnostics at early times and must rely on circuit diagnostics.

Chapter 3

Conclusion

In this thesis, we have addressed two prominent questions about coronal mass ejections: what is a mechanism by which CMEs may go from slow-rise to fast-acceleration, and should impulsive (fast) and gradual (slow) CMEs be categorized as different events?

The experimental results described in this dissertation offer evidence that torus instability is a mechanism by which a magnetic flux tube may go from slow rise to fast-acceleration. The thesis analyzes the plasma apex of the plasma with three different diagnostics: imaging, magnetic, and circuit analysis. Each diagnostic has its own strengths and weaknesses, but the combination of all three provides a complete picture of plasma dynamics. Specifically, the hoop force causes the plasma to expand into a region of intermediate strapping field (IS), where apex expansion is slowed by strapping force. The plasma slowly rises in this strapping region, until the apex passes a critical height corresponding to the onset of torus instability, and quickly accelerates. This slow-rise to fast-acceleration is captured by camera images, confirmed by magnetic probes measurements, and matches the inductance calculated from circuit analysis. All three diagnostics match quantitatively.

The application of no strapping field (NS) results in acceleration at lower heights, and little acceleration (and even deceleration) by the time the plasma reaches the magnetic probe, similar to impulsive CMEs. The application of large strapping field (LS) completely confines the plasma, matching confined solar eruptions. Thus, given a customized current profile, we can produce gradual eruptions, impulsive eruption,

and confined eruptions by varying the amplitude of strapping field.

The most dramatic transition from slow-rise to fast-acceleration occurs when the current pulse peaks as the plasma is crossing the instability threshold. This was demonstrated by varying the profile of the driving pulse, and using features in the magnetic traces to estimate the plasma velocities before the magnetic probes, and at the magnetic probes. This time dependence of the current profile not found in the torus instability model, but is a prediction of the flux injection model for solar eruptions, a model which captures CME dynamics by fitting a voltage profile to the footpoints.

Both torus instability and flux injection models provide a technique for producing impulsive and gradual eruptions. Torus instability creates these these two classes of CMEs by varying the strength and decay index of the strapping field. Flux injection creates these two types of CMEs by adjusting the duration of the voltage pulse applied across the two footpoints. Both models conclude that impulsive and gradual CMEs have the same underlying physics.

Our experimental results confirm that impulsive eruptions and gradual eruptions can be produced by varying the current profile, and by varying the strapping field strength. We propose that both mechanisms are involved in solar dynamics, and suggest a simple model unifying the two theories. Our model implements the torus instability for a nearly-circular plasma connected to a power supply, unifying the essential ideals from flux injection with torus instability.

Bibliography

[1] N. P. Savani, A. Vourlidas, A. Szabo, M. L. Mays, B. J. Thompson, I. G. Richardson, R. Evans, A. Pulkkinen, and T. Nieves-Chinchilla. Predicting the magnetic vectors within coronal mass ejections arriving at Earth. *arXiv:1502.02067 [astro-ph, physics:physics]*, February 2015. arXiv: 1502.02067.

[2] J.F. Freddy Hansen and Paul M. P.M. M Bellan. Experimental demonstration of how strapping fields can inhibit solar prominence eruptions. *The Astrophysical Journal*, 563(563):183–186, December 2001.

[3] S. K. P. Tripathi and W. Gekelman. Laboratory Simulation of Arched Magnetic Flux Rope Eruptions in the Solar Atmosphere. *Physical Review Letters*, 105(7):1–4, August 2010.

[4] A. Vourlidas, B. J. Lynch, R. A. Howard, and Y. Li. How Many CMEs Have Flux Ropes? Deciphering the Signatures of Shocks, Flux Ropes, and Prominences in Coronagraph Observations of CMEs. *Solar Physics*, August 2012.

[5] JT Gosling. The solar flare myth. *Journal of geophysical research*, 98(93), 1993.

[6] E.W. Cliver and H.S. Hudson. CMEs: How do the puzzle pieces fit together? *Journal of Atmospheric and Solar-Terrestrial Physics*, 64(2):231–252, January 2002.

[7] R.L. Moore, A.C. Sterling, H.S. Hudson, and J.R. Lemen. Onset of the magnetic explosion in solar flares and coronal mass ejections. *The Astrophysical Journal*, 552:833–848, 2001.

[8] a. a. van Ballegooijen and PCH Martens. Formation and eruption of solar prominences. *The Astrophysical Journal*, 343, 1989.

[9] SK Antiochos, CR DeVore, and JA Klimchuk. A model for solar coronal mass ejections. *The Astrophysical Journal*, 510:485–493, 1999.

[10] W Van Tend and M Kuperus. The development of coronal electric current systems in active regions and their relation to filaments and flares. *Solar Physics*, 59:115–127, 1978.

[11] TG Forbes and PA Isenberg. A catastrophe mechanism for coronal mass ejections. *The Astrophysical Journal*, 1991.

[12] T. Torok, B. Kliem, and V. S. Titov. Ideal kink instability of a magnetic loop equilibrium. *Astronomy & Astrophysics*, 413(3):4, 2004.

[13] James Chen and Valbona Kunkel. Temporal and Physical Connection Between Coronal Mass Ejections and Flares. *The Astrophysical Journal*, 717(2):1105–1122, July 2010.

[14] Vernon H. Chaplin. High Time Resolution Spectroscopic Measurements of Electron Temperature in the SSX plasma. 2007.

[15] Deepak Kumar. *Experimental Investigations of Magnetohydrodynamic Plasma Jets*. PhD thesis, 2009.

[16] C. a. Romero-Talamas, P. M. Bellan, and S. C. Hsu. Multielement magnetic probe using commercial chip inductors. *Review of Scientific Instruments*, 75(8):2664–2664, 2004.

[17] Eve Stenson. *Fields, forces, and flows: what laboratory experiments reveal about the dynamics of arched plasma structures*. PhD thesis, 2012.

[18] Edward Ramsden. *Hall-Effect Sensors Theory and Application*. Newnes, 2006.

[19] National Research Council (U.S.), editor. *Severe space weather events: understanding societal and economic impacts: a workshop report*. National Academies Press, Washington, D.C, 2008.

[20] M. L. Kaiser, T. A. Kucera, J. M. Davila, O. C. St Cyr, M. Guhathakurta, and E. Christian. The STEREO Mission: An Introduction. *Space Science Reviews*, 136(1-4):5–16, November 2007.

[21] D. N. Baker, X. Li, A. Pulkkinen, C. M. Ngwira, M. L. Mays, A. B. Galvin, and K. D. C. Simunac. A major solar eruptive event in July 2012: Defining extreme space weather scenarios: DEFINING EXTREME SPACE WEATHER SCENARIOS. *Space Weather*, 11(10):585–591, October 2013.

[22] Pete Riley. On the probability of occurrence of extreme space weather events. *Space Weather*, 10(2):S02012, February 2012.

[23] B. P. Filippov, N. Gopalswamy, and A. V. Lozhechkin. Non-radial motion of eruptive filaments. *Solar Physics*, 203(1):119–130, October 2001.

[24] R. A. Howard, A. F. Thernisien, Ch. Marque, A. Vourlidas, and N. Patel. Modelling of CMES for the STEREO Mission. volume 592, page 727, September 2005.

[25] J. W. Dungey. Interplanetary Magnetic Field and the Auroral Zones. *Physical Review Letters*, 6(2):47–48, January 1961.

[26] Yihua Zheng, Peter Macneice, Dusan Odstrcil, M. L. Mays, Lutz Rastaetter, Antti Pulkkinen, Aleksandre Taktakishvili, Michael Hesse, M. Masha Kuznetsova, Hyesook Lee, and Anna Chulaki. Forecasting propagation and evolution of CMEs in an operational setting: What has been learned: FORECASTING CMEs. *Space Weather*, 11(10):557–574, October 2013.

[27] Vic Pizzo, Annette Parsons, Douglas Biesecker, Dusan Odstrcil, George Millward, and Steve Hill. Wang-Sheeley-Arge-Enlil Cone Model Transitions to Operations. *Space Weather*, 9(3):n/a–n/a, March 2011.

[28] Stephen S. Hall. Scientists on trial: At fault? *Nature News*, 477(7364):264–269, September 2011.

[29] P. F. Chen. Coronal Mass Ejections: Models and Their Observational Basis. *Living Reviews in Solar Physics*, 8(1), 2011.

[30] S. Liu, H. Q. Zhang, and J. T. Su. Comparison of Nonlinear Force-Free Field and Potential Field in the Quiet Sun. *Solar Physics*, 270(1):89–107, March 2011.

[31] Jie Zhang, Xin Cheng, and Ming-de Ding. Observation of an evolving magnetic flux rope before and during a solar eruption. *Nature communications*, 3:747–747, January 2012.

[32] Tahar Amari, Aurélien Canou, and Jean-Jacques Aly. Characterizing and predicting the magnetic environment leading to solar eruptions. *Nature*, 514(7523):465–469, October 2014.

[33] B. Kliem and T. Torok. Torus Instability. *Physical Review Letters*, 96(25):255002–255002, June 2006.

[34] JT Gosling, E Hildner, and RM MacQueen. The speeds of coronal mass ejection events. *Solar Physics*, 1976.

[35] Joan Feynman and Alexander Ruzmaikin. A High-Speed Erupting-Prominence CME: A Bridge Between Types. *Solar Physics*, 219(2):301–313, February 2004.

[36] B Vrsnak, D. Ruzdjak, D. Sudar, and N. Gopalswamy. Kinematics of coronal mass ejections between 2 and 30 solar radii: What can be learned about forces governing the eruption? *Astronomy and Astrophysics*, 423(2):717–728, August 2004.

[37] V. Yurchyshyn, S. Yashiro, V. Abramenko, H. Wang, and N. Gopalswamy. Statistical Distributions of Speeds of Coronal Mass Ejections. *The Astrophysical Journal*, 619(1):599, January 2005.

[38] J. Chen and J. Krall. Acceleration of coronal mass ejections. *J. Geophys. Res*, 108(A11):1410–1410, 2003.

[39] T. Török and B. Kliem. Numerical simulations of fast and slow coronal mass ejections. *Astronomische Nachrichten*, 328(8):743–746, October 2007.

[40] J. Chen. Effects of toroidal forces in current loops embedded in a background plasma. *The Astrophysical Journal*, 338:453–453, 1989.

[41] James Chen. Comment on "Torus Instability". *Physical Review Letters*, 99(9):099501, August 2007.

[42] Paul Murray Bellan. *Fundamentals of plasma physics*. Cambridge University Press, Cambridge, UK ; New York, 2006.

[43] Masaaki Yamada, Russell Kulsrud, and Hantao Ji. Magnetic reconnection. *Reviews of Modern Physics*, 82(1):603–664, March 2010.

[44] Kazunari Shibata and Tetsuya Magara. Solar Flares: Magnetohydrodynamic Processes. *Living Reviews in Solar Physics*, 8, 2011.

[45] Russell M. Kulsrud. Magnetic reconnection in a magnetohydrodynamic plasma. *Physics of Plasmas (1994-present)*, 5(5):1599–1606, May 1998.

[46] Masaaki Yamada. Review of controlled laboratory experiments on physics of magnetic reconnection. *Journal of Geophysical Research: Space Physics*, 104(A7):14529–14541, July 1999.

[47] Auna Louise Moser. *Dynamics of magnetically driven plasma jets: An instability of an instability, gas cloud impacts, shocks, and other deformations*. PhD thesis, California Institute of Technology, 2012.

[48] P. A. Sweet. The Neutral Point Theory of Solar Flares. volume 6, page 123, 1958.

[49] EN Parker. Sweet's mechanism for merging magnetic fields in conducting fluids. *Journal of Geophysical Research*, 1957.

[50] Hantao Ji, Masaaki Yamada, Scott Hsu, and Russell Kulsrud. Experimental Test of the Sweet-Parker Model of Magnetic Reconnection. *Physical Review Letters*, 80(15):3256–3259, April 1998.

[51] E. N. Parker. The Solar-Flare Phenomenon and the Theory of Reconnection and Annihiliation of Magnetic Fields. *The Astrophysical Journal Supplement Series*, 8:177, July 1963.

[52] HE Petschek. Magnetic field annihilation. *Proceedings of the AAS-NASA Symposium*, 1964.

[53] D. Biskamp. Magnetic reconnection via current sheets. *Physics of Fluids (1958-1988)*, 29(5):1520–1531, May 1986.

[54] M. E. Mandt, R. E. Denton, and J. F. Drake. Transition to whistler mediated magnetic reconnection. *Geophysical Research Letters*, 21(1):73–76, January 1994.

[55] B. N. Rogers, R. E. Denton, J. F. Drake, and M. A. Shay. Role of Dispersive Waves in Collisionless Magnetic Reconnection. *Physical Review Letters*, 87(19):195004, October 2001.

[56] P. A. Cassak, M. A. Shay, and J. F. Drake. Catastrophe Model for Fast Magnetic Reconnection Onset. *Physical Review Letters*, 95(23):235002, November 2005.

[57] T. G. Forbes. A review on the genesis of coronal mass ejections. *Journal of Geophysical Research*, 105(A10):23153, 2000.

[58] Y. Fan and SE Gibson. Onset of coronal mass ejections due to loss of confinement of coronal flux ropes. *The Astrophysical Journal*, 668(2):1232–1245, October 2007.

[59] a. S. Savcheva, a. a. van Ballegooijen, and E. E. DeLuca. Field Topology Analysis of a Long-Lasting Coronal Sigmoid. *The Astrophysical Journal*, 744(1):78–78, January 2012.

[60] T. Wiegelmann. Nonlinear force-free modeling of the solar coronal magnetic field. *Journal of Geophysical Research*, 113(A3):A03S02–A03S02, January 2008.

[61] Jason P. Byrne, Shane A. Maloney, R.T. James McAteer, Jose M. Refojo, and Peter T. Gallagher. Propagation of an Earth-directed coronal mass ejection in three dimensions. *Nature Communications*, 1(6):1–8, September 2010.

[62] R. H. Munro, J. T. Gosling, E. Hildner, R. M. MacQueen, A. I. Poland, and C. L. Ross. The association of coronal mass ejection transients with other forms of solar activity. *Solar Physics*, 61(1):201–215, February 1979.

[63] BC Low. Coronal mass ejections, magnetic flux ropes, and solar magnetism. *Journal of Geophysical Research. A. Space Physics*, 106:25–25, 2001.

[64] PCH Martens and NPM Kuin. A circuit model for filament eruptions and two-ribbon flares. *Solar Physics*, 122(2):263–302, 1989.

[65] M Kuperus and MA Raadu. The support of prominences formed in neutral sheets. *Astronomy and Astrophysics*, 1974.

[66] P. M. Bellan. Why current-carrying magnetic flux tubes gobble up plasma and become thin as a result. *Physics of Plasmas*, 10(5):1999–1999, 2003.

[67] David Alexander. *The sun*. Greenwood guides to the universe. Greenwood Press/ABC-CLIO, Santa Barbara, Calif, 2009.

[68] H. Carmichael. A Process for Flares. *NASA Special Publication*, 50:451, 1964.

[69] P A Sturrock. Model of the High-Energy Phase of Solar Flares. *Nature*, 211(5050):695–697, August 1966.

[70] T. Hirayama. Theoretical model of flares and prominences. *Solar Physics*, 34(2):323–338, February 1974.

[71] R. A. Kopp and G. W. Pneuman. Magnetic reconnection in the corona and the loop prominence phenomenon. *Solar Physics*, 50(1):85–98, September 1976.

[72] J. T. Gosling, E. Hildner, R. M. MacQueen, R. H. Munro, A. I. Poland, and C. L. Ross. Mass ejections from the Sun: A view from Skylab. *Journal of Geophysical Research*, 79(31):4581–4587, November 1974.

[73] E. Hildner, JT Gosling, RT Hansen, and JD Bohlin. The sources of material comprising a mass ejection coronal transient. *Solar Physics*, 45(2):363–376, 1975.

[74] Markus Aschwanden. *Physics of the Solar Corona.* Springer Praxis Books. Springer Berlin Heidelberg, 2005.

[75] Y. Liu, J. G. Luhmann, K. E. J. Huttunen, R. P. Lin, S. D. Bale, C. T. Russell, and A. B. Galvin. Reconstruction of the 2007 May 22 Magnetic Cloud: How Much Can We Trust the Flux-Rope Geometry of CMEs? *The Astrophysical Journal Letters*, 677(2):L133, April 2008.

[76] A. A. van Ballegooijen and P. C. H. Martens. Magnetic fields in quiescent prominences. *The Astrophysical Journal*, 361:283–289, September 1990.

[77] DM Rust and A Kumar. Helical magnetic fields in filaments. *Solar Physics*, 1994.

[78] Sara F. Martin. Conditions for the Formation and Maintenance of Filaments - (Invited Review). *Solar Physics*, 182(1):107–137, September 1998.

[79] R. L. Moore and B. J. Labonte. The filament eruption in the 3b flare of July 29, 1973 - Onset and magnetic field configuration. volume 91, pages 207–210, 1980.

[80] J Chen, C Marqué, and A Vourlidas. The flux-rope scaling of the acceleration of coronal mass ejections and eruptive prominences. *The Astrophysical Journal*, (Chen 1989):452–463, 2006.

[81] B. J. Lynch, S. K. Antiochos, C. R. DeVore, J. G. Luhmann, and T. H. Zurbuchen. Topological Evolution of a Fast Magnetic Breakout CME in Three Dimensions. *The Astrophysical Journal*, 683(2):1192, August 2008.

[82] E. V. Stenson and P. M. Bellan. Magnetically Driven Flows in Arched Plasma Structures. *Physical Review Letters*, 109(7):075001–075001, August 2012.

[83] Bojan Vršnak. Dynamics of solar coronal eruptions. *Journal of Geophysical Research: Space Physics*, 106(A11):25249–25259, November 2001.

[84] V Shafranov. Plasma Equlibrium in a Magnetic Field. *Review of Plasma Physics*, 2(103):117–124, 1966.

[85] Glenn Bateman. MHD instabilities. *Cambridge, Mass., MIT Press, 1978. 270 p.*, 1, 1978.

[86] Jeffrey P. Freidberg. *Plasma physics and fusion energy*. Cambridge University Press, Cambridge, 2007.

[87] John David Jackson. *Classical electrodynamics*. Wiley, New York, 3rd ed edition, 1999.

[88] EB Rosa. The self and mutual inductances of linear conductors. *Bulletin of Bureau of Standards*, 1908.

[89] N. Cooke. Self-inductance of the elliptical loop. *Proceedings of the Institution of Electrical Engineers*, 110(7):1293, 1963.

[90] Tomislav Zic, Bojan Vrsnak, and Marina Skender. The magnetic flux and self-inductivity of a thick toroidal current. *Journal of Plasma Physics*, 73(05):741–756, 2006.

[91] David J. Griffiths. *Introduction to Electrodynamics*. Prentice Hall, 3 edition, 1999.

[92] Kenro Miyamoto. *Plasma physics for nuclear fusion*. MIT Press, Cambridge, Mass, rev. ed edition, 1989.

[93] Oscar Olmedo and Jie Zhang. Partial Torus Instability. *The Astrophysical Journal*, 718(1):433–440, July 2010.

[94] H Ji, H Wang, and EJ Schmahl. Observations of the Failed Eruption of a Filament. *The Astrophysical Journal*, pages 135–138, 2003.

[95] Yan Li and Janet Luhmann. Coronal Magnetic Field Topology over Filament Channels: Implication for Coronal Mass Ejection Initiations. *The Astrophysical Journal*, 648(1):732, September 2006.

[96] P. Démoulin and G. Aulanier. Criteria for Flux Rope Eruption: Non-Equilibrium Versus Torus Instability. *The Astrophysical Journal*, 718(2):1388–1399, August 2010.

[97] Carolus J. Schrijver, Christopher Elmore, Bernhard Kliem, Tibor Torok, and Alan M Title. Observations and modeling of the early acceleration phase of erupting filaments involved in coronal mass ejections. *The Astrophysical Journal*, (2001):586–595, 2008.

[98] Rory J Perkins. *Experimental and Analytic Studies of Merging Flux Tubes*. PhD thesis, 2011.

[99] B. M. Bein, S. Berkebile-Stoiser, a. M. Veronig, M. Temmer, N. Muhr, I. Kienreich, D. Utz, and B. Vršnak. Impulsive Acceleration of Coronal Mass Ejections. I. Statistics and Coronal Mass Ejection Source Region Characteristics. *The Astrophysical Journal*, 738(2):191–191, September 2011.

[100] W. Dean Pesnell, B. J. Thompson, and P. C. Chamberlin. The Solar Dynamics Observatory (SDO). *Solar Physics*, 275(1-2):3–15, October 2011.

[101] James R. Lemen, Alan M. Title, David J. Akin, Paul F. Boerner, Catherine Chou, Jerry F. Drake, Dexter W. Duncan, Christopher G. Edwards, Frank M. Friedlaender, Gary F. Heyman, Neal E. Hurlburt, Noah L. Katz, Gary D. Kushner, Michael Levay, Russell W. Lindgren, Dnyanesh P. Mathur, Edward L. McFeaters, Sarah Mitchell, Roger A. Rehse, Carolus J. Schrijver, Larry A. Springer, Robert A. Stern, Theodore D. Tarbell, Jean-Pierre Wuelser, C. Jacob Wolfson, Carl Yanari, Jay A. Bookbinder, Peter N. Cheimets, David Caldwell, Edward E. Deluca, Richard Gates, Leon Golub, Sang Park, William A. Podgorski, Rock I. Bush, Philip H. Scherrer, Mark A. Gummin, Peter Smith, Gary Auker, Paul Jerram, Peter Pool, Regina Soufli, David L. Windt, Sarah Beardsley, Matthew Clapp, James Lang, and Nicholas Waltham. The Atmospheric Imaging Assembly (AIA) on the Solar Dynamics Observatory (SDO). *Solar Physics*, 275(1-2):17–40, June 2011.

[102] X. Cheng, J. Zhang, Y. Liu, and M. D. Ding. Observing Flux Rope Formation During the Impulsive Phase of a Solar Eruption. *The Astrophysical Journal Letters*, 732(2):L25, May 2011.

[103] T. Kosugi, K. Matsuzaki, T. Sakao, T. Shimizu, Y. Sone, S. Tachikawa, T. Hashimoto, K. Minesugi, A. Ohnishi, T. Yamada, S. Tsuneta, H. Hara, K. Ichimoto, Y. Suematsu, M. Shimojo, T. Watanabe, S. Shimada, J. M. Davis, L. D. Hill, J. K. Owens, A. M. Title, J. L. Culhane, L. K. Harra, G. A. Doschek, and L. Golub. The Hinode (Solar-B) Mission: An Overview. *Solar Physics*, 243(1):3–17, September 2007.

[104] Deepak Kumar, AL Moser, and PM Bellan. Energy efficiency analysis of the discharge circuit of Caltech Spheromak Experiment. *Plasma Science, IEEE*, 38(1):47–52, 2010.

[105] B. Kliem, J. Lin, T. G. Forbes, E. R. Priest, and T. Török. Catastrophe versus Instability for the Eruption of a Toroidal Solar Magnetic Flux Rope. *The Astrophysical Journal*, 789(1):46, July 2014.

[106] Yan Xu, Chang Liu, Ju Jing, and Haimin Wang. On the Relationship between the Coronal Magnetic Decay Index and Coronal Mass Ejection Speed. *The Astrophysical Journal*, 761(1):52–52, December 2012.

[107] Y. Liu. Magnetic Field Overlying Solar Eruption Regions and Kink and Torus Instabilities. *The Astrophysical Journal*, 679(2):L151–L151, June 2008.

[108] E.V. Eve V. Stenson and P.M. Paul M. Bellan. Dual-Species Plasmas Illustrate MHD Flows. *IEEE Transactions on Plasma Science*, 36(4):1206–1207, August 2008.

[109] Harley Flanders. Differentiation Under the Integral Sign. *The American Mathematical Monthly*, 80(6):pp. 615–627, 1973.

[110] Fred Riewe. Nonconservative Lagrangian and Hamiltonian mechanics. *Physical Review E*, 53(2):1890–1899, February 1996.

[111] Eqab Rabei, Tareq Alhalholy, and A Taani. On Hamiltonian Formulation of Non-Conservative Systems. *Turkish Journal of Physics*, 24:213–221, February 2014.

[112] T. G. Forbes, J. A. Linker, J. Chen, C. Cid, J. Kota, M. A. Lee, G. Mann, Z. Mikic, M. S. Potgieter, J. M. Schmidt, G. L. Siscoe, R. Vainio, S. K. Antiochos, and P. Riley. CME Theory and Models. *Space Science Reviews*, 123(1-3):251–302, October 2006.

[113] Nancy Crooker, J. A. Joselyn, and Joan Feynman, editors. *Coronal mass ejections*. Number 99 in Geophysical monograph. American Geophysical Union, Washington, D.C, 1997.

[114] CW Barnes and PA Sturrock. Force-free magnetic-field structures and their role in solar activity. *The Astrophysical Journal*, 1972.

[115] JJ Aly. On some properties of force-free magnetic fields in infinite regions of space. *The Astrophysical Journal*, 283:349–362, 1984.

[116] P. A. Sturrock. Maximum energy of semi-infinite magnetic field configurations. *apj*, 380:655–659, October 1991.

[117] L. A. Rachmeler, C. E. DeForest, and C. C. Kankelborg. Reconnectionless CME Eruption: Putting the Aly-Sturrock Conjecture to Rest. *The Astrophysical Journal*, 693(2):1431, March 2009.

[118] G. Aulanier, E. E. DeLuca, S. K. Antiochos, R. A. McMullen, and L. Golub. The Topology and Evolution of the Bastille Day Flare. *The Astrophysical Journal*, 540(2):1126, September 2000.

[119] T. G. Forbes. Numerical simulation of a catastrophe model for coronal mass ejections. *Journal of Geophysical Research*, 95(A8):11919, 1990.

[120] E. W. Jr Hones. Transient phenomena in the magnetotail and their relation to substorms. *Space Science Reviews*, 23(3):393–410, May 1979.

[121] T Sakurai. Magnetohydrodynamic interpretation of the motion of prominences. *Publications of the Astronomical Society of Japan*, 1976.

[122] Tyan Yeh. Bifurcation and stability of long-wavelength helical hydromagnetic equilibria. *Physics of Fluids (1958-1988)*, 16(4):516–528, April 1973.

[123] AW Hood and ER Priest. Kink instability of solar coronal loops as the cause of solar flares. *Solar Physics*, 1979.

[124] T. Torok and B. Kliem. Confined and ejective eruptions of kink-unstable flux ropes. pages 97–100, 2005.

[125] VS Titov and P Demoulin. Basic topology of twisted magnetic configurations in solar flares. *Astronomy and Astrophysics*, 720:707–720, 1999.

[126] B. Vršnak, V. Ruždjak, and B. Rompolt. Stability of prominences exposing helical-like patterns. *Solar Physics*, 136(1):151–167, 1991.

[127] V. Kunkel and J. Chen. Evolution of a Coronal Mass Ejection and Its Magnetic Field in Interplanetary Space. *The Astrophysical Journal*, 715(2):L80–L83, June 2010.

[128] J. Krall, J. Chen, and R. Santoro. Drive mechanisms of erupting solar magnetic flux ropes. *The Astrophysical Journal*, 539(2):964–982, 2000.

[129] S. Hsu and P. Bellan. Experimental Identification of the Kink Instability as a Poloidal Flux Amplification Mechanism for Coaxial Gun Spheromak Formation. *Physical Review Letters*, 90(21):1–4, 2003.

[130] E. Oz, C. E. Myers, M. Yamada, H. Ji, R. M. Kulsrud, and J. Xie. Experimental verification of the Kruskal-Shafranov stability limit in line-tied partial-toroidal plasmas. *Physics of Plasmas (1994-present)*, 18(10):102107, October 2011.

[131] W Manchester, T. Gombosi, and D DeZeeuw. Eruption of a buoyantly emerging magnetic flux rope. *The Astrophysical Journal*, (2001):588–596, 2004.

[132] M. R. Brown, D. M. Cutrer, and P. M. Bellan. Motion and equilibrium of a spheromak in a toroidal flux conserver. *Physics of Fluids B: Plasma Physics*, 3(5):1198–1198, 1991.

[133] M. R. Brown. Experimental studies of magnetic reconnection. *Physics of Plasmas*, 6(5):1717–1717, 1999.

[134] T. C. Hender, J. C. Wesley, J. Bialek, A. Bondeson, A. H. Boozer, R. J. Buttery, A. Garofalo, T. P. Goodman, R. S. Granetz, Y. Gribov, O. Gruber, M. Gryaznevich, G. Giruzzi, S. Günter, N. Hayashi, P. Helander, C. C. Hegna, D. F. Howell, D. A. Humphreys, G. T. A. Huysmans, A. W. Hyatt, A. Isayama, S. C. Jardin, Y. Kawano, A. Kellman, C. Kessel, H. R. Koslowski, R. J. La Haye, E. Lazzaro, Y. Q. Liu, V. Lukash, J. Manickam, S. Medvedev, V. Mertens, S. V. Mirnov, Y. Nakamura, G. Navratil, M. Okabayashi, T. Ozeki, R. Paccagnella, G. Pautasso, F. Porcelli, V. D. Pustovitov, V. Riccardo, M. Sato, O. Sauter, M. J. Schaffer, M. Shimada, P. Sonato, E. J. Strait, M. Sugihara, M. Takechi,

A. D. Turnbull, E. Westerhof, D. G. Whyte, R. Yoshino, H. Zohm, the ITPA Mhd, and Disruption and Magnetic Control Topical Group. Chapter 3: MHD stability, operational limits and disruptions. *Nuclear Fusion*, 47(6):S128, June 2007.

[135] SC Hsu and PM Bellan. Study of magnetic helicity injection via plasma imaging using a high-speed digital camera. *Plasma Science, IEEE Transactions on*, 30(1):10–11, 2002.

[136] L. Lindberg and C. T. Jacobsen. Studies of Plasma Expelled from a Coaxial Plasma Gun. *Physics of Fluids (1958-1988)*, 7(11):S44–S50, November 1964.

[137] Xiang Zhai and Paul M Bellan. An earth-isolated optically coupled wideband high voltage probe powered by ambient light. *The Review of scientific instruments*, 83(10):104703–104703, October 2012.

[138] WF Ray. High frequency effects in current measurement using Rogowski coils. In *Power Electronics and Applications*, pages 1–9. IEEE, 2005.

[139] Paul Bellan. *Spheromak: A practical Application of Magnetohydrodynamic Dynamos and Plasma Self-Organization*. Imperial College Press, 2000.

[140] I. H. Hutchinson. *Principles of plasma diagnostics*. Cambridge University Press, Cambridge ; New York, 2nd ed edition, 2002.

[141] M. W. Bongard, R. J. Fonck, B. T. Lewicki, and A. J. Redd. A Hall sensor array for internal current profile constraint. *Review of Scientific Instruments*, 81(10):10E105, 2010.

[142] I. Duran, J. Stockel, G. Mank, K. H. Finken, G. Fuchs, and G. Van Oost. Measurements of magnetic field fluctuations using an array of Hall detectors on the TEXTOR tokamak. *Review of Scientific Instruments*, 73(10):3482–3482, 2002.

[143] Yang Jeong-hun, Kyoung-Jae Chung, YoungHwa An, Bong Ki Jung, Jong Gab Jo, and Y. S. Hwang. Design of a dual sensor probe array for internal field measurement in Versatile Experiment Spherical Torus. *Review of Scientific Instruments*, 83(10):10D721, 2012.

[144] H. Pfister, W. Gekelman, J. Bamber, D. Leneman, and Z. Lucky. A fully three-dimensional-movable, 10-m-long, remotely controllable probe drive for a plasma discharge device. *Review of Scientific Instruments*, 62(12):2884–2889, December 1991.

[145] G.N. Harding, W.H. Mitchell, and E.H. Putley. A Hall effect device for measuring the magnitude and direction of a magnetic field at 4řK. *Solid-State Electronics*, 9(5):465–469, May 1966.

[146] Winfield Hill Paul Horowitz. *The Art of Electronics.* Cambridge University Press, 1989.

[147] Henry W Ott. *Noise Reduction Techniques in Electronic Systems.* AT&T Bell Laboratories, 1988.

[148] Auna L Moser and Paul M Bellan. Magnetic reconnection from a multiscale instability cascade. *Nature*, 482(7385):379–81, February 2012.

[149] Vernon H. Chaplin. *Battery-Powered RF Pre-Ionization System for the Caltech Magnetohydrodynamically-Driven Jet Experiment: RF Discharge Properties and MHD-Driven Jet Dynamics.* phd, California Institute of Technology, 2015.

[150] WR Smythe. *Static and dynamic electricity.* McGraw-Hill Book Company, 1950.

[151] RH Good. Elliptic integrals, the forgotten functions. *European Journal of Physics*, 119, 2001.

[152] C.-P. Lu, G.D. Hager, and E. Mjolsness. Fast and globally convergent pose estimation from video images. *IEEE Transactions on Pattern Analysis and Machine Intelligence*, 22(6):610–622, June 2000.

[153] Long Quan and Zhongdan Lan. Linear N-point camera pose determination. *IEEE Transactions on Pattern Analysis and Machine Intelligence*, 21(8):774–780, August 1999.

[154] G. Schweighofer and A. Pinz. Robust Pose Estimation from a Planar Target. *IEEE Transactions on Pattern Analysis and Machine Intelligence*, 28(12):2024–2030, December 2006.

[155] D. M. Rust and A. Kumar. Evidence for Helically Kinked Magnetic Flux Ropes in Solar Eruptions. *The Astrophysical Journal Letters*, 464:L199, June 1996.

[156] Herbert Goldstein, Charles P. Poole, and John L Safko. *Classical mechanics*. Addison-Wesley, 2001.

[157] Murai Tanisli and Kudret Ozdas. Hamilton Formulation for the Analysis of RLC Circuits. *Physics Essays*, 15(3):322–326, September 2002.

[158] K. W. H. Stevens. The Wave Mechanical Damped Harmonic Oscillator. *Proceedings of the Physical Society*, 72(6):1027, December 1958.

Appendix A

Useful Mathematical Relations

The following are useful mathematical relations.

A.1 Vector identities

Useful vector identities include:

$$\nabla \cdot (\nabla \times \mathbf{A}) = 0 \tag{A.1}$$

$$\nabla \cdot (\alpha \mathbf{B}) = \alpha(\nabla \cdot \mathbf{B}) + \mathbf{B} \cdot \nabla\alpha \tag{A.2}$$

$$\nabla \times (\nabla \times \mathbf{A}) = -\nabla^2 \mathbf{A} + \nabla(\nabla \cdot \mathbf{A}) \tag{A.3}$$

$$\nabla \cdot (\mathbf{A} \times \mathbf{B}) = \mathbf{B} \cdot \nabla \times \mathbf{A} - \mathbf{A} \cdot \nabla \times \mathbf{B} \tag{A.4}$$

A.2 Cylindrical coordinates

$$\hat{\mathbf{r}} = \cos\phi\hat{\mathbf{x}} + \sin\phi\hat{\mathbf{y}}$$

$$\hat{\boldsymbol{\phi}} = -\sin\phi\hat{\mathbf{x}} + \cos\phi\hat{\mathbf{y}}$$

Laplace of a scalar function f

$$\nabla^2 f = \frac{\partial^2 f}{\partial r^2} + \frac{1}{r}\frac{\partial f}{\partial r} + \frac{1}{\rho^2}\frac{\partial^2 f}{\partial \phi^2} + \frac{\partial^2 f}{\partial z^2} \tag{A.5}$$

Laplace of a vector function $\mathbf{A}$

$$\nabla^2 \mathbf{A} = \left(\nabla^2 V_r - \frac{2}{r^2}\frac{\partial V_\phi}{\partial \phi} - \frac{V_r}{r^2}\right)\hat{\mathbf{r}} + \left(\nabla^2 V_\phi + \frac{2}{r^2}\frac{\partial V_r}{\partial \phi} - \frac{V_\phi}{r^2}\right)\hat{\boldsymbol{\phi}} + \left(\nabla^2 V_z\right)\hat{\mathbf{z}}$$

A.3 Math

The Gamma function is a extension of the factorial function and can be applied to non-integers. The formal definition is

$$\Gamma(t) = \int_0^\infty x^{t-1} e^{-x} dx,\ \Gamma(n) = (n-1)!$$

Elliptical integrals are considered generalizations of inverse trigonometric functions. The elliptical integral of the first kind is defined as

$$K(m) = \int_0^{\pi/2} \frac{d\theta}{(1 - m\sin^2\theta)^{1/2}} \quad 0 < m < 1$$

and elliptical integral of the second kind is defined as

$$E(m) = \int_0^{\pi/2} (1 - m\sin^2\theta)^{1/2} d\theta \quad 0 < m < 1$$

Liebnitz integral rule [109] in three-dimensional, time dependent form integral form is

$$\frac{D}{Dt}\int \mathbf{F}(\mathbf{r},t)\cdot d\mathbf{A} = \int \left(\frac{\partial \mathbf{F}(\mathbf{r},t)}{\partial t} + (\nabla\cdot\mathbf{F})\mathbf{v}\right)\cdot d\mathbf{A} + \oint (\mathbf{F}\times\mathbf{v})\cdot d\mathbf{l} \tag{A.6}$$

where $\mathbf{F}$ is a vector field integrated over the vector flux area $\mathbf{A}$. The area is bounded by curve $\oint d\mathbf{l}$ and moving with velocity $\mathbf{v}$.

A.4 Fractional derivatives

A.4.1 Definition

There are multiple definitions of a fractional derivative and specific details can be found in Riewe [110]. Lacroix proposed extending the "powers of t" derivative definition

$$\frac{d^n t^m}{dt^n} = \frac{m!}{(m-n)!} t^{m-n}$$

yielding

$$\frac{d^n f(t)}{dt^n} = \frac{d^n}{dt^n} \sum_m a_m t^m = \sum_m a_m \frac{\Gamma(m+1)}{\Gamma(m-n+1)} t^{m-n} \tag{A.7}$$

where Γ is the Gamma function.

An alternative proposal by Lioiuville started from the exponential representation of integer order derivatives

$$\frac{d^n e^{at}}{d(t+\infty)^n} = a^n e^t$$

and defined fractional derivatives as a summation of exponential representations of integer order derivatives

$$\frac{d^n}{d(t+\infty)^n} f(t) = \frac{d^n}{d(t+\infty)^n} \sum_m c_m e^{a_m t} \tag{A.8}$$

Here, the expression $d/d(t+\infty)$ is used instead of d/dt to denote that fractional derivatives do not depend on the value of the function at time t, but on the values for all times starting at $-\infty$ up to time t.

This is one of those bizarre incidences where the formal definitions in Eqs. A.7 and A.8 are not equivalent and no simple definition applies to both functions [110]. Instead, it has become common practice to use the integral definition proposed by Liouville and Riemann, which defines the fractional integral as a negative fractional derivative:

$$\frac{d^{-v} f(t)}{d(t-c)^{-v}} = \frac{1}{\Gamma(v)} \int_c^t (t-t')^{v-1} f(t') dt' \quad \Re(v) > 0 \tag{A.9}$$

and then defines the fractional derivative as

$$\frac{d^u f(t)}{d(t-c)^u} = \frac{d^n}{dt^n}\frac{d^{-v} f(t)}{d(t-c)^{-v}} \tag{A.10}$$

where n is the smallest integer greater than $\Re(u)$ and $v = n - u$. This is similar to taking an improper fraction u and splitting it into an integer component n and a fractional component v, except here we choose the smallest integer n larger than u and have a negative fractional derivative. The derivations of Eq. A.10 from Eq. A.9 emphasize that a fractional derivative is not only determined by the behavior at time t, but determined by the values of the function for the entire interval from c to t. Thus, Eq. A.10 simplifies to Eq. A.8 and Eq. A.7 when $c = -\infty$ and $c = 0$, respectively.

A.4.2 Properties

Fractional derivatives share many common properties with regular derivatives. In particular, they reduce to regular derivatives

$$\frac{d^u x}{d(t-c)^u} \rightarrow \frac{d^u}{dt^u} \tag{A.11}$$

if u is an integer. Theoretical manipulations of fractional derivatives often omit the constant $-c$ and employ short-hand notation

$$x_{(1/2)} = \frac{d^{1/2} x}{dt^{1/2}} \tag{A.12}$$

In general, fractional derivatives

- are linear:

$$\frac{d^u}{d(t-c)^u}[Af(t) + Bg(t)] = A\frac{d^u}{d(t-c)}f(t) + B\frac{d^u}{d(t-c)^u}g(t)$$

- do not usually yield zero when applied to any constants except 0. In general,

$$\frac{d^u A}{d(t-c)^u} = \frac{A(t-c)^{-u}}{\Gamma(1-u)}$$

- have anti-derivatives such that an anti-derivative of order u is the same as a derivative of order $-u$, so

$$\frac{d^u}{d(t-c)^u}\frac{d^{-u}f(t)}{d(t-c)^{-u}} = f(t)$$

- obey the composition rule with their anti-derivatives so that

$$\frac{d^u}{d(t-c)^u}\left[\frac{d^v}{d(t-c)^v}f(t)\right] = \frac{d^{u+v}}{d(t-c)^{u+v}}f(t) \tag{A.13}$$

  when $v \leq 0$ and $uv \geq 0$.

They have a rich list of additional properties, including being amenable to approximation by finite differencing, integrable by parts which are all outlined by Riewe. These additional details are not required for the calculations in this thesis and are not included but the interested reader is encourage to refer to Refs. [110, 111] for an excellent quick-start on applying fractional derivatives to a Hamiltonian and Lagrangian formulation.

Appendix B

Plasma concepts

B.1 Plasma equations: from individual particles to MHD

At its core, a plasma is an ionized gas in which electromagnetic forces play an important role. The most complete description of a plasma requires tracking individual charges and applying Lorentz forces. Since no assumptions are made, this approach is the "most accurate," yet the tracking of every single particle, a number which may reach 10^{27} for inertial confinement fusion plasmas [42], is exceedingly tedious, computationally expensive, and is almost certain to drown out the big picture.

A large amount of tedium can be removed by combining particles which have similar position and velocities into a single "volume" in phase space and studying that volume. For a single species in one dimension, this approach is represented by a distribution function $f(x, v_x, t)$. The conservation of particles at time t, with position between x and $(x + dx)$ and velocity between v and $v + dv$ has the form

$$\frac{\partial f}{\partial t} + v_x \frac{\partial f}{\partial x} + \frac{\partial f}{\partial v_x}(a_x f) = 0$$

where a_x (the one dimensional acceleration) has value $a_x(x, v + dv, t)$ and $a_x(x, v, t)$ at $v + dv$ and v, respectively. The equation is generalizable to three dimensions:

$$\frac{\partial f}{\partial t} + \mathbf{v} \cdot \frac{\partial f}{\partial \mathbf{x}} + \frac{\partial}{\partial \mathbf{v}} \cdot (\mathbf{a} f) = 0$$

If multiple species are allowed, then the collisions between those species can cause jumps in phase space by effectively "creating" and "annihilating" particles [42]. Collisions are formalized for a given species σ as follows:

$$\frac{\partial f_\sigma}{\partial t} + \mathbf{v} \cdot \frac{\partial f_\sigma}{\partial \mathbf{x}} + \frac{\partial}{\partial \mathbf{v}} \cdot (\mathbf{a} f_\sigma) + = \sum C_{\sigma\alpha}(f_\sigma) \tag{B.1}$$

where $C_{\sigma\alpha}(f_\sigma)$ is the rate of change of f_σ due to collisions between species σ and species α. To keep the system "physical," the collision operator $C_{\sigma\alpha}$ must satisfy conservation of particles, conservation of momentum, and conservation of energy when budgeting across all species.

The next level of approximation is to go from phase space (both position and velocity) back to real space (position only) by integrating over the velocity space. This is known as the "two fluids" approximation to plasmas. While the mathematics is applicable to any number of particle types, a typical plasma comprises two species[1]: electrons and ions. Before proceeding, it is important to define certain quantities. In particular we define the number density of particles at a given location and time to be

$$n_\sigma(\mathbf{x}, t) = \int f_\sigma(\mathbf{x}, \mathbf{v}, t) d^3v$$

and the momentum density at the same location and time to be

$$n_\sigma(\mathbf{x}, t)\mathbf{u}_\sigma(\mathbf{x}, t) = \int \mathbf{v} f_\sigma(\mathbf{x}, \mathbf{v}, t) d^3v$$

where $\mathbf{u}_\sigma(\mathbf{x}, t)$ is the mean velocity of a given species. This process of multiplying a function by some $\mathbf{v}^n$ before integrating in velocity space is known as taking the "moment" of the function. In the example above, the number density $n_\sigma(\mathbf{x}, t)$ corresponds to taking the "zeroth" moment ($n = 0$) while the momentum density $n_\sigma \mathbf{u}_\sigma$ corresponds to the "first" moment ($n = 1$).

To derive the "two fluids" approximation, we take the moments of the Vlasov

[1] Dusty plasmas are examples of three species plasmas: dust particles, ions, and electrons. Electron plasmas and positron plasmas are examples of single species plasmas.

equations (Eq. B.1). For example, the zeroth moment is given by

$$\int \left[\mathbf{v} \cdot \frac{\partial f}{\partial \mathbf{x}} + \frac{\partial}{\partial \mathbf{v}} \cdot (\mathbf{a} f) + \frac{\partial f}{\partial t} \right] d\mathbf{v} = \sum_{\sigma} \int C_{\sigma\alpha}(f_\sigma) d\mathbf{v}$$

which is solved by applying the conservation of particles to the collision operator on the right hand side and by noting that the velocity integral on the left hand side commutes with both time and space derivatives, since $\mathbf{x}$, $\mathbf{v}$, and t are independent variables. The details behind resolving these integrals are given in plasma physics textbooks [42, 74] and the solutions are summarized here.

The zeroth moment of the Vlasov equation yields the species continuity equation:

$$\frac{\partial n}{\partial t} + \nabla \cdot (n_\sigma \mathbf{u}_\sigma) = 0 \tag{B.2}$$

The first moment of the Vlasov equation gives the species momentum equation:

$$m_\sigma \left[\frac{\partial (n_\sigma \mathbf{u}_\sigma)}{\partial t} + \frac{\partial}{\partial \mathbf{x}} \cdot (n_\sigma \mathbf{u}_\sigma \mathbf{u}_\sigma) \right] = n_\sigma q_\sigma (\mathbf{E} + \mathbf{u}_\sigma \times \mathbf{B}) - \frac{\partial}{\partial \mathbf{x}} \cdot \overleftrightarrow{\mathbf{P}}_\sigma - \mathbf{R}_{\sigma\alpha} \tag{B.3}$$

where

- the velocity is written as $\mathbf{v} = \mathbf{v}'(\mathbf{x}, t) + \mathbf{u}(\mathbf{x}, t)$, thus explicitly separating the random component of the velocity ($\mathbf{v}'(\mathbf{x}, t)$) from the mean velocity ($\mathbf{u}(\mathbf{x}, t)$).
- the pressure tensor is defined as: $\overleftrightarrow{\mathbf{P}}_\sigma = m_\sigma \int \mathbf{v}'\mathbf{v}' f_\sigma d\mathbf{v}'$
- the net frictional drag force due to collisions between species σ and α is given by: $\mathbf{R}_{\sigma\alpha} = \nu_{\sigma\alpha} m_\sigma n_\sigma (\mathbf{u}_\sigma - \mathbf{u}_\alpha)$

The pressure term is often assumed to be isotropic for mathematical convenience so that $-\partial/\partial \mathbf{x} \cdot \overleftrightarrow{\mathbf{P}}_\sigma$ simplifies to $-\nabla P_\sigma$, where $P_\sigma = (m_\sigma \int \sum_{j=1}^{N} v_j'^2 f_\sigma d^N \mathbf{v}')/N$. The expression can be further simplified by introducing the convective derivative

$$\frac{D}{Dt} = \frac{\partial}{\partial t} + \mathbf{u}_\sigma \cdot \nabla$$

which characterizes the temporal rate of change for an observer moving with the mean

fluid velocity. Equation B.3 can now be rewritten as

$$n_\sigma m_\sigma \frac{D\mathbf{u}_\sigma}{Dt} = n_\sigma q_\sigma(\mathbf{E} + \mathbf{u}_\sigma \times \mathbf{B}) - \nabla P_\sigma - \mathbf{R}_{\sigma\alpha} \tag{B.4}$$

where the terms on the right hand side represent the Lorentz force, the gradient of the pressure, and friction forces, respectively. We can continue to take higher order moments indefinitely but an *ad hoc* assumption in the form of an equation of state must be made eventually to provide closure to the system of equations. Plasma physicist take the second moment of the Vlasov equation to get an energy evolution equation before making an assumption about the heat flux to make the equations self-consistent.

One heat flux assumption is $v_{char} \ll v_{T\sigma}$, where v_{char} is the characteristic velocity and $v_{T\sigma} = \sqrt{2k_B T_\sigma / m_\sigma}$ is the thermal velocity, so that the heat flux dominates all other terms. In this isothermal limit, the equation of state is

$$P_\sigma = n_\sigma \kappa T_\sigma \qquad T_\sigma = constant \tag{B.5}$$

Another heat flux assumption is $v_{char} \gg v_{T\sigma}$ so that the heat flux and collisional terms are small compared to the other terms. In this adiabatic limit, the equation of state is

$$P_\sigma \sim n_\sigma^\gamma \qquad \gamma = \frac{N+2}{N} \tag{B.6}$$

where N is the dimensionality of the system. The combination of Eqs. B.2, B.4, the energy evolution equation, an equation of state (Eq. B.5 or Eq. B.6), and Maxwell's equations make up the two-fluid description of the plasma.

The final level of approximation, magnetohydrodynamics (MHD), transitions from a multiple-fluid description to a single-fluid description of the plasma. For a two species plasma, this transition is from the *two-fluid* (mean ion velocity ($\mathbf{u}_i$) and the mean electron velocity ($\mathbf{u}_e$)) description to a center-of-mass velocity description. The

center-of-mass velocity is defined as

$$\mathbf{U} = \frac{1}{\rho_m} \sum_\sigma m_\sigma n_\sigma \mathbf{u}_\sigma \qquad \rho = \sum_\sigma m_\sigma n_\sigma$$

and ρ_m is the total mass density. It is helpful to keep in mind that $\mathbf{U} \approx \mathbf{u}_i$ since ions are more massive than electrons. The relative ion-electron motion is defined to be the current density:

$$\mathbf{J} = \sum_\sigma n_\sigma q_\sigma \mathbf{u}_\sigma$$

The continuity equation in the center of mass description is obtained by multiplying the zeroth moment of the Vlasov equation by the species mass m_σ and summing over all species to get Eq. B.8. Similarly, the equation of motion is calculated by multiplying the first moments of the Vlasov equation by the species mass m_σ and then summing over all species while invoking quasi-neutrality (i.e., $\sum_\sigma n_\sigma q_\sigma \approx 0$).

Collisions are assumed to be sufficient[2] so that the pressure term is fully isotropic and has the single adiabatic law form of Eq. B.11 for a three-dimensional system. The resulting equation (Eq. B.9) is one of two equations which relate $\mathbf{U}$ and $\mathbf{J}$. The other equation is obtained by looking at the *two-fluids* electron equation of motion (Eq. B.4) for low-frequency phenomena with large spatial scales. In particular, if the characteristic time scale is long compared to the electron cyclotron motion, then $m_e D\mathbf{u}_e/Dt \ll e(\mathbf{u}_e \times \mathbf{B})$ and can be neglected[3]. By invoking quasi-neutrality, the following relations can be shown: $\mathbf{u}_e \times \mathbf{B} = (\mathbf{u}_i - \mathbf{J}/(n_e e)) \times \mathbf{B} \approx (\mathbf{U} + \mathbf{J}/(n_e e)) \times \mathbf{B}$ and $\mathbf{R}_{ei} = -\nu_{ei} m_e \mathbf{J}/e$. Thus, the electron equation of motion simplifies to a generalized Ohm's law:

$$\mathbf{E} + \mathbf{U} \times \mathbf{B} - \frac{1}{n_e e}\mathbf{J} \times \mathbf{B} + \frac{1}{n_e e}\nabla(n_e \kappa T_e) = \eta \mathbf{J} \tag{B.7}$$

where $\eta = m_e \nu_{ei}/(n_e e^2)$ is the plasma electrical resistivity. The $\mathbf{J} \times \mathbf{B}$ term is known

[2]In lieu of assumptions about collisions, the pressure term is $\nabla \cdot \overleftrightarrow{\mathbf{P}}$ where $\overleftrightarrow{\mathbf{P}} = \sum_\sigma \int m_\sigma \mathbf{v}'\mathbf{v}' f_\sigma d\mathbf{v}$ and $\mathbf{v}'$ is the random variation from the MHD mean velocity $\mathbf{U}$. A double adiabatic regime is required if the collisions are insufficient to equilibriate the temperature parallel to the direction of the magnetic field vs perpendicular to the magnetic field.

[3]This approximation is reasonable for $\mathbf{u}_{e,\perp}$ (velocities perpendicular to **B)** but may be unreasonable for $\mathbf{u}_{e,\parallel}$ (velocities parallel to B) since $\mathbf{u}_{e,\parallel} \times \mathbf{B} = 0$.

as the Hall term and if it is retained, the system is called Hall MHD. The $\nabla(n_e \kappa T_e)$ term is due to the gradient in the electron pressure and the ηJ is a resistive term.

Additional assumptions can be made to simplify the generalized Ohm's law by dropping the Hall term. If the pressure term in the MHD equation of motion (Eq. B.9) is negligible, then the Hall term will scale as $\sim \omega/\omega_{ci}$ and can be neglected if the system's characteristic frequency (ω) is small compared to the ion cyclotron frequency (ω_{ci}). Alternatively, if the electron-ion collision frequency is large compared to the electron cyclotron frequency, i.e., if $\nu_{ei} \gg \omega_{ce}$, then $\eta \mathbf{J} \gg \mathbf{J} \times \mathbf{B}/(n_e e)$, so the Hall term can also be dropped.

By convention, plasma physicists use the curl of Eq. B.7 (which yields the induction equation) rather than Ohm's law. The density gradient tends to be parallel to the temperature gradient in plasmas [42] so the thermal electromotive force term $(n_e e)^{-1} \nabla n_e \times \nabla \kappa T_e$ is dropped. As a result, the electron pressure term is also ignored in Ohm's law, yielding Eq. B.10, and the system is called Resistive MHD. The MHD equations are summarized as the following:

- The continuity equation:

$$\frac{\partial \rho_m}{\partial t} + \nabla \cdot (\rho_m \mathbf{U}) = 0 \tag{B.8}$$

- The equation of motion:

$$\rho_m \frac{D\mathbf{U}}{Dt} = \mathbf{J} \times \mathbf{B} - \nabla P \tag{B.9}$$

- Ohm's law for resistive MHD:

$$\mathbf{E} + \mathbf{U} \times \mathbf{B} = \eta \mathbf{J} \tag{B.10}$$

- Faraday's law:

$$\nabla \times \mathbf{E} = -\frac{\partial \mathbf{B}}{\partial t}$$

- Ampere's law in the limit of velocities much less than the speed of light:

$$\nabla \times \mathbf{B} = \mu_0 \mathbf{J}$$

- Divergence free condition:

$$\nabla \cdot \mathbf{B} = 0$$

- Energy equation of state:

$$\frac{P}{\rho_m^{5/3}} = const \tag{B.11}$$

  where $\gamma = 5/3$ for an adiabatic equation of state.

MHD focuses on low-frequency, long-wavelength, and magnetic behavior of the plasma. Thus the following conditions are required for MHD to be valid:

- Quasi-neutrality meaning that the characteristic length scale must be much larger than the Debye length (λ_D).

- The plasma must be collisional. This means that collision time is much less than the time scales of interest so that the pressure can be approximated as isotropic and the system is at a near Maxwellian.

- Characteristic velocity is much slower than the speed of light, meaning that the displacement term is dropped from Ampere's law.

- Characteristic time scale of phenomena is long compared to electron cyclotron motion qB/m so that the electron inertia term can be dropped.

B.2 Frozen-in flux

In the limit when resistance is negligible ($\eta \to 0$), Eq. B.7 becomes Ideal Ohm's law:

$$\mathbf{E} + \mathbf{U} \times \mathbf{B} = 0 \tag{B.12}$$

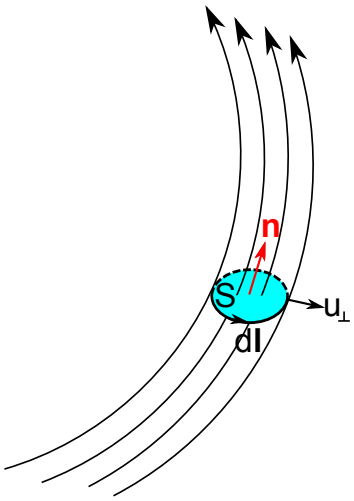

Figure B.1: Flux surface S moving with some velocity $\mathbf{u}_\perp$ with respect to the magnetic field line.

and the system is known as Ideal MHD.

In Ideal MHD, the magnetic flux is frozen into the plasma. The general proof defines the flux $\Phi(t)$ as

$$\Phi(t) = \int \mathbf{B} \cdot \mathbf{n} dS \tag{B.13}$$

where the surface S and surface normal $\mathbf{n}$ are shown in Fig. B.1. Reference [42] shows that

$$\frac{D\Phi(t)}{Dt} = \int_S \left[\frac{d\mathbf{B}}{\partial t} + \nabla \times (\mathbf{B} \times \mathbf{U}) \right] \cdot \mathbf{n} dS$$

so that

$$\frac{d\mathbf{B}}{\partial t} = \nabla \times (\mathbf{U} \times \mathbf{B}) \tag{B.14}$$

implies

$$\frac{D\Phi(t)}{Dt} = 0 \tag{B.15}$$

Since Eq. B.14 is met by taking the curl of Eq. B.12, Eq. B.15 holds in ideal MHD.

Reference [86] contains a rigorous interpretation of Eq. B.15. Using the three-dimensional, time-dependent Liebnitz integral rule (Eq. A.6) and $\nabla \cdot \mathbf{B} = 0$, the total derivative of Eq. B.13 is

$$\frac{D\Phi(t)}{Dt} = \int \frac{\partial \mathbf{B}}{\partial t} \cdot \mathbf{n} dS + \oint \mathbf{B} \times \mathbf{u}_\perp \cdot d\mathbf{l}$$

where the surface S is moving with some arbitrary velocity $\mathbf{u}_\perp$. Per plasma convention, we use $\perp$ to denote perpendicular to the magnetic field lines. Faraday's law can be used on the surface integral and Stoke's theorem can be used on the line integral to obtain:

$$\frac{D\Phi(t)}{Dt} = -\int (\nabla \times \mathbf{E}) \cdot \mathbf{n} dS + \int \nabla \times (\mathbf{B} \times \mathbf{u}_\perp) \cdot \mathbf{n} dS$$

Use Eq. B.12 to set $\mathbf{E} = \mathbf{B} \times \mathbf{U}_\perp$, and combining the integrals yields

$$\frac{D\Phi(t)}{Dt} = -\int (\nabla \times (\mathbf{B} \times \mathbf{U}_\perp) \cdot \mathbf{n} dS + \int \nabla \times (\mathbf{B} \times \mathbf{u}_\perp) \cdot \mathbf{n} dS = \oint \mathbf{B} \times (\mathbf{u}_\perp - \mathbf{U}_\perp) \cdot d\mathbf{l}$$

so

$$\frac{D\Phi(t)}{Dt} = 0 \implies \mathbf{u}_\perp = \mathbf{U}_\perp \tag{B.16}$$

which means that flux passing through any arbitrary cross section is conserved when the plasma moves with the magnetic field lines. The converse is not necessarily true, e.g., the field lines may move without any corresponding motion to the plasma in specific situations. For an insightful discussion, see (Sec. 3.5.5 of Ref. [42]).

B.3 Vacuum field

The simplest magnetic field configuration is one created by currents located outside of the region of interest. Since there are no local currents, the system satisfies

$$\nabla \times \mathbf{B}_{vac} = 0 \tag{B.17}$$

which means that it can be represented by a scalar function χ such that $\nabla\chi = \mathbf{B}_{vac}$. Taking the curl of Eq. B.17, applying the vector identity (Eq. A.3), and recalling that $\nabla \cdot \mathbf{B} = 0$ yields

$$\nabla^2 \chi = 0 \tag{B.18}$$

which is Laplace's equation. Laplace's equation is intrinsically linear, which means that any of the coordinates may be expressed as Fourier modes [42]. This linearity also permits the use of symmetries to simplify Laplace's equation into standard mathematical equations. For example, if there were symmetry along the z and ϕ direction, then Fourier analysis of those directions yields solutions of the form $\exp(im\phi + ikz)$. For a given m and k, Laplace's equation (Eq. A.5) now has the form

$$\frac{\partial^2 \chi}{\partial r^2} + \frac{1}{r}\frac{\partial \chi}{\partial r} - \left(\frac{m^2}{r^2} + k\right)\chi = 0$$

and can be reduced to a modified Bessel's equation with a substitution of $s = kr$.

One property of Laplace's equation (and thus inherited by vacuum fields) is that the solution is uniquely determined by the boundary conditions. This is not the case for non-vacuum fields since the solution for a non-vacuum field is determined by the boundary condition and the currents within the domain.

This can be used to demonstrate that the vacuum field is the lowest energy state of a field which satisfies a given boundary condition. To start, consider a volume V bounded by a surface S over which boundary conditions are specified. Let $\mathbf{B}_{min}(\mathbf{r})$ be a solution corresponding to the lowest energy state. Suppose there is another solution of the form $\mathbf{B}(\mathbf{r}) = \mathbf{B}_{min}(\mathbf{r}) + \delta\mathbf{B}(\mathbf{r})$ where $\delta\mathbf{B}(\mathbf{r})$ is some small, arbitrary variation about $\mathbf{B}_{min}(\mathbf{r})$. Since $\mathbf{B}(\mathbf{r})$ and $\mathbf{B}_{min}(\mathbf{r})$ satisfy the same boundary conditions, $\delta\mathbf{B}(\mathbf{r}) = 0$ at S. The magnetic energy W of $\mathbf{B}(\mathbf{r})$ is given by $2\mu_0 W = \int (\mathbf{B}_{min} + \delta\mathbf{B})^2 \, dV$ which can be rewritten as

$$2\mu_0 W = \int_V B_{min}^2 dV + 2\int_V \mathbf{B}_{min} \cdot \delta\mathbf{B} dV + \int_V (\delta B)^2 dV$$

Since $\delta\mathbf{B}$ is arbitrary, it can always be chosen to be anti-parallel to $\mathbf{B}$ so that $2\int_V \mathbf{B}_{min} \cdot \delta\mathbf{B} dV < 0$. Since $\delta\mathbf{B}$ is assumed to be small, this would imply that $2\int_V \mathbf{B}_{min} \cdot \delta\mathbf{B} dV + \int_V (\delta B)^2 dV < 0$, which contradicts the initial assumption that $\mathbf{B}_{min}$ is the lowest energy state. To prevent this contraction, we require that $\int_V \mathbf{B}_{min} \cdot \delta\mathbf{B} dV = 0$ for all

$\delta\mathbf{B}$. We rewrite the restriction as

$$\int_V [\nabla \cdot (\delta\mathbf{A} \times \mathbf{B}_{min}) + \delta\mathbf{A} \cdot \nabla \times \mathbf{B}_{min}]\, dV = 0 \tag{B.19}$$

where $\delta\mathbf{B} = \nabla \times \delta\mathbf{A}$, and we applied a vector identity (Eq. A.4). The divergence term is converted to a surface integral and vanishes because $\delta\mathbf{A} \to 0$ at the boundary surface S to satisfy the boundary conditions. Since $\delta\mathbf{A}$ is arbitrary, Eq. B.19 is satisfied only if $\nabla \times \mathbf{B}_{min} = 0$, which is the vacuum field condition.

An important consequence is that magnetic configurations satisfying a boundary condition but also containing currents within the domain are not in the lowest energy state, and thus may have free energy to drive boundary-condition preserving instabilities.

B.4 Force-free fields.

Although vacuum fields represent the absolute minimum energy configuration in parameter space, there is a family of higher energy configurations, which represent local minimums of energy called force-free states. These states contain currents, but the currents have oriented themselves to be parallel to the magnetic field, so $\mathbf{J} \times \mathbf{B}$ vanishes. A plasma in a higher energy configuration may relax into a force-free state and remain in that state, despite the availability of a lower energy vacuum state, since there is no force to mediate such a transition.

The condition $\mathbf{J} \times \mathbf{B} = 0$ implies that $\mathbf{J}$ is parallel to $\mathbf{B}$ (i.e., $\mu_0\mathbf{J} = \alpha\mathbf{B}$) or $\mathbf{J} = 0$, which means that electric currents flow (if they exist) flow along field lines. Ampere's law can be rewritten as

$$\nabla \times \mathbf{B} = \alpha\mathbf{B} \tag{B.20}$$

An additional condition can be attained by recalling that the divergence of the curl of a vector is zero (Eq. A.1), so

$$0 = \nabla \cdot (\nabla \times \mathbf{B}) = \nabla \cdot (\alpha\mathbf{B}) = \alpha(\nabla \cdot \mathbf{B}) + \mathbf{B} \cdot \nabla\alpha = \mathbf{B} \cdot \nabla\alpha \tag{B.21}$$

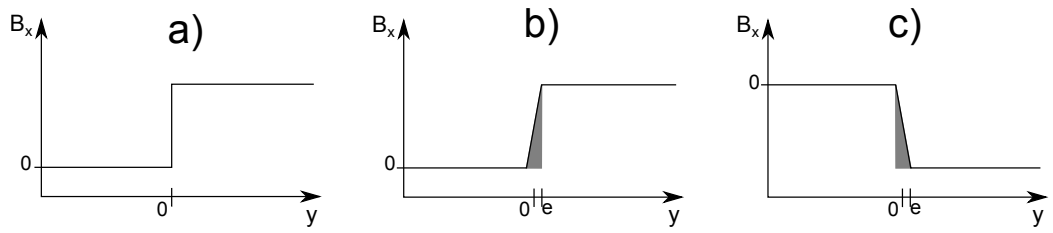

Figure B.2: Magnetic pressure and $\mathbf{J} \times \mathbf{B}$ for different configurations.

where Eq. A.2. Equation B.21 states that α is constant along a given field line. If α is constant everywhere within the domain, the system is called a *linear force-free field.* Otherwise, it is called a *nonlinear force-free field.*

B.5 Magnetic pressure and JxB forces

When solar observers attempt to explain the dynamics of solar eruptions, they often rely on the concept of "magnetic pressure," e.g., there is a force associated with the gradient of the magnetic pressure pointed from the region of high pressure to the region low pressure. In contrast, laboratory plasma experimentalists prefer to use currents and the Lorentz force to analyze plasma dynamics. The choice between studying magnetic fields and studying currents appears to be one of convenience. Solar physicists are unable to probe the sun to measure the currents so they rely on magnetic data through spectroscopic effects like the Zeeman effect. Experimentalists have direct control over many of the currents associated with the system and use those currents to recreate the necessary magnetic boundary conditions.

In theory, both the $\mathbf{J} \times \mathbf{B}$ approach and magnetic pressure (B^2) approach are equivalent. In practice, force calculations by way of magnetic pressure are indirect and the user must take care to properly assess the geometry. Consider the magnetic configuration shown in Fig. B.2 (a). The magnetic field is along the $\hat{x}$ direction and is described to be zero for $y < 0$ and finite and positive for $y > 0$. Through Ampere's law,

$$\mathbf{J} \times \mathbf{B} = \frac{1}{\mu_0}(\nabla \times \mathbf{B}) \times \mathbf{B} = \frac{1}{\mu_0}\left(-\frac{\partial B_x}{\partial y}\right)\hat{\mathbf{z}} \times B_x\hat{\mathbf{x}} = -\frac{\mu_0}{2}\frac{\partial}{\partial y}\left(B_x^2\right)\hat{\mathbf{y}}$$

The force associated with the pressure clearly points in the $-\hat{\mathbf{y}}$ direction, but there appears to be no obvious currents, and thus no $\mathbf{J} \times \mathbf{B}$ force. In reality, there is no such thing as an infinite slope like the one shown at $y = 0$ in Fig. B.2 (a), and if one zooms into a small region of size ε around $y = 0$ as shown in Fig. B.2 (b), one finds a finite slope corresponding to a finite $-\partial B_x/\partial y$ which represents a thin layer of current flowing along the $\hat{z}$ direction. From the $\mathbf{J} \times \mathbf{B}$ point of view, the force associated with the magnetic configuration is determined by currents flowing in the thin region around $y = 0$, thus reducing the study of the magnetic configuration into the study a localized region. Similarly, if the magnetic field were inverted like shown in Fig. B.2 (c), both the $\partial B_x/\partial y$ and B_x terms would flip polarity; the $\mathbf{J} \times \mathbf{B}$ approach and the magnetic pressure approach continue to give the same force.

The essential physics is contained in the behavior of the localized region over which currents flow, so both approaches are identical when given perfect information. In practice, scientists have a difficult time measuring magnetic field in the corona and solar models extrapolate the coronal magnetic field from photospheric magnetic measurements [32, 58]. The imprecise spatial resolution and uncertainty about magnetic measurements means that important local regions capturing key dynamics may be overlooked. Even scientists who advocate strongly for thinking about magnetic pressure recognize that the "dynamics of huge phenomena such as CMEs may be controlled by detailed plasma processes that occur in relatively tiny regions" [9].

Appendix C

CME models

Reviews of CME models can be found in the works of Low [63], Forbes et al. [112], and Chen [29]. Certain textbooks by Aschwanden [74] and Crooker et al. [113] are also excellent resources.

C.1 CSHKP flare model

The Carmichael-Sturrock-Hirayama-Kopp-Pneuman (CSHKP) flare model is a 2D reconnection model which describes the evolution of a flare along a vertical plane. While no single model describes all possible flares, the CSHKP model fits most of the observations and is accepted as the "standard model" of flares. In particular, it explains the power source of the flares, the coronal streamer structure, the rising prominence, the brightening of the chromospheric footpoints, the flare signatures in X-ray, EUV, and Hα, and the increased height and footpoints separation of the magnetic structure. The standard model presents the physical mechanisms behind these observations, which include the solar wind energy source, magnetic reconnection, synchrotron radiation, shock acceleration, and Joule heating. A representative summary from the four papers is shown in Fig. C.1.

Carmichael [68] introduced the mechanical energy of the solar wind as the power source of solar flares: he suggested that the solar wind deposits magnetic energy into the flare. This deposited energy is stored in the form of twisted field lines (see Fig. C.1 (a). Flares and the events that accompany flares are the manifestation of the

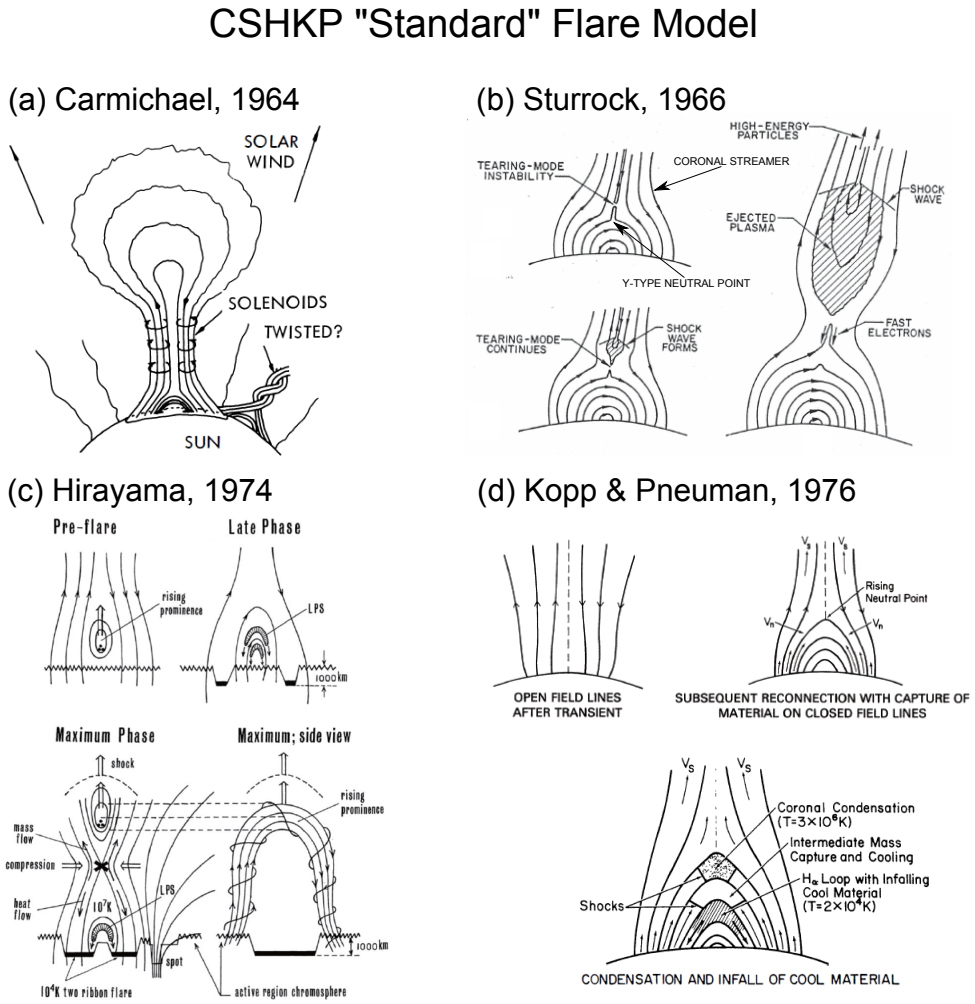

Figure C.1: CSHKP phenomenological models for flares.

occasional release of this stored energy.

Sturrock [69] stressed the importance of coronal streamers (aka helmet streamers) containing flux of opposite polarity. The pinching of the current sheet above the Y-type neutral point results in a tearing-mode instability which reconnects magnetic field lines. This reconnection leads to the development of strong electric fields which accelerate both electrons and protons. Plasma[1] is "sling-shot" into the upper portion of the streamer, resulting in higher energy energy particles and shock waves, while some electrons (which are caught in the closed field lines) accelerate towards the surface of the sun. The shocks from the ejected plasmas are expected to produce Type II solar radio bursts by kilovolt electron acceleration at the shock front[2]. The deflection of sun-directed electrons by a magnetic mirror mechanism produces Type IV radio burst through synchrotron radiation. Fig. C.1 (b) is a summary of this process.

Hirayama [70] proposed that the pre-flare process can be attributed to a rising prominence which leaves a magnetic cavity in its wake. The compression of this cavity from both sides (see Fig. C.1 (c) Maximum phase) near the X point generates Joule-heated downward flow towards the chromosphere, where the flows brighten the chromospheric footpoints and evaporate. These evaporated protons fill the newly reconnected field lines with dense, heated plasma capable of producing soft X-ray-emitting flare loops. These X-ray flare loops cool through thermal conduction and radiation until they are detectable as EUV flares and eventually as two-ribbon Hα flares.

Kopp and Pneuman [71] proposed that the post-flare loop prominence systems are the closing of magnetic field lines which were torn open by flare outbursts. They examined the cooling process of material supplied to the prominence region by enhanced solar wind outflow along open field lines. They found threes stages of cooling (See Fig. C.1 (d): Condensation and infall of cool material) which correspond to loop structures in X-ray, EUV, and Hα. Their mechanism predicts the continuous rise of

[1]The plasma contains almost all the protons and the majority of electrons.

[2]This is similar to electrons accelerated in the Earth's bow shock.

the Y-type neutral point, which means that newly connected field lines have larger height and wider footpoint separation.

While the CSHKP model can explain what happens during and after a flare, it does not discuss what causes the system to go unstable, i.e., it does not discuss why a prominence arises in the first place. The answer to that question is intimately related to the study of CMEs. Modern models have adapted CSHKP to fit observations from new satellites (e.g., Yohkoh, SOHO, SDO) and advances in magnetic reconnection physics.

C.2 Aly-Sturrock constraint

Prior to the work of Aly in 1984, many solar physicists did not consider the topology of the magnetic field for a maximum energy state in a force-free configuration. The ongoing understanding was that twisting motion on the photosphere would inject energy into the corona in the form of net current. This current would reconfigure itself until it was everywhere parallel to the magnetic field, resulting in a force-free state. Intuitively, it seems like the injected energy will eventually surpass the energy of an open field configuration, thus permitting energetically favorable transitions from a twisted state to an open field state. Early solar models accepted this assumption as plausible. To make this idea rigorous, Barnes and Sturrock [114] simulated a sunspot of one polarity within a region of opposing polarity. By sufficiently rotating the sunspot, they calculated more free energy in their force-free configuration than an open field configuration with the same vertical magnetic flux at the surface.

Aly [115] used the Virial theorem to study three-dimensional force-free magnetic configurations in an infinite domain, e.g., a half-space or the exterior of a sphere. After applying the appropriate boundary conditions[3], he found an upper bound on the energy of force-free states and conjectured that the maximum energy force-free configuration may be lower than the corresponding open field configuration. He pos-

[3]For a domain like the sun, the magnetic field is normal to the surface and decays to zero as the distance goes to infinity.

tulated that the magnetic field of Barnes and Sturrock [114] is artificially confined by their simulation, which introduces an unphysical pressure at the boundary that prevents the field from expanding when shear is increased. Sturrock [116] agreed with Aly's conjecture and established that the maximum energy configuration for a simply linked force-free field is the open field state. This result is known as the Aly-Sturrock constraint and plays a central role in the development of modern solar models.

Modern methods of bypassing the Aly-Sturrock restriction include:

- Not requiring the magnetic configuration to fully open by creating a current sheet of finite length. For example, resistive processes may prevent the formation of the long current sheets associated with open field lines.
- Using a multi-polar configuration. This is one of the main motivators for the Breakout model for CMEs (See Sec. C.3.3).
- Considering non-force-free effects like gas pressure and gravity [116].
- Assuming that the magnetic field contains detached magnetic field lines and thus is not simply linked to the solar surface. This occurs in the creation of a "disconnected" flux tube.
- Recognizing that real eruptions occur in 3D and can slip past field lines instead of forcing them to open up [117].

Regardless of the bypass method, the Aly-Sturrock constraint is a gentle reminder to take care when modeling complicated phenomena. Intuition, while helpful, can and does break down, resulting in unphysical assumptions.

C.3 Sheared arcade models: Magnetic reconnection

These models have ties to the CSHKP flare model. Like the flare model, sheared arcade models focus heavily on the role of magnetic reconnection. The common feature of these models is that a flux rope is created by reconnection during the

eruption. Since the details behind solar magnetic reconnection are far from settled, many of these models are highly phenomenological.

C.3.1 Tether-cutting

The tether-cutting model draws heavy inspiration from the CSHKP flare model and was presented by Moore and Labonte [79] after observing

- strongly sheared magnetic field across the neutral line in the chromosphere and in the filament.
- $H\alpha$ brightening and mass motion along the neutral line prior to filament eruption and onset of the flare.
- The pre-flare brightening and flare brightening that were in the vicinity of the steepest magnetic field gradient.

In their model, the filament is supported by a dip in the magnetic field, which is strongly sheared near the filament and the neutral line. This shear decreases with distance from the neutral line so that the strongly sheared field is enclosed within an arcade of loops, which are nearly perpendicular to the neutral line. This arcade field provides a downward magnetic tension force which is balanced by an outward magnetic pressure force that is building up within the sheared region. This gradual build up of shear leads to the destabilization of the filament due to reconnection beneath the filament. The reconnection also produces the initial brightening of flare ribbons. In 2001, Moore et al. [7] updated this description to also accommodate confined (failed) eruptions.

An adapted version of Moore et al's tether cutting figure is shown in Fig. C.2. Before the onset, the sheared core field has two oppositely curved elbow regions to give the core field its sigmoidal form. As the footpoints twist, the field near the footpoints shear, causing reconnection between AB and CD at the *x-point* (red in Fig. C.2), thereby marking the onset of an eruption. The cause of this reconnection is unspecified but is believe to be due to anomalous resistivity or due to nonlinear terms

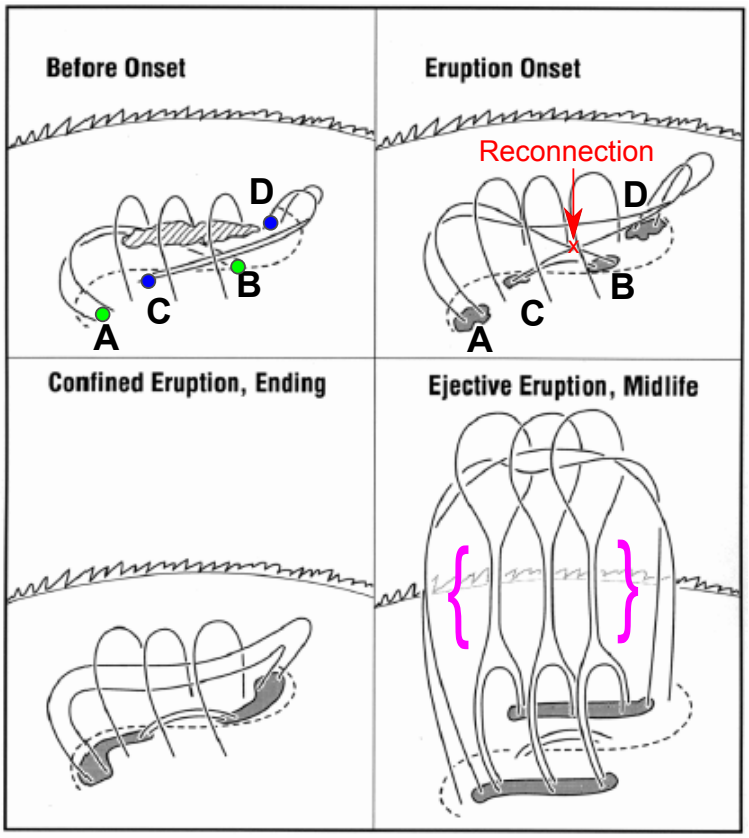

Figure C.2: Adapted from Ref. [7]. "This version is tailored to bipoles having sigmoidally sheared and twisted core fields and accommodates confined explosions as well as ejective explosions. The rudiments of the field configuration are shown before, during, and after the onset of an explosion that is unleashed by internal tether-cutting reconnection. The dashed curve is the photospheric neutral line, the dividing line between the two opposite-polarity domains of the bipoles magnetic roots. The ragged arc in the background is the chromospheric limb. The gray areas are bright patches or ribbons of flare emission in the chromosphere at the feet of reconnected field lines, field lines that we would expect to see illuminated in SXT images. The diagonally lined feature above the neutral line in the top left panel is the filament of chromospheric temperature plasma that is often present in sheared core fields."

in the General Ohm's law (e.g., Hall term or electron inertia term in Eq. B.7). Before reconnection, lines AB (endpoints marked by green circles) and CD (endpoints marked by blue circles) acted like "tethers" that restrained the plasma. After reconnection, the resulting long field line AD has upwards concavity so magnetic tension is expected to pull AD upwards. The short loop CB has downwards concavity and so is pulled downwards by magnetic tension. Moore et al. likened this process to the cutting of tethers. The reconnection also induces upwards mass motion and creates the observed $H\alpha$ brightening.

If sufficient shearing exists to start a "runaway reconnection," the explosive release of free energy causes bulk upward motion of mass. This upward motion has two end states: (1) the motion stops in the solar atmosphere (confined eruption) or (2) the motion escapes the solar atmosphere (ejective eruption). The specific cause for the confined case is not explained but the model speculates that it may be related to the flux content of the core field vs the overlying envelope field and the height at which reconnection occurs. An x-point with high initial height may not break all the tethers associated with the overlying field. In contrast, ejective eruptions are expected to blow out the overlying and the twisted flux rope. Here the reconnection is expected to be long lived, thus forming tall vertical current sheets as shown within the purple braces in Fig. C.2.

C.3.2 Flux cancellation

Van Ballegooijen and Martens [8] proposed a "flux cancellation" method to explain the disappearance of photospheric magnetic flux at the neutral line separating magnetic flux of opposite polarity [112]. Their proposed mechanism (shown in Fig. C.3) outlines how arched field lines can evolve to the helical field structure of a flux rope. They concluded that flux cancellation can produce helical field lines, which may support prominence plasma, but that eruptions may not occur in a two-dimensional model due to the Aly-Sturrock constraints.

Modern solar theory groups the flux cancellation model with tether-cutting. Flux-

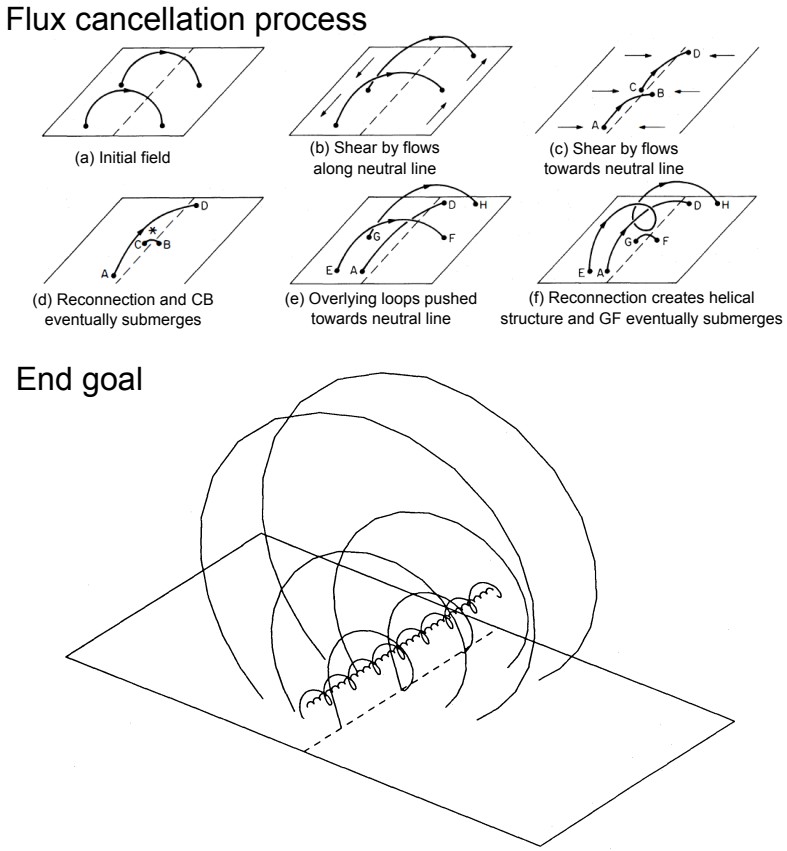

Figure C.3: Cartoon demonstrating the basic concepts of flux cancellation. The initial field (a) is sheared by flows along (b) and towards (c) the neutral line. This leads to reconnection in (d) and the submergence of lower loop CB. The overlying loops are also sheared (e) to eventually create the recognizable helical flux rope structure (f) and the flux line GF submerges. (from Ref. [8]).

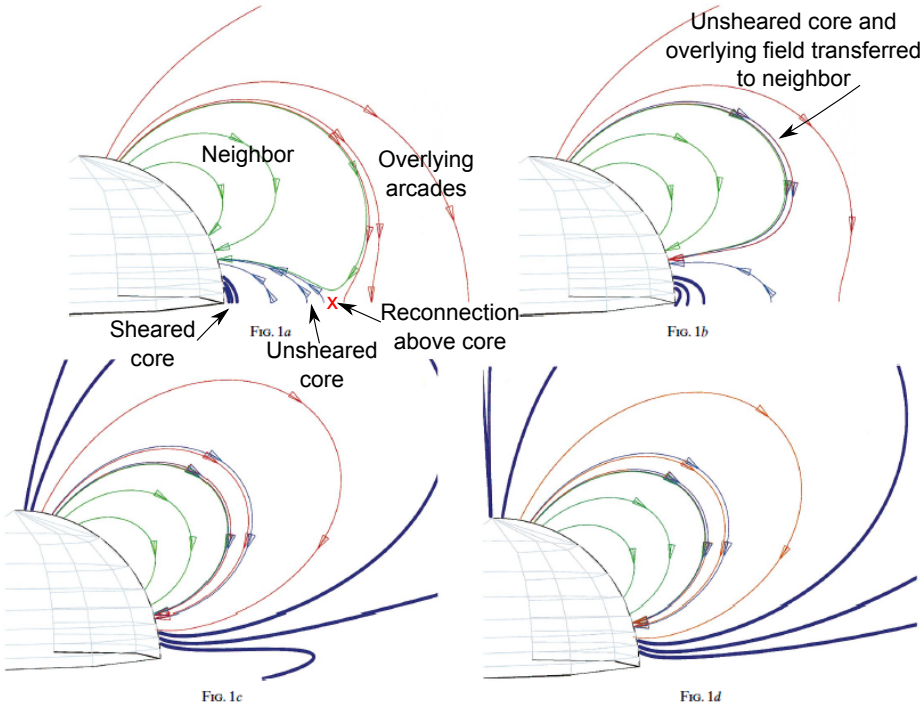

Figure C.4: Adapted from Ref. [9]. "(a) Initial potential magnetic field. The field is symmetric about the axis of rotation and the equator, so only one quadrant is shown. The photospheric boundary surface is indicated by the light gray grid. Magnetic field lines are colored (red, green, or blue) according to their flux system. Two types of blue field lines are indicated: higher-lying light blue unsheared field and low-lying dark blue field that is sheared later in the simulation. (b) Force-free field after a shear of $\pi/8$. The field lines shown correspond to those in (a) and are traced from the same footpoint position on the photosphere as in (a). (c) As above, but for a shear of $3\pi/8$. (d) As above, but for a shear of $\pi/2$."

cancellation may apply to the gradual evolution in the photosphere whereas tether-cutting is more applicable to impulsive processes in the coronal [29].

C.3.3 Breakout

Antiochos et al. [9] introduced a quadrupole flux system containing: an enclosed core region (blue), overlying arcades (red), two neighboring systems (green), and a null point above the core flux system as shown in Fig. C.4. Confinement comes from the unsheared core field (thin blue lines) and the overlying arcade (red) whereas the eruption is powered by the sheared flux (dark blue lines). Reconnection permits the system to evolve by transferring unsheared flux from the red and blue systems to

the green systems. This evolution allows the initially enclosed dark blue sheared flux to escape while keeping all unsheared flux systems (red, green, and thin blue lines) closed so as to not violate the Aly-Sturrock energy limit.

A key feature of the breakout model is that the quadrupolar magnetic configuration does not have a unique "open" field lines configuration which satisfies the boundary condition. Instead, a collection of boundary-satisfying configurations with energies between E_{max} and E_{min} exist. E_{max} is associated with a fully open core flux (blue) and arcade flux (red) but closed neighbors fluxes (green). E_{min} is associated with an incremental opening of the core flux while the rest of the system remains closed. The expansion energy can build up because the shear core fields (dark blue lines) are initially far from the reconnection null point, thus permitting a quasi-static evolution with negligible reconnection and dissipation at the null point. The energy is expected to build up to values greater than E_{min} while the central flux system expands upwards. As the central flux system expands upwards, it presses against the null point to form a current layer. If gas pressure and resistivity are considered, the system undergoes magnetic reconnection in this current layer and transfers flux associated with the unsheared core field and overlying arcades into the neighboring systems. This process by which the restraining fields are removed is like the peeling of an onion [29]. The final state is a fully open sheared flux system with total energy that is less than the initial state.

The breakout model is different from other models because it requires a quadrupolar magnetic field. Li and Luhmann [95] studied 80 CME events and concluded that bipole magnetic fields occur three times more often than quadrupolar magnetic field. Nevertheless, Aulanier et al. [118] presented the first evidence in support of this model by examining the topology and evolution of the Bastille Day Flare. They approximated the extrapolated coronal magnetic field as a quadrupolar magnetic structure and located a null point above the core flux system.

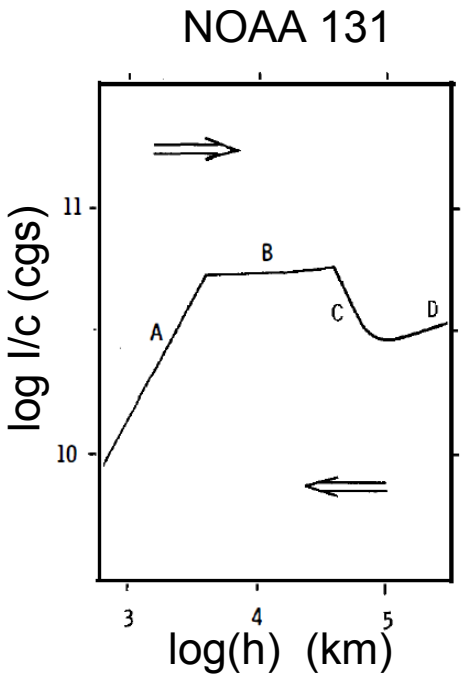

Figure C.5: Adapted from Fig. 3 of Ref. [10]. Magnitude of equilibrium current I vs height for region NOAA 131 for which $h_1 = 1600$ km and $h_2 = 12000$ km. The arrows indicate the direction of the Lorentz force for a perturbation from equilibrium. A and B correspond to regions $h < h_1$ and $h < h_2$, respectively. C and D correspond to $h > h_2$. The Lorentz force due to interactions with the ambient field dominates in regions A, B, and C where gravity dominates for regions D.

C.4 Flux rope models: Loss of equilibrium

These models are all based on the assumption of a pre-existing flux rope. The loss of equilibrium of the flux rope drives other processes. For example, the flux pile up generated by the motion of the flux rope drives reconnection [119].

C.4.1 Circuit model

Van Tend and Kuperus [10] presented a circuit model now considered to be one of the earliest "loss of equilibrium" type models. Their generalized model considers the forces acting on a wire carrying current I with mass per unit length m at height h above a conducting surface. Unlike later models, their model does not include ideal MHD concepts like frozen flux but instead focuses on the three following forces: (1) the Lorentz force when the wire interacts with its image current, (2) the Lorentz force

when the wire interacts with the ambient field, and (3) gravity. The ambient field is assumed to be horizontal at the location of the wire and the total field in the corona is then taken as a superposition of the field from the current and the ambient field. The force balance equation is then written as

$$\frac{\mu_0 I^2}{\pi h} = IB(h) + mg \tag{C.1}$$

where g is the gravitational constant of the sun and $B(h)$ is the magnetic field as a function of height. They create $\log(I)$ vs $\log(h)$ equilibrium figures (e.g., Fig. C.5) by assuming that $B(h) \approx const$ for low heights, $B(h) \sim h^{-1}$ for heights comparable to the width of the solar prominence (h_1), $B(h) \sim h^{-3}$ for heights comparable to the entire active region (h_2), and $mg \approx const$. The slope is positive for regions A, B, and C which correspond to a stable equilibrium whereas it is negative and unstable for region C. The model assumes that multiple parallel currents in the active region which will tend to attract and coalesce into single current channel with much larger current. The system is expected to erupt when currents at low altitudes reach a value greater than the maximum found in branch B.

While this model is simple by modern standards, the essential ideas provide the building blocks for many later models. One consequence of the Kuperus model is the restriction on the polarity of the ambient magnetic field. The orientation of the ambient field must produce a force which resists the tendency of the wire to erupt (i.e., the polarity of the ambient field must be a strapping field configuration). The opposite situation (anti-strapping field) is generally unfavorable to the formation of solar structures, unless gravitational forces dominate.

C.4.2 Catastrophe: no neighboring equilibrium

Forbes and Isenberg [11] extended the van Tend & Kuperus description to include MHD concepts and laid the groundwork for their two stage catastrophe model. In the first stage, the magnetic energy of the system slowly increases due to transfer of magnetic flux from the photosphere to the corona. This evolution happens over a few

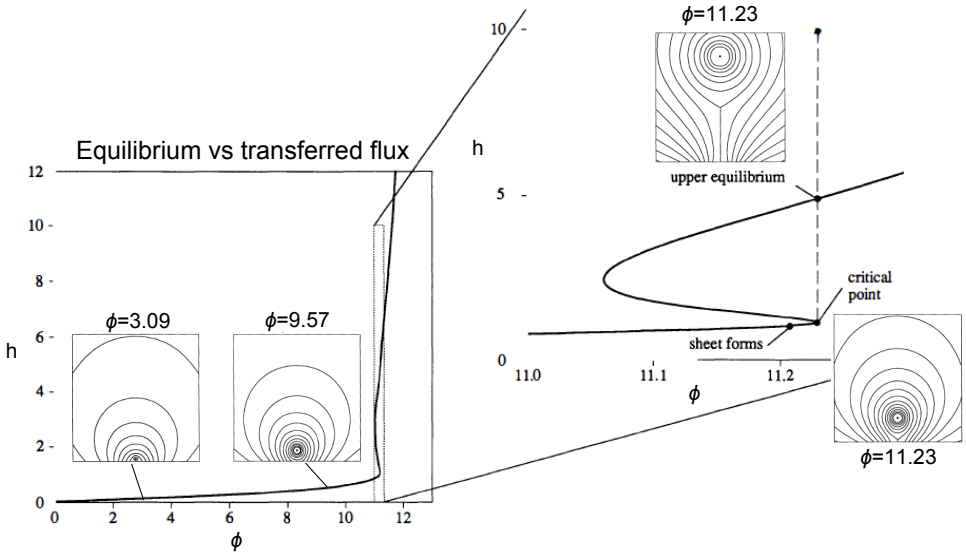

Figure C.6: Adapted from Figs. 3-4 in Ref. [11]. The graph is a normalized equilibrium height h as a function of the reconnected flux ϕ for $r = 10^{-5}$. As ϕ increases, the filament follows the lower branch of the equilibrium curve towards the critical point (lower equilibrium) at $\phi = 11.23$. At the critical point, the equilibrium solution has an additional solution at the upper equilibrium and the plasma is expected to erupt upwards. The contours are the vector potential of the filament. The contour levels are not the same in all the plots though the relative location of the rising current channel is at the center of the concentric contour lines.

days and the system evolves quasi-statically through a series of equilibrium states. In the second stage, the configuration evolves rapidly following loss of equilibrium. This second stage lasts a few Alfven time scales and is very rapid compared to the evolution in the first stage. No flux is transferred from the photosphere to the corona during this phase.

Their set-up considered the equilibrium of a infinitely-long, current-carrying cylinder of constant radius r and uniform current density above a conductive photosphere. The internal, local equilibrium balances the pinch force and the thermal pressure. The external, global equilibrium balances the expansion force associated with the image current and the retraining force associated with the external strapping field. The external field is a vacuum field with boundary specified by the following vector potential function:

$$\mathbf{A}(x,0) = \frac{md}{x^2+d^2} - \phi(t)$$

where the first term is a line dipole of strength m at depth d and the second term is a slowly varying function of time representing the transfer of magnetic flux from the photosphere to the corona.

The model considers the quasi-static evolution of MHD equilibrium caused by the gradual transfer of flux, ϕ, from the photosphere to the corona. This is unlike other models like Breakout (Sec. C.3.3), and Tether-cutting (Sec. C.3.1) which use reconnection to release magnetic energy. Instead, the Forbes reconnection process in the model is inspired by the energy storage process that occurs in the Earth's magnetosphere prior to an aurora storm [120]. Figure C.6 shows the equilibrium solution as a function of height as well as the corresponding vector potential contours at those heights. This early model has all the basic features of later catastrophe models but its primary weakness is that no catastrophe occurs unless the filament radius is 10^{-3} times smaller than the length scale of the photospheric field, which is unlikely to occur on the sun.

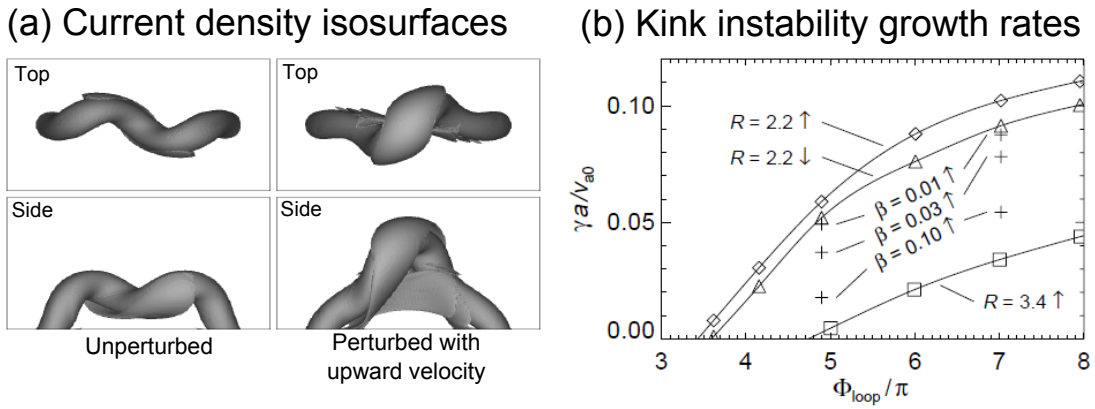

Figure C.7: Adapted from Figs. 3 and 5 of Ref. [12]

C.4.3 Kink instability

Sakurai [121] was among the first to consider the kink instability in the context of solar filaments. He performed linear stability analysis on an infinitely long cylinder of incompressible fluid with constant density, radius R, and magnetic field with profile $B_r = 0$, $B_\phi = B_\phi(r)$, and $B_z = B_\phi P/r$, where r, ϕ, z are the standard cylindrical coordinates and $2\pi P$ is the pitch of the field lines. Displacements whose wavelength $(2\pi/k)$ are longer than the characteristic filament length L are not considered by introducing the criterion $(kP)_{cutoff} = 2\pi P/L = 1/N$. The kink instability occurs when P/R decreases or N increases, which corresponds to when the plasma winds up, increases its radius, or increases its effective length. Non-linear MHD simulations showed that a kinked cylindrical plasma can reproduce the initial growth rate of erupting filaments but the plasma does not erupt. Sakurai explain this discrepancy by citing the work of Yeh [122], who showed that a given magnetic flux configuration may not have an accessible cylindrical equilibrium but can access a stable helical equilibrium. This is consistent with the perspective of laboratory plasmas where the kink instability is considered a mechanism by which the plasma relaxes to a lower energy state and not a process by which the plasma escapes confinement.

Hood and Priest [123] furthered the Sakurai model by including the stabilizing effect of line-tying to flux ropes connected to the photosphere and deriving a critical twist value above which the flux rope is unstable. More recent results by Torok et al.

[12] and Torok and Kliem [124] studied ideal kink mode for a force-free coronal loop of characteristic density ρ_0 and field B_0 in a background field [125]. To quantify loop twist, they defined $\Phi = lB_\phi(r)/(rB_z(r))$[4], where r is now the along minor radius of the loop, l is the length of the current-carrying flux system, B_ϕ is the azimuthal field, and B_z is the axial field.

Their unperturbed solutions produced current density iso-surfaces with the characteristic sigmoid and a localized dip at the center as shown in the first column of Fig. C.7 (a). These features are typically found in solar loops. In order to initiate upward motion along the sigmoid center (as shown in the second column of Fig. C.7 (a)), they introduced a velocity perturbation for five Alfven time scales ($\tau_a = L/v_{a0}$ where $v_{a0} = B_0/\sqrt{\mu_0\rho_0}$), resulting in upward mass motion and a nearly vertical current sheet. This current sheet did not show up in cylindrical models. They varied Φ_{loop} by changing the number of field line turns about the torus axis (N_t) and produced fits of their results (Fig. C.7(b)). The instability criterion is $\Phi_{crit} \approx 3.5\pi$ for a loop with aspect ratio $R/a \approx 5$ where $R = 2.2$ (triangles and diamonds in Fig. C.7(b)). The upward velocity perturbation (diamonds) lowered the critical threshold by a small amount compared to the unperturbed situation (triangles). Even with the upward velocity perturbation, a larger aspect ratio ($R/a \approx 8$ where $R = 3.4$) results in a higher instability threshold (squares) than the unperturbed lower aspect ratios cases. The instability threshold also changes as thermal pressure is added (plus signs). Regardless of velocity perturbations, aspect ratio, or β, all the loops eventually enter a nonlinear saturation phase and do not erupt globally. Torok et al. conclude that the kink instability may explain confined eruptions, like the event observed by Ji et al. [94], but is not a mechanism for global eruptions.

Observations of eruptions show a strong correlation between the twist of a loop structure and the likelihood of eruption [126]. It is tempting to use the kink instability to explain eruptions since linear models show that the kink growth rate matches observed eruption growth rates. While the twist of a loop structure correlates with the likelihood of an eruption, it would be erroneous to conclude causality. Instead,

[4] $\Phi = 2\pi N$, where N is defined in the cylindrical Sakurai model.

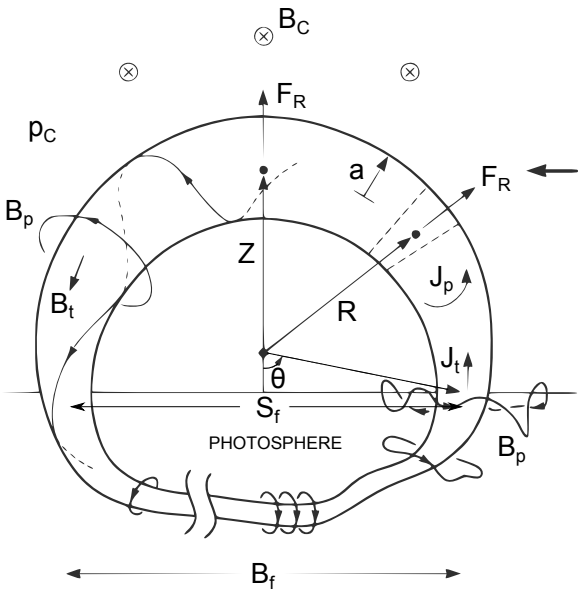

Figure C.8: Adapted from Ref. [13]. A current channel of major radius R, minor radius a, footpoints separation S_f. The channel contains magnetic fields B_p and B_t. The subphotospheric field is incoherent with $B_p \ll B_t$.

Torok concludes that the kink instability may perturb the plasma from its equilibrium state, permitting the onset of torus instability. This matches the results of laboratory plasma physics, where the kinking of the flux rope and the expansion of the flux rope are both caused by an increase in the current. The kinking and expansion are thus correlated but not causally linked.

C.4.4 Torus instability

This model is discussed in detail in Sec. 2.3.4.

C.4.5 Flux injection

Most solar models are "store and release" type models which build up energy slowly prior to the eruption and evolve with little energy injection during the eruption. In contrast, a dynamo model rapidly generates magnetic flux by real-time stressing of the magnetic field during an eruption [74]. Chen [40] introduced such a dynamo mechanism in his "flux injection," model where the flux injection corresponds to a

specified increase in the poloidal flux $\Phi_p(t)$.

Recognizing that toroidal dynamics for laboratory plasmas have been thoroughly studied by Shafranov [84], Chen adapts these "toroidal forces" to the solar configuration where plasmas are not surrounded by metallic conducting walls. In particular, Chen examines the dynamics for the portion of a loop found above the photosphere while the portion below the photosphere is presumed to be connected to a solar dynamo. The footpoints are assumed to be immobile because they are on dense sub-photospheric plasma. The loops are fitted to a circle at three points: two fixed footpoints and a third point representing the height of the apex of the loop. This apex height Z is related to the major radius of the loop R as follows:

$$R = \frac{Z^2 + S_f^2/4}{2Z} \tag{C.2}$$

where S_f represents the separation of his footpoints. Chen considers both forces along the major radius R and along the minor radius a. His equation of motion for the apex center of mass is

$$M\frac{d^2R}{dt^2} = \frac{\Phi_p^2}{c^4L^2R}\left[\left\{\ln\left(\frac{8R}{a}\right) - 1 + \frac{l_i}{2}\right\} + \frac{1}{2}\beta_p - \frac{1}{2}\frac{\bar{B}_t^2}{B_{pa}^2} + 2\left(\frac{R}{a}\right)\frac{B_{strap}(Z)}{B_{pa}}\right] + F_g + F_d \tag{C.3}$$

where the forces are hoop force in the curly braces, thermal pressure force, magnetic tension force, strapping field force, gravitational force, and drag forces. Specifically, Φ_p is the poloidal flux enclosed by the partial torus, c is the speed of light, L is the self inductance of the system, l_i is the internal inductance of the system, B_t is the toroidal magnetic field, B_{pa} is the poloidal magnetic field at $r = a$, and B_{strap} is ambient strapping field.

The model considers a wide range of forces making it relevant for CMEs from early eruption onset to the Earth impact. The model captures the eruption dynamics by fitting to a seven-parameter $d\Phi/dt$ profile [13]. This fit of the poloidal flux rate can capture, with 99 percent accuracy, the dynamics of a CME [127]. Krall et al. [128] performed a comparison of (1) flux injection to (2) quasi-static arcade shearing

models, (3) magnetic store and release models, and (4) thermal injection models and found that models (1) and (3) reproduce key features both near the sun and in the interplanetary medium. Furthermore, they concluded that only flux injection obtained a detailed match to near Sun dynamics.

The presence of footpoints is another feature of the flux injection model. Chen and Krall [38] used loop curvature arguments to determine the acceleration for loops described by Eq. C.2. They predicted that peak acceleration will occur between $Z_\star$ and Z_m, where $Z_\star = S_f/2$ and $Z_m \simeq 3Z_* = 1.5S_f$. The peak acceleration is then predicted to lie within

$$Z_* < Z_{max} < Z_m$$

and has been successfully applied to solar eruptions [80].

The flux injection model has many features found in the Caltech experimental set-up. Caltech plasmas have footpoints and $d\Phi_p/dt$ is the voltage at the footpoints. Like the Caltech set-up, the flux injection model assumes that the plasma is powered by a current source [40]. The excellent match between the flux injection model and the dynamics of coronal mass ejections supports the use of a current source for the Caltech experiment [104].

C.5 Convergence towards a standard model

As models describing CMEs mature, there is gradual convergence towards a standard model. The solar community has already accepted that tether cutting and flux cancellation are the same process, applied to the corona and the photosphere, respectively. While supporters of "break-out" and "tether-cutting" still argue about whether reconnection occurs "above" or "below" the highly-sheared field region, both processes use magnetic reconnection to create the flux rope and drive the eruption. This has motivated the categorizing of breakout as a kind of "external tether cutting" [29].

Loss of equilibrium type models also are converging as scientists agree on the fundamental forces involved. The Van Tend & Kuperus circuit model represents an

implementation of catastrophe model [29] in cylindrical geometry. In both circuit and catastrophe models, the system evolves along a series of equilibria until the driving mechanism (usually an increase in current) pushes the system to a regime without an equilibrium and the system erupts. The torus instability and catastrophe models are now accepted by their respective proponents [105] as describing the same critical threshold from two different perspectives. While catastrophe specifies a pre-eruptive evolution and avoids consideration of unstable equilibria away from the critical threshold, torus instability does not specify the pre-eruptive evolution and focuses on the family of unstable equilibria. Since both models are based on the same force balance equation, they produce an onset of eruption at the same point [105].

The kink instability and certain aspect of flux injection remain distinct from the other models. The kink instability is not an eruption mechanism and is a parallel plasma process caused by the current. Flux injection distinguishes itself from other solar models by permitting energy transfer during the eruption process. Laboratory experiments can tie both the kink instability and flux injection models to existing solar models. Laboratory plasma loops can kink and erupt since no simplifying assumptions are made. Energy can also be injected into laboratory plasmas by an external power supply and the kink instability has been observed and quantified in laboratory experiments [129, 130].

While scientists still debate about whether or not solar eruptions contain pre-existing flux ropes, it is prudent to note that the descriptions from both sides look remarkably similar. The flux cancellation end goal (Fig. C.3) looks like a current carrying flux rope emerging from the photosphere [131]. It is to no surprise that plenty of observational evidence can be produced to back each side. Nevertheless, the quest for scientific understanding continues: nature is self-consistent, and so the solar physics community will inevitably converge on a standard CME model.

Appendix D

Operational Details

One striking feature of the Caltech experiment is the tens of Megawatts of power during the plasma life-time. This energy injection rate is greater than the Caltech on-site power generation capability and would be prohibitively expensive to sustain. Fortunately, the plasma only exists for a few microseconds so the energy usage is negligible. Megawatts-scale experiments can be powered by standard 120 V outlets through pulse-power techniques. These technique take advantage of long charging times to build up energy within a capacitor. This energy is released by fast switches over extremely short time scales, producing tremendous power output.

This chapter discusses the operational details of plasma breakdown, strapping field, and diagnostics. The focus will be on describing hardware though relevant theory will also be presented.

D.1 Experimental setup

A representation of the experimental setup can be found in Fig. D.1. The vacuum chamber axis defines the z-axis of the coordinate system. The cathode and anode define the x-y plane, with the gap separating cathode from anode defining the origin. The bias coils (purple) generate arched magnetic fields similar to a horseshoe magnet. Fast gas valves puff gas through the center of the bias coils, creating spatially non-uniform gas distributions with higher densities near the nozzle. The electrodes, bias coils, and gas system make up the plasma gun, which is used to form plasmas

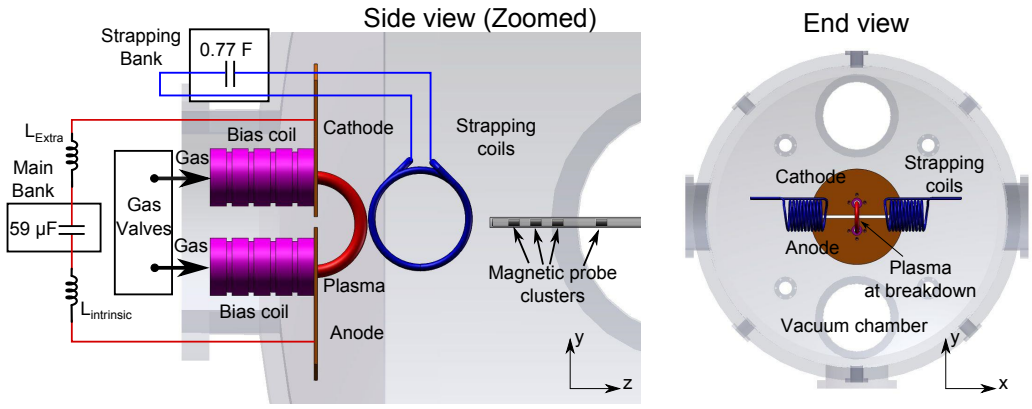

Figure D.1: Representative side and end view of experimental set-up.

(red). High voltage applied to the electrodes by a 59 μF capacitor ionizes gas to form an arched plasma much smaller than the vacuum chamber (Fig. D.1 End view). The capacitor is typically charged to 2.5-5 kV driving 30-70 kA of current which flows in the y direction at the plasma loop apex. Additional inductance (L_{extra}) can be added to the intrinsic inductance of the system ($L_{intrinsic}$) to slow down the current pulse.

A 0.77 F capacitor bank powers two 7.6 cm diameter strapping field coils (blue) mounted 9.5 cm in front of the electrode. The strapping coils each have 11 turns and are placed in a coaxial configuration inside the chamber to produce strapping field in the x direction, so that the $J_y \times B_x^{strap}$ force inhibits plasma loop expansion where J_y is the electric current density in the plasma loop.

The timing is programmed to a set of function generators which coordinate the entire events across millisecond and microsecond time scales. Once programmed, each experimental shot is mostly automated and the user is in charge of manually starting the capacitor charging process.

D.2 Vacuum system

Experiments before June 2012 were done in a 2 m long and 1.4 m diameter stainless steel vacuum ("Alpha") chamber, whereas experiments after June 2012 were done in a smaller 1.5 m long and 1 m diameter ("Bravo") stainless steel chamber (Fig. D.2). Both chambers are considerably larger than the plasma, thus simulating a "half infinite

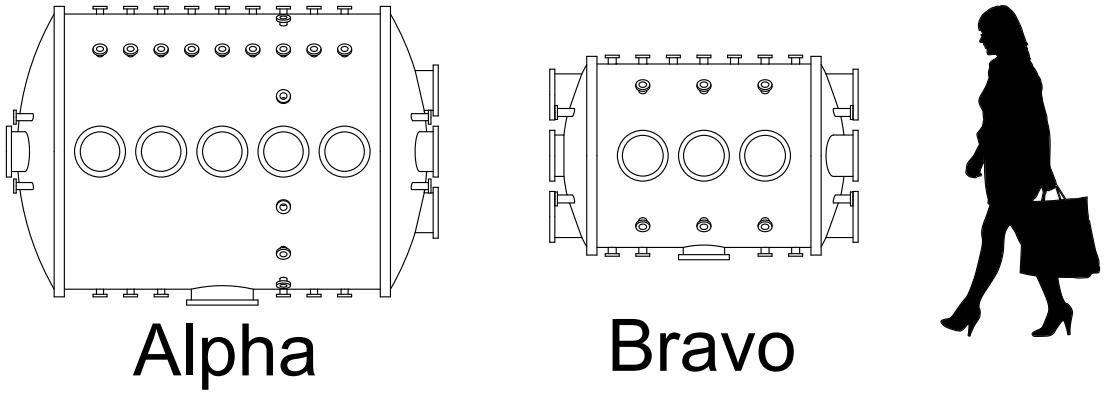

Figure D.2: Scaled rendering of the Alpha and Bravo chambers compared to a 5-foot human being.

space." This contrasts most plasma experiments, which have conduction walls that are close to the plasma in order to suppress instabilities [132–134]. This configuration limits the plasma-wall interactions to the region near the plasma footpoints and allows the plasma loop to expand to many times its original size. These features permit the experiment to simulate the boundary conditions of a solar eruption.

Bravo vacuum chamber is held at 10^{-7} torr to 10^{-8} torr by a turbo pump backed with a scroll pump. The scroll pump takes the chamber from atmosphere (760 torr) to 10^{-3} torr. The turbo-pump kicks in at around 10^{-1} torr and brings the chamber to 10^{-7}-10^{-8} torr. The pumping rate is comparable across all gasses including Helium. In contrast, Alpha chamber uses a cryo-pump, which has much higher pumping throughput but is unable to pump Helium.

D.3 Plasma gun

The plasma gun comprises: copper electrodes, bias coils, and gas injection mechanism assembled in a co-planar spheromak gun configuration [135]. This co-planar configuration creates plasmas which are accessible to diagnostics immediately after breakdown, permitting direct plasma measurements at early stages (See Fig. D.3 (a)). In contrast, the early plasma details are difficult to access in the co-axial spheromak gun design [133, 136]. Figure D.3 (b) is a cartoon of co-axial spheromak formation at

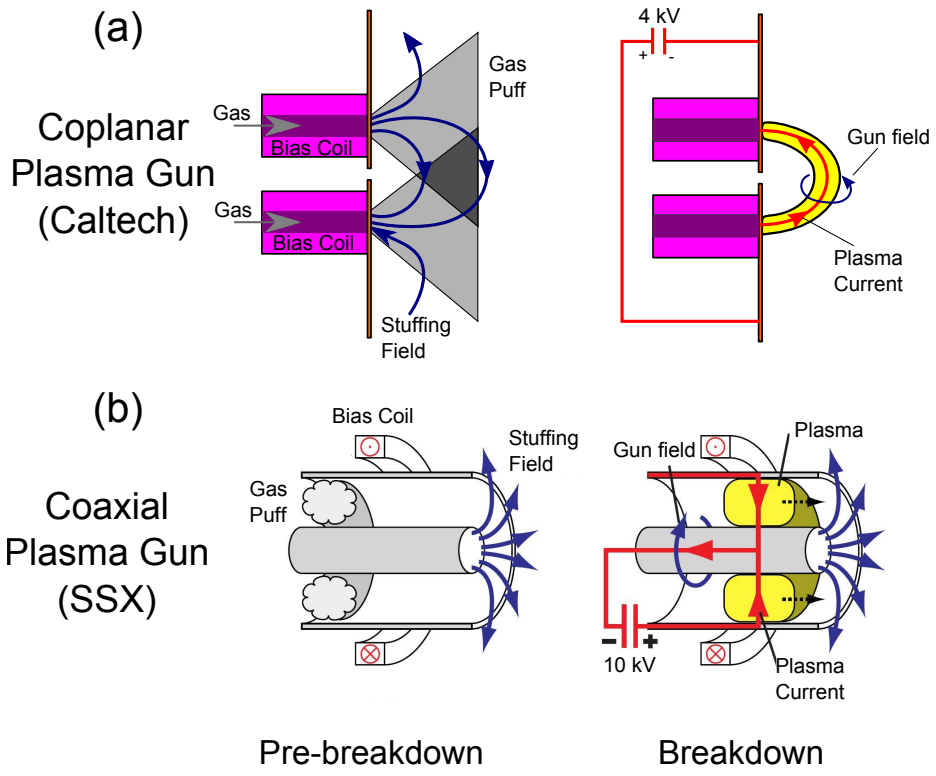

Figure D.3: Plasma breakdown process for (a) co-planar and (b) co-axial plasma guns. (SSX coaxial cartoon adapted from Ref. [14])

the Swarthmore Spheromak Experiment (SSX) [14]. Unlike with the co-planar gun, the plasma breaks down within the barrel of the co-axial gun and is not accessible until after it leaves the muzzle.

Nevertheless, both techniques have the same basic breakdown process:

1. Vacuum field (known as bias field or stuffing flux) is generated by bias coil(s) at sufficiently slow (typically ms) time-scales to penetrate into the electrodes.

2. Gas is injected into the electrode region by fast gas valves to create spatially non-uniform gas pressure. This typically occurs ms before breakdown.

3. High voltage is applied across the electrodes over a fast (typically μs) time-scale. This high voltage initiates a Paschen process which breaks down the gas, creating plasma.

D.3.1 Bias coils

The bias coils produce horseshoe-like magnetic field configurations similar to the bipole field of solar geometries. A typical vacuum field is shown in Fig. D.4 (a). The different shades of green represent magnetic field lines originating at difference distances from the bias coil center; darker lines are closer to the axis of the coil. The bias coils are powered by capacitor banks discharged a few millisecond before plasma formation. This creates a magnetic field that lasts milliseconds after breakdown. The plasma lasts for microseconds so the bias field is considered constant over the timescale of the plasma. Typical bias field strength is about 1-3 kG at the footpoint and 250G near at the plasma apex.

One of the bias field effects is to evolve the plasma from a loop shape to a sigmoid shape, as shown in Fig. D.4 (b). This sigmoid shape is determined by the direction of the bias field compared to the direction of current current flow within the loop. The resulting sigmoid will be be reverse-S-shaped (Fig. D.4 (c)) or S-shaped (Fig. D.4 (c)) depending on whether the bias field is parallel or anti-parallel with the current.

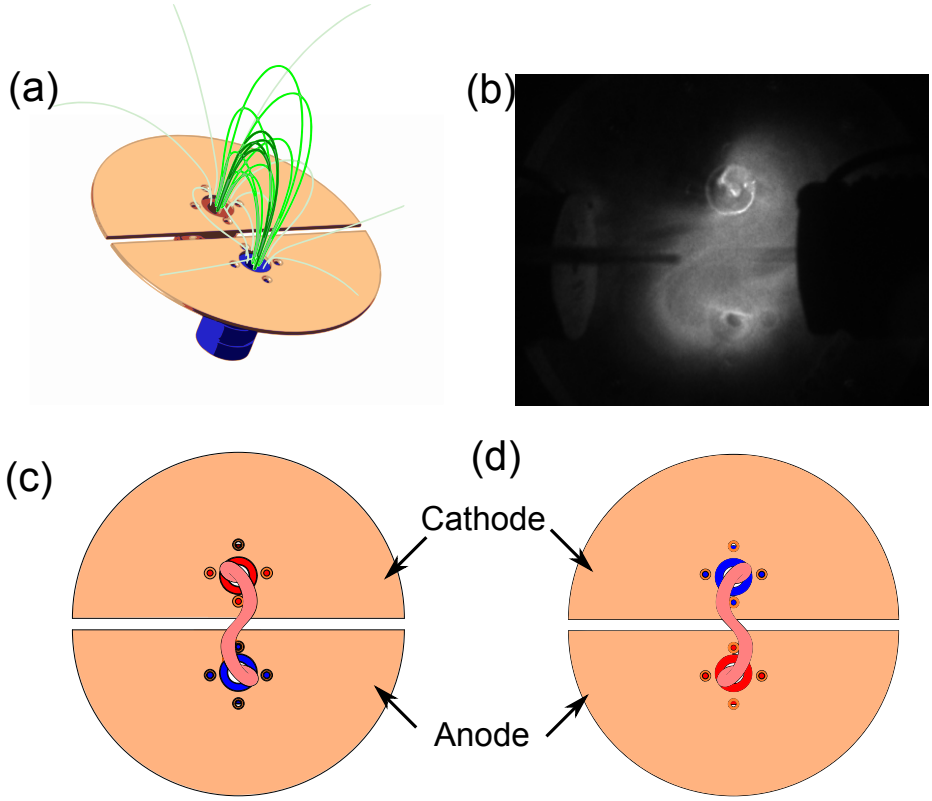

Figure D.4: (a) Simulation of horse-shoe shaped field-lines generated by the red and blue bias coils. Darker color lines represent field line that are closer to the axis of the coils. (b) Cooke camera image of left-handed (reverse-S) sigmoid. The current flows from bottom foot-point to top foot-point and is anti-parallel to the bias field. (c) The bias field goes from the top (red) coil to the bottom (blue) coil, creating a reverse S sigmoid. (d) The bias field goes from the bottom (red) to the top coil (blue) creating a right-handed sigmoid (S shape).

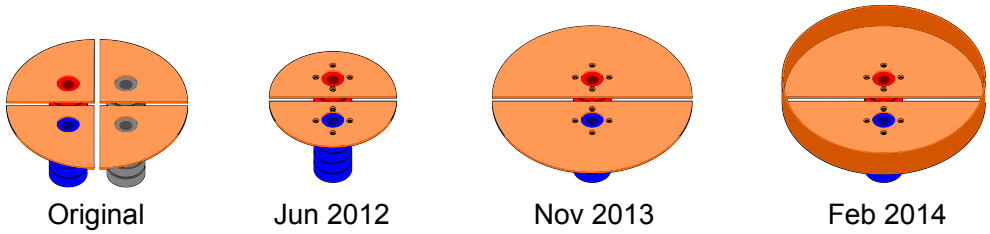

Figure D.5: Evolution of the electrodes over the thesis work. The blue and red parts represent the polarity of the bias coils used to construct horse-shoe-shaped magnetic fields.

D.3.2 Gas injection

The experiment is designed with flexible gas delivery system. This permits the creation of plasmas of different gas species: Hydrogen, Helium, Nitrogen, and Argon. This thesis focuses on Hydrogen plasmas since their lower mass allows the plasma to quickly respond to changing magnetic forces.

Fast gas valves separate the high pressure (60-100 psi) gas lines from the vacuum chamber. These gas valves are normally kept closed by springs held under compression. Milliseconds before the plasma breakdown, a capacitor bank sends a current pulse into the coil producing image currents that pushes the valve open. Gas enters the chamber at roughly the sound speed and the amount of gas entering the chamber scales linearly with the applied voltage over the operating parameter. Spectroscopic measurements by Perkins ([98], p.88) report an electron density of $n_e = (6.5 \pm 1.0) \times 10^{20}$ m^{-3} at 500V and $n_e = (12.2 \pm 2.3) \times 10^{20}$ m^{-3} at 550 V. For a majority of the thesis, the capacitor bank powering the gas valve is held at 525 V corresponding to $\sim 10^{21}$ particles.

D.3.3 Copper electrodes

Four copper electrode designs were used in this thesis and Fig. D.5 shows the different designs over time. Electrodes play an important role in setting the plasma boundary conditions; early designs did not include electrodes so the plasma arced to the vacuum chamber. The original quad gun contains four quadrants and could produce two plasma loops simultaneously. When creating a single loop, the location of the plasma

is asymmetric with respect to the strapping field coils. Experiments began using a smaller, symmetric electrode design in June 2012. The electrode size was increased in Nov. 2013. Larger electrodes impose boundary conditions over a larger portion of the vacuum chamber and help with shot-to-shot reproducibility. A copper skirt was added to the edges of the large electrodes in Feb. 2014 to further reduce plasma arcing.

D.3.4 High Voltage Main Bank

A 59 μF capacitor in the main bank supplies the necessary high voltage across the electrodes to break down the neutral gas. Minutes before breakdown, an Ultravolt 10 kV power supply begins charging the capacitor to a user-specified voltage (typically 2.5 kV - 6 kV). When the capacitor reaches the specified voltage, the bank disconnects the capacitor power supply, sends out a "Ready" signal, and waits for instructions. When asked to "fire", the bank toggles a krytron switch which activates the ignitron switch. The ignitron connects the high voltage capacitor to the electrode driving 30 kA - 70 kA after breakdown.

D.3.5 Paschen breakdown

The transition from neutral gas to plasma follows the Paschen breakdown criterion. The Paschen mechanism describes electrons accelerated by the electric field from high voltage applied across the electrodes. Accelerated electron are expected to collide with neutral atoms, potentially liberating additional electrons. If there is enough energy in the accelerated electron and liberated electron, this process leads to a breakdown chain reaction. This type of breakdown strongly depends on the presence of sufficient gas particles and sufficient space over which the avalanche process can develop. This results in a dependence on the parameter pd, where p is the gas pressure and d is the distance over which significant breakdown takes place.

The full relationship is known as the Paschen breakdown law and is described by

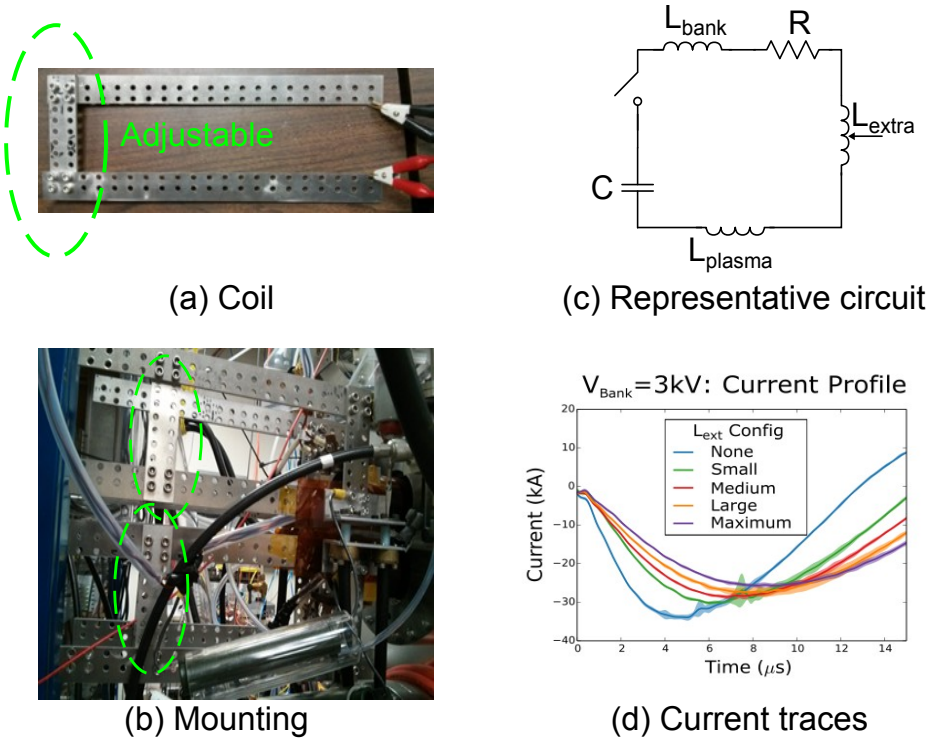

Figure D.6: (a) Simple construction of the coil. (b) Picture demonstrating how the coil is mounted on the plasma gun. The coils in the image are adjusted to be in the "Large" configuration. (c) Representation of the plasma discharge circuitry. The system capacitance and resistance are C and R, respectively. The total system inductance can be changed by adding an adjustable L_{extra}. (d) The current profile for different coil configurations when the plasma bank is charge to 3 kV.

the equation

$$V_B = \frac{Apd}{\ln(pd) + B}$$

where V is the breakdown voltage, p is the pressure, and d is the gap distance. A and B are constants which vary depending on the gas used.

D.4 Variable inductor

A variable coil (L_{extra} in Fig. D.1) can be added to plasma circuitry to modify the inductance of the system as shown in Fig. D.6 (a). The coil is made using flat Aluminum plates held together by nuts and bolts. Holes are drilled at regular spacings along the plate, permitting easy adjustment of the inductance by adjusting

Config	L_{ext} (nH)	I_{peak} (kA)	t_{peak} (μs)
None	0	-33.9	4.8
Small	140	-30.2	6.1
Medium	210	-28.7	6.9
Large	290	-27.6	7.7
Max	370	-26	8.6

Table D.1: Measured value of the inductance

the coil connection points. Tabletop measurements using a LC meter show that the inductance scales linearly with the holes used to make the connection. Inductance measurement at four standard connection locations are summarized in Table D.1. The coils are mounted as shown in Fig. D.6 (b). The standard set-up uses two sets of coils placed in parallel with the plasma gun. Each set comprises two coils in series with the plasma gun so the equivalent inductance of the four coils is approximately that of a single coil. This approximation does not take into account coil-coil interactions and coil-chamber interactions but is expected to be accurate.

This additional inductance modifies the current trace by increasing the characteristic frequency of the corresponding RLC circuit as shown in Fig. D.6 (c). The under-damped solution to an RLC circuit is given by

$$i(t) = A\exp(-\alpha t)\sin(t\sqrt{\omega_0^2 + \alpha^2} + \delta) \tag{D.1}$$

where $\alpha = R/2L$ is the damping factor and $\omega_0 = 1/\sqrt{LC}$ is the natural frequency. Thus, an increase in L decreases the peak current and delays current peak by decreasing the damping factor and increasing the natural frequency, respectively. This is shown in Fig. D.6 (d).

D.4.1 Current source

Adding L_{extra} ensures that the experiment acts like a current source. Kumar et al. [104] performed efficiency analysis on the Caltech Spheromak Experiment. They found that the combined impedances of the ignitron switch and the cables dominate the impedance of the plasma, and concluded that the spheromak experiment

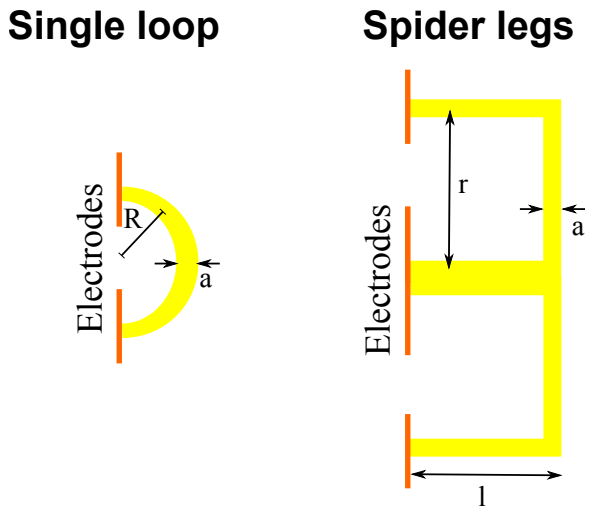

Figure D.7: Geometry of single plasma loop and Ref. [15] representation of eight spider legs.

circuit acts like a current source. While this assumption is valid for the spheromak experiment, it may not be a good assumption for the solar loop experiment.

The solar loop plasma inductance is likely larger than the spider-legs spheromak inductance. Kumar calculated the inductance by modeling the spheromak experiment current path as a co-axial cable. One way to compare the solar and spheromak inductance is to note that the spheromak experiment creates eight currying-carrying plasma loops in parallel (spider legs). This approximation estimates that the solar loop inductance may be up to eight times the spheromak inductance.

Consider the geometry shown in Fig. D.7. Suppose $R = 4$ cm and $a = 1$ cm, the inductance of the loop (Eq. 2.2) gives ≈ 80 nH. This can be estimated as 40 nH for a half circle or as 80 nH if image currents "complete" the circle. The inductance of the spider legs configuration [15] is

$$L = \frac{\mu_0 l}{2\pi} \ln\left(\frac{r}{a}\right) \tag{D.2}$$

which is like the inductance of a coaxial cable. Applying Eq. D.2 to spider legs with $r = 4$ cm, $l = 4$ cm, and $a = 1$ cm gives ≈ 10 nH of inductance, which is four to eight times smaller than the single loop inductance. Ref. [104] estimates the total series inductance in the discharge circuit (215 nH) is much greater than the plasma

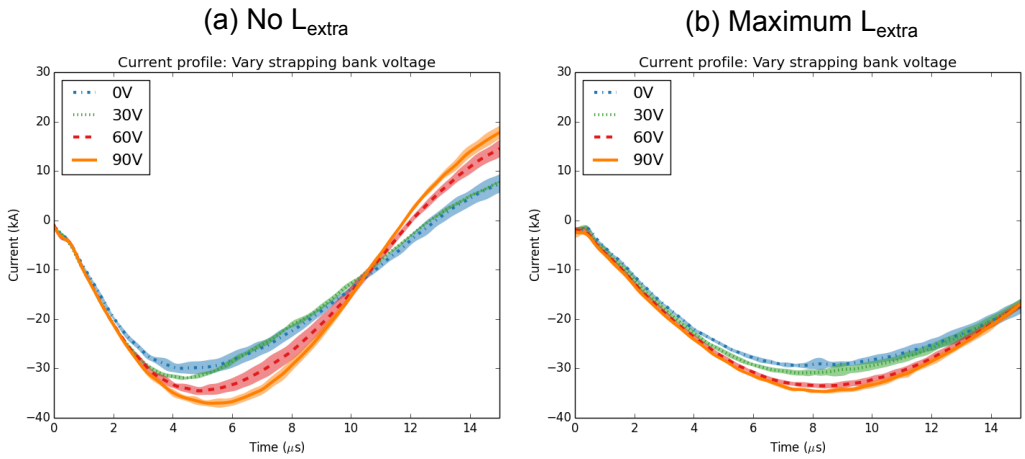

Figure D.8: (a) Variation in the current profile for different strapping fields when $L_{extra} = 0$ nH. (b) when $L_{extra} = 370$ nH. Shaded region represents shot-to-shot variations.

inductance (30-50 nH) and concludes that the system acts like a current source. This assumption breaks down if single loop plasmas are four to eight times the inductance of the spider legs plasmas.

Kumar et al. [104] note that the ignitron inductance changes as a function of current. They report $L_{ignitron} \approx 50$ nH, 170 nH, and 800 nH at ~ 80 kA, ~ 10 kA, and ignitron turn-off, respectively. When calculating the total discharged circuit inductance (typically 215 nH), ignitron inductance (typically 170 nH) dominates other components inductance. Since the ignitron inductance is highly dependent on current, the system inductance may also be highly variable.

The addition of L_{extra} to the intrinsic system inductance ($L_{intrinsic}$ in Fig. D.1) ensures that the total inductance of the discharge circuit is much greater than the single plasma loop inductance. This ensures that the plasma boundary conditions can be considered a current source. Figure D.8 shows variations in the current profile as a function of the strapping bank voltage. A higher strapping bank voltage means a stronger strapping field, resulting in a smaller plasma with lower inductance. Lower plasma inductance correspond to higher peak current. The relative change in peak current for different strapping configurations is much larger when $L_{extra} = 0$ nH (Fig. D.8 (a)) than when $L_{extra} = 370$ nH (Fig. D.8 (b)). The shaded regions around the

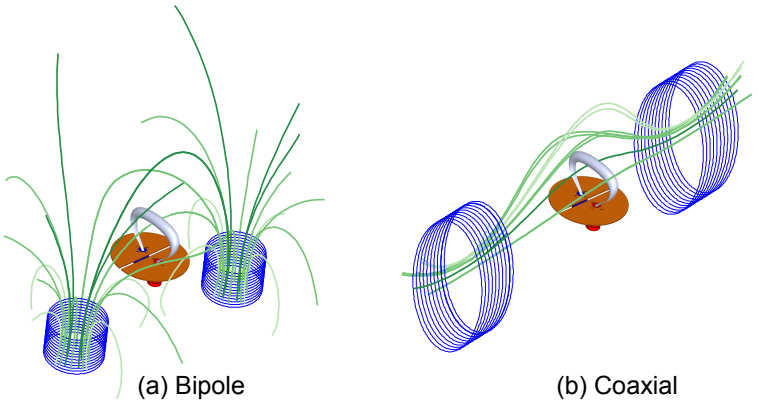

Figure D.9: Strapping field lines (green) produced by (blue) coils (a) in bipole configuration (b) in coaxial configuration.

current traces represent shot-to-shot variations for a given configuration.

D.5 Strapping field assembly

A strapping field[1] is an external magnetic field perpendicular to the plane of the current loop with polarity so that the $\mathbf{J} \times \mathbf{B}$ force resists plasma loop expansion. There are two common configurations which can generate this strapping field: a bipole (Fig. D.9 (a)) and a coaxial type configuration configuration (Fig. D.9 (b)). Both configurations place two coils on the opposite side of the plasma loop. The bipole configuration places two coils with opposite magnetic polarities on a parallel plane to the electrode. A coaxial configuration places two coils with the same magnetic polarity on a parallel plane to the plasma.

D.5.1 Strapping bank

The power source for a strapping field is a 0.77 μF capacitor bank containing hundreds of electrolytic capacitors electrically in parallel. A 2000 Watts Kaiser XLS202 charges the capacitor to the desired voltage. The capacitors are designed operate up to 450 V, corresponding to 78 kJ of energy[2]. Energy is safely dissipated through two high

[1] In the tokamak literature, this field is called a vertical field.
[2] A rifle bullet has about 2 kJ of energy.

Name	N	ID (in)	OD (in)	Length (in)	L	R (mΩ)
"Encore coils"	33	12	15.5	1.625	500 μH	26.5
"Welding cable coils"	13	8	12	3	60 μH	small
"Custom coils"	11	3.5in	3.5in	4.3	6.5 μH	small

Table D.2: Parameters of strapping coils used

power resistors found above the bank by pressing the "Emergency Stop" button. The bank uses an Silicon-Controlled Rectifier (SCR) for triggering and has a protective diode protect the capacitors from large negative voltage swings. Dave Felt designed a custom triggering control circuit to integrate the strapping bank with the electronic timing of the plasma experiment. The control system permits both local and remote operation. Normal operation of the bank is as follows:

1. Toggle the breaker, and press "On."
2. Set the desired strapping voltage and hit "Start."
3. When the system reaches the desired voltage, it sends an optical "Ready" signal and waits for an incoming optical "fire" trigger.
4. The strapping bank isolates the power supply when it detects an incoming "fire" signal and then activates the SCR to discharge the capacitors to the attached load.
5. After discharge, the bank waits a few seconds before reconnecting the power supply.
6. The user can repeat the process or hit "Emergency Off," followed by toggling the breaker to turn off the strapping bank.

D.5.2 Strapping coils

The primary role of the strapping coils is to create the strapping field, which can reproduce the slow-rise to fast-acceleration of laboratory plasmas. Initially, the strapping

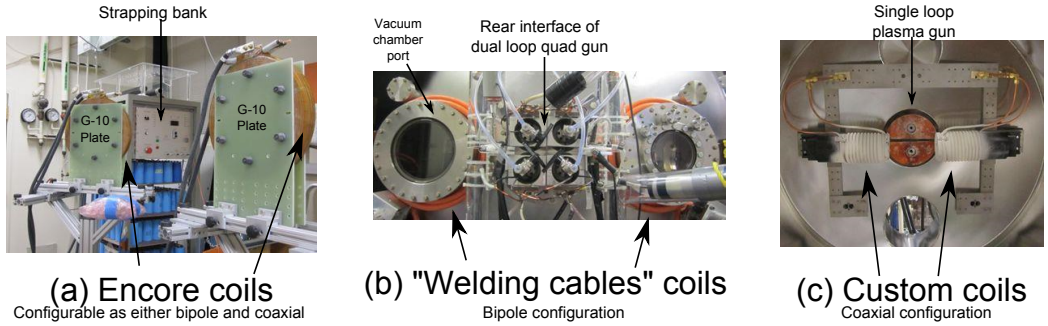

Figure D.10: Overview of different coil configurations. (a) and (b) are outside the vacuum chamber, behind the plasma gun. (c) is inside the vacuum chamber in front of the plasma gun.

coils were large commercial coils placed outside of the vacuum chamber. These "Encore coils" were original used to generate steady-state magnetic field for the Encore tokamak experiment [132]. The coils are sandwiched between two G-10 plates (Fig. D.10 (a)) and mounted on adjustable stands. The stands are adjustable to mm precision along the x and z axes and to cm precision along the y axis. The stands can also be rotated so that the coils can be in co-axial configuration, bipole configuration, or some in-between configuration.

While this approach is optimized for flexibility in strapping coils placement, it was not successful for the following reasons:

1. magnetic forces threatened to knock over the support structure if too much current were pulsed through the coils;

2. the coils were far from the plasma due to spacing limitations;

3. the large coils produce fields which did not decay sharply over the length scale of the plasma.

The first problem limits the amount of current that could be pulsed through the Encore coils, resulting in weaker strapping field. This weaker strapping field was unable to significantly influence plasma dynamics, since the coils are located outside the vacuum chamber, far from the electrode.

One method of strengthening the coil support is to wind welding cables around the port of the vacuum chamber. This approach fixes the location of the strapping

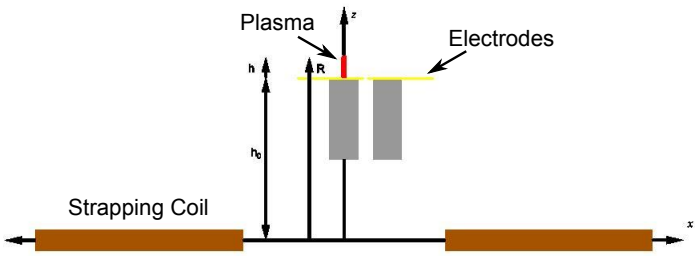

Figure D.11: Welding cable coils are large and placed a distance h_0 behind the plane of the electrodes.

coils but allows much more current to flow through the coils. "Welding cable coils" are first made from six turns of thick (4/0) welding cables around the chamber port. These coils permit high current, but cable straps between the strapping bank and the coils fail when 26 kA is pulsed into the coils; these straps keep the cables from whipping about due to magnetic forces. The strong magnetic forces broke the straps and ejected an unknown projectile at high speeds[3].

Smaller (1/0) orange welding cables replaced the (4/0) welding cables. These smaller coils (Fig. D.10 (b)) could be wrapped 13 times around the port. Since inductance scales as the number of turns squared, the quadrupled inductance leads to manageable current flow while still providing strong enough magnetic fields to influence the plasma.

Unfortunately, there is a fundamental limitations to using large coils placed outside the vacuum chamber. Large coils produced strapping fields with large decay length. The decay index of an axisymmetric field is given by

$$n = -\frac{R}{B}\frac{dB}{dR} \tag{D.3}$$

where R is the distance from an axis. Even though the bipole configuration is not axisymmetric, Eq. D.3 can be calculated along the z-axis of Fig. D.11. The coils are some distance h_0 behind the electrodes and we define $h = R - h_0$ to be the height of

[3]This projectile is observed flying away from the strapping bank, but its trajectory was obscured at later times. Even though visual confirmation was obstructed, a sound was heard when the projectile collided with an unknown object. This projectile has not been found.

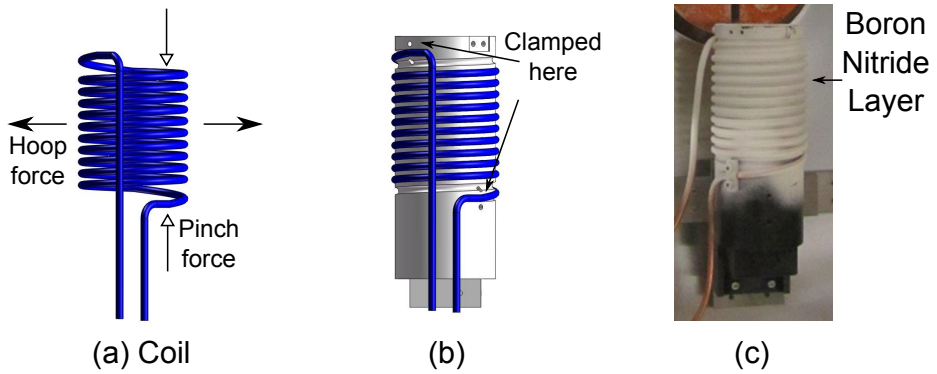

Figure D.12: (a) Magnetic forces on coil when pulsed with current. (b) Coil mounted on Delrin support structure. (c) Photo of coil.

the plasma from the electrodes. The plasma experiences a effective decay index given by

$$n_{eff} = -\frac{h}{B}\frac{dB}{dh} = \frac{h}{R}n. \tag{D.4}$$

Equation D.4 shows that large coils placed outside the vacuum chamber produce fields that look uniform from the perspective of the plasma.

Smaller coils inside the vacuum chamber are necessary to produce strapping fields which have sharp gradients and are strong enough to influence the plasma. There is no convective cooling inside the vacuum chamber so heating is a potential issue. In order to accommodate water or air cooling, 1/4 in copper tubing was chosen as the base-material for the coil. A custom mounting structure is required because currents pulsed through the coil introduce powerful magnetic forces. The hoop force pushes the coil outwards while the pinch force squishes the coil (Fig. D.12 (a)). A professionally machined Delrin form factor is used to wind the coils and clamps placed at the coil ends hold everything together. The coils will be near the plasma so an insulating Boron Nitride layer was added to help prevent electric arcing to the coils.

The current generated by the strapping set-up is on the order of kAs and low tens of kAs depending on the coil used. The custom-coil currents at different strapping bank voltages are measured by a Rogowski coil. The linear fit corresponds to

$$I_{coil} = 80 \times V_{strap} - 136$$

Hall sensor measurements at different strapping bank voltages show that

$$B_{x,peak} = \frac{125\ G}{15\ V} V_{strap}$$

where $B_{x,peak}$ is the peak B_x field along the chamber axis.

D.5.3 Mounting assembly

The magnetic pressure scales with the square of the magnetic field and the pressure from a 1 Tesla field is about 4 times atmospheric pressure. Strong support structures are required to stabilize the coil from magnetic forces. The first support structure was designed from heavy-duty 80/20 Inc parts (Fig. D.13 (a)). The structure is designed to not have closed conductive loops so the base is not square and the perpendicular bars on the top are separated by plastic. The Encore coil is sandwiched between two Garolite (G-10) plates (Fig. D.13 (b)) held together by fiberglass bolts. The G-10 plates are attached to linear slides through regularly spaced holes (Fig. D.13 (c)). permitting discrete adjustments of the coil position. This structure provides maximum flexibility for coil positioning but it is not strong enough for the magnetic forces involved. When pulsed with current, the Encore coils attracted/repel each other in co-axial and bipole configurations, respectively. This limited the current that can be pulsed through the coil which acted as a ceiling on possible magnetic field strengths.

The main challenge for mounting the custom coil inside the vacuum chamber is the vacuum-air interface. We use MDC electric feedthroughs designed for high power (Fig. D.13 (d)) to send current from the strapping bank to the strapping coils. The feedthroughs are 1/4 in copper tubing, which permits cooling fluid to be pushed through the coil tubing if necessary. Experimental tests showed that the coil did not heat significantly, so no cooling was necessary. Nevertheless, the support structure is there should future experiments require cooling the strapping coils.

The strapping coils are placed on adjustable carriages (Fig. D.13 (e)) which are attached to a steel support structure. The steel has holes drilled at periodic locations,

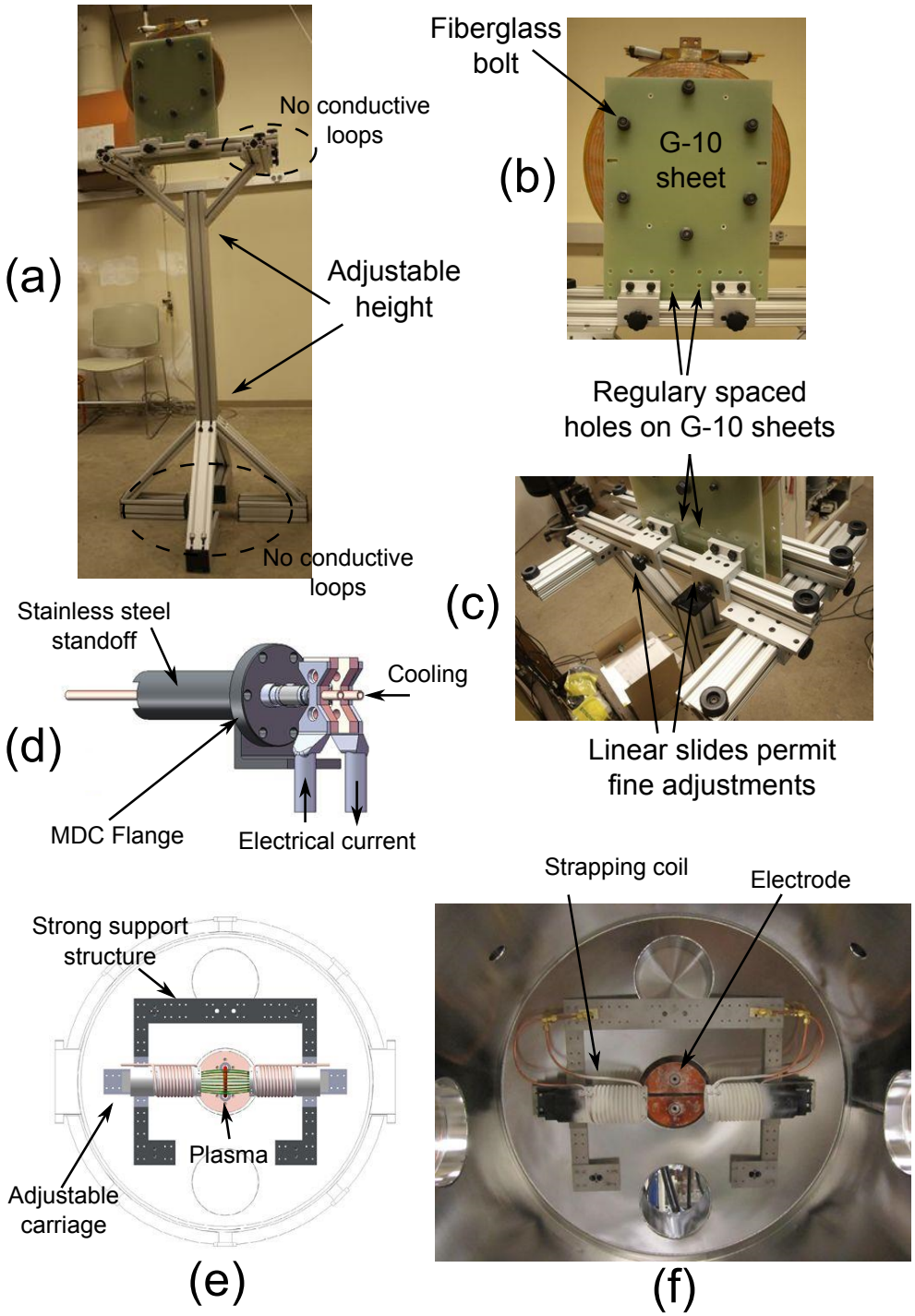

Figure D.13: (a) Custom support structure for Encore coils. The structure is designed to not have closed conductive loops. (b) Two G-10 sheets sandwich the coils. Regularly spaced holes on the sheet allow discrete displacement. (c) Linear slides permit fine adjustments of coil position. (d) MDC flange with two 1/4" copper tubing for current input and output. The tubing is hollow and the system designed so that a cooling medium be injected into the pipes. (e) Schematic view of plasma coil support structure. Adjustable carriages can be mounted to different holes on the support structure allowing flexible placement of the coils. (f) End-view photo of strapping coils set-up.

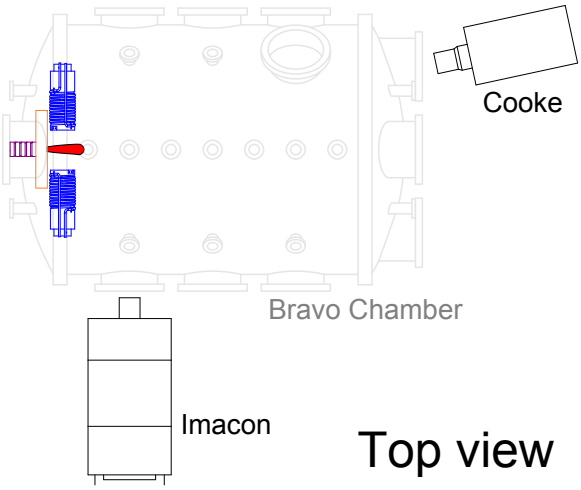

Figure D.14: Typical position of Imacon and Cooke cameras viewed from above the experiment. The plasma, strapping coils, electrodes, and bias coils are shown in red, blue, orange, and purple, respectively.

permitting flexible placement of the carriage. Once placed, the carriages are held down by metal bolts. The support structure connected to four points corresponding the 2.75" ports on the chamber. These ports have MDC flanges with custom stainless steel standoffs (Fig. D.13 (d)) and are attached to the support structure by screws, threaded rods, and coupling nuts. This set-up provides the rigid support structure to resist strong magnetic forces but also the flexibility to adjust the coil placement.

D.6 Diagnostics

The work in this thesis will rely on three techniques: imaging diagnostics, magnetic diagnostics, and circuit analysis. Each technique has its own strengths and weaknesses, but together they construct a robust picture of the plasma dynamics.

D.6.1 Imaging

Ultra-high speed cameras image the plasma as it evolves. Two cameras were used for the majority of the thesis work: the Imacon200, and the Cooke camera.

The Imacon200 is an Intensified CCD movie camera which uses a pyramid shaped beam-splitter to split incoming light into eight micro-channel plate image intensifiers.

Each channel has separate high speed electronics, permitting independent capture of 10-bit, 1200 x 980 pixels images. Each channel is also capable of taking two frames per shot by using an interline transfer architecture[4]. In practice, the interline transfer process requires about 2 μs to complete. Triggering before completion results in ghosting and reverse-ghosting effects. Additionally, one of the eight channels has malfunctioned and so Imacon movies are limited to 14 frames. The Cooke camera is a single channel ICCD camera with greater dynamic range (12 bit) and (1280 x 1024) resolution, but is limited to a single frame per experimental run. The primary role of the Cooke is to provide another view of the plasma to resolve projection effects.

The cameras are typically placed around Bravo chamber as shown in Fig. D.14. The Imacon looks through the first port and is either angled to look at the plasma gun or oriented to be perpendicular to the plane of the plasma expansion. The perpendicular view is normally used to study evolving dynamics of the plasma apex. Images provide invaluable information about the global position and velocity of the plasma. The camera can capture the timing and location of important events like plasma detachment, plasma kink instability, and localized brightening. By placing spectroscopic filters in front of the camera, it is possible to isolate the dynamics of different species of gasses when more than one gas species is present [108].

Camera images can be misleading because they do not show the full picture. Perkins measured significant plasma activity occurring in the UV and X-ray regime [98]. Furthermore, the current and voltage trace remain smooth and oscillating even when camera images show diffuse or no plasma activity. Stenson suggests [17] that the magnetic structure may be much larger than the bright emission structure. Overall, images are amenable to quantitative analysis but require careful calibration (see Sec. G.1).

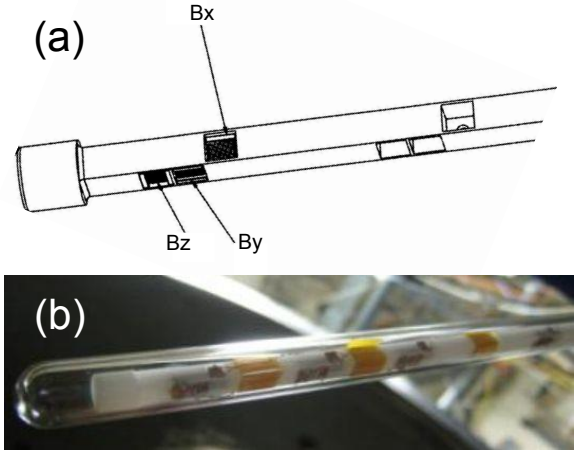

Figure D.15: (Adapted from Refs. [16] and [17]) (a) Commercial inductors placed are placed in retention fixture allow high spatial resolution. (b) Image of solar magnetic probe.

D.6.2 Magnetic probe array

The most common magnetic diagnostic technique is the use of a "B-dot" probe. When the magnetic flux Φ through an N-turns coil changes, a voltage ξ is induced in the coil according to Faraday's law

$$\xi = -N\frac{d}{dt}\int_S \mathbf{B}\cdot d\mathbf{A} \tag{D.5}$$

where S is the surface encompassed by a single turn, and $\mathbf{B}$ is the magnetic field passing through the surface S. If $\mathbf{B}$ is sufficiently uniform over the surface S so that the magnetic field may be approximated as constant, the Eq. D.5 reduces to

$$\xi = -NA\frac{dB_\perp}{dt}$$

so $B_\perp$ can be determined by integrating the voltage output the coil.

In order to obtain 3-D magnetic field measurements, three coils are placed per-

[4]This technique opens every other photo-sites during the first frame. After the shutter is closed, the charge is transferred to adjacent closed photo-sites. This transfer occurs quickly due to the proximity of the open and closed sites.

pendicular to each other to form a cluster. The coils in a cluster need to be small and close together to obtain high spatial resolution. Unfortunately, small coils are difficult to hand-wind, thin wires notoriously fragile, and tiny support structures difficult to make. Romero-Talamas et al. [16] proposed a design that replaced hand-wound coils with commercial chip inductors and placed these inductors inside a plastic retention fixture with machined cut-outs (Fig. D.15 (a)). Shreekrishna Tripathi built the magnetic probe array shown in Fig. D.15 (b)) based on the Romero-Talamas design. The array comprises twelve channels corresponding four three-axis clusters. The four clusters are placed at 17.5 cm, 19.5 cm, 21.5 cm, and 25.5 cm in front of the electrode along the chamber axis.

The probe provide in situ measurement of the plasma's magnetic field as it expands into the chamber. In addition, the position of the probe is fixed and is used to provide precise localized measurements of plasma behavior. The known separation of the probe clusters and their placement allows measurement of the plasma's instantaneous velocity at the probe. Features in the magnetic trace can also be used to precisely time arrival of the plasma. These magnetic diagnostic techniques are discussed in more detail in Sec. G.2.

D.6.3 Hall sensors

Semi-conductors sensors employing the Hall effect can also be used to measure the magnetic field. A full description can be found in Sec. E.

D.6.4 Voltage measurements

Voltage measurements were taken by two different voltage probes: a Tektronix P6015 high voltage probe, and a solar-cell-powered isolated voltage probe [137]. Both probes are electrically isolated from the data-acquisition digitizers by an optic-link[5]. The P6015 is connected to an Analog Module 732T/R optic link designed to work in steady-state whereas the isolated voltage probe has a diode-photodiode pair which

[5]Electrical signals are converted to optical signals which are transmitted over a length of fiber optics before being converted back into electrical signal

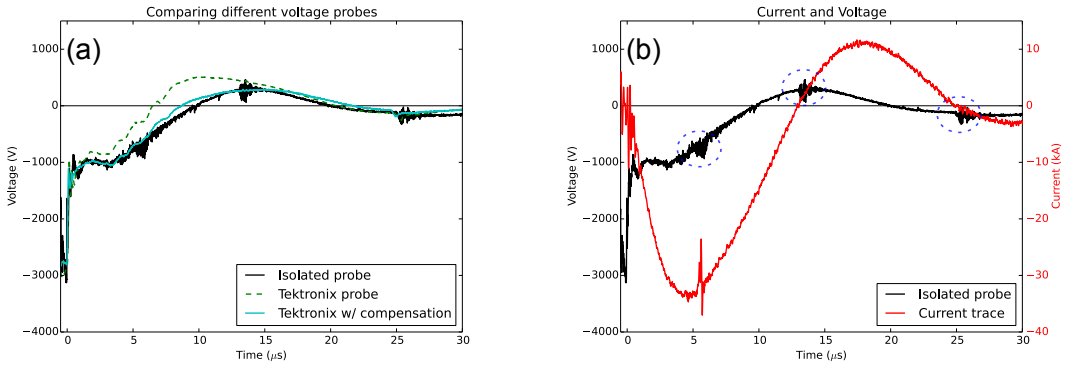

Figure D.16: (a) A comparison of the signals measured by the isolated high voltage probe and the Tektronix high voltage probe. Each signal represents average of about 10 shots. (b) Comparing voltage and current trace. The voltage probe indicates bursts of noise (dashed blue circles) when the current trace flips polarity and or has a disruptive spike..

operates only for a few ms during plasma experiments. Both probes give similar traces when properly calibrated.

The P6015 High-Voltage Probe has a 1000-to-1 attenuation factor and can measure frequencies from DC to 75 MHz. It is designed to be attached to an oscilloscope with input resistance of 1 MΩ and parallel capacitance of 12 pF to 60 pF. The built-in compensation allows fine adjustments for impedance matching. This matching prevents distortions such as the rounding of corners due to poor high frequencies transmission or the drooping of square wave plateaus due to poor low frequency transmissions. Unfortunately, the Analog Module optic link has characteristic impedance of 33 kΩ, which results in signal distortion when directly attached to the P6015 probe. Perkins [98] added a 50 kΩ resistor in series with the 33 kΩ Analog Module transmitter and found that the voltage distortions changed. He guessed that the impedance mismatch introduced unwanted integration of the input signal and corrected this distortion by adding a 7 pF capacitor[6] in parallel to the 50 kΩ resistor.

Figure D.16 (a) shows a comparison between the Tektronix probe[7] and the isolated magnetic probe. Each probe trace represents an averaging of about ten identical

[6]Determined by trial-and-error.

[7]The grounding clip is attached for these shots. There are also differences due to not using the grounding clip.

shots. The isolated probe (cyan) and the Tektronics probe (dashed line) were measured simultaneously and the qualitative difference between the two is visible. The Tektronix probe has signs of drooping (i.e. poor low frequency transmission) and earlier zero-crossing with dramatic rise to positive voltage when compared to the isolated probe. When compensation is added to the Tektronix probe, the signal (red) *quantitatively* matches the isolated probe signal at early times with minor variations at later times. The shots for the isolated probe and uncompensated Tektronix probe (Shot: 1928-1928) were taken on the same day at 3 kV, whereas the shots for the Tektronix probe with compensation (Shots: 1969-1977) were taken a month later and scaled from 2.67 kV. Taking into account the difference in experimental date and main bank voltage, the quantitative match (after rescaling) is remarkable and suggests that the most reliable measurements voltage are from the isolated probe and the Tektronix probe with compensation. A comparison of the Tektronix probe with compensation and the isolated voltage probe for the same shots yields an even better match.

All three probes show activity when the current switches polarity at around 25 μs. The isolated high voltage probe also shows an enhancement of noise (circled in Fig. D.16 (b)) when the current trace flips polarity at around 13 μs and when there is a spike in the current trace at 6 μs. When used properly, it is reasonable to trust the measurement of the isolated voltage probe. A common configuration in this thesis is to have the high voltage probe measuring the voltage across the plasma while using the Tektronix probe to measure voltage across the plasma and the adjustable inductor (L_{ext} in Fig. D.6 (c)).

D.6.5 Current Measurements

A Rogowski coil is a device commonly used to measure AC current. It is usually constructed by helical windings of wires about a flexible length of plastic tubing. The tubing is then bent into a hoop shape and the wire is returned through the center of the coil so that both terminals are now at the same end of the hoop (Fig. D.17).

For a Rogowski coil with N turns, major radius b, and minor radius a, the voltage

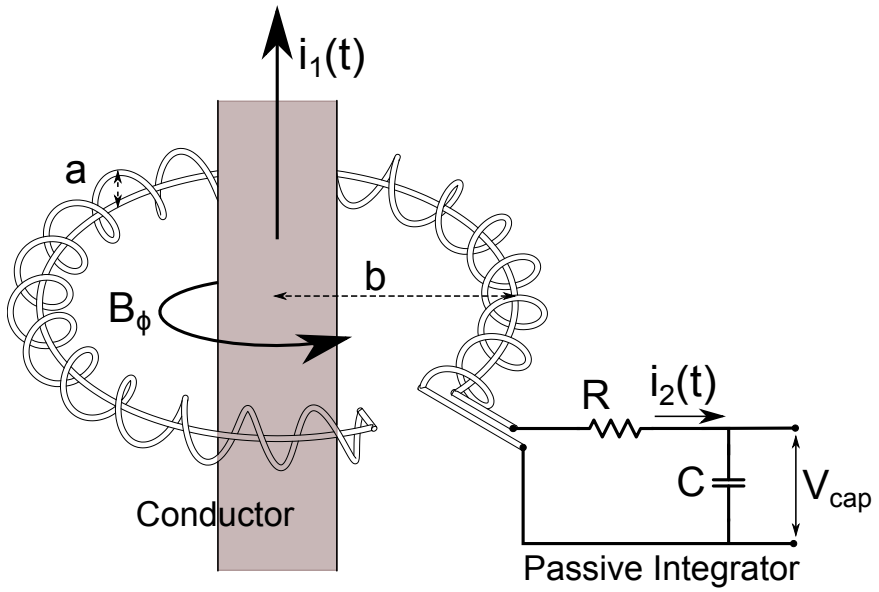

Figure D.17: Rogowski coil with a built in passive integrator. This particular configuration is effective at measuring current at high frequencies where $i_2 R \gg V_{cap}$ but not so high so that $i_2 R \gg L di_2/dt$, where L is the inductance of the Rogowski coil.

follows Faraday's law

$$\xi_{Rogowski} = -\frac{\partial \Phi}{\partial t} = -A\frac{\partial B}{\partial t} = -AN\frac{\mu_0}{2\pi b}\frac{\partial i_1(t)}{\partial t}$$

where $A = \pi a^2$ is the pick-up area of the Rogowski coil and $i_1(t)$ is the current within the central conductor.

Rogowski coils are considered "air-core" devices since the wire is not wound about a metal form. Thus, the coil is not prone to saturation and has a linear response over a wide range of currents. The Rogowski coil does not electrically perturb the circuit since the coil is not in electrical contact center conductor. While the current carrying conductor is in the center of the Rogowski coil in Fig. D.17, the voltage produced is independent of the conductor position within the coil for frequencies below 1MHz [138]. For $f > 1$ MHz, the Rogowski coil introduces a non-negligible inductance into the relevant circuit equation.

The circuit equation which describes a Rogowski coil of self-inductance L con-

nected to a passive integrator (Fig. D.17) is described by

$$\xi_{Rogowski} + L\frac{di_2(t)}{dt} + i_2(t)R + \frac{\int^t i_2(t')dt'}{C} = 0 \tag{D.6}$$

where R and C are the resistor and capacitor of the integrator, respectively [139]. If the inductive drop across the coil is small ($L(di_2(t)/dt) \ll i_2R$) and the voltage drop across the capacitor is also small ($\int^t i_2(t')dt'/C \ll i_2R$) then the current flowing through the capacitor ($i_2(t)$) is given by

$$i_2(t) = -\frac{\xi_{Rogowski}}{R} = -AN\frac{\mu_0}{2\pi Rb}\frac{\partial i_1(t)}{\partial t}$$

so the voltage across the capacitor is then

$$V_{cap}(t) = \frac{\int^t i_2(t')dt'}{C} = \frac{N}{RC}\frac{a^2\mu_0}{2b}i_1(t)$$

which is directly proportional to the current flowing through the wire: $i_1(t)$.

Appendix E

Hall magnetic sensing

E.1 Introduction

The measurement of magnetic fields is critical to the study of plasma behavior. Unlike many astrophysical plasmas, laboratory plasmas are directly accessible to diagnostics. The most common measurement techniques use magnetic pickup (B-dot) probes and Hall sensors [140], where the choice between B-dot probes and Hall sensors boils down to the timescale of the target. Caltech spheromak experiments use B-dot probes to measure plasma dynamics on the microsecond time scale [16]. In contrast, Pegasus Toroidal Experiment [141] and TEXTOR [142] use arrays of hall sensors to measure magnetic fields with time scales of tens-of-milliseconds. Other experiments [143] combine hall sensors and B-dot probes for magnetic measurements at both short and long time scales.

Magnetic fields are spatially dependent vector quantities. A flexible mounting mechanism, capable of volumetric measurements, is necessary to completely describe the magnetic field. There has been significant progress in volumetric measurements using B-dot probes. The Magnetic Reconnection Experiment (MRX) rotates a rake-shaped B-dot probe array to obtain volumetric measurements [130]. The Large Plasma Device (LAPD) uses motorized actuators [144] to precisely place magnetic probes at target locations. LAPD creates highly reproducible plasmas, and obtains volumetric measurements by adjusting probe placement over many repetitions. In contrast, there is significantly less progress for volumetric measurement using Hall

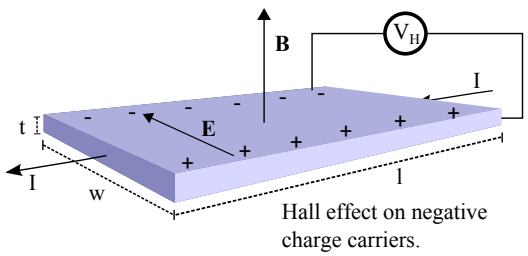

Figure E.1: Hall effect when the magnetic field is perpendicular to the sensor.

sensors.

Harding et al. [145] report one of the earliest attempts to measure the 3-D magnetic field with Hall sensors. The authors place three small InSb Hall plates, mounted perpendicular to one another, to measure 3-D magnetic field in a liquid Helium-filled space. This approach measures magnetic field at a single location, and has limited spatial resolution due to the size of the Hall plates. Bongard et al. [141] and Jeong-hun et al. [143] use an array of Hall sensors to measure a single magnetic field component along one axis. Duran et al. [142] mount nine sensors on three perpendicular planes, to obtain 3-D magnetic measurements along one axis.

These single axis measurements systems can characterize highly-symmetrical magnetic field configurations, but they are insufficient for experimental set-ups that lack symmetry. Caltech solar-relevant plasma experiments have complicated asymmetric magnetic fields [82]. In particular, the iron-core bias coils behave non-linearly for high current flows, making the magnetic fields difficult to model. The bias fields produced by the coils must also diffuse through copper electrodes at some locations. The diffusion introduces a delay between the timing of the magnetic field inside the vacuum chamber, and the timing of the current pulse used to create the magnetic field. Magnetic field lines diffusing through the copper electrodes peak later than magnetic field lines passing through regions without copper, creating magnetic field profiles with non-trivial spatial and temporal dependence.

E.2 Hall effect theory

Figure E.1 shows the basic principle of the Hall effect. A uniform magnetic field is applied to a current carrying plate. As charges flow through the plate, the Lorentz force deflects charge carriers to the edges of the plate where the charges build up. The build-up of charge creates an electric field which introduces an electric force that opposes the magnetic force. This charge build-up continues until electric and magnetic forces cancel each other out, and charges travel unperturbed through the plate.

Consider a constant current I flowing through a Hall sensor immersed in a constant magnetic field $\mathbf{B}$, as shown in Fig. E.1. The Lorentz equation relates electric and magnetic forces:

$$q\mathbf{E} = q\mathbf{v}_d \times \mathbf{B}$$

where $\mathbf{E} = V_H/w$; V_H is the Hall voltage, and w is the width of the current channel. The current, I, is given by $I = neAv_d$, where v_d is the drive velocity of the charged particles, e is the charge of the particle, n is the carrier number density, and A is the cross section area of the current flow ($A = Wt$ in Fig. E.1). The Hall voltage is given by

$$V_H = \frac{IB}{nqt} = K_{HOC} IB \sin\phi \tag{E.1}$$

where K_{HOC} is the open-circuit sensitivity constant, and ϕ is the angle between the sensor and the magnetic field. From Eq. E.1, $V_H \propto B$, so the magnetic field is directly measured. The inverse dependence between V_H and n means that conductors produce little Hall voltage. Practical Hall sensors were not common until advancements in semi-conductors. Table E.1 contains typical carrier concentrations.

It is also possible to apply a constant voltage V_{in} across the length l of the hall sensor. In this configuration, we define the charge mobility as $\mu = \mathbf{v}/\mathbf{E}$, where $\mathbf{v}$ is the velocity of the charger carrier and $\mathbf{E}$ is the applied electric field. A constant

Material	Carrier Concentration (cm^{-3})
Copper	8.4×10^{22}
Silicon	1.4×10^{10}
Germanium	2.1×10^{12}
Gallium-Arsenide	1.1×10^{7}

Table E.1: (Reproduced from from Table 1.1 of Ref. [18]) Intrinsic carrier concentration at $300^o K$

voltage V_{in}, applied across the length l, yields

$$E = \frac{V_{in}}{l} = \frac{v}{\mu} \implies v = \frac{\mu V_{in}}{l}. \tag{E.2}$$

Substituting Eq. E.2 into the Lorentz equation gives

$$q\frac{V_H}{w} = q\frac{\mu V_{in}}{l} B \sin\phi$$

so the Hall voltage is

$$V_H = \mu V_{in} \frac{w}{l} B \sin\phi.$$

The Hall voltage, in a constant voltage configuration, is proportional to B and charge mobility, and inversely proportional to the length of the device.

E.3 Design and construction

While often thought to only be useful at DC or very low frequencies, there is no frequency limit to the Hall effect [18]. The Hall effect is present at high frequencies, but its signal is overwhelmed by electrical interference associated with inductive pick-up. We use printed circuit boards (PCBs) to limit the inductive pick-up area in order to get a respectable noise-to-signal ratio at 50 kHz. The complete Hall sensor assembly (control circuit and the PCB footprints for Halls sensors) are printed on a single PCB. This design scales to multiple Hall sensor assemblies and the cost per assembly decreases with increasing number of assemblies. We construct a mounting system which maps the magnetic field within a desired volume. This mounting sys-

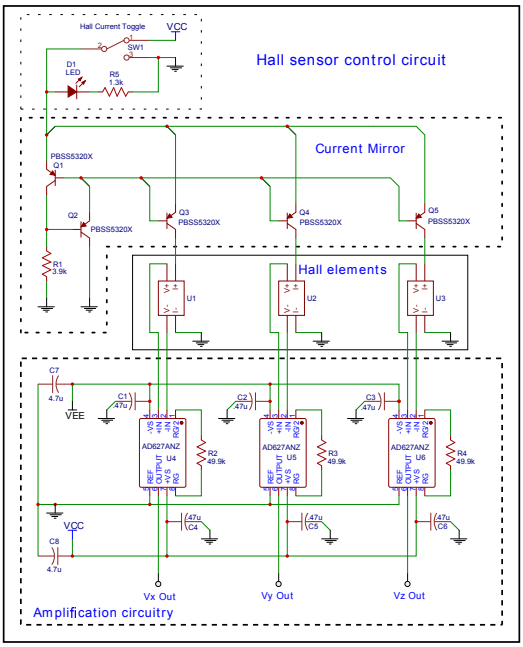

Figure E.2: The hall sensor control circuit has three parts: current mirror, hall elements, and amplification circuitry. A current mirror is used to provide the same amount of current to each hall element and the differential output is processed by the instrument amplifiers

tem accommodates multiple sensor assemblies for rapid volumetric measurement of the magnetic field.

E.3.1 Design

There are three sections in a typical Hall sensing assembly: the sensors, the power source, and the amplification circuitry. The complete circuitry for our assembly is shown in Figure E.2.

We use surface mount GaAs sensors[1] with 1.8-2.4 V/T sensitivity, and 2% linearity for magnetic fields between $0-3$ Teslas. In theory, one can operate Hall sensors with a constant voltage source, or a constant current source. For most applications, constant current mode is used to avoid additional circuitry for temperature dependence; V_H has $0.05\%/°C$ temperature dependence in constant current mode, and $0.3\%/°C$ in constant voltage mode [18]. The Caltech experiment generates significant electrical

[1] Chen Yang CYSJ106C

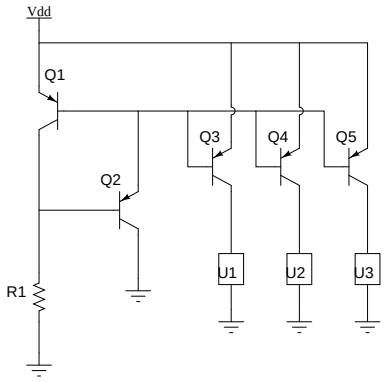

Figure E.3: The current passing through the transistor Q1 is theoretically mirrored through transistors Q3, Q4, and Q5. The amplitude of this current is determined by the value of V_{dd} and R1. Transistor Q2 prevents the circuit from saturating if one of the loads (U1, U2, U3) fail.

interference, so the data-acquisition elements are placed far from the vacuum chamber. We uses long cables to connect the Hall sensors to the digitizers. These long cables introduce parasitic capacitance and carry a voltage drop in a constant voltage configuration. In contrast, a constant current configuration provides the same current irrespective of cable length.

By using a constant current source, we keep the circuitry simple while avoiding issues of temperature dependence and voltage drops over long cables. We find that the sensor gain is unstable during the first few minutes of constant current operation. Sensor performance quickly stabilizes after the components have reached operating temperature, typically after 10 minutes.

A current mirror is provides the same current to three Hall sensors; each sensor measures a different magnetic field component. Figure E.3 shows the schematics of a current mirror [146]. The current passing through transistor $Q1$ is mirrored through transistors $Q3$, $Q4$, $Q5$. The current amplitude is

$$I \approx (V_{dd} - V_{BE})/R1$$

which is determined by the value of V_{dd} and $R1$, given sufficient Base-Emitter voltage (V_{BE}) across $Q1$.

We use the same model for all transistors on the control board, so V_{BE} and I are the comparable across all transistors. If one of the loads ($U1$, $U2$, or $U3$) were to malfunction (e.g., form an open circuit), the corresponding transistor (Q3, Q4, or Q5) robs current from $Q1$, thereby reducing current for other loads. Adding $Q2$ mitigates this problem [146]. Given a power supply with V_{dd}=15 V, SPICE simulations determine the optimal resistance value ($R1 = 3.9$ kΩ) to provide 5 mA to each Hall elements.

Hall elements output small differential signals riding on large DC common mode signals. Amplification circuitry is used to reject common mode and to enhance the Hall signal. The design of amplification circuitry involves trade-offs between differential gain, gain stability, input offset voltage, input bias current, common-mode rejection, bandwidth, and noise [18]. We use the monolithic AD627 instrument amplifier, which is considered optimized for Hall sensing [18]. This choice significantly simplifies our circuitry. The AD627 limits the bandwidth of the Hall sensor to about 45kHz when operating with a Gain of 9. The bandwidth restriction is not a problem since the magnetic frequencies of interest are below 1 kHz.

E.3.2 Construction

The entire circuitry shown in Fig. E.2 can be printed on a single PCB as shown in Fig. E.4. The control circuitry section and the PCB footpoints section of the hall sensors are separated. Hall sensors are placed on each respective footpoints (purple circle in Fig. E.4). The sensors are assembled into three perpendicular 90 degree plates as shown in Fig. E.5 (a), forming a 3-D sensor. A polycarbonate angle piece provides structural stability to the PCB pieces and the assembly is placed inside a polycarbonate protective shell as shown in Fig. E.5 (b). The cylinder is filled with non-corrosive RTV silicone, which protects the PCB plates from physical damage and fixes the relative alignment of the axes. Imperfections in alignment are corrected during the calibration process.

The 3-D sensor is placed on a sliding carriage comprising: a Delrin mounting piece,

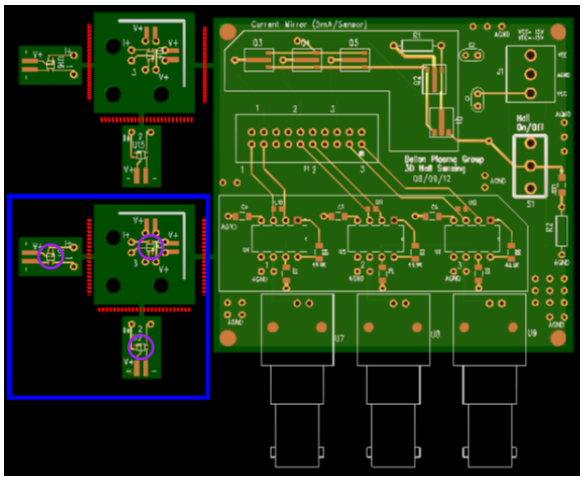

Figure E.4: PCB representation of circuitry in Figure E.2. Both the control circuitry and the surface mounts for two 3-axis sensors are printed in the same board. The boards are cut along the dotted red lines. Hall elements are placed on the footpoints marked by the purple circle and the components enclosed in blue are assembled and placed perpendicular to one another like in Fig. E.5 (a).

an Ultra High Molecular Weight (UHMW) Polyethylene sliding base, and a Delrin adapter between the mounting piece and the base (Fig. E.5 (b)). This modular design is highly flexible, permitting easy adaptation across different experiments.

Figure E.5 (c) shows how six sliding carriages with sensor assemblies are placed on a 24 in x 24 in polycarbonate board with horizontal cutouts. The horizontal cutouts allow continuous horizontal displacement of the sensor carriage, and the regular pattern of the horizontal cutouts permits carriage placement along discrete locations in the vertical direction. Thumbscrews are tightened to keep the carriages fixed once in the desired location.

The polycarbonate board can be moved along the chamber axes by sliding along two stainless steel rails shown in Fig. E.5 (d). The rails are mounted between two 2.75 in ports from the top of the chamber. This aligns the rail to the chamber axis. This set-up permits continuous measurement along two axes and discrete measurements along the remaining axes. Each hall sensor assembly (carriage, sensor, and control board) is completely independent and many assemblies can be placed onto the polycarbonate board to make volumetric measurements of the magnetic field.

Ethernet cables provide a reliable, low cost method of connecting the signal from

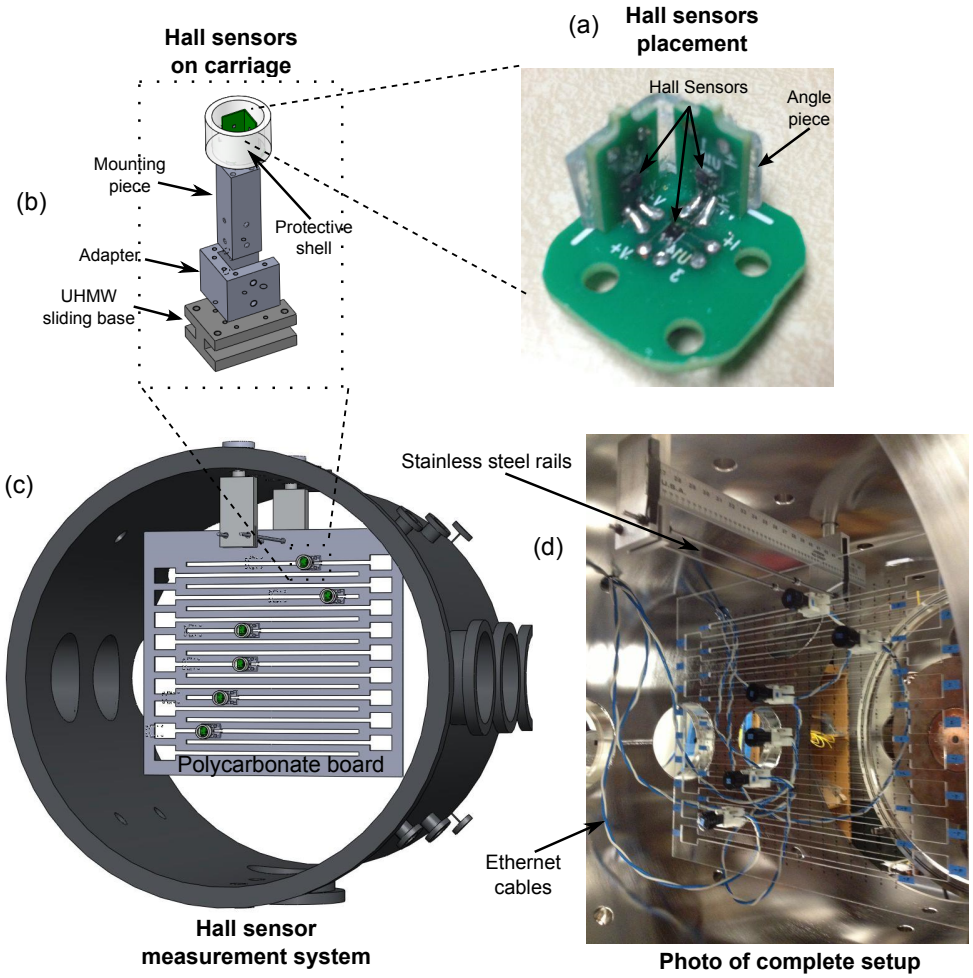

Figure E.5: (a) 3-axis hall sensor element made by placing PCB pieces perpendicular to each other. A polycarbonate angle supports the plates. (b) An exploded view of a hall sensor mounted on a carriage. The sensors are surrounded by a polycarbonate shell filled with RTV silicone. (c) Six sensors are mounted on a board. The entire set-up is mounted on the vacuum chamber ports. (d) Photo of set-up. The blue and white Ethernet cables bring current to and carry the output signals from the hall sensors.

the control board to the sensor. Unshielded twisted cables work well up to 100 kHz frequency[2] [147]. This frequency limit is well above the 1 kHz design requirement for measurements of bias field and strapping field.

This mounting system is not vacuum compatible, and requires that the chamber be at atmosphere when taking measurements. For our experiment, the bias field and strapping field operate identically whether under atmosphere or under vacuum. We require vacuum to generate plasmas, but plasma time scales are too fast for the Hall sensors so vacuum compatibility is not a design requirement.

E.4 Calibration

To calibrate the 3-axis hall sensor, we use a Helmholtz coil and adapt the B-dot probe calibration technique described in [47] to Hall sensors. A Helmholtz coil comprises two identical coils of n turns and radius R placed in a coaxial configuration with a separation distance of R. If the same current I is sent through both coils, they generate a uniform magnetic field:

$$B = \left(\frac{4}{5}\right)^{3/2} \frac{\mu_0 n I}{R} \tag{E.3}$$

in the region between the coils.

We start by letting $\mathbf{B}$ be the vector that corresponds to the actual magnetic field and let $\mathbf{V}$ be the vector that corresponds to the voltage output of each of three hall sensor (one sensor for each axis). The linear transformation $\mathbb{M}$ is defined so that: $\mathbf{B} = \mathbb{M}\mathbf{V} \implies \mathbb{M}^{-1}\mathbf{B} = \mathbf{V}$. Thus,

$$\mathbf{V} = \begin{pmatrix} V_x \\ V_y \\ V_z \end{pmatrix} = \begin{pmatrix} M_{xx}^{-1} & M_{xy}^{-1} & M_{xz}^{-1} \\ M_{yx}^{-1} & M_{yy}^{-1} & M_{yz}^{-1} \\ M_{zx}^{-1} & M_{zy}^{-1} & M_{zz}^{-1} \end{pmatrix} \begin{pmatrix} B_x \\ B_y \\ B_z \end{pmatrix} \tag{E.4}$$

where V_x, V_y, and V_z corresponds to the voltage output of the Hall sensors, which is proportional to the B_x, B_y, and B_z component of the magnetic field. We now apply

[2] Twisted-pair can go up to 10 MHz for special applications.

three different uniform magnetic field (one for each axis) to the probe to calculate the M_{ij} terms. For example, if we apply $\mathbf{B} = B_z\hat{\mathbf{z}}$, then Eq. E.4 becomes

$$\begin{pmatrix} V_{x,z} \\ V_{y,z} \\ V_{z,z} \end{pmatrix} = \begin{pmatrix} M_{xx}^{-1} & M_{xy}^{-1} & M_{xz}^{-1} \\ M_{yx}^{-1} & M_{yy}^{-1} & M_{yz}^{-1} \\ M_{zx}^{-1} & M_{zy}^{-1} & M_{zz}^{-1} \end{pmatrix} \begin{pmatrix} 0 \\ 0 \\ B_z \end{pmatrix} = \begin{pmatrix} M_{xz}^{-1}B_z \\ M_{yz}^{-1}B_z \\ M_{zz}^{-1}B_z \end{pmatrix}$$

where the additional index 'z' in $V_{x,z}$, $V_{y,z}$, $V_{y,z}$ denotes voltage readings from calibrations involving a field along the $\hat{\mathbf{z}}$ direction. Applying Eq. E.3 yields

$$M_{iz}^{-1} = \left(\frac{5}{4}\right)^{3/2} \frac{RV_{i,z}}{\mu_0 n I_z}$$

where $i \in \{x, y, z\}$. This process is repeated , M_{iy}^{-1} and M_{ix}^{-1}, thus building a complete matrix:

$$\mathbb{M}^{-1} = \left(\frac{5}{4}\right)^{3/2} \frac{R}{\mu_0 n} \begin{pmatrix} \frac{V_{x,x}}{I_x} & \frac{V_{x,y}}{I_y} & \frac{V_{x,z}}{I_z} \\ \frac{V_{y,x}}{I_x} & \frac{V_{y,y}}{I_y} & \frac{V_{y,z}}{I_z} \\ \frac{V_{z,x}}{I_x} & \frac{V_{z,y}}{I_y} & \frac{V_{z,z}}{I_z} \end{pmatrix}$$

We numerically invert $\mathbb{M}^-$ to calculate $\mathbb{M}$.

E.5 Measurement of vacuum field

The portable nature of the Hall sensor set-up permits magnetic field measurements across different experiments.

E.5.1 Quad gun and large "welding cables" strapping coil

Initial strapping fields are made with the "welding cable" strapping coils (Sec. D.5.2). These coils are mounted on ports outside the vacuum chamber (Fig. E.6 (a)), so magnetic field must diffuse through the stainless steel chamber before reaching the plasma domain. The coils are in a bipole strapping configuration (Sec. D.5). The left

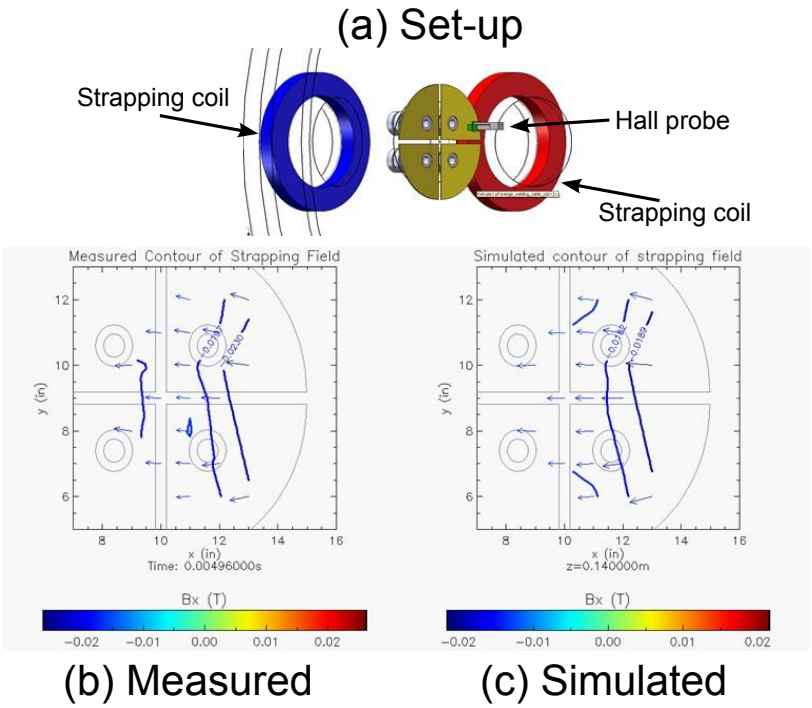

Figure E.6: (a) Set-up with placement of "welding cable" strapping coils, "quad" plasma gun, and Hall probe. (b) Measured magnetic field from hall sensors. (c) Simulated magnetic field.

(blue) coil produces bore field oriented out of the vacuum chamber, whereas the right (red) coil produces bore field oriented into the chamber. Magnetic measurements at a given time ($t = 5$ ms), along a plane ($z = 14$ cm) are visualized in Fig. E.6 (b). The measurements confirm uniform 200 G magnetic field oriented in the $-\hat{\mathbf{x}}$ direction. Simulations of the "welding cable" coils (Fig. E.6 (c)) match the measured profile to within 20%. The simulations use measured currents as input, but do not include magnetic diffusion, nor account for distortions from eddy currents. The excellent match between measured and simulated data suggests that diffusion effects do not play a significant role over the time-scale of the strapping field.

The Hall sensors can also be used to measure the bias field from the "quad" plasma gun (Sec. D.3). Two bias coils located behind the cathode and anode (E.7 (a)) produce an arched magnetic structure. The lower coil produces a field oriented into the vacuum chamber ($\hat{\mathbf{z}}$ direction) whereas the upper coil produces a field oriented out of the vacuum chamber ($-\hat{\mathbf{z}}$ direction), similar to the magnetic field of a horse-shoe

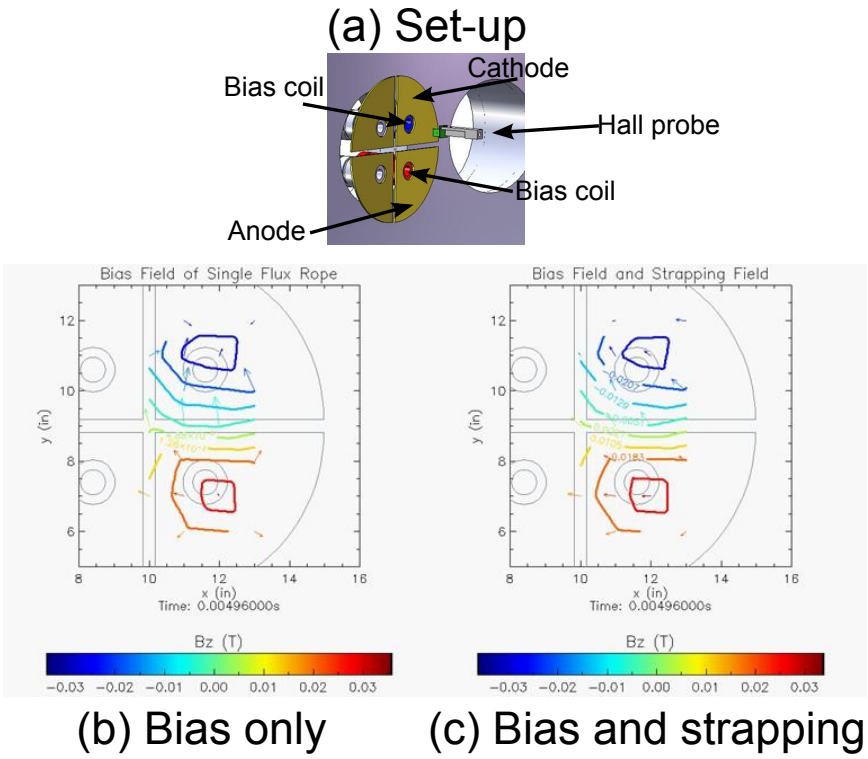

Figure E.7: (a) Set-up highlight the activated bias coils and hall probe. (b) Measurement of magnetic field due to bias coils (c) Measurement of magnetic field including magnet.

Figure E.7 (b) visualizes magnetic field measurements of the bias coils: the contour lines represent the B_z component of the magnetic field and the arrows represent the B_x and B_y component of the magnetic field. A red-blue color table denotes magnetic field amplitudes ranging from -350 G to 350 G. Figure E.7 (b) shows shows magnetic field lines emerging from the bottom bias coil and curving upwards, before going down into the top bias coil, consistent with a flared magnetic tube structure [66]. The application of strapping field super-imposes a strong B_x strapping component onto the bias field. This is verified by measurements shown in Fig. E.7 (c). The magnetic field in Fig. E.7 (c) no longer has the flared magnetic tube structure of Fig. E.7 (a), consistent with the field line visualizations in Fig. F.4.

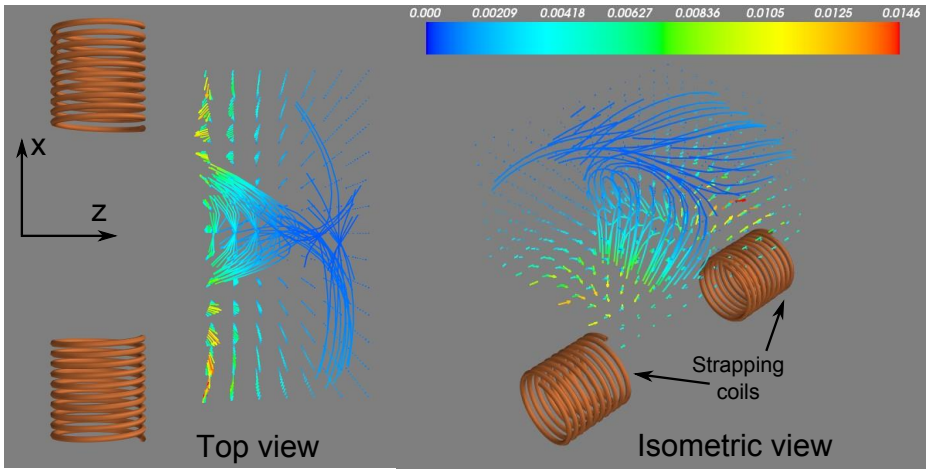

Figure E.8: Visualization of magnetic field in region above strapping coils. Magnetic field strength is in Teslas.

E.5.2 Single loop solar experiments

Later strapping fields are made with smaller coils inside the vacuum chamber. Figure E.8 shows measurements[3] of magnetic field in the region above the strapping coils. The field measurements include both the bias field and strapping field, but the bias coils (not shown) are so far from the measurement region, that the magnetic field is strictly from the strapping coils. The bore strapping field is approximately 0.025 Tesla but sharply drops off, eventually reaching a null point at $z \approx 30$ cm.

These measurements are obtained using the set-up shown in Fig. E.5 (d). One disadvantage of this set-up, is that the polycarbonate board can collide with the strapping coils, which are also mounted inside the vacuum chamber. This prevents magnetic measurements at low heights, near the bias coils. Nevertheless, the modular nature of the 3-D Hall sensor carriages means that an alternate support structure can be adapted to the domain of interest. Such a support structure is shown in Fig. E.9 (a). Multiple 3-D Hall sensor carriages are mounted along a polycarbonate cut-out. The cut-out is mounted to an angle-bracket which is attached along slots in the support structure. The entire assembly can be moved along the axis of the strapping coils, providing volumetric magnetic field measurements.

Magnetic measurements along the plane of the plasma is shown in Figs. E.9 (b),

[3]These measurements are by Patricio Arrangoiz.

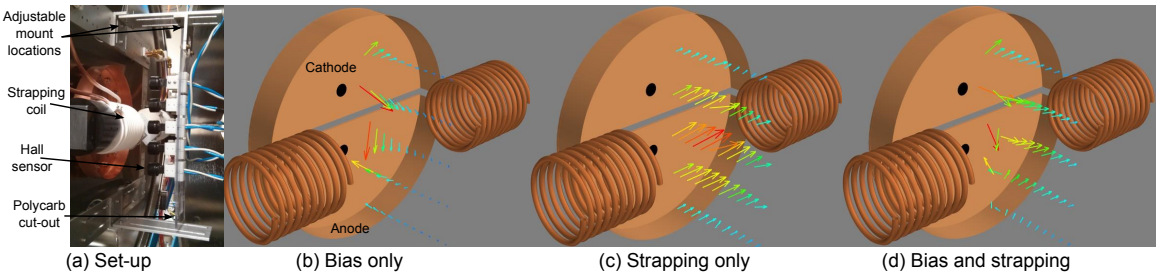

Figure E.9: (a) Support structure for Hall sensors near the electrodes. The set-up permits the adjustments of Hall sensor placement along all three directions. (b) Measured bias field along a single plane. (c) Measured strapping field along a plane. (d) Magnetic measurements of both bias and strapping field.

(c), and (d). The magnetic field produced by the bias coils is shown in Fig. E.9 (b). In Fig. E.9 (b), field lines start from the cathode and arch towards the anode, consistent with a left-handed sigmoid configuration (see Fig. G.11). The strapping coils in coaxial configuration produce strapping field oriented along the axis of the coils (Fig. E.9 (c)). When strapping field and bias field are combined, the result is an arched structure near the electrodes which transitions to primarily strapping field by the strapping coil axis (Fig. E.9 (d)).

E.6 Conclusion and discussion

This chapter presents the design, construction, and usage of a simple, flexible, and scalable method for obtaining volumetric magnetic measurements using Hall sensors. The control board and mounting template for a single sensor are designed for a single PCB print job, permitting the creation of as many, or as few, 3-D Hall sensors as necessary. Each 3-D sensor comprises three 1-D sensor placed perpendicular to each other, permitting measurement all three components of the magnetic field. The three sensors are supported by a polycarbonate angle, a protect shell, and are mounted on a carriage. The carriage is designed to be compatible with different mounting systems, which can be adapted around obstructions in the domain of interest.

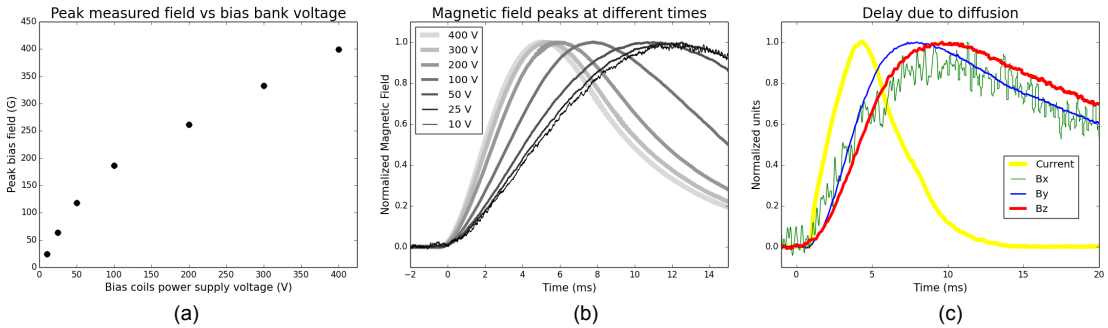

Figure E.10: (a) Peak magnetic field not a linear function of voltage. (b) The profile of the magnetic field pulse varies with differing bias bank voltage. (c) Bias magnetic field profile differs from measured bias coil current.

E.6.1 Non-linear coil behavior

Even a single 3-D Hall sensor can reveal useful information about non-linear coil behavior. The bias coils have a ferrite cores which enhance the magnetic field produced by the coil, but introduce non-linear behavior. These coils are also placed inside brass tubes that can couple with currents flowing in the coil, effectively changing the inductive load of the coil. These complicated effects result in earlier peaking of the magnetic field when the capacitor bank power supply is charged to higher voltages (Fig. E.10 (a)). The magnetic field increases linearly when the bias bank is charged to less than 50 V, but the slope changes for bias bank values above 100 V. Similarly, the profile of the magnetic field in time changes as a function of bias bank voltage. The bank rises and decays more slowly at lower bias bank voltages, resulting in earlier peaks for higher voltages. Proper bias bank timing is essential, since the plasma lifetime is on the order of μs. Poor triggering leads to dramatically lower bias field strength than expected, making plasma analysis difficult.

E.6.2 Compensating for diffusion through electrodes

Caltech experiments often place bias coils behind copper electrodes [2, 82, 148], so the magnetic field produced by the coils must diffuse through copper before entering the domain of the plasma. The Hall sensors have been instrumental in determining the peak time of the magnetic field profile. In the Pre-ionization experiment [149], the

measured magnetic field in the chamber peaks ~ 4 ms after the peaking of the bias bank discharge current. Another experiment, the Crossed Flux Tubes experiment, has large conductive surface areas due to the candelabra-shaped plasma gun. The current trace (yellow) and the measured bias field are shown in Fig. E.10 (c). The copper electrodes introduce eddy currents, which delay the peaking of the bias field, compared to the peaking of the bias coil currents profile. This delay time is usually different for each component of the magnetic field, ranging from 4 μs - 7 μs. For the traces shown in Fig. E.10 (c), this would correspond to a factor of 2 difference in the bias field.

Appendix F

Simulating magnetic field lines

F.1 Magnetic field of current loop

The off-axis magnetic field of a loop with current I and radius a (Fig. F.1) is discussed in Smythe [150] and solved by taking the curl of the magnetic vector potential $\mathbf{A}$. Good [151] proposed a more direct method using the Biot-Savart equation:

$$B = \frac{\mu_0 I}{4\pi} \oint \frac{d\mathbf{l} \times \mathbf{r}}{r^3} \tag{F.1}$$

where $d\mathbf{l} \times \mathbf{r} = az\cos\phi d\phi\hat{\boldsymbol{\rho}} + az\sin\phi d\phi\hat{\boldsymbol{\phi}} + (a^2 - a\rho\cos\phi)d\phi\hat{\mathbf{z}}$. By symmetry, $\mathbf{B}_\phi = 0$ and

$$B_\rho = 2\frac{\mu_0 I}{4\pi}\int_0^\pi \frac{az\cos\phi}{(z^2 + a^2 + \rho^2 - 2a\rho\cos\phi)^{3/2}}d\phi \tag{F.2}$$

$$B_z = 2\frac{\mu_0 I}{4\pi}\int_0^\pi \frac{a^2 - a\rho\cos\phi}{(z^2 + a^2 + \rho^2 - 2a\rho\cos\phi)^{3/2}}d\phi \tag{F.3}$$

The trick is to let $b = (z^2 + a^2 + \rho^2)/(2a\rho)$ and $m = 2/(1+b) = 4a\rho/(z^2 + (a+\rho)^2)$ and then use the following relations:

$$\int_0^\pi \frac{d\phi}{(b \pm \cos\phi)^{3/2}} = \frac{m}{2 - 2m}\sqrt{2m}E(m)$$

$$\int_0^\pi \frac{\pm\cos\phi d\phi}{(b \pm \cos\phi)^{3/2}} = \sqrt{2m}K(m) - \frac{2-m}{2-2m}\sqrt{2m}E(m)$$

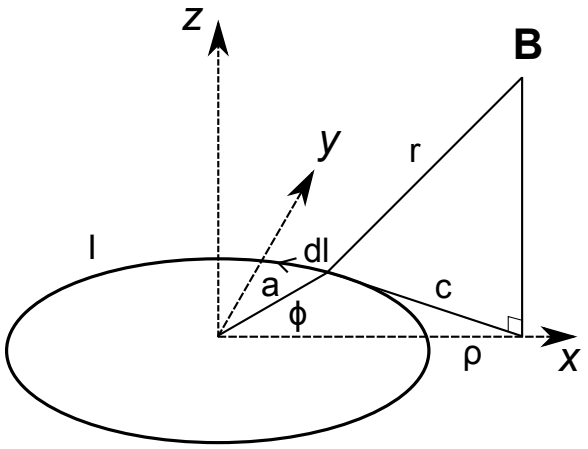

Figure F.1: Set-up for calculating the magnetic field for a loop of radius a with current I.

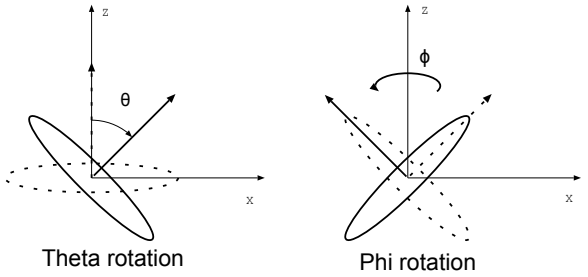

Figure F.2: Phi and theta rotation are rotations about the y and z axis, respectively.

where $E(m)$ and $K(m)$ are elliptic integrals of the first and second kind, respectively. Equations F.2 and F.3 evaluate to yield

$$B_\rho = \frac{\mu_0 I z}{2\pi\rho}\left(\frac{\alpha}{4a\rho}\right)^{1/2}\left(\frac{2-\alpha}{2-2\alpha}E - K\right)$$

$$B_z = \frac{\mu_0 I}{2\pi\rho}\left(\frac{\alpha}{4a\rho}\right)^{1/2}\left(\rho K + \frac{a\alpha - (2-\alpha)\rho}{2-2\alpha}E\right)$$

which are the accepted solutions.

F.2 Visualizing

Complicated magnetic field configurations can be constructed by combining multiple loops and storing them in an array. Each row of the array represents a single loop

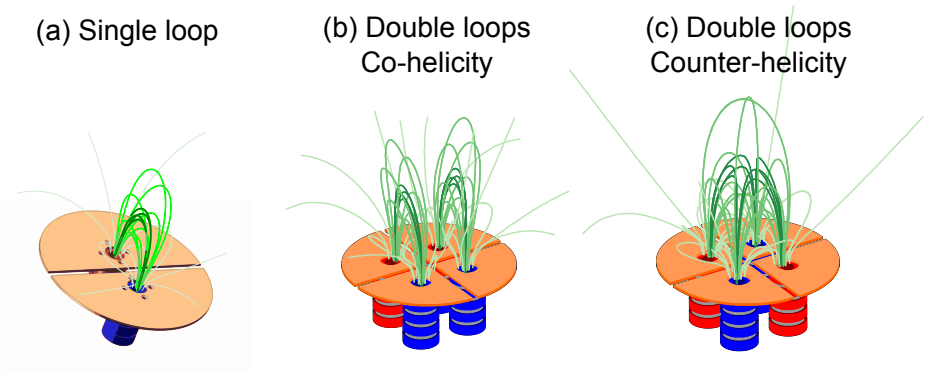

Figure F.3: Darker lines represent field lines which originate closer to the center of the coil.

and is ordered by the following format:

Current	Radius	x-center	y-center	z-center	θ	ϕ

which captures the total current in the loop, loop radius, and loop center. The loop is rotated by θ along the y-axis and then byϕ along the z-axis as shown in Fig. F.2.

Field line tracing is accomplished by solving the differential equation

$$\frac{d\mathbf{r}}{ds} = \frac{\mathbf{B}}{B} \tag{F.4}$$

which can be split into individual components:

$$\begin{aligned}
\tfrac{dx}{ds} &= \tfrac{B_x}{B} = \hat{\mathbf{x}} \cdot \hat{\mathbf{B}} \\
\tfrac{dy}{ds} &= \tfrac{B_y}{B} = \hat{\mathbf{y}} \cdot \hat{\mathbf{B}} \\
\tfrac{dz}{ds} &= \tfrac{B_z}{B} = \hat{\mathbf{z}} \cdot \hat{\mathbf{B}}
\end{aligned}$$

IDL's Runge-Kutta method (rk45) was used to solve the differential equation, where the initial value problem is posed as an evolution over space (s) instead of time (t).

Some vacuum field visualizations are shown in Fig. F.3. The basic configuration with two bias coils form the standard horseshoe-shaped magnetic (Fig. F.3 (a)). When pairs of coils are used, they create more complicated magnetic field configurations like the co-helicity configuration (Fig. F.3 (b)) and the counter-helicity config-

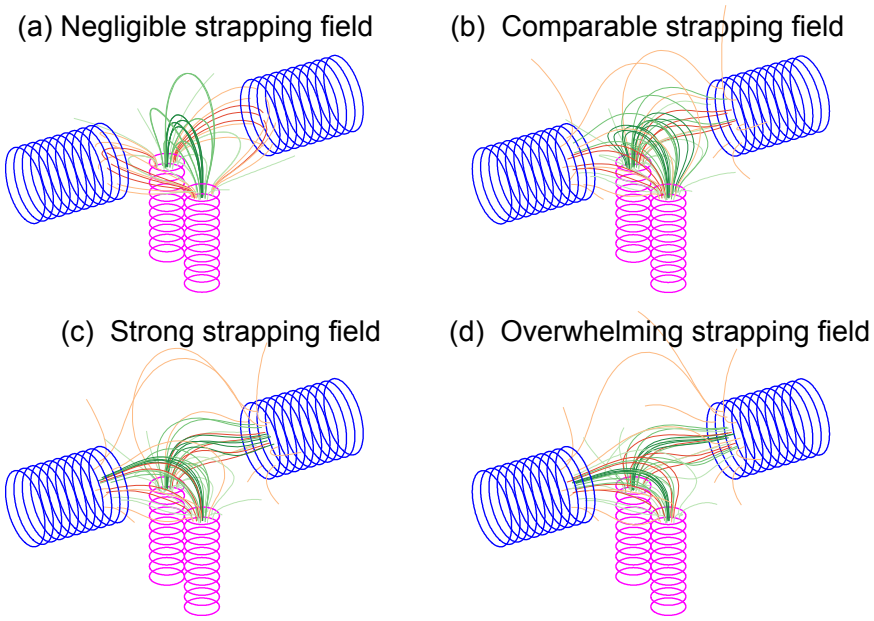

Figure F.4: Field line trace for superposition of bias field from purple coils with varying strapping field from blue coils. Green/red represent field lines from the bias/strapping coils, respectively. Darker field lines are closer to the axis of their source loop.

uration (Fig. F.3 (c)). In all the figures, darker lines represent field lines originating near the center of the coil. In the co-helicity configuration, the magnetic field can be separated into two distinct arches, whereas in the counter-helicity configuration all four coils are linked in one quadrupolar configuration. The complicated nature of the magnetic field lines stresses the importance of doing proper magnetic field line tracing instead of naively drawing cartoons of magnetic features.

The situation is more complicated when strapping coils are present. Solar scientists commonly separate the magnetic field of two sources when drawing cartoons involving magnetic field lines. They start by drawing a magnetic flux rope and then draw a transverse strapping field applied to the rope. In reality, the field lines are a super-position of the magnetic fields from the two sources, and the final result may or may not look like a flux rope structure. Figure F.4 shows the super-position of the bias field for different strapping field configurations. Field lines originating from the bias coils (purple) are shades of green whereas field lines from the strapping coils (blue) are shades of red. Darker field lines are closer to the axis of their source loops.

When the strapping field is negligible, the field lines are determined by the bias coils (Fig. F.4 (a)) and even field lines which start near the strapping coils connect to the field lines of the much stronger bias coils. When the two fields are comparable (Fig. F.4 (b)), the arched magnetic field structure is still present, as shown by the darker green lines, but some of the lighter green lines are connected to the strapping coils. As the strapping field gets stronger (F.4 (c) & (d)), the field lines from the bias coils connect to the strapping coils more than with each other.

A direct consequence of a strong strapping field (or any strong transverse field) is that the magnetic field lines between the bias coils are not connected to each other. This makes plasma breakdown more difficult, since individual particles follow field lines from the bias coils to the strapping coils.

Appendix G

Diagnostic techniques

G.1 Imaging diagnostics

The cameras used in the experiment are not fixed, so the ability to extract camera parameters from images is critical for quantitative analysis. This problem involves determining the *position* and *orientation* of the camera and is known as the *pose* problem in computer vision. Many algorithms have been published to help determine the *pose* of a given camera but the majority of algorithms are too complicated to implement [152] or assume the use of a checkerboard-like pattern for calibration [153, 154]. These algorithms can correct for lens aberration and chromatic distortions but these features provide minimal potential gain at the expense of excessive work. In particular, the placement of a checkerboard inside the vacuum chamber along the plane of plasma expansion is particularly unappealing.

G.1.1 Fish-eye effect

One way to improve the field of view of camera imaging is to use a fisheye lens at the cost of introducing distortion at the edges. Since camera lens are designed to follow specific mapping functions, this distortion can theoretically be corrected for. A standard lens has a normal mapping function defined by the equation:

$$r = f_\infty \tan\theta = f_\infty \frac{H}{D} \tag{G.1}$$

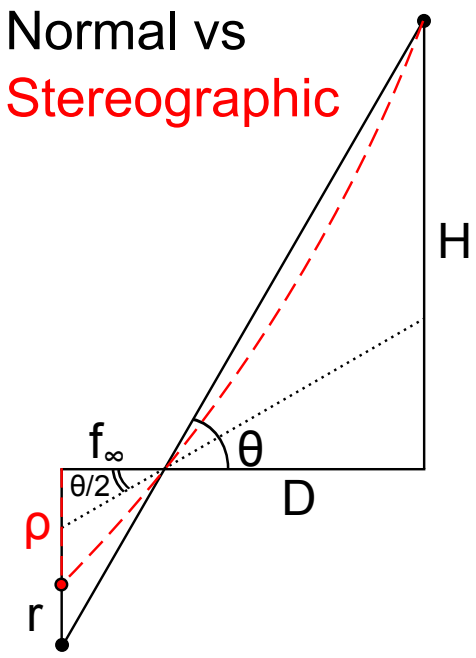

Figure G.1: Representations of normal (solid) vs stereographic (dashed) projections. The same point of displacement H at a distance D maps into $\rho < r$, thus allowing the stereographic projection to have a wider field of view.

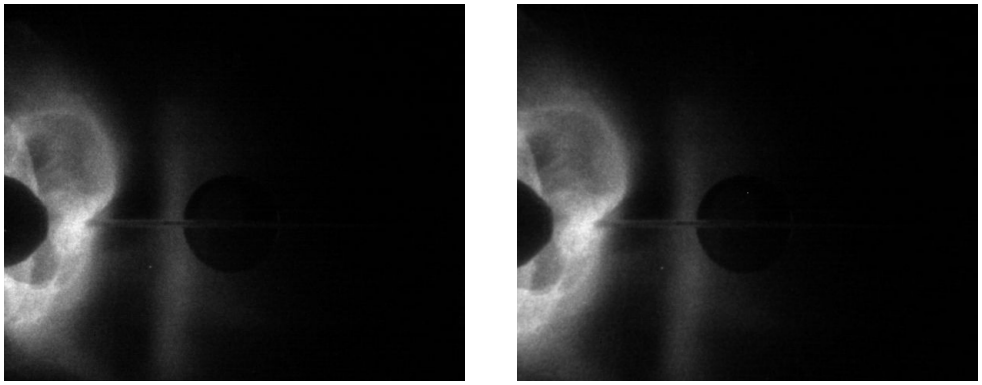

Figure G.2: Uncorrected image (left) and corrected image (right). The corners show the most noticeable change. The corrected image has also been cropped so that the final image has the same number of pixels. The resampling can sometimes introduce artifacts like the small white dot in the opposing port (large black circle in center of image).

where f_∞ is the focal length and r is the distance from the center of the image, H is the distance from the optical axis, and D distance from the object to the lens when the lens focus is set to infinity[1] (See black lines in Fig. G.1). There are four common types of fish-eye lens with different mapping functions: stereographic, equidistant, equisolid, and orthographic. The Rokinon[2] fish-eye lens is a stereographic type fish-eye lens with mapping function

$$\rho = 2f_\infty \tan\frac{\theta}{2}, \tag{G.2}$$

which is demonstrated by the dashed red lines in Fig. G.1. Given a specific planar distance D, an image taken by a fish-eye lens can be corrected for along that plane by using

$$r = \frac{4\rho f^2}{4f^2 - \rho^2}$$

In practice, this is not so easy because images are stored as 2D arrays which represent discrete pixel locations. A code which corrects for fish-eye effects needs to interpolate the pixel values to form higher resolution bins, apply the inversion, and re-sample at the original resolution. Fortunately, the image library OpenCV has a built-in *remap* function that takes care of the dirty work of interpolating and re-sampling. In order to use the *remap* function, the user specifies a function g which relates the target image to the source image. For example, one would specify Eq. G.2, which relates the fish-eye target image to the desired non-fish-eye source image.

The error from using the fish-eye lens on the Imacon camera is about 10% at the edge of the image. This fish-eye lens is designed for a standard Nikon SLR camera but the 10% distortion is significantly lower than expected. The culprit is the difference in the physical dimensions of the Imacon CCD (10 mm x 8.7 mm) and the standard Nikon APS-C CCD (24 mm x 16 mm). The lens optics expects a larger Nikon CCD and the projected image is scaled accordingly. The Imacon CCD only captures the center portion of the image as shown by the dotted rectangle in Fig. G.3, resulting in around 10% error at the edge and nearly 20% error at the corners.

[1] When the user focuses on an object at distance D, the lens has been moved to satisfy the thin lens equation so the distance from object to lens is D plus a small correction.

[2] Rokinon is a re-branding of the Samyang brand.

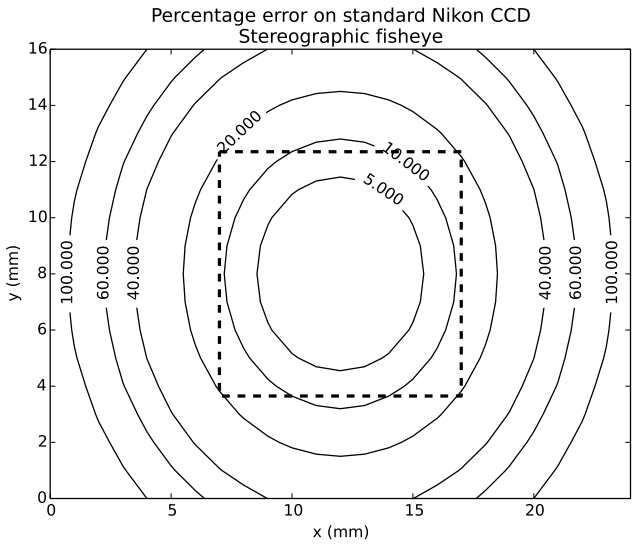

Figure G.3: Percentage error on Nikon CCD from using the fisheye lens. The dotted square represents the much smaller Imacon CCD, for which the distortion is limited to 20% near the corners.

G.1.2 Distance calibration

The chamber port visible in loop expansion images is an excellent choice for calibration purposes. The port has a known diameter (10.16 cm) and the center of the port is at $z = 34$ cm along the chamber axis ($z = 0$ at the electrode surface). Since the Imacon camera looks through the window on the opposite side of the chamber, the port is found in most plasma images. If a normal lens is used or a correction function applied when a fish-eye lens is used, then the distance from the camera and the length scale of each pixel can be calculated by Eq. G.1.

Instead of attempting to click on the port center, a robust method of locating the port center is to fit a circle to the port and use the fitted center point. Even when given a specific region of the picture to analyze, most automatic circling-finding routines struggle to locate the black circle which corresponds to the opposing port. For example, the OpenCV's Hough transform algorithm results in many false positives and failed to find the opposing port (Fig. G.4 (a)). The easiest method is to manually click on points around the circle and perform a least squares fit (Fig. G.4 (b)).

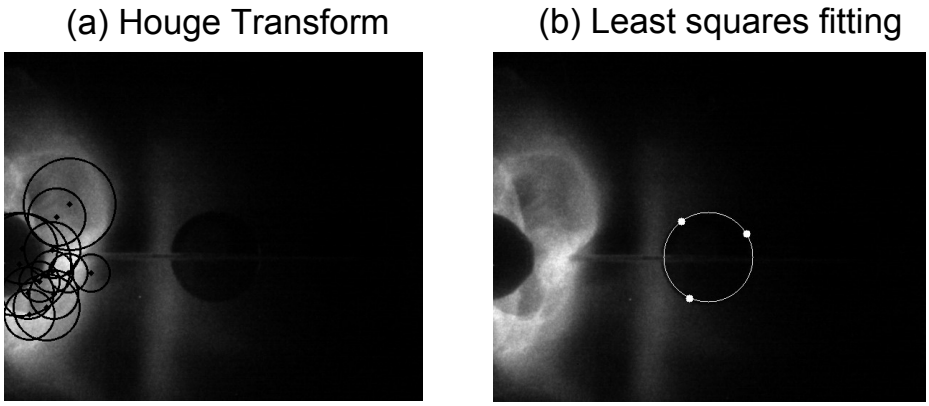

Figure G.4: (a) Automatic circle finding algorithm fails to locate the port but finds many false positives. (b) A least squares fit easily captures the port from three user clicks.

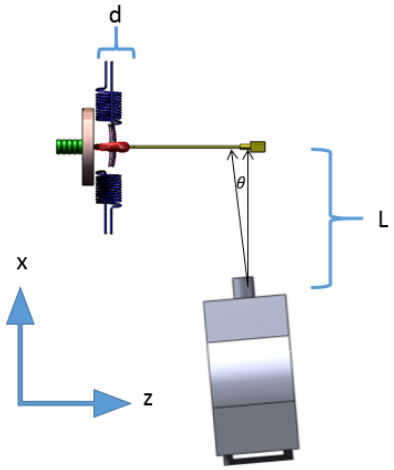

Figure G.5: Set-up as viewed from top of chamber. Since $L \gg d$, a small θ may result in $L \sin\theta \approx d$.

G.1.3 Correcting for angles

Consider the situation where the Imacon camera is not perfectly parallel with the x-axis like in Fig. G.5. Since the distance from the camera to the chamber axis (L) is large compared to the initial size of the plasma (d), a small angle rotation (θ) of the camera along a parallel axis to the y-axis (yaw) can result in a non-negligible correction $L \sin\theta$. Similarly, the camera may also be rotated along an axis parallel to the $\hat{z}$ axis (pitch). Since the camera is mounted on a tripod, it does not rotate along the axis parallel axis to the x axis (roll).

The rotation matrices R_y (yaw) and R_z (pitch) of the camera generally do not commute. Since there is no rotation about the x-axis (roll), it is possible to independently calculate the yaw and pitch angle. To see this, note that a rotation parallel to the y-axis changes the x and z components but does not modify the y component. Similarly, a rotation parallel to the z-axis does not modify the z component. The z-coordinate of fixed objects should be used to to calculate the y-axis rotation and the y-coordinates used to calculate the z-axis rotation. The calibration order does not matter and the yaw and pitch can be calculated independently.

The following algorithm can determine the camera orientation angle if the locations of two reference object ($\mathbf{r}_1$ and $\mathbf{r}_2$) are known. For many plasma images, the center of the opposing port of the vacuum chamber and the center of the far strapping coil is used. Their locations are known with respect to the coordinate system defined in Sec. 1.10.1. The point $\mathbf{r}_1$and $\mathbf{r}_2$ are then mapped by a linear transformation[3] to image points $\mathbf{i}_1$and $\mathbf{i}_2$. If the size of the CCD pixels are known, then Δx_1 and Δx_2 can be calculated from $\mathbf{i}_1$ and $\mathbf{i}_2$. The focal length f is determined by the lens used and the following distances are measured: distance from the camera to the coil (L), from the camera to the rear port (D), and between the coil and the port (b). A diagram of this process for calculating the rotation θ about the y axis is shown in Fig. G.6 (a).

From the diagram, one can see that

$$\tan(\psi_1) = \frac{\Delta x_1}{f},\ \tan(\psi_1 + \psi_2) = \frac{\Delta x_1 + \Delta x_2}{f}.$$

The summation of angles formula is

$$\tan(\psi_1 + \psi_2) = \frac{\tan\psi_1 + \tan\psi_2}{1 - \tan\psi_1 \tan\psi_2}$$

which solves for $\tan\psi_2$ from Δx_1, Δx_2, and f. Define $\phi = \psi_1 + \theta$ so that

$$\frac{b + x}{L} = \tan(\phi + \psi_2) = \frac{\tan\phi + \tan\psi_2}{1 - \tan\phi \tan\psi_2}. \tag{G.3}$$

[3]Specifically, this is the gnomonical transformation found in standard lens, i.e., a non-fish-eye lens.

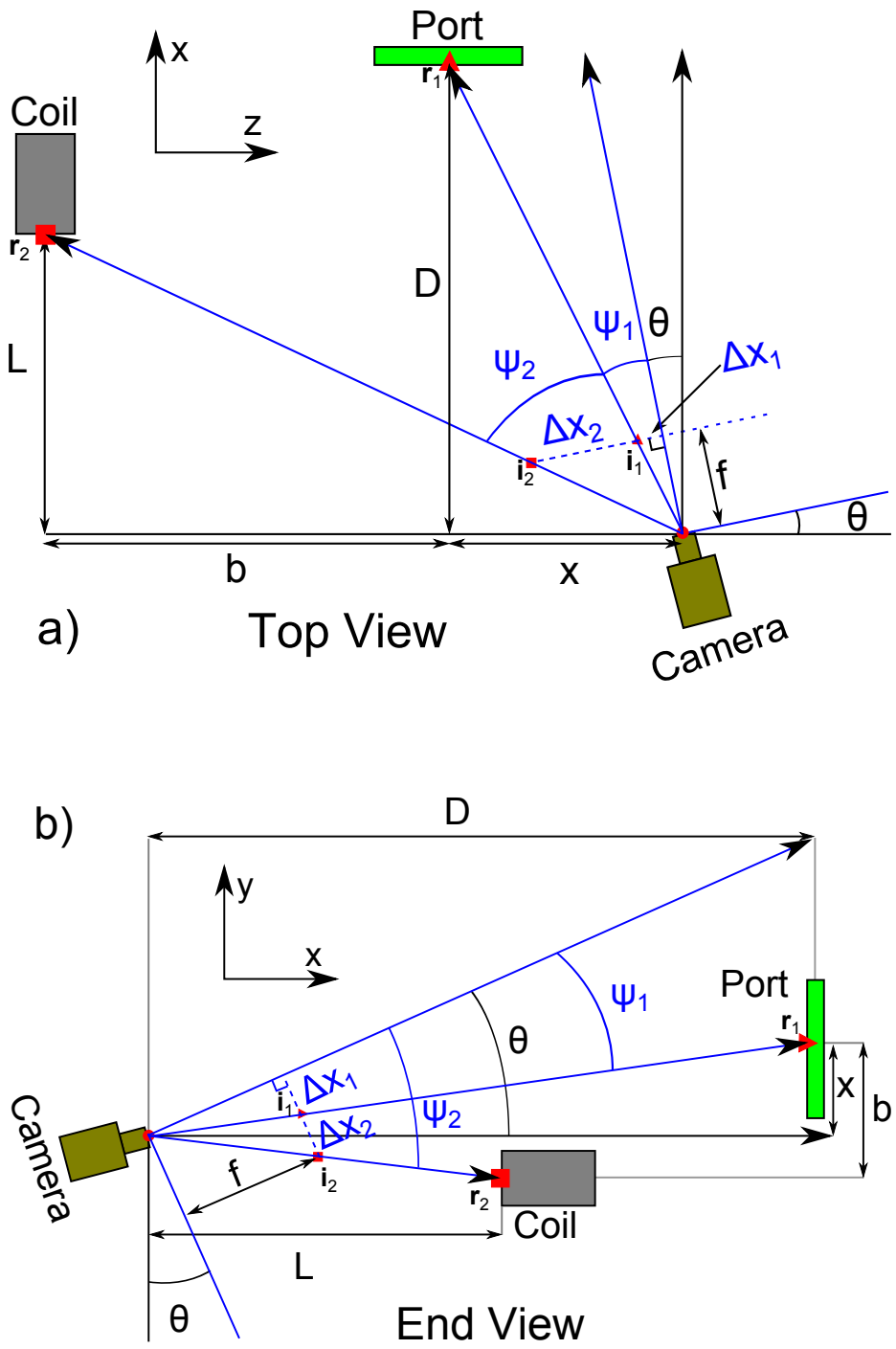

Figure G.6: (a) Method of determining a rotation θ about the y axis. Here, f is the focal length of the lens and Δx_1 and Δx_2 are the displacement of the objects on the image. b is the distance along the $\hat{z}$ direction between the port and the coil center while $b + x$ is the distance from the coil to the camera. In general, black lines correspond to measurements in the unrotated system and blue lines correspond to quantities in the rotated system. (b) The same technique applied to rotations about the z axis.

Substitute $\tan\phi = x/L_1$ into Eq. G.3 to obtain

$$\frac{b+x}{L} = \frac{m + L\tan\psi_2}{L - x\tan\psi_2}$$

which can be put in quadratic form:

$$x^2 + bx + L(L - \frac{b}{\tan\psi_2}) = 0$$

yielding solutions

$$x = \frac{-b \pm \sqrt{b^2 - 4L(L - b/\tan\psi_2)}}{2}$$

Of the two solutions, the likely solution is the one with smaller value, but it is easy to separate the physical solution from the non-physical solution. The angle θ is then obtained by taking

$$\theta = \arctan\left(\frac{x}{D}\right) - \psi_1$$

This process can also be applied to calculate rotation about the z axis as shown in Fig. G.6 (b).

G.1.4 Determining the length of a plasma

Once the position and orientation of the camera are known, it is straightforward to convert an image point $\mathbf{i}$ to the corresponding point $\mathbf{p}$ on a target plane. This permits the generation of height vs time plots by tracking a specific feature from frame to frame or the calculations of relevant features like the length of the plasma loop as it evolves.

G.1.5 Computer enhanced-humans

Images of plasmas are difficult to analyze using standard feature detection algorithms. The plasma are amorphous, translucent, and obscured by objects in the vacuum chamber. They are also dynamic and have some degree of variation between experimental runs. Most automated algorithms will then either locate static features like the strap-

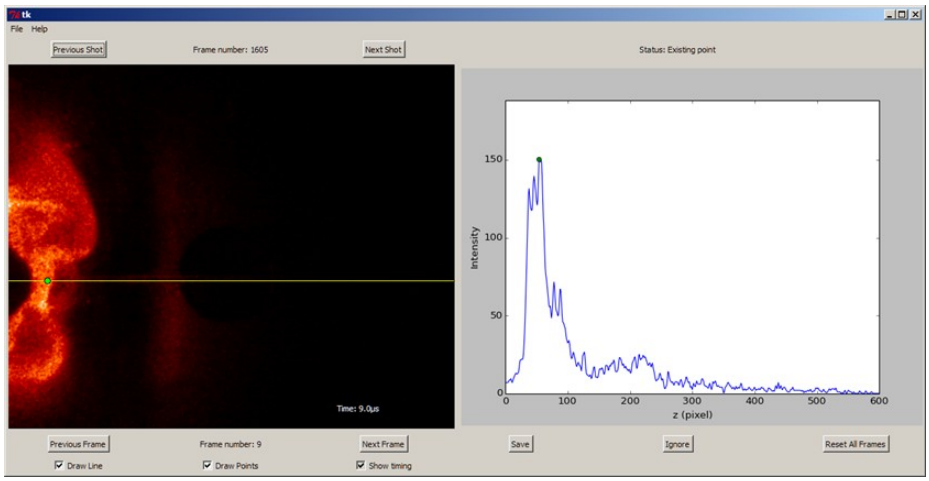

Figure G.7: Plasma apex tracking program.

ping coils and the electrodes, or locate nonexistent features. Reflections of the plasma off the vacuum chamber further confound automatic algorithms.

Human beings have considerable advantages when it comes to picking out plasma features from images. Moving, amorphous, and dynamic features in noisy environments are much easier for humans to identify and track, as evolution has tuned our visual systems for such a purpose. The disadvantages are the subjective and inconsistent nature of human judgment. Human beings are also much slower than computers, particularly at repetitive, algorithmic tasks.

A compromise is to write a program that displays the relevant intensity information next to the image. Humans pick out plasma features while the computer locates local intensity extrema corresponding to those features. The GUI of such a program is shown in Fig. G.7. The program locates the vacuum chamber axis from calibration information and draws a yellow line on the image to denote the axis. The program then displays the pixel intensity along this yellow line. The user then clicks on interesting plasma features along the yellow line to see the corresponding intensity information.

The program features easy switching between frames to study how the plasma evolves and to follow persistent features. The program also permits the user to selectively ignore frames where the plasma is obscured.

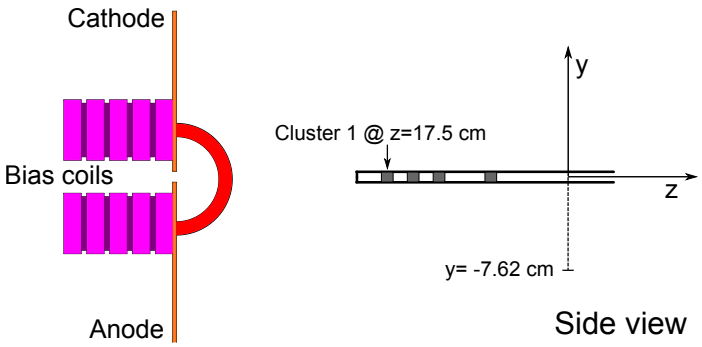

Figure G.8: Schematic with typical magnetic probe placement relative to the plasma gun.

G.2 Magnetic diagnostics

The magnetic probe array has four three-axis clusters placed at 17.5 cm, 19.5 cm, 21.5 cm, and 25.5 cm along the chamber axis (z-axis). The probe can be raised or lowered along the direction of gravity (y-axis). The probe is normally placed at three locations along the y-axis: $y = 7.62$ cm, $y = -7.62$ cm, and $y = 0$ cm. This probe can be rotated around the y axis to make measurements outside of the $y - z$ plane but this option is not used in this thesis.

Magnetic diagnostics are less reproducible than imaging and current diagnostics. Nevertheless, different plasma configurations demonstrate distinct features in the magnetic traces which can be quantified and analyzed. Figure G.9 (a) shows the magnetic field of a typical plasma, measured by the first probe cluster. The plasma apex starts from a height of $z = 4-6$ cm at $t = 0$ and grows until it impacts the cluster at $z = 17.5$ cm. The B_x component shows a small initial rise followed by a large dip. This is expected since the current channel is nominally toroidal, meaning that there is greater magnetic pressure inside the current loop than outside of the loop. The B_x component typically corresponds to the axial current flowing within the plasma so the polarity reversal indicates the magnetic axis. The B_y and B_z component describe the field along the magnetic axis.

There are shot-to-shot variations in the magnetic traces which can be seen by comparing Fig. G.9 (a) to Fig. G.11 (a). Nevertheless, useful features persist within a given configuration permitting quantitative analysis of plasma behavior. Since there

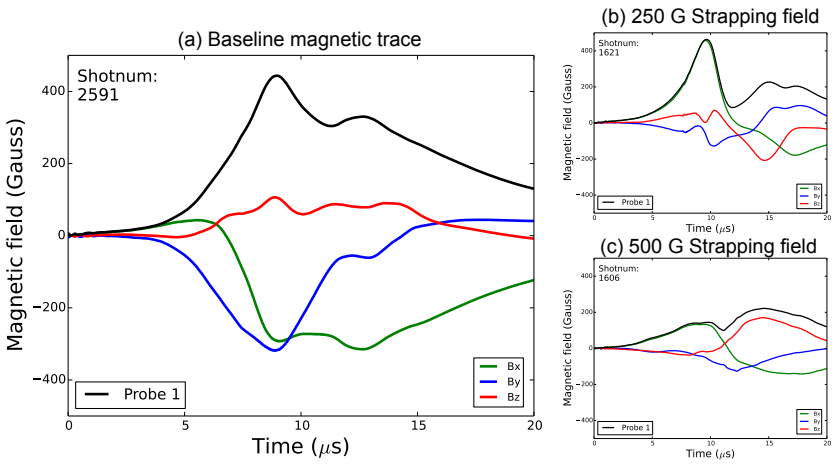

Figure G.9: (a) Typical magnetic traces showing all three component of the magnetic field. The magnetic trace changes dramatically ((b) and (c)) when strapping field is applied.

are four co-linear probe clusters, persistent features between the four probes track plasma dynamics. Of the three components, the B_x component is the most robust. When no strapping field is applied, the B_x polarity reversal is a distinct feature. The application of strapping field complicates the analysis: strapping flux may be "frozen" into the plasma and the plasma may rotate. When a 250 G strapping field is applied to the plasma, the B_x component dominates (Fig. G.9 (b)), so the B_x peak time matches the time when camera images show the bright plasma apex reaching the magnetic probes. The application of an even stronger strapping field (Fig. G.9 (c)) decreases the overall amplitude of the magnetic field, suggesting a wide current channel, but no physically-meaningful persistent features have been identified for tracking purposes.

While magnetic analysis contain valuable data, the qualitative changes in the magnetic trace means that magnetic diagnostics should be compared to camera images to isolate useful features. This thesis focuses on two B_x features (Fig. G.10): the polarity reversal of B_x for the no-strapping field configuration and the peak B_x for the 250 G strapping configuration. The red diamonds in Fig. G.10 correspond to the time when the bright leading edge of the plasma apex reaches the corresponding magnetic probe.

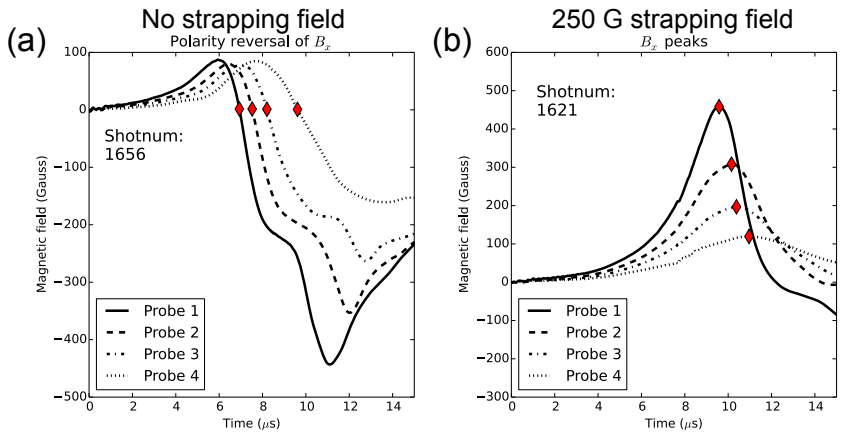

Figure G.10: Measurement of the B_x component of the magnetic field across all four probe clusters. (a) The B_x component switches signs when the plasma passes the probe and provides velocity information about the plasma. (b) When a strong strapping field is applied, the magnetic flux is frozen and carried by the dense region of the plasma. One should employ the peak of the B_x instead of the zero-crossing,

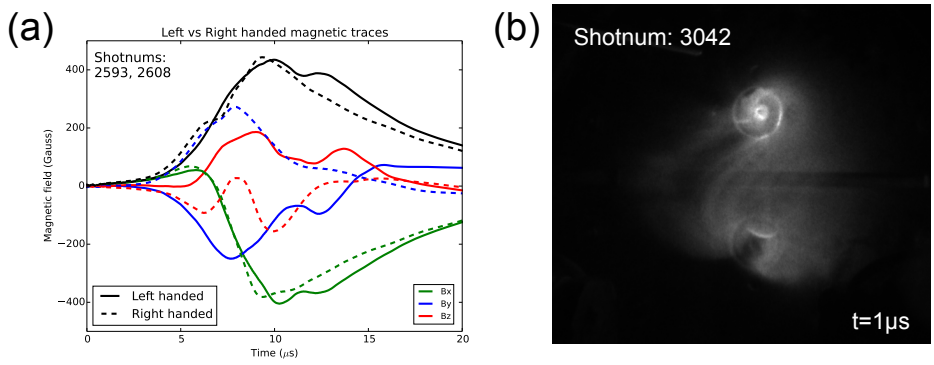

Figure G.11: (a) Three component magnetic traces comparing left and right handed plasmas. (b) Cooke camera end-on imaging of reverse-S left-handed plasma.

G.2.1 Sigmoid structure

Plasma loops are believed to relax into sigmoids which are twisted, force-free, magnetic structures structures [155]. These sigmoid structures can be S-shaped or reverse-S-shaped depending on whether the plasma is right-handed or left-handed, respectively. The plasma is right-handed/left-handed when the field produced by the bias coils (purple in Fig. G.8) is parallel/anti-parallel to the direction of the current flow between anode and cathode. Most plasmas in this thesis have a left-handed configuration, but right-handed configurations are also possible.

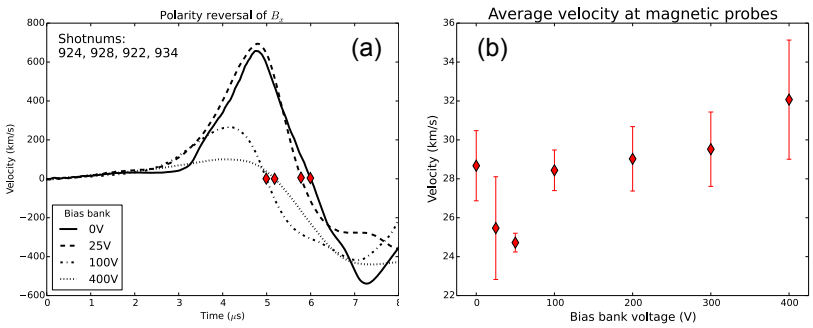

Figure G.12: (a) Polarity reversal of B_x used for qualitatively different configurations. (b) This technique can give good measurements provided that the feature being tracked persists across probe clusters.

Figure G.11 (a) compare the three component magnetic traces for a left-handed (solid lines) plasma to a right-handed (dashed lines) plasma. The total magnetic field component (black) is comparable between both configurations. The B_x component (green) represents the field produced by the current channel and is similar since both configurations have the same same net current from anode to cathode. The B_y (blue) and B_z (red) components are reversed when comparing the two configurations. Figure G.11 (b) is a end-on image of a left-handed plasma at $t = 1\mu s$.

G.2.2 Plasma velocity measurements

The B_x polarity reversal in the magnetic trace is an excellent measurement of plasma arrival time at each probe cluster. Since the location of the probe clusters are fixed and known, these magnetic measurements can provide quantitative velocity measurements. The average velocity of the plasma apex from $z = 17.5$ cm to $z = 24.5$ cm can be obtained by a linear fit of information from each cluster and extracting an average velocity. This process is repeated over many shots to obtain robust measurements. This can quantify the apex velocity of Hydrogen plasmas as a function of different parameters, provided that other diagnostics are used to ensure the results are consistent. For example, Figure G.10 shows that the probe signal can change significantly when strapping field is applied. Likewise, the B_x component varies significantly when the amplitude of bias field is adjusted as shown in Fig. G.12 (a). Nevertheless, it is

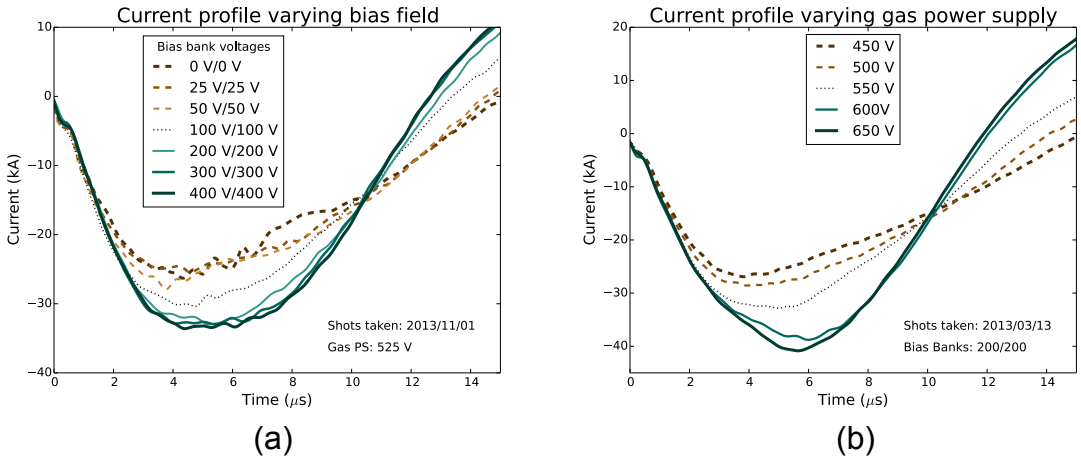

Figure G.13: Current profile while (a) varying the bias bank voltages, and (b) varying the gas power supply voltages.

still possible to use the B_x polarity reversal to extract apex velocity information as a function of bias bank voltage if a particular feature remains consistent as shown in Fig. G.12 (b). The comparable velocity across a wide range of bias bank voltages suggests that the bias field does not play a significant role in the dynamics of the apex, consistent with imaging diagnostics.

G.3 Circuit analysis techniques

G.3.1 Analysis using the current trace

The energy stored in a capacitor is given by $CV^2/2$, whereas the energy stored in an inductor is $LI^2/2$. Suppose the capacitor were charged to a voltage V, and then discharged into an inductor. In an ideal LC circuit, the energy transfers between inductor and capacitor so that

$$I_{max} = V\sqrt{\frac{C}{L}}. \tag{G.4}$$

If the capacitance and voltage are fixed between shots, then I_{max} increases for smaller L, and decreases for larger L. Kumar et al. [104] identify two main sources of variable inductance for Caltech experiments: the ignitron and the plasma. The ignitron

inductance depends on the amount of current flowing through the device. Kumar et al. estimate $L_{ignitron} \approx 50$ nH, 170 nH, and 800 nH at nominal$\sim$ 80 kA, $\sim$ 10 kA, and ignitron turn-off, respectively, so smaller nominal currents mean higher ignitron inductances. If the nominal current through the ignitron is the same, then the ignitron inductance can be characterized by a nominal value, and the expanding plasma is the primary source of variable inductance.

Equation 2.2 states that $L \sim \mu_0 R \ln(R/a)$, where R is the major radius, and a is the minor radius, so the plasma inductance increases as the plasma grows larger, and decreases as the plasma becomes smaller. Since R/a is found in the logarithmic term, it is common to assume self-similar plasma expansion [33, 82, 93], implying that $R/a \sim const$, so $L \sim \mu_0 R$. Equation G.4 assumes an ideal LC circuit, but the argument continues to hold if the resistance exists, provided that the resistance between between the two shots are comparable. This is a reasonable assumption, since Caltech plasmas are inductive loads [104], meaning that plasma resistance is negligible.

Figure G.13 (a) shows how varying the voltage of the bias coil power supplies changes the profile of the current trace[4]. Each power supply energizes a different coil, though both power supplies are adjusted to the same voltage. Figure G.13 (a) suggests that bias bank voltages above 200V behave differently than those below 50V, consistent with the magnetic measurements shown in Fig. G.12 (a). Stronger bias fields are expected to increase the tension force (Sec. 2.3.2), resulting in more compact plasmas. Applying the concepts from Eq. G.4 to Fig. G.13 suggest that plasmas with stronger bias field have higher peak currents, corresponding to smaller plasma inductance, and consistent with stronger tension force. This seems to contradict apex velocity measurements from magnetic probe data (Fig. G.12 (b)) which show that the bias field has little impact on plasma apex velocity. Plasma images, however, show that lower bias fields result in earlier onset of instability at the plasma footpoints, causing rapid expansion of the plasma legs, while not significantly affecting the plasma apex.

[4]Each trace represents the average of three shots.

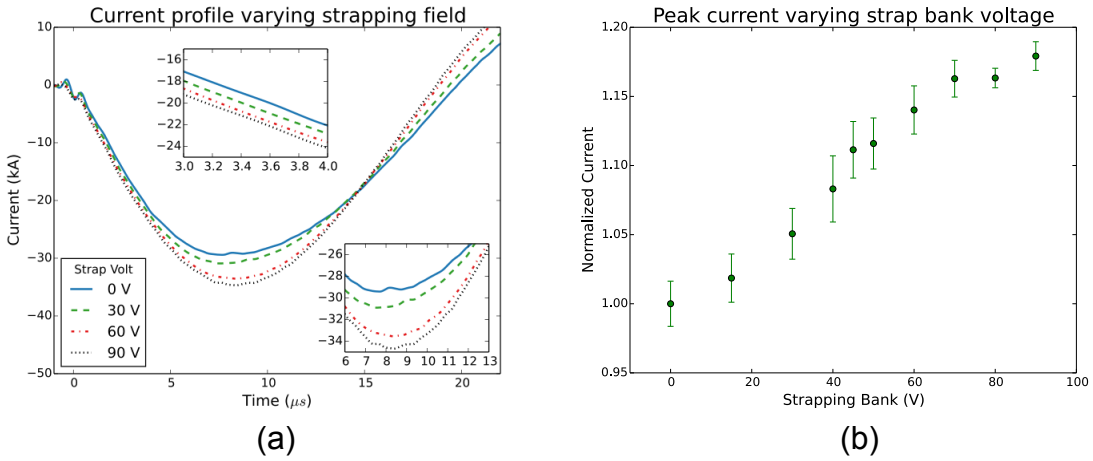

Figure G.14: (a) Current profile while varying strapping field. (b) Normalized peak current while varying the strapping bank voltage.

The power supply of the fast gas valves controls the amount of neutral gas injected into the vacuum chamber. Plasma density is varied between $\sim 10^{20}$ m^{-3} and $\sim 10^{22}$ m^{-3} by adjusting the charging voltage of the power supply. For a given main bank charging voltage, dense plasmas expand slower than diffuse plasmas, since the same electric energy ($CV^2/2$) must accelerate a more massive plasma. Figure G.13 (b) shows how varying the power supply voltage affects the profiles of the current trace[5]. Higher gas power supply voltages result in greater peak currents, consistent with slower expanding plasmas.

The application of strapping field inhibits plasma loop expansion, lowering the plasma loop inductance. This corresponds to an increase in the current, as shown in Fig. G.14 (a). Each trace in Fig. G.14 (a) represents the averaging of between 10-30 shots, so the separation between different current traces is robust. Figure G.14 (b) quantifies the separation of the peak current as a function of strapping field. Each point in Fig. G.14 (b) is normalized to the peak current for the no-strapping-field configuration.

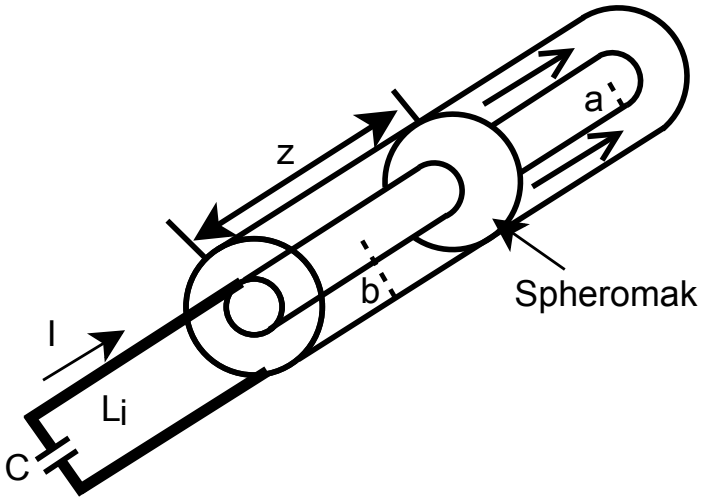

Figure G.15: Schematics of coaxial railgun. A conductive spheromak propagates down a coaxial guide representing an LC circuit with increasing L.

G.3.2 Simple rail-gun model

In the experiment, the plasma inductance is expected to grow as the plasma expands. It is possible to gain insight about the behavior of the plasma by using the mechanical description of a spheromak rail-gun with two canonical coordinates.

A simple Lagrangian description of a coaxial rail-gun with a spheromak armature (Fig. G.15) can be found in Chapter 16 of Ref. [139]. The electro-mechanical model employs the z axis and the charge Q as canonical coordinates. The system has variable inductance with some initial inductance L_i that increases linearly as a function of z (e.g., $L = L_i + l'z$, where l' is an inductance per unit length). Since the increasing inductance is due to coaxial transmission line, $l' = (2\pi)^{-1}\mu_0 \ln(b/a)$, where a is the inner conductor radius, b is the outer conductor radius, and z is the spheromak position.

The effective kinetic energy terms are: $m\dot{z}^2/2$ and $L\dot{Q}^2/2$, where $L = L_i + l'z$ is the total inductance of the system. The initial potential energy of the system is given by $U = Q^2/(2C)$, where Q is the stored charge on a capacitor C.

[5] Each trace represents the average of at least five shots.

The Lagrangian can then be written as

$$L = T - U = \frac{1}{2}m\dot{z}^2 + \frac{1}{2}(L_i + l'z)\dot{Q}^2 - \frac{Q^2}{2C} \tag{G.5}$$

Applying the Lagrange's equations

$$\frac{d}{dt}\left(\frac{\partial L}{\partial \dot{q}_j}\right) - \frac{\partial L}{\partial q_j} = 0$$

one obtains the following equations of motion:

$$\ddot{z} = \frac{l'\dot{Q}^2}{2m}$$
$$\ddot{Q} = -\frac{1}{L_0 + l'z}\left(l'\dot{z}\dot{Q} + \frac{Q}{C}\right)$$

which are amenable to numerical solutions after defining $w = \dot{z}$ and $I = \dot{Q}$ to obtain four coupled, first order ODEs:

$$\dot{w} = \frac{l'I^2}{2m}$$
$$\dot{z} = w$$
$$\dot{I} = -\frac{1}{L_i + l'z}\left(l'wI + \frac{Q}{C}\right)$$
$$\dot{Q} = I$$

The initial conditions are $I = 0$, $Q = 3$, $Z = 0$, and $W = 0$ with $L_0 = C = 1$ and $l' = 0.1$. The simulated current trace over time is compared to experimental data in Fig. G.16. In order to compare simulated parameters to measured parameters, the dimensionless parametrization[6] summarized in Table G.1 are used. As shown in Fig. G.16, the time scales are the same order of magnitude but the simulated current trace is too large and does not decay fast enough. This is expected since resistive dissipative forces are not included in the Lagrangian formulation but exist in the experiment. Resistive dissipation can account for the discrepancy between simulation and measurement but Lagrangian (and Hamiltonian) derivations of mechanics have no direct method for dealing with dissipative forces.

[6]Many of the values are taken from Ref. [15] and summarized in Table G.2.

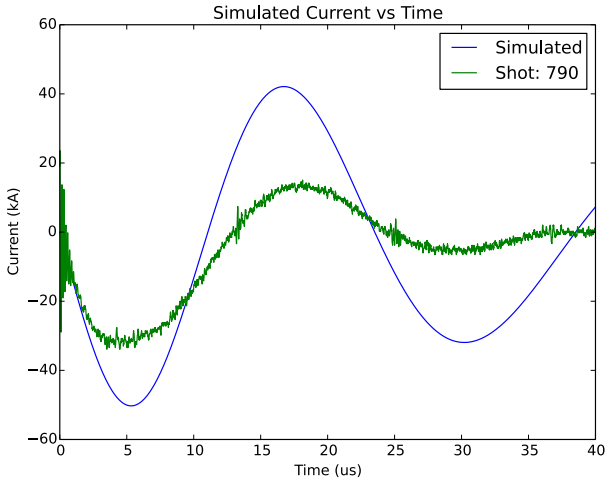

Figure G.16: Comparison between a basic simulation of current as a function of time and the measured current.

Dimensionless Param	Value	Comment
L_0	170 nH	Ignitron inductance
C_0	59 μF	Capacitor
Q_0	59 mC	Chosen so $V_0 = 1kV$
t_0	3.167 μs	$\sqrt{L_0 C_0}$
I_0	18.5 kA	Q_0/t_0
Z_0	53mΩ	L_0/t_0

Table G.1: Dimensionless parameters.

Parameter	Estimated value	Comment
C_b	59 μF	Capacitance of bank
ω_d	2.7×10^5 rad/s	Damped Frequency of Discharge
R_p	5 mΩ	Plasma resistance
L_p	30 nH	Plasma inductance
$\omega_d L_p$	$3 - 13$ mΩ	Plasma inductive impedance
$\dot{L}_p$	$6 - 7$ mΩ	Rate of change of plasma inductance
R_c	8 mΩ	Cable resistance
R_i	$21 - 22$mΩ	Ignitron resistance
L_i	170nH	Ignitron inductance
$\omega_d L_i$	45 mΩ	Ignitron inductive impedance

Table G.2: Parameters obtained from Ref. [15]

G.3.3 Adding resistive dissipation

There are several methods of adding dissipation to a Lagrangian (or Hamiltonian) description of the system. The best known method uses the Rayleigh Dissipation function described by Goldstein [156] and has been applied to RLC circuits with an arbitrary number of time-independent components by Tanisli and Ozdas [157]. Stevens [158] created a pseudo-Lagrangian by introducing a factor of $A\exp(Rt/L)$ where A is an arbitrary constant. This allowed him to get the equation of motion for a RLC circuit, but he obtained canonical momentum and Hamiltonian which were somewhat unphysical. Riewe [110] outlines several additional methods such as reverse-time systems and systems where the friction is explicitly built into the Hamiltonian, but concluded that these methods are difficult to implement. Riewe developed an approach which follows the same patterns as conventional calculus of variations, but his generalized equations include fractional derivatives.

We will derive equations of motions for dissipative spheromak gun by employing both approaches.

G.3.4 Rayleigh Dissipation

Rayleigh Dissipation functions apply when the frictional forces are proportional to velocity and have the form $F_{fx} = -k_x v_x$. In the one-dimensional case, Rayleigh's function is

$$\mathfrak{F} = \frac{1}{2} k_x v_x^2$$

and can be generalized to obtain $\mathbf{F}_f = -\nabla_v \mathfrak{F}$. The physical interpretation of the dissipation function is the work done by the system against friction, and thus $2\mathfrak{F}$ is the rate of energy dissipation due to friction. The relevant Lagrange equation becomes

$$\frac{d}{dt}\left(\frac{\partial L}{\partial \dot{q}_j}\right) - \frac{\partial L}{\partial q_j} + \frac{\partial \mathfrak{F}}{\partial \dot{q}_j} = 0 \tag{G.6}$$

In our system, the dissipative force is due to the resistance which is associated with

the "velocity" of Q. The Rayleigh Dissipation function is

$$F_f = -R\dot{Q} \implies \mathfrak{F} = \frac{1}{2}R\dot{Q}^2 \tag{G.7}$$

Applying Eq. G.6 to Eqs. G.5 and G.7 result in the following equations of motion:

$$\ddot{z} = \frac{l'\dot{Q}^2}{2m}$$
$$\ddot{Q} = -\frac{1}{L_i + l'z}\left(\dot{Q}(l'\dot{z} + R) + \frac{Q}{C}\right)$$

Define $w = \dot{z}$ and $I = \dot{Q}$ to get the following system of equations:

$$\dot{w} = \frac{l'I^2}{2m}$$
$$\dot{z} = w$$
$$\dot{I} = -\frac{1}{L_i + l'z}\left(I(l'w + R) + \frac{Q}{C}\right)$$
$$\dot{Q} = I$$

We use $R = R_p + R_c + R_i = 35m\Omega$ in the simulation, where values for R_p, R_c, and R_i are obtained from Table G.2. Figure G.17 compares the simulated results to the analytic RLC solution and to average measured current for four different shots. While the overall shapes are similar, the increasing inductance from the simulation matches the measurements better than the constant inductance from the analytic solution.

G.3.5 Fractional derivative approach

A brief overview of some of the definitions and properties of fractional derivatives can be found in Sec. A.4. In particular, the formal definition (Eq. A.10), the transition to short-hand notation (Eq. A.12), the reduction of a fraction derivative of integer order to a standard derivative (Eq. A.11), and the composition rule (Eq. A.13) are used in the following derivation.

The fractional derivative approach modifies the original Lagrangian in Eq. G.5 by adding an imaginary term with partial fractions. If a Lagrangian contains a potential with terms proportional to $(d^{1/2}x/dt^{1/2})^2$, then the equation of motion contains a term

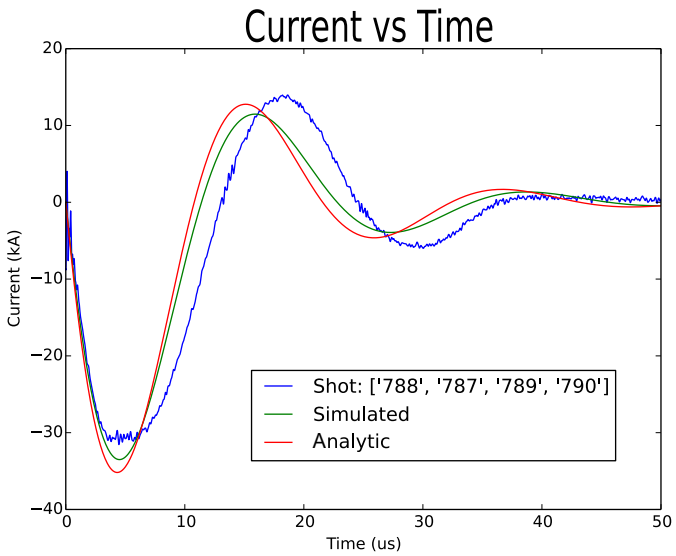

Figure G.17: Compare simulation to data when resistance is taken into account

proportional to $[d^{2n}x/dt^{2n}]$, where n is any positive integer [111]. Since we expect to have a $-IdQ/dt = -R(d^{2\times 1/2}Q/dt^{2\times 1/2}]$ term in the equation of motion, it is prudent to guess a modifier of the form $iR/2\times[d^{1/2}Q/d(t-b)^{1/2}]^2$, and start with the following Lagrangian:

$$L = \frac{1}{2}m\dot{z}^2 + \frac{1}{2}(L_i + l'z)\dot{Q}^2 - \frac{Q^2}{2C} + \frac{i}{2}R\left[\frac{d^{1/2}Q}{d(t-b)^{1/2}}\right]^2,$$

which can be put into shorthand form:

$$L = \frac{1}{2}m\dot{z}^2 + \frac{1}{2}(L_i + l'z)\dot{Q}^2 - \frac{Q^2}{2C} + \frac{i}{2}RQ^2_{(\frac{1}{2},b)} \tag{G.8}$$

The generalized Euler-Lagrange equation for fractional derivatives is given by Eq. 52 in Ref. [110]:

$$\sum_{n=0}^{N}(-1)^{s(n)}\frac{d^{s(n)}}{d(x-b)^{s(n)}}\frac{\partial L}{\partial q_{r,s(n)}} = 0, \tag{G.9}$$

where $N = 2$ because the system has two different orders: the 1/2 fractional derivative, and the first derivative. Following the notation of Riewe, $s(0) = 0$, $s(1) = 1/2$, $s(2) = 1$, where $s(N)$ indicates the highest order derivative, and $s(1)$ represents the

lowest non-zeroth-order derivative[7]. The general Euler-Lagrange equation (Eq. G.9) simplifies to

$$\frac{\partial L}{\partial q_0} + i\frac{d^{1/2}}{d(t-b)^{1/2}}\frac{\partial L}{\partial q_{(\frac{1}{2},b)}} - \frac{d}{dt}\frac{\partial L}{\partial q_1} = 0 \tag{G.10}$$

Applying Eq. G.10 with $q = z$ to Eq. G.8 yields

$$\ddot{z} = \frac{l'\dot{Q}^2}{2m}$$

as the equation of motion for the z coordinate.

For the Q coordinate, the three terms in Eq. G.10 evaluate to

$$\frac{\partial L}{\partial Q} = -\frac{Q}{C}$$

$$-\frac{d}{dt}\frac{\partial L}{\partial \dot{Q}} = -(L_i + l'z)\ddot{Q} - l'\dot{z}\dot{Q}$$

$$i\frac{d^{1/2}}{d(t-b)^{1/2}}\frac{dL}{dQ_{(1/2,b)}} = -R\frac{d^{1/2}}{d(t-b)^{1/2}}Q_{(\frac{1}{2},b)} = -R\dot{Q}$$

where we note $d^{1/2}(Q_{(1/2,b)})/d(t-b)^{1/2} = dQ/dt$ by the composition rule, by the reduction of fractional derivatives with integer order to regular derivatives. The equation of motion is then given by:

$$-\frac{Q}{C} - (L_i + l'z)\ddot{Q} - l'\dot{z}\dot{Q} - R\dot{Q} = 0$$

so

$$\ddot{Q} = \frac{-\left[(l'\dot{z} + R)\dot{Q} + \frac{Q}{C}\right]}{(L_i + l'z)}$$

The fractional derivative approach can be extended to situations that are not covered by the Rayleigh dissipation. Rabei et al. [111] used the fractional formulation to derive the Lagrangian for dissipative forces that are proportional to $(\dot{x})^{1/2}$ and $(\dot{x})^2$, and generalized their result to any dissipative force of the form $(\dot{x})^p$ for $p \geq 0$.

[7] $s(0)$ is the zeroth order and corresponds to terms without derivatives. It is not counted towards N, the number of different orders.

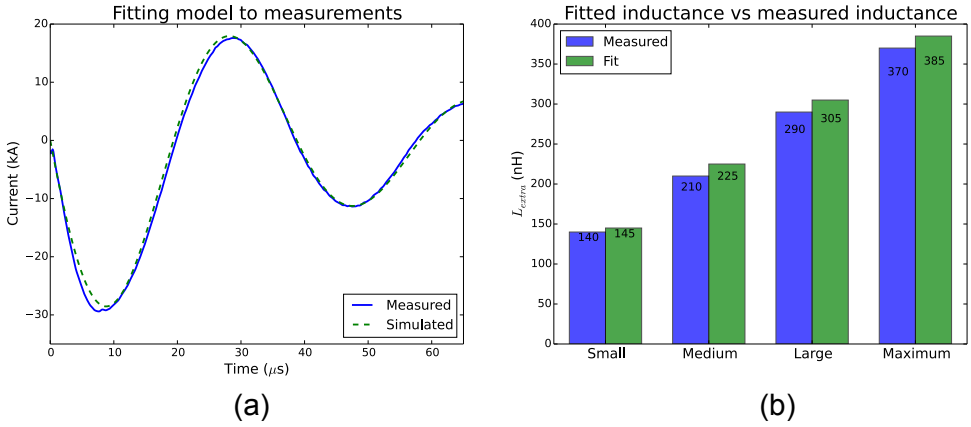

Figure G.18: (a) Varying L_i and R to obtain best fit to current trace in "Maximum" L_{extra} configuration, (b) Measured L_{extra} compared to estimate from fit.

G.3.6 Fitting to the model

The values L_i, R, and l' can be fit to a current trace by non-linear, fitting functions built into the Python SciPy library. The choice of fit interval, and the number of free parameters are important. The current trace has many oscillations over a long time period (Fig. G.18 (a)), but only the first oscillation is associated with the plasma[8]. Nevertheless, nominal information about the system inductance (L_i), and the system resistance (R) can be obtained by setting $l' = 0$[9], and fitting over available measurements[10]. Figure G.18 (a) shows the best model fit to the measured current for plasmas created in "Maximum" L_{extra} (See Sec. D.4) configuration. The measured and model differ at early times, with the measurements showing larger currents than the model, meaning that the plasma is smaller at breakdown than its nominal length, consistent with the arguments in Sec. G.3.1.

We fit the model to different L_{extra} configurations and obtain nominal values for R, and L_i. The value of L_{extra} is calculated by subtracting the nominal L_i for experiments with extra inductance, from nominal L_i for the base case with no additional inductance. The results are summarized in Fig. G.18 (b) and match quantitatively

[8]The plasma arch is believed to detach from the electrodes before the current switches polarity. Other measurements indicate a new current channel forming a current polarity reversal

[9]This is equivalent to the analytic RLC solution, with fixed C.

[10]Measurements are typically averaged from over 10 shots.

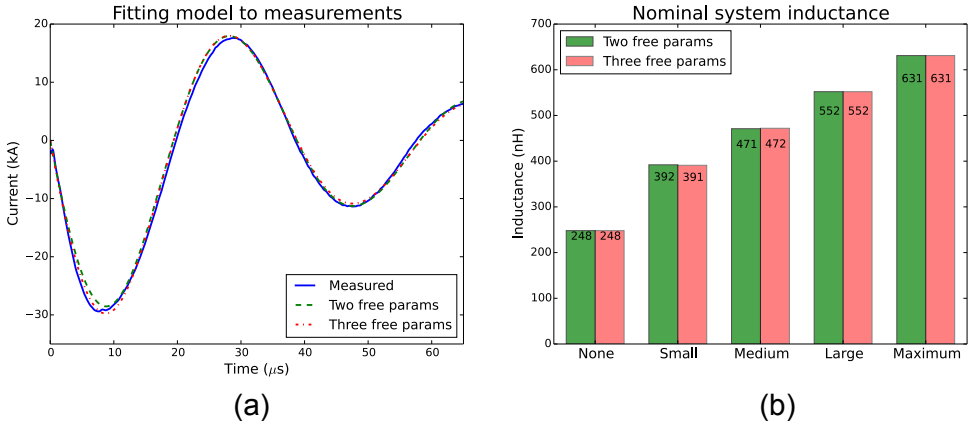

Figure G.19: (a) Measured current in 'Maximum' configuration compared to model fits with two/three free parameters. (b) Calculated nominal system inductance from model

with established measurements. The nominal resistance across the L_{extra} configurations range from 27-37 mΩ with average value 33 ± 4 mΩ. The nominal L_i =248 nH, 392 nH, 471 nH, 552 nH, and 631 nH for None, Small, Medium, Large, and Extra configurations, respectively.

One way to obtain better model fits is to add the charging voltage as another free parameter[11]. This yields a better fit at early times, as shown in Fig. G.19 (a), by increasing the resistance 10% compared to the two-free parameter fits, and by increasing the effective charging voltage 10% compared to the actual value. The nominal system inductance is unchanged by this additional free parameter (Fig. G.19 (b)), suggesting that the nominal inductance is robust.

It is possible to isolate the impact of individual free parameter, by restricting the fit interval to the first 14 μs. Imaging and magnetic diagnostics are available during this time, and can validate quantities obtained from fitting. The plasma arch is also expected to be reproducible during this early time, and the arch is connected[12] to the electrodes, and therefore connected to the power supply. The advantage of fitting to a single free parameter, is the ability to isolate the essential physics corresponding to a given experimental adjustment. Figure G.20 shows the measured current trace for

[11] This approach is equivalent to fitting the analytic under-damped RLC solution (Eq. D.1) with free parameters A, R, and L.

[12] The plasma legs go unstable and detach from the footpoints at later times.

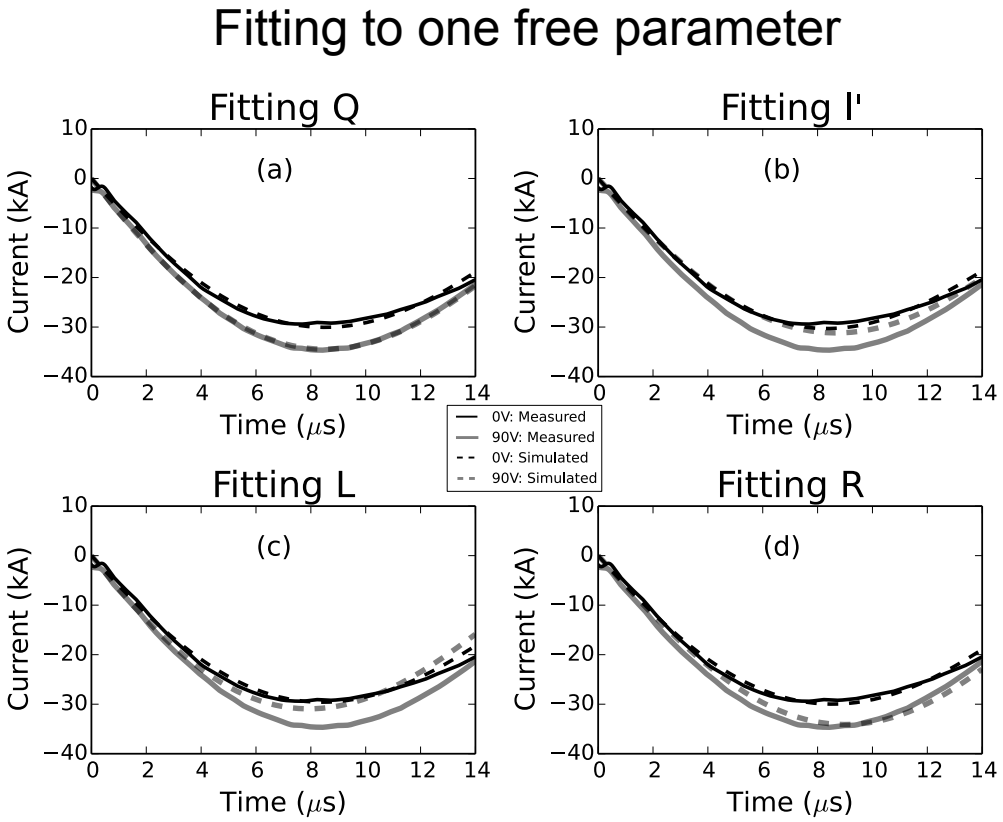

Figure G.20: Fitting current trace profile associated with two different strapping bank voltages (0 V and 90 V), by adjusting free parameters: (a) Q, (b), l', (c) L, (d) R.

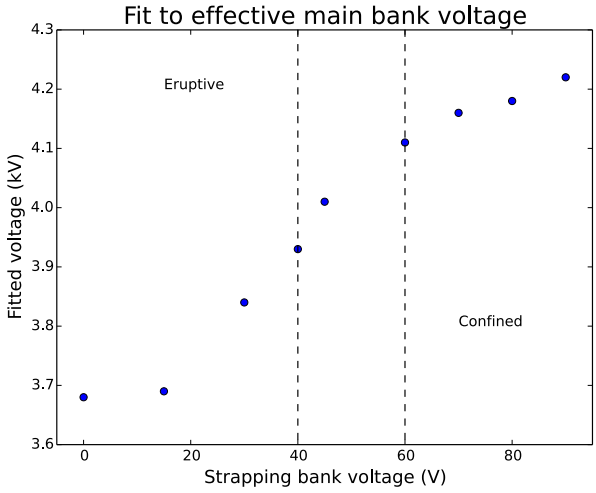

Figure G.21: Best fitted main bank voltage as function of strapping bank voltage.

configurations with no strapping field (thin dark lines), and configurations where the strapping field power supply is powered to 90 V (thick gray lines). The dotted lines show the best non-linear fits. The most effective parameter over this time is Q (Fig. G.20 (a)), which is directly proportional to the voltage of the main bank capacitor, since C is fixed and normalized. The parameters associated with inductance (l', L) match the current profile for one value of strapping field, but are unable to fit over all values of strapping field (Figs. G.20 (b) and (c)). This suggests that the application of strapping fields produce current traces with higher peak values, effectively raising the charging voltage of the main capacitor bank. Adjusting the effective charging voltage does not capture all the physics (Compare 0 V, measured and simulated, in Fig. G.20 (a)), since the system inductance L increases as the plasma expands. Nevertheless, the relative effectiveness of charge (compared to inductance) as a fit parameter indicates that the system can be considered a current source[13]. Figure G.20 (d) suggests that adjusting R can also produce respectable fits to the current trace, but the fits predict that $R \approx 27$ mΩ for 0 V strapping field, and $R \approx 9$ mΩ for 90 V strapping field. This factor of 3 decrease in resistance seems unphysical, and the predicted 9 mΩ is too small compared to measurements in Ref. [104].

Figure G.21 summarizes the fit parameters of Fig. G.20 (a) over different strapping

[13]See Sec. D.4.1 for discussion

field values. There is a strong match to Fig. G.14 (b), consistent with the conclusion that Q is a good fit parameter over different strapping bank voltages. Camera images show that plasmas are "confined" for strapping voltages above 60 V, and are eruptive for strapping voltages below 40 V, consistent with Fig. G.21.